UNIVERSITY OF CALIFORNIA SAN DIEGO

Piscine defense and hydro-actuated deformation strategies: Paths to Bioinspired Design

A dissertation submitted in partial satisfaction of the

requirements for the degree of Doctor of Philosophy

in

Materials Science and Engineering

by

Haocheng Quan

Committee in charge:

Professor Marc A. Meyers, Chair
Professor Shengqiang Cai
Professor Javier E. Garay
Professor David A. Gough
Professor Michael T. Tolley

2019

The Dissertation of Haocheng Quan is approved, and is acceptable in quality and form for publication on microfilm and electronically:

_____

_____

_____

_____

_____

Chair

University of California, San Diego

2019

DEDICATION

To my parents and my sister

Haocheng Quan

TABLE OF CONTENTS

LIST OF FIGURES

LIST OF TABLES

ACKNOWLEDGEMENTS

First and foremost, I am deeply indebted to my advisor, Prof. Marc A. Meyers. He has taught me, both consciously and unconsciously, how to do great scientific research. The joy and enthusiasm he has for his research was contagious and motivational, substantially influencing me to dedicate myself to the same field. I am grateful to all his contributions of time, ideas, and funding to make my Ph.D. study productive, stimulating, and extraordinarily dynamic. I also enjoyed the unforgettable experience of being his teaching assistant for 4 years, which refreshed and strengthened my knowledge on structural materials and basic solid mechanics, although it is not an easy job then. Inspired by his lifestyle, I became a devout disciple of physical exercise, including running, boxing, biking, and lifting. He demonstrates the importance of health for a productive scholar. As a man who has never been sick, Professor Meyers keeps coming to work almost every day, even most weekends. He has provided us an excellent example by his action, not by what he said: keep reading, thinking, doing and writing, stay curious about all the unexplored world and make yourself stronger, both physically and mentally. I wish I could be a scholar like him, who can have a fun, fickle, flirtatious Musa and a solid, serious, strong Scientia on each of arm.

I also greatly appreciate Prof. Robert O. Ritchie at UC Berkeley and all my committee members at UCSD, including: Prof. Shengqiang Cai, Prof. David Gough, Prof. Javier Garay and Prof. Michael Tolley. Prof. Ritchie provided us the opportunity to use the beamline facility in Lawrence Berkeley National Lab (LBNL) and mentored me a lot on the fracture toughness of biological materials. Working with him is always joyful and motivational. I really appreciate all his effort on our coauthored papers and his contribution is vital for them to be published successfully. I deeply thank Prof. Gough for offering me the teaching assistantship of our MAS

classes for several years. As a knowledgeable and considerate instructor, his lectures are fascinating and fruitful, providing me an exciting opportunity to deepen my understanding of polymers. Prof. Garay is a real gentleman, sending the warmest greetings every day when we met on campus. The comments and suggestions he raised in my senate exam are really constructive and inspiring for me to enhance my thesis. Prof. Cai and Prof. Tolley are always very generous to offer me to use the various equipment in their labs. I also made beautiful friendship with their group members through our collaboration. Without their help, I probably have to stay here for two more years.

The former and current members of Meyers group have contributed immensely to my personal and professional time at UCSD. I am grateful to Professor Bingfeng Wang, who introduced me to Prof. Meyers and convinced him to accept me as his graduate student. Shiteng is a great friend and mentor, enlightening me a lot on the knowledge about materials science. I still want to thank Dr. Wen Yang, who introduced many experimental techniques to me when I felt helpless at the beginning. Vincent and Everett are experts on a lot of equipment and Andrei is my comrade-in-arms. For all other colleagues, Eric, Tane, Andrew, Steve, Bin, Tarah, Daniel (Yu), Senhat, Audrey, Rachael, Josh, Gaia, Boya, Camila, Yufei, Arnoud and Marine, each piece of time I spent with them is memorable. I am also thankful to all the research staffs from various institutes who have provided tremendous help when I was stuck in many experiments, especially Mason Mackey, Eric Bushong, Guillaume Castillon in NCMIR (National Center of Microscopy Image Research) and Eric Schaible, Dula Parkinson in LBNL.

The support from my family is indispensable for my study in US. My father and mother are the greatest parents in the world. I am deeply grateful to their encouragement and financial support in the last 6 years. Their understanding and patience light up the darkness during some

hard time, providing me both psychological and economic security. My beloved little sister always has faith in me and hold me up as her example, which ‘pushes’ me to move forward and never give up.

Last but not least, I appreciate 6-year company of my dearest roommate and coffee buddy, Zezhou Li. Instead of a colleague, he is more like a family. We have fully supported each other and gone through countless sufferings, constructing this eternal friendship by our nightly drink. I also thank him for taking care of my Husky Oreo when I was absent.

Financial support is key to the success of this work. The work presented in this dissertation was supported principally by a Multi-University Research Initiative through the Air Force Office of Scientific Research of the United States (AFOSR-FA9550-15-1-0009). Additional funding sources include the National Science Foundation, Division of Materials Research, Ceramics Program Grant 1006931; The synchrotron small angle X-ray scattering (SAXS) and micro-computed tomography (μ-CT) data were collected at beamline 7.3.3 and beamline 8.3.2 of the Advanced Light Source, respectively through the Mechanical Behavior of Materials Program at the Lawrence Berkeley National Laboratory, which is supported by the Director of the Office of Science, Office of Basic Energy Sciences of the U.S. Department of Energy under Contract No. DE-AC02-05CH11231; some μ-CT and all transmission electron microscopy imaging (TEM) was performed at NCMIR at the University of California, San Diego, and funded by National Institutes of Health Grant P41GM103412 to Mark H. Ellisman.

Section 2.3 in Chapter 2, in part, is a reprint of the material as it appears in “A comparative study of piscine defense: The scales of *Arapaima gigas*, *Latimeria chalumnae* and *Atractosteus spatula*” Journal of the Mechanical Behavior of Biomedical Materials, vol 73, pp 1-16, 2017. This

work was coauthored by V. Sherman, W. Yang, R. O. Ritchie and M. A. Meyers. The dissertation author is the second author of this work.

Section 2.4 in Chapter 2, in part, is in preparation for publication with coauthors D. Kisailus and M. A. Meyers. The dissertation author is the first author of this work.

Chapter 3, in full, is published as "Novel Defense Mechanisms in the Armor of the Scales of the "Living Fossil" Coelacanth Fish", Advanced Functional Materials, vol 28, pp1804237, 2018. This work was coauthored by W. Yang, E. Schaible, R. O. Ritchie and M. A. Meyers. The dissertation author is the first author of this work.

Chapter 4, in part, is under peer review for publication with coauthors W. Yang, M. Lapeyriere, E. Schaible, R. O. Ritchie and M. A. Meyers. The dissertation author is the first author of this work.

Chapter 5, in part, is under peer review for publication with coauthors W. Yang, R. O. Ritchie and M. A. Meyers. The dissertation author is the joint first author of this work. The dissertation author is the first author of this work.

Chapter 6, in part, is in preparation for publication with coauthors Z. Tang, W. Yang, R. O. Ritchie and M. A. Meyers. The dissertation author is the first author of this work.

Chapter 7, in part, is in preparation for publication with coauthors A. Pirosa, W. Yang, R. O. Ritchie and M. A. Meyers. The dissertation author is the first author of this work.

VITA

2019 Ph.D. Materials Science and Engineering

University of California, San Diego, La Jolla, CA, USA

Dissertation: Piscine defense and hydro-actuated deformation strategies: Paths to Bioinspired Design

Advisor: Professor Marc A. Meyers

2014 M.S. Materials Science and Engineering

University of California, San Diego, La Jolla, CA, USA

2013 B.E. Materials Science and Engineering

Donghua University, Shanghai, China

PUBLICATIONS

Haocheng Quan, Wen Yang, Eric Schaible, Robert O. Ritchie and Marc A. Meyers, Novel defense mechanisms in the armor of the scales of the legendary Coelacanth fish, ***Advanced Functional Materials***, 2018, 28, 1804237.

Wen Yang, **Haocheng Quan** (joint first author), Marc A. Meyers and Robert Ritchie, Arapaima Fish Scale: One of the Toughest Flexible Biological Materials, in revision.

Haocheng Quan, Wen Yang, Marine Lapeyriere, Robert O. Ritchie and Marc A. Meyers, Structure and mechanical adaptability of a modern elasmoid fish scale from common carps, 2019, submitted.

Haocheng Quan, Zixiang Tang, Wen Yang, Robert O. Ritchie and Marc A. Meyers, Active defense mechanisms of thorny catfish, 2019, in preparation.

Haocheng Quan, David Kisailus and Marc A. Meyers, Hydro-actuated highly reversible deformation in biological materials - a review article, 2019, in preparation.

Haocheng Quan, Arnaud Pirosa, Wen Yang, Robert O. Ritchie and Marc A. Meyers, The contribution of gradient porosity to the hygroscopic movement of pine cones, 2019, in preparation.

Marc André Meyers and **Haocheng Quan**, The use of the h-index to evaluate and rank academic departments, ***Journal of Materials Research Technology***, 2017, 6, 304-311.

Vincent R. Sherman, **Haocheng Quan**, Wen Yang, Robert O. Ritchie and Marc A. Meyers**,** A comparative study of piscine defense: The scales of Arapaima gigas, Latimeria chalumnae and Atractosteus spatula, ***Journal of the mechanical behavior of biomedical materials***, 2017, 73, 1-16.

Jessica A. Sandoval, Saurabh Jadhav, **Haocheng Quan**, Dimitri D. Deheyn and Michael T. Tolley, Reversible, amphibious adhesion to rough surfaces inspired by the clingfish suction disc, 2019, in revision.

Andrei Pissarenko, Wen Yang, **Haocheng Quan**, Katherine A. Brown, Alun William, William G. Proud, Marc A. Meyers, Tensile behavior and structural characterization of pig dermis, ***Acta Biomaterialia***, 2019, 86, 77-95.

Seth Dike, Wen Yang, **Haocheng Quan**, Andrei Pissarenko, Marc A. Meyers, On the Gular Sac Tissue of the Brown Pelican: Structural Characterization and Mechanical Properties, in preparation.

Shiteng Zhao, Bimal Kad, Eric Hahn, Laura Chen, Yekaterina Opachi, Karren More, Bruce Remington, Christopher Wehrenberg, Jerry LaSalvia, Wen Yang, **Haocheng Quan**, Marc Meyers, Shock-induced Amorphization in Covalently Bonded Solids, DYMAT, 2018.

Haocheng Quan, Yuanlong Shao, Chengyi Hou, Qinghong Zhang, Hongzhi Wang* and Yaogang Li**, Room- temperature synthesis of 3-dimentional Ag-graphene hybrid hydrogel with promising electrochemical properties, ***Materials Science and Engineering: B***, 2013, 178, 769-774.

Chengyi Hou, **Haocheng Quan**, Yourong Duan, Qinghong Zhang, Hongzhi Wang* and Yaogang Li*, Facile synthesis of aqueous-dispersible Cu_2O nanocrystal-reduced graphene oxide hybrid as promising cancer therapeutic agent, ***Nanoscale***, 2013,5, 1227-1232.

PATENT

Yaogang Li, **Haocheng Quan** and Zhifu Liu, A method to assemble silica nanospheres on polymer fibers, *Chinese Patent*, application No. 201210303135.6.

ABSTRACT OF DISSERTATION

Piscine defense and hydro-actuated deformation strategies: Paths to Bioinspired Design

by

Haocheng Quan

Doctor of Philosophy in Materials Science and Engineering

University of California, San Diego, 2019

Professor Marc André Meyers, Chair

Mother nature is an ingenious master on developing efficient structural and functional materials, which manifest various fascinating properties that are superior to synthetic materials. Here, we systematically investigate two topics: the materials design for piscine defense and hydro-actuated reversible deformation of plant organs. In each topic, we selected several types of

biological materials to study and unravel the connection between their intelligent hierarchical structure and superb mechanical properties.

We selected three fish and fully investigated the structure and mechanical properties of their scales. The first is the legendary lobe-finned fish coelacanth, which is extant for 400 million years. This defense is provided by primitive elasmoid scales having a double-twisted Bouligand structure of collagenous lamellae. The collagen fibrils in coelacanth scale form bundles which are embedded in a matrix composed of fibers arranged perpendicular to the layered structure, providing added rigidity and resistance to deformation. The second one we studied is a more evolved scale from common carp. Carp has typical modern elasmoid fish scales which are commonly found on most current teleosts. Like coelacanth scale, the outer surface of carp scale is composed of mineralized layers and the inner core is comprised of collagenous lamellae. The lamella orientations in carp scale follows a single twisted Bouligand pattern, with a rotation angle of 36°. Moreover, perpendicular to the lamellae, thinner collagen fibrils, which are called threading fibrils here, form a "sheet-like" structure oriented from the basal part to the external layer. Using *in situ* synchrotron small-angle x-ray scattering during uniaxial tensile testing, the deformation mechanisms of the collagen in these two scales are identified in terms of fibril stretching, reorientation, sliding, bending and delamination. The third scale we studied is from one of the largest freshwater fish, Arapaima, which has successfully survived in piranha-infested seasonal lakes of the Amazon. To quantitatively investigate the scale's fracture toughness, we developed a new fixture and measured the *J*-integral based fracture toughness of the scale and find that the crack-growth toughness as high as ~200 $kJ \cdot m^{-2}$, which is one of the toughest flexible biological materials. This toughness is primarily the result of multiple mechanisms which are identified by

in situ SEM observation. Our results may bring some critical thinking for developing novel armor materials.

Instead of evolving body armor to protect themselves passively, some fish develop powerful weapons to defend actively. We fully investigated the thorny catfish (Doradidae; order Siluriforme), which has barbed pectoral fin spines and mid-lateral scutes that work *in concert* to provide an active mechanical defense capability. The structural design of these two weapons is very impressive, including a hollow structure, porous components, and gradient transitions, leading to an outstanding performance by maintaining strength, toughness and light weight synergistically. These designs can provide inspiration for developing new structural materials.

The second topic we studied is the hydro-actuated reversible deformation in plant organs. Plants have developed many intelligent strategies to respond to external stimuli, significantly benefiting their survival. Here we studied a classic: pine cone, which opens to release the pods upon drying and can reclose upon rehydrating. We unraveled a novel mechanism of reversible deformation actuated by hydration. Our findings provide an interdisciplinary perspective combining materials science, structural engineering and biology, as well as offering some design models for development of novel smart responsive materials which have improved mechanical properties and biocompatibility yet simpler strategy.

CHAPTER 1: INTRODUCTION AND OBJECTIVES

1.1 Biological materials science

Materials science is an interdisciplinary field that studies the structure, properties, and performance of all the substances which can be used by human for all kinds of purposes. Among them, biological materials, also called natural materials, are both the oldest and newest ones. Much earlier than the appearance of the all the 'typical' materials that we are familiar with, like metals, ceramics and polymers, human was using biological materials formed in nature, including bones, antler, wood, skins, and furs, as structural materials for weapons, buildings, tools as well as other purposes like clothing and ignition (Figure 1-1). However, biological materials being added as a subdiscipline of materials science and engineering, started as late as in 1990s.

Nowadays, people are looking at the biological systems from a perspective of materials science in different scales (Figure 1-2). At the organism level, the mechanics behind the locomotion of many animals generates a great source of inspiration for improving the efficiency of transportation or designing more functional robotics. At the tissue level, the toughening mechanisms of bone, teeth and skin not only inspire engineers to create novel high-performance structural materials, but also help the medical doctors and pharmacologists to cure the related diseases[1]. At the cell level, stiffness changes of the cell are related to oncogenesis and thus time-saving and user-friendly equipment for cancer diagnosis is developed by detecting differences in mechanical properties of cells[2,3]. All the way down to the molecular level, incorporating nanotechnology and molecular biology, biological nanomaterials play a vital role in the treatment of many fatal diseases. Without any exaggeration, the development of biological materials science is indeed the future of the advances in materials science and engineering.

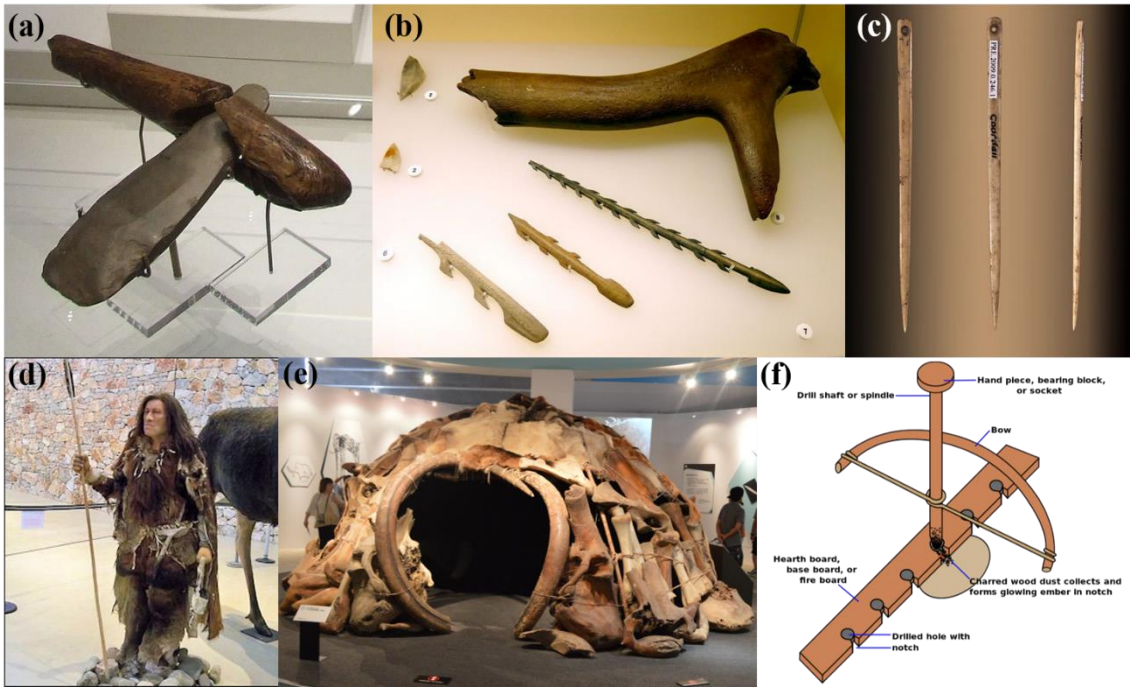

Figure 1-1 Biological materials used in stone age. (a) A Neolithic stone axe with a wooden handle, found at Ehenside Tarn. It is on display in the British Museum, London. (b) Harpoons and Lyngby Axe (an axe made of antler) dated to around the 11th millennium BCE and belonging to the Mesolithic Age. (c) Flat bone sewing needle found at Gourdan Cave, Haute-Garonne, France. It belongs to the western European Magdalenian culture (c. 17,000 - c. 10,000 years ago) of the Late- or Upper Palaeolithic industry (c. 50,000/40,000 - c. 10,000 years ago). (d) A model of early modern man wearing fur garments. (e) A replica of a Mammoth Bone Hut based on finds from Mezhyrich in the Central Ukraine. (f) Diagram of a bow drill designed for fire starting, which is used in Mehrgarh.

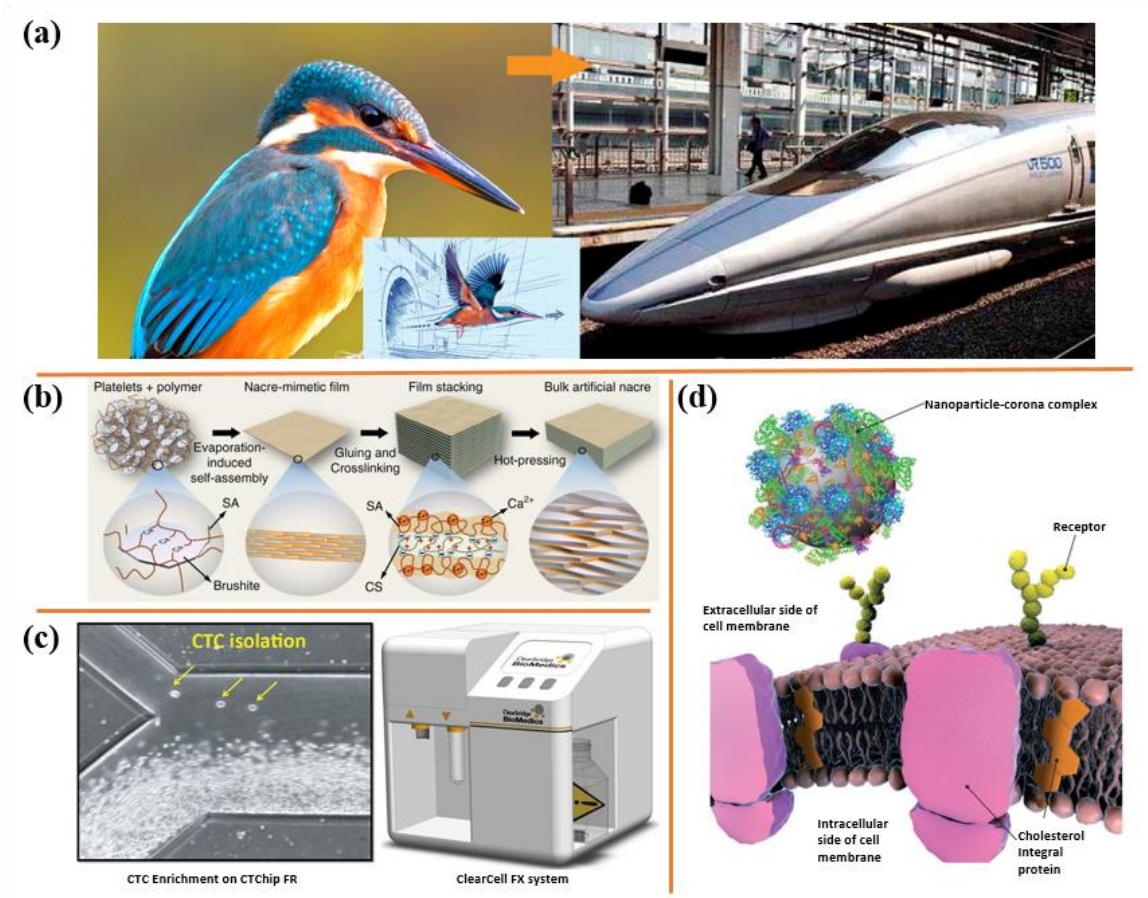

Figure 1-2 Biological materials used in modern technology. (a) The design of Shinkansen train nose is inspired by kingfisher.s beak. (b) Schematic illustration of the fabrication of nacre inspired tough ceramics. (c) Isolation of circulating tumor cells (CTCs) based on the difference of size and deformability between tumer cells and normal cells and the equipment based on such technology, ClearCell FX, which can enrich wholly intact and viable Circulating Tumour Cells (CTCs) from small amounts of blood in a relatively short time. (d) The nanoparticle–corona complex interacting with a cell membrane recptor, which is the key of the biological identity of the nanoparticle for drug delivery[4].

1.2 Structural biological materials

From the perspective of materials science, many biological systems have numerous outstanding properties that are superior to the synthetical materials; the mechanical properties are the most distinguishable ones[5]. Spider silk is super strong, nacre, bone and skin are extraordinarily tough, and bird beaks, feathers and plant stems are extremely light but have excellent bending or buckling resistance[6-11]. The materials listed above are composed of common biominerals and biopolymers, the mechanical properties of which are not impressive compared with synthetic materials. However, manipulating them through an intricate and ingenious hierarchical fashion, mother nature creates these high-performance biological materials, enabling the organisms to survive in their living environments. Bone and skin are two excellent examples.

The appearance of bone is the main advantage for vertebrates in evolution, which provides support and protection to many organs, extending the effective length of limbs, expanding the activity radius, as well as encouraging the development of a strong muscular system protected by an environment sensitive dermis[12]. The mechanical properties of bone exhibit great strength coupled with excellent toughness, which are often mutually exclusive in most synthetic materials[13]. Bone achieves such impressive performance by combining the mineralized collagen fibrils and hydroxyapatite nanocrystals in seven levels of hierarchy and the prevailing toughening mechanisms can be classified into two categories: the intrinsic ones and the extrinsic ones, depending on whether the region they dominate in is in front of the crack tip or behind the crack tip (Figure 1-3)[8,14], respectively. At the smallest level, on the scale of the tropocollagen molecules and mineralized collagen fibrils, (intrinsic) toughening, that is, plasticity, is achieved through the mechanisms of molecular uncoiling and intermolecular sliding of molecules. At coarser levels, on the scale of the fibril arrays, microcracking and fibrillar sliding act as plasticity mechanisms and

contribute to the intrinsic toughness. At micrometer dimensions, the breaking of sacrificial bonds at the interfaces of fibril arrays contributes to increased energy dissipation, together with crack bridging by collagen fibrils. At the largest length scales, in the range of tens to hundreds of micrometers, the primary sources of toughening are extrinsic and result from extensive crack deflection and crack bridging by uncracked ligaments; both mechanisms are motivated by the occurrence of microcracking.

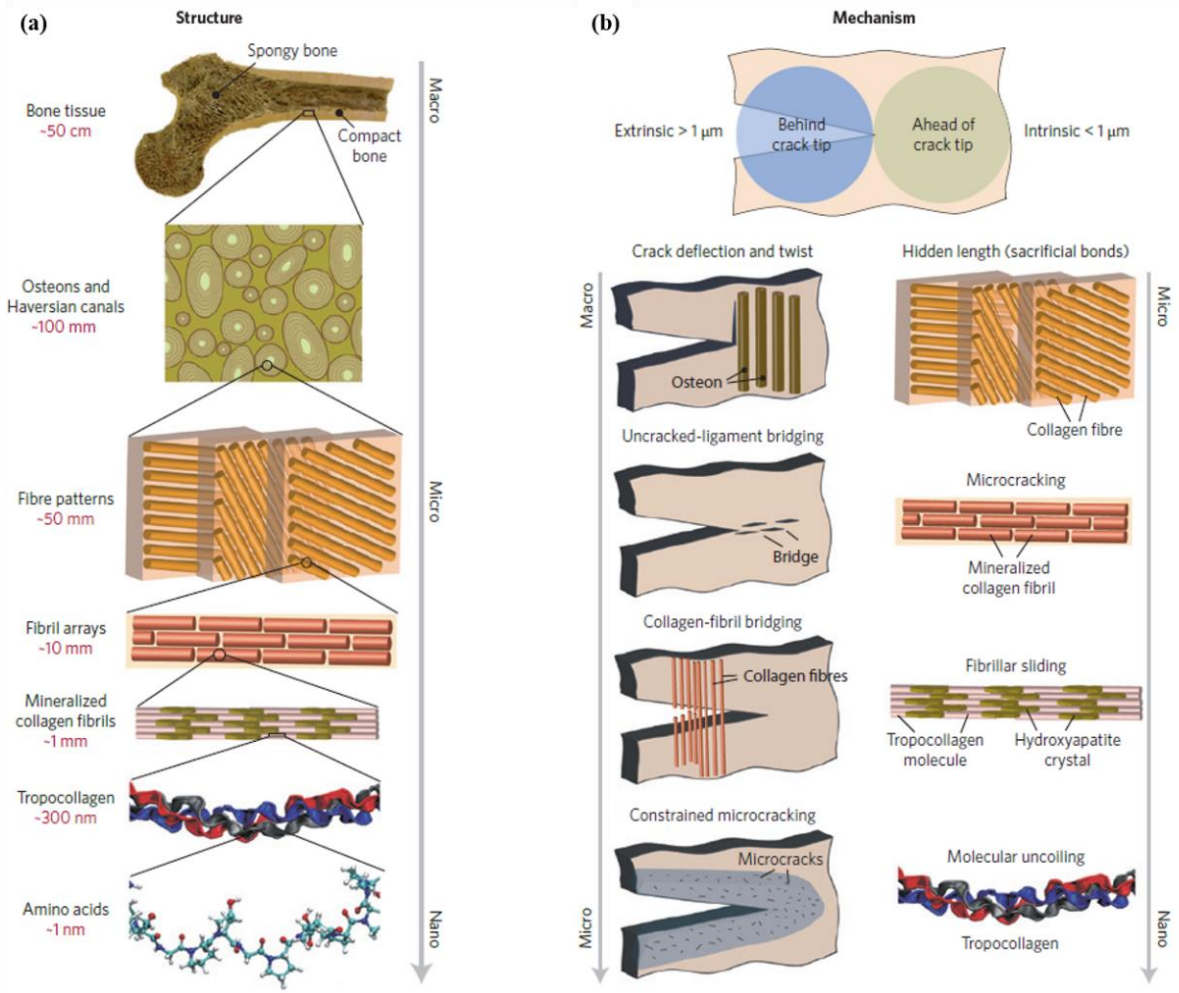

Figure 1-3 The structure and toughening mechanisms of bone. (a) The structure of bone showing the seven levels of hierarchy[14]. (b) The prevailing intrisinc and extrinsic toughening mechanisms in bone[8].

Skin is another very important structural material in our human body providing the first protection barrier for our body from the outside. Such protection requires great mechanical properties[4]. The stereotype of skin for most people is soft, tender and probably weak. However, skin is much tougher than people thought. Figure 1-4 shows a man completing a suspension base jump, which involves throwing himself off a cliff while attached to a parachute via hooks embedded in the back. During this entire process, the penetrated skin was never teared under the impressive load, which indicated the tough nature of our skin. Generally, the skin of most mammals has two layers: the epidermis and the dermis layers, the later one composed of abundant curvy collagen fibers. These curvy collagen fibrils act to enhance skin's tear resistance through their rearrangement towards the tensile-loading direction, with rotation, straightening, stretching, and sliding/delamination before fracture, which makes it an excellent damage tolerant material (Figure 1-5)[4].

Figure 1-4 The highest base suspension to date. Over two minutes the jumper was suspended under canopy from piercings through the flesh and skin on his back.

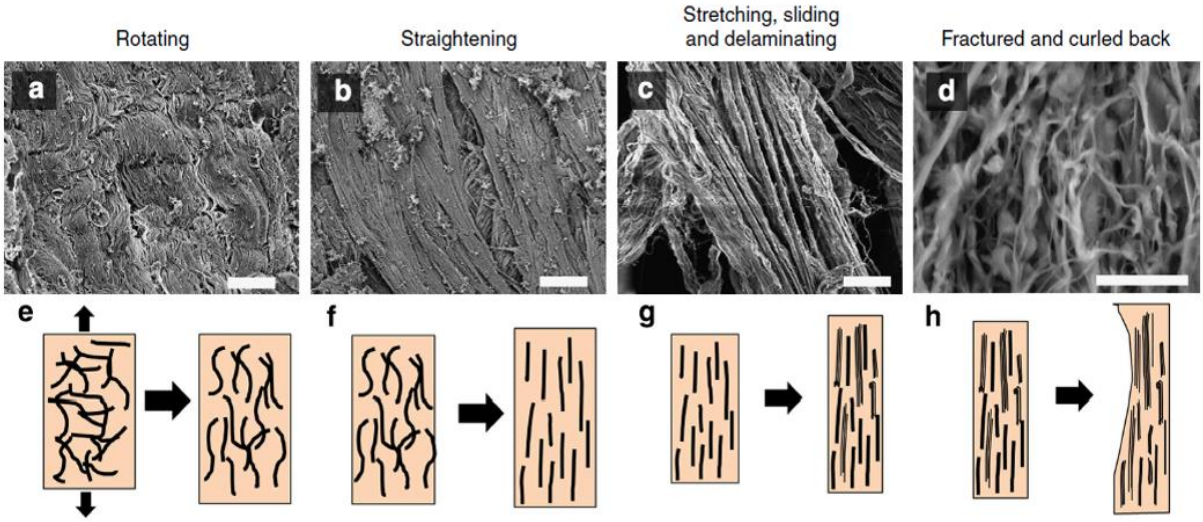

Figure 1-5 Mechanistic stages of the tensile loading of skin[4]. SEM images (a–d) and schematic drawings (e–h) of the mechanisms during the four stages of tensile loading of rabbit skin, black arrows in (e) represent the direction of tension testing. (a,e) Curved collagen fibrils are oriented along the tensile axis; (b,f) collagen fibrils are straightening, larger and larger amount of the fibrils re-orient close to the tensile axis; (c,g) collagen fibrils are stretching, sliding, delaminating and orientated completely along the tensile axis; (d,h) collagen fibrils are fractured and curled back. Scale bars in (a–d) are 20, 20, 20, 50 mm, respectively.

Besides bone and skin, there are numerous other examples which manifest how ingenious mother nature is to develop these efficient and high-performance biological structural materials with only limited building blocks and under mild conditions. Studying the connections between the complex structure and the outstanding mechanical properties is the key to help materials scientists and engineers to tap new sources of designing novel structural materials in many emerging fields. It is quite challenging since understanding and mimicking the masterpieces that take nature billions of years to create is a very brain-squeezing work, but as materials science student who work in this field for 5 years, I do feel it is an exciting and promising field.

1.3 Passive responsive materials produced by biological systems.

With artificial intelligence being implemented into multiple applications worldwide, intelligent devices are rapidly emerging in systems like robots, self-driving vehicles, portable health monitors, and personal assistive devices. This is also important in the manufacturing industry, where new challenges are demanded for developing novel materials; one of the important developments includes intelligent or smart materials. The most distinct characteristic of these new types of materials is that they have tunable properties that can be changed by external stimuli in order to achieve desired performance. The smart material, itself, is a machine, and can sense specific signals (stimuli) and provide a corresponding response without external interference. Many types of smart materials have been successfully developed, such as self-diagnosis materials[15,16], self-degradable materials[17,18], and self-repairable/healing materials[19-21], self-coloring materials[22,23], self-shaping/morphing materials[24-26]. Among these categories, the most widely investigated ones are self-shaping materials (also called shape-memory materials), which have the ability to change, or even program in some cases, their shape or morphology based on external stimuli. A wide range of self-shaping materials have been fabricated, including assorted alloys[27], polymers[28], ceramics[29], and their composites[30]. The triggers to induce their designed morphology include heat, light, electricity, magnetic fields, moisture, or other solvents. These synthetic smart self-shaping materials play an important role in various applications including actuation systems of robotics[31,32], camouflaging armor[33], biomedical devices[34,35] and drug delivery[36,37]. Nevertheless, the major stumbling block towards the development of self-shaping materials, especially with respect to interaction with the human body, is their biocompatibility. Either their material compositions are toxic or their triggering and operating environments (e.g., high temperature, electric/magnetic fields, ultraviolet light and special

solvents) are harmful to our health. In order to develop self-shaping materials (as well as other smart materials), which have better biocompatibility and can be stimulated and operated in mild environments, researchers are looking to nature and trying to derive inspiration from natural materials.

Driven by billions of years of evolution, nature has developed innumerable self-tunable intelligent materials which are crucial for the survival of species in various environments[5,13,38]. . Some of them are active, meaning that the responsiveness of the tunable properties relies on the metabolism of the living organisms. For example, chameleons[39] and some species of squid[40] are able to actively tune their skin color to camouflage themselves. Echinoderms, like sea cucumbers, can reversibly modify the stiffness of their dermis by rapidly regulating the interaction between the collagen fibrils and the soft reinforced matrix, which plays an important role in complex locomotion, postural maintenance, defense, and reproductive strategies[41,42]. Plants have also evolved many intelligent strategies to actively respond to external stimuli, significantly benefiting their survival. The two most famous representatives are mimosa[43] and Venus flytrap[44], both of which can achieve expeditious reversible deformation of their leaves triggered by the loss of turgor in the plant cells. These stress responses are vital to their self-defense or predation.

Another class of responsive natural materials that is exciting more interest in the materials science and structural engineering community includes plant organs and animal tissues that display passive stimulation. Their underlying deformation mechanisms are completely determined by the structural design. Therefore, understanding these actuation strategies can provide inspiration to develop novel smart responsive materials. The most common examples are reversible shape change triggered by changes in moisture content, which are prevailing strategies for plants to disperse their seeds and improve germination. Pine cones, ice plant seed capsules, carrotwood seed pods and some

pea pods are able to release their seeds in the most favorable environments by actuating structures driven by humidity change[45-47]. The seeds of wild wheat and the storks' bill (*Erodium cicutarium*) can bury themselves in soil through reversible hygroscopic bending or coiling, which significantly increase their survivability[48,49]. Some biological materials produced by animals also have a similar capability. Keratinous materials like bird feathers, sheep horns and animal hairs are able to both recover their shape and retain mechanical properties through hydration effects[50-53]. Spider silk is an excellent example of a natural biopolymer displaying higher reversible supercontraction stimulated by humidity change[54,55].

In Section 2.4, we reviewed the best-known examples of highly reversible deformation in biological materials. Although we focus more on plant organs, we also include some animal tissues. The reviewed structures display purely passive deformations, which rely on their hierarchical structural designs, with actuation driven by hydration. We present three hydro-actuation mechanisms for the selected plant samples and one general recovery mechanism for animal tissues. In the last section, we also provide some current developments on synthesized smart materials inspired by these biological materials, including self-shaping materials at different length scales and artificial muscle fibers that can generate impressive forces. This review provides an interdisciplinary perspective, incorporating materials science, structural engineering, and biology, and offers design models for the development of novel smart responsive materials which have improved mechanical properties and biocompatibility. In Chapter 7, we studied a classic example, pine cone, in detail and unraveled a novel mechanism for its hydro-actuated reversible deformation.

1.4 Objectives

After millions of years of evolution, fish developed scales as a dermal armor covering their entire body, which provide effective protection from impact and penetration due to predatory attack through a multi-layered hierarchical structure. Moreover, fish scales are assembled in an imbricated way, which improves the stress distribution caused by predatory attack, and also enables the overall flexibility of the fish body. In the research component of fish scales, we aimed to:

1. Investigate the structure and mechanical behavior of scales from three fish: coelacanth, carp and arapaima.
2. Use the synchrotron small angle x-ray scattering (SAXS) to reveal and compare the toughening mechanisms of the collagenous layer in coelacanth scales and carp scales.
3. Design new fixture and measure the fracture toughness of arapaima scales.
4. Unravel the locking mechanisms of the pectoral spines of thorny catfish and mimic the structural design by 3D printing.
5. Characterize the structure and test the mechanical properties of the pectoral spines and midlateral scutes of thorny catfish.

Hygroscopic movement, the moisture-driven deformation is prevailing in the tissue of plants, especially in the tissue containing or connecting the seeds. They enable the plants to disperse their seeds in the favorable condition and burry the seeds into the soil by themselves, significantly increasing the survivability of the seeds. The opening and closure of pine cone is a classic example and people just found that after million years it still has such function. In the research component of pine cone, we aim to:

1. Summarize the hydro-actuation mechanisms of the reversible deformation in biological systems.
2. Characterize the hierarchical structure of each layer in pine cone
3. Unravel the more complete mechanisms for hydro-actuated reversible bending of pine cone.
4. Measure the moisture sorption isotherm and the actuation force of isolated pine cone scales.
5. Synthesize layered hydrogels with different porosity to mimic this hydration-induced bending actuation.

CHAPTER 2: BACKGROUND

2.1 Natural flexible dermal armor

Many animals possess flexible dermal armor for protection, which is an example of evolutionary convergence. Different species, like fish (sharks, arapaima and alligator gars), reptiles (alligators, crocodiles, lizards and turtles) and mammals (armadillos and pangolin), live in totally different environments but have evolved the dermal armor to protect them from the predatory attack, although the materials comprising them may be different[11].

Figure 2-1 shows six species whose dermal armors have been well studied[55-59]. Arapaima gigas and alligator, shown in Figure 2-1 (a) and (b), respectively, are two types of fresh-water fish but they have two entirely different scales covering their bodies. Arapaima has elasmoid scales, which are the prevailing type of scales for current teleosts and are very tough. They resist the penetration of the predators' teeth by the mineralized outer layer and dissipate the stored energy through the great deformability in collagenous inner layer, which makes them a great damage tolerant material[56]. The fossil record of the alligator gar traces its existence to the Early Cretaceous, over a hundred million years ago and their scales, ganoid scales, are a type of quite primitive tissue. These scales are thick and rigid, usually constructed by two or four layers with relatively high mineralization, resulting in excellent penetration resistance[57]. The detailed structure and mechanical behavior of these two types of scales will be provided in Section 2.3. Figure 2-1 (c-f) presents four types of dermal armor in mammals and reptiles, two for each, respectively. Except for the pangolin, the dermal armor of armadillo, turtle and alligator are all osteoderm-based.

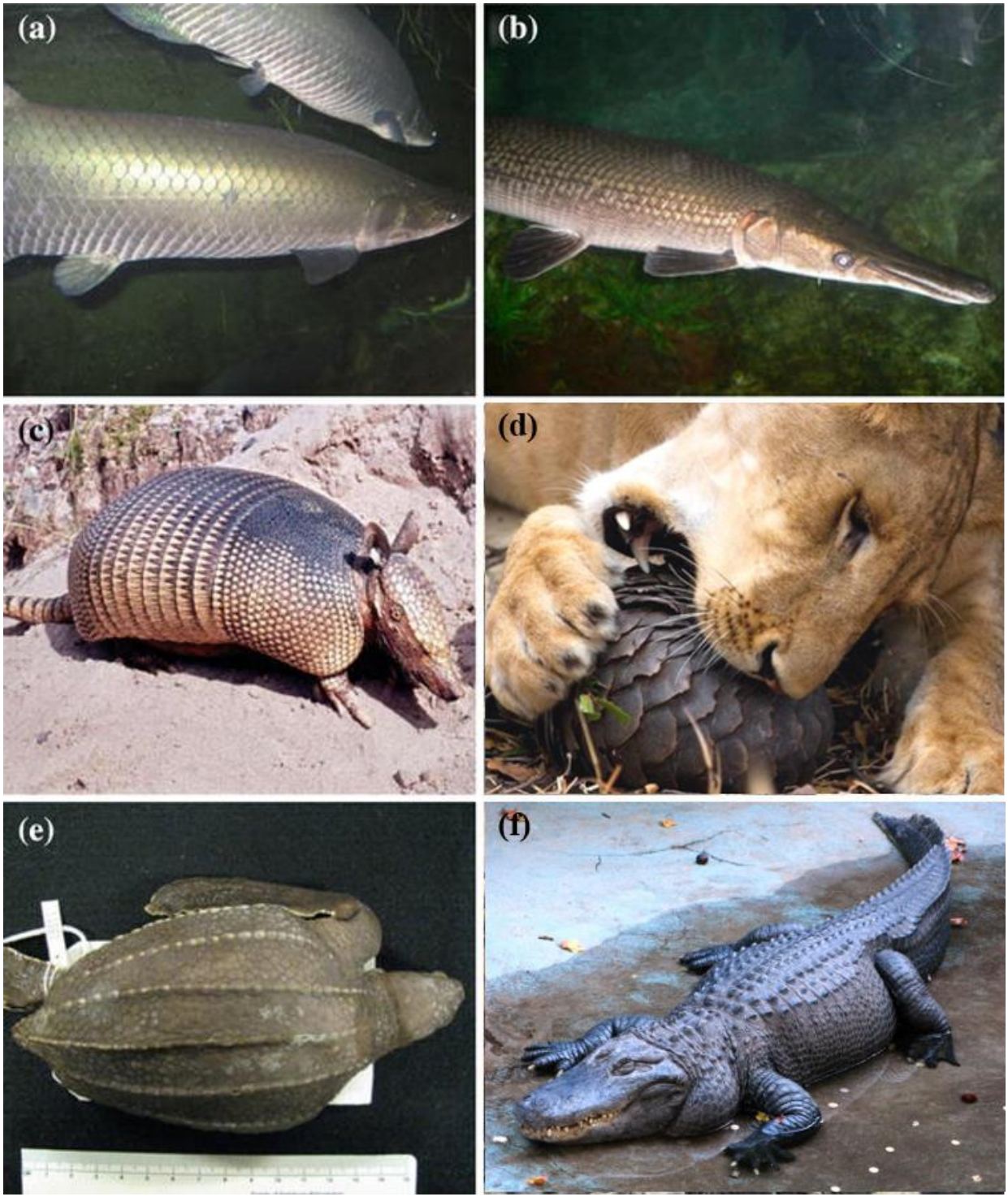

Figure 2-1 The dermal armor from the selected animals[50-55]: (a) arapaima gigas, (b) alligator gar, (c) armadillo, (d) pangolin, (e) leatherback turtle and (f) alligator.

Osteoderm, as the name indicates, is the mineralized dermis (bony skin) with structure resembles bone. Different from the scales, which are partially overlapped on the fish body, most osteoderms on terrestrial animals are juxtaposed and connect by collagen fibers to provide the flexibility. This is due to the surface topography of dermal armor in terrestrial animals, which is not governed by the fluid mechanics requirements, which is very necessary for aqueous creatures[11]. Figure 2-2 (a) presents the hierarchical structure of the osteoderm in the armadillo (*Dasypus novemcinctus*)[58]. It covers the entire body except the soft belly. The very top surface is the epidermis layer, which is composed of α -keratin and serves as a waterproofing layer. Below the epidermis, the osteoderms show three characteristic regions: an external dense bone, a central porous bone, and an internal dense bone layer, as shown in the cross-sectional image in Figure 2-2 (a). This sandwich structure (a foam core enclosed by dense outer shell) is a very common strategy for biological materials to reduce the density along with maintaining the stiffness and energy absorption capability[58]. The shape of the osteoderm plate varies on different parts of the body and they are all connected with non-mineralized collagen fibers, which are also called Sharpey's fibers. These robust fibers not only ensure the integrity and toughness of the tiling systems but also provide the flexibility. The osteoderm itself, similar with bone, has mineralized collagen fibers inside embedded in the mineral matrix, which strengthen the material in tension and significantly improves the deformability. These materials with different mechanical properties are structured in such a hierarchical way to confer excellent protection for many mammals and reptiles from predatory attack.

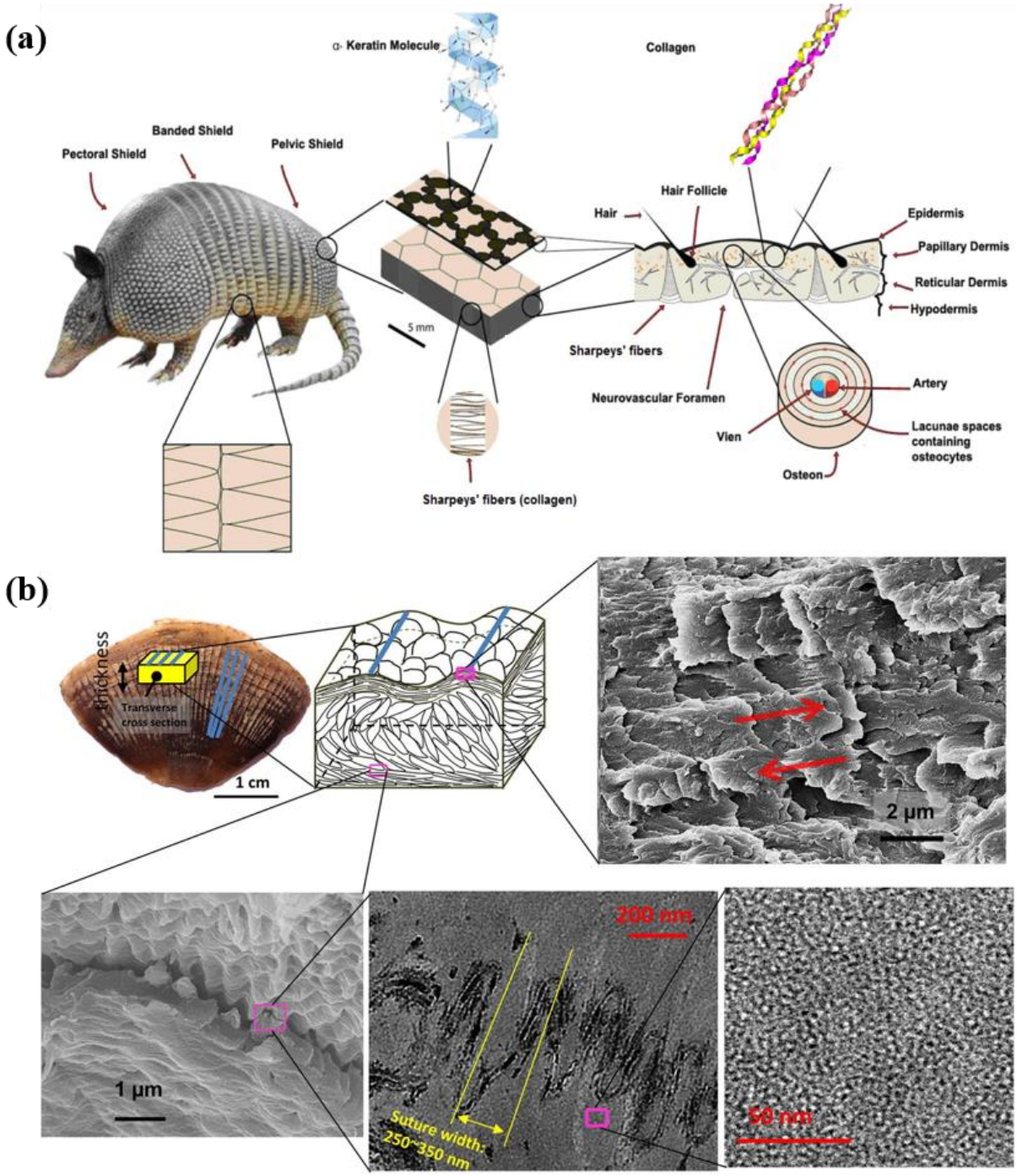

Figure 2-2 Hierarchical structure of the dermal armor for two animals[52,53]. (a) The osteoderm-based dermal armor for armadillo. (b) The keratin-based dermal armor for pangolin.

Pangolin is a rare case that the terrestrial mammal armored by a pure keratin-based protection layer. Similar with the arrangement of fish scales, the pangolin scales are also overlapped with neighboring ones to provide flexibility; the overlap ratio depends on species[56]. Figure 2-2 (b) shows the structure of the pangolin scale from the nano- to meso-level. The scales have a cuticle structure on the top surface which is composed of 3 ~ 5 layers of loosely attached keratinized cells. The core consists of three regions: a dorsal region of flattened cells comprising crossed lamellae parallel to scale surface, a middle region filled with tilted and less flattened cells with usually larger dimensions forming lamellae, and a ventral region that is similar to the dorsal region. At the microscopic level, the nanostructure is composed of filaments with 3 ~ 5 nm diameter. Each lamella is built up by one layer of cells, crossed fibers connecting the adjacent lamellae. Also at the nanoscale, the scales show an interlocking interface between lamellae, which results from the suture-like cell membrane complex between keratinized cells. Such suture structure improves bonding and shear resistance, which increases the strength and damage tolerance and makes the scale an excellent armor material.

Different species have evolved flexible and hard dermal armor. This independent evolution process is an excellent example of evolutionary convergence. These dermal armors in fish, reptiles and mammals are different in form, structure and components, all provide outstanding protection, which is now inspiring researchers to create synthetic systems based on similar concepts.

2.2 Evolution and classification of fish scales

The ability to mineralize a skeleton is one of the major innovations of vertebrates, providing protection and enhancing locomotion[60]. In the evolution history of skeleton mineralization, most of the early skeletonizing vertebrates possessed a mineralized integument including various surface components and/or enclosed mineralized elements, which constitute the dermal skeleton. The fish scale is a primary example. The evolution of fish scale is part of the evolution of the integumentary skeleton in non-tetrapod vertebrates[11].

2.2.1 Introduction to the integument skeleton

Vertebrate integument system forms a continuous, heterogeneous covering of the body surface and it is usually comprised of two distinct layers: the epidermis and dermis. They separate from one another at the early stage of ontogeny by a basement membrane, and from underneath muscle by the hypodermis[58]. When it develops maturely, caused by the accumulation of keratin and phospholipids with bound calcium, the epidermis is stratified and becomes hardened, serving as a permeability barrier and providing mechanical protection[58]. In the same stage, many cells in the epidermis layer are highly specialized and some of them are involved in the formation of non-skeletal epidermal scales and integumentary appendages, such as feathers, hairs, claws, beaks, nails, and pangolin scales[61]. Furthermore, in the case of the fish scale, the epidermis layer is penetrated by the mineralized tissue formed in the dermis layer, generating the surface features of the outer layer of fish scale[60].

The layer underneath the epidermis is the major component of the integument, dermis, a fibrous connective tissue that only appears in vertebrate cephalochordate[62]. It offers both physical and metabolic support to the epidermis and is also the structural framework for the other integumentary elements[63]. In vertebrates, the dermis is a thick, collagenous fibrillar framework

comprised of type I collagen and an amorphous ground substance[64]. The cells in the dermis layer are mostly fibroblasts; some undifferentiated cells are involved in the mineralization process for the fish scales. Dermis is structurally also composed of two layers[65]. The outer layer (close to the epidermis layer) is more loosely and irregularly arranged, containing blood vessels, nerves and pigment cells, while the inner layer (close to the muscle) is comprised of more tightly packed large bundles of collagen fibrils. The deepest collagen layers form lamellar and orthogonal arrangements which structurally resembles the arrangement of collagen layers in lamellar bone and in the elasmoid scales[66]. The collagen-rich inner layer in the dermis is the stress-resisting component that endows the excellent mechanical behavior of the integument.

2.2.2 The development of fish scales

The fish scale is a form of integument skeleton, also called dermal skeleton, which can be understood as mineralized skin. The formation of the fish scale is involved in the mineralization of the integument elements which diverse in different tissues in the current fish scales. This mineralization process originates from two fundamental types of cell condensation: odontogenic and osteogenic[65,67,68].

The odontogenic condensation is the foundation of forming odontogenic organs (teeth), which initiates the dental tissue such as enamel, enameloid, dentine, and bone of attachment. For example, the ganoid and dentine layers in ganoid scales, the odontodes in coelacanth scales and the limiting layer on the modern elamsoid scales are all formed by this process. The cells involved in the odontogenic condensation are a well-delimited population of densely organized mesenchymal cells, the dental (=odontogenic) papilla[60].

The osteogenic condensation, also called osteogenic primordium, is the foundation of developing integumentary elements which form bone and fibrous connective tissue in fish scale or, more generally, in the integument skeleton in vertebrates. This process typically happened in dermis layer, where the collagen fibrils are integrated in the organ development. At the initial stage, the pre-existing collagen matrix is rapidly remodeled by the osteoblasts, synthesizing new materials including various collagens and non-collagenous proteins which are incorporated into this matrix. This provides a favorable environment for the deposition of bone matrix and mineralization of the pre-existing matrix. The plywood-like tissues in elasmoid scales, the lamellar bone in ganoid scales and the scutes and dermal plates of armored catfish, are formed from this process. The cells involved in the osteogenic condensation are mesenchyme cells without well-delimited papilla and they differentiate from scleroblasts with osteogenic competence[60].

Most of the elements in the integumentary skeleton in current non-tetrapods originate from the types of cell condensation introduced above. However, they generate a large variety of structures which significantly confuses people who are not experts in anatomy or ichthyology. For example, the term ‘scale’ is commonly applied for both keratinized tissue (pangolin scales) and mineralized organs (fish scales, carapace or dermal plates). Moreover, ‘mineralized scales’ refers to an enormous diversity of integumentary skeletons, ignoring they are comprised of different tissue compositions and originate from different development processes. Therefore, in the classification of integumentary skeletons, including fish scales, is quite confusing for non-professionals, and many terms are misused in scientific articles, especially in the field of studying structural biological materials, where fish scale is a very hot topic now. Here, we try to classify the fish scales based on their tissue compositions and origins, inspired by the work done by anatomists Sire et al[60,65,66].

2.2.3 Tissue diversity of the fish scales

Since the classification of fish scales is based on the tissue components and developmental origins, an introduction to tissue diversity of fish scales is necessary. As mentioned in Section 2.2.2, all the different types of tissues in fish scales are categorized as either odontogenic (more like teeth) or osteogenic (more like bone). These two categories can form elements separately (e.g. teeth or dermal plates) or can be combined together in some scales (e.g. ganoid scales of bichirs). Additional subcategories are divided by the degree of mineralization, content of collagen and the relative amounts of other components. Following the classification by Sire et al.[60], four main groups of well-recognized tissues are identified in fish scales.

Hypermineralized (capping) tissues

Hypermineralized tissues are a group of hard, protective tissues which form the cap of teeth as well as the outer layer of some fish scales[60]. The characteristics of hypermineralized tissues are crystalline (mostly hydroxyapatite crystals), acellular (or cell-poor), avascular, non-collagenous (collagen-poor), and manifest relatively high hardness. The common hypermineralized tissues include enamel, neameloid, ganoine, hyaloine and the limiting layer. Enamel is homogeneous and highly mineralized without any collagen or cells inside. Enameloid is quite similar with enamel from aspects of topology and function, except that the crystalline arrangement is less ordered than enamel and a loose network of thin collagen fibrils are present in the organic phase before fully maturing. Both enameloid and enamel have been identified in the scales of shark, ray, ray-finned fish (bichirs, gars, teleosts, etc.) and the juvenile stage of some amphibians. Ganoine is a shiny, acellular, non-collagenous tissue which originates in epidermis and has been found in the top layer of ganoid scales. The two most famous examples are ganoid scales of bichirs and gars (alligator gars). It is also a relatively hard tissue which provides great penetration resistance for these fish.

Hyaloine is a non-collagenous hypermineralized tissue covering the surface of the post-cranial scutes in armored catfish. It is comparable to ganoine in ganoid scales but unlike the ganoine which is arranged in multiple layers and directly covered by epidermis, the top surface layer in hyaloine is always separated from the bottom epidermal layer cells by a narrow space filled with mesenchyme cells[60]. The limiting layer is a well-mineralized tissue with little collagen (Sharpey's fibers), covering the surface of the exposed region of teleost elasmoid scales.

Dentine

Dentine is a collagen-rich, highly mineralized tissue developed via an odontogenic pathway, which is also the characteristic of teeth and tooth-related organs. In general, dentine is associated with enamel or enameloid since they have same origin. During the development of dentine, predentine, an unmineralized matrix, which contains principally type I collagen and various glycosaminoglycans, is formed first and followed by mineralization. The dentine in mature state is composed of 75% minerals, 20% organic and 5% liquid. In current living vertebrates, dentine is usually formed with structures of well-aligned tubules and canaliculi containing cells[60].

Plywood-like (or Bouligand) tissues

Plywood-like tissues are collagen-rich fibrous tissues exhibiting a plywood-like organization consisting of numerous lamellae of collagen. The collagen fibrils in each layer are arranged in parallel but between adjacent layers the orientation of lamella is off-set by certain angle, making the stacked successive layers form a plywood like structure. There are two main types of orientation in the existing plywood-like tissues. The first one is the orthogonal, which typically exists in dermis and some fish scales. The second one is twisted plywood-tissue, which is identified in bones and fish scales. The twisting system with constant off-set angle is also called Bouligand structure or helicoidal structure in the literature on biological materials. A similar

structure is also found in the exoskeleton in crustaceans, although the fibrils there are chitin. Most plywood-like tissues are cell and vascular absent and the mineralization also varies. For example, plywood-like tissue in ganoid scales of bichir are highly mineralized and that in elasmoid scales are only slightly mineralized. Attributed to the collagen-rich composition, the plywood-like tissues are responsible for carrying tensile stress as in most fish scales, which can strengthen the tissue in tension and bring up excellent toughness through plastic deformation. Some terms appear in the description of components in integumentary skeleton, like stratum compactum of the dermis, lamellar bone, isopedine and elasmodine, are all plywood-like tissues with minor structural differences[60].

Bony tissue

Bony tissues in fish scales have many different structures, such as woven-fibered, parallel-fibered, laminated, etc. Their formation originates from osteogenic condensation. Similar to the formation of human bone, these bony tissues are modeled and remodeled by osteoblasts and osteoclasts, by forming an organic framework of polymerized collagen followed by mineralization by hydroxyapatite. These two components with completely different mechanical properties are structured in a hierarchical way to provide a unique combination of strength and toughness, which commonly conflict with each other in synthetic materials[13].

Most of the scales in the currently existing fish are comprised of all or some of the tissues introduced above. They work together synergistically to provide most efficient protection for the fish in various environments.

2.2.4 Classification of fish scales

Based on the formation and characteristics of diverse tissues in the fish scales introduced in the last section, the scales of the currently existing fish can be divided into four categories: placoid scales, ganoid scales, elasmoid scales and scutes or dermal plates.

Placoid scales, shown in Figure 2-3 (a), have a structure resembling our teeth and are also referred as odontodes in anatomical research. The schematic of the structure is illustrated in the inset of Figure 2-3 (a). They have an inner core consisting of a pulp cavity covered by a layer of dentine; the top surface is a thin layer of enamel. They ride on a layer of bony tissue which connects to the dermis and upper part of the whole structure penetrated through the epidermis. Sharks, rays, skates and many other cartilaginous fish have such a type of scale covering their whole body without overlapping, which plays a more important role in reducing drag force by water than in protecting the fish body[66].

The ganoid scale is a very ancient tissue and is one of two structural forms of rhombic scales; the other one is cosmoid scale. Ganoid scales typically appear on the ray-finned fish while cosmoid scales are unique to the early lobe-finned fish. They both consist of hypermineralized tissues and a thick bony base, and in the evolutionary trend it clearly shows a reduction (becoming structurally simpler). The cosmoid scales are completely extinct, thereby not being listed here as an independent group. The scales on current existing lobe-finned fish (coelacanth and lungfish) are much more structurally reduced and more like elasmoid scales[60]. Ganoid scales are still found in two of living ray-finned fish: polypterids (bichirs and reedfish) and lepisosteids (gars)[57,69]. The ganoid scales of bichir and alligator gar have been widely studied on how they offer excellent protection through the multi-layered structure. The birchir (*Polypterus senegalus*) has quad-layered ganoid scales and components from surface to basal layer are ganoine, dentine, isopedine

and bony tissue, respectively. Alligator gar possesses more evolved ganoid scales, as shown in Figure 2-3 (b), which only have two layers: a ganoine layer on the surface and a bony layer at the base. The detailed structure and mechanical properties of ganoid scales are provided in Section 2.3.1.

Elasmoid scale is the most common scales in the living fish, including most of the 26,000 species of teleosts[60]. Figure 2-3 (c) shows the elasmoid scales They are thin, imbricated collagenous plates with similar fundamental structure, although their morphology and mineralization may vary from species to species. Usually they are composed of three layers: the limiting layer, external layer and inner layer elasmodine. The limiting layer is the most superficial layer riding on the external surface but only distributed on the exposed region. It is highly mineralized and usually in the form of scattered denticles, making the fish body rough and hard. Right beneath the limiting is the mineralized external layer with woven fibers inside and covering the entire scale. Its surface is relatively smooth with continuous or discontinuous ridges. The basal layer of elasmoid scales is the thickest collagenous layer (elasmodine) with a plywood-like structure. The upper part of the elasmodine layer (inner core) is mineralized with hydroxyapatite but the mineralization does not penetrate deep and the rest large region is composed of completely unmineralized collagen fibrils. The unique deformation of the collagen fibrils in the inner core confers an excellent toughness to the scale which is vital for the protective function. The detailed structure, mechanical behavior and toughening mechanisms is provided in Section 2.3.2.

Scutes and dermal plates are structurally similar and they appear on some teleosts replacing the elasmoid scales[60]. Scutes are typical of armored catfish, as shown in Figure 2-3 (d), with a bony layer capped by a layer of hyaloine (see hypermineralized tissue in Section 2.2.3). The surface of these scutes are also covered by scattered highly mineralized denticles which are tooth-

like elements. Dermal plates are pure bony plates without hypermineralized tissue covering the surface. Gasterosteiforms (e.g. tube-snouts, sticklebacks, the sand eel, etc.), tetraodontiforms (e.g. boxfish, porcupinefish, pufferfish, etc.), and syngnathiforms (e.g. seahorse, shrimpfish, pipefish, etc.) all have dermal plates covering or partially covering their bodies.

In general, most of the current existing fish have the scales belonging to one of the four categories classified above. However, this classification is defined by anatomists and ichthyologists and not well-familiar to most of the materials science researchers, resulting in a lot of misuse in the fish-scale related research in biological materials. Therefore, it is necessary to clarify the classifications of fish scale based on the understanding gained in this study through the literature on the anatomy, ichthyology and paleontology. Candid criticisms and necessary corrections are greatly appreciated.

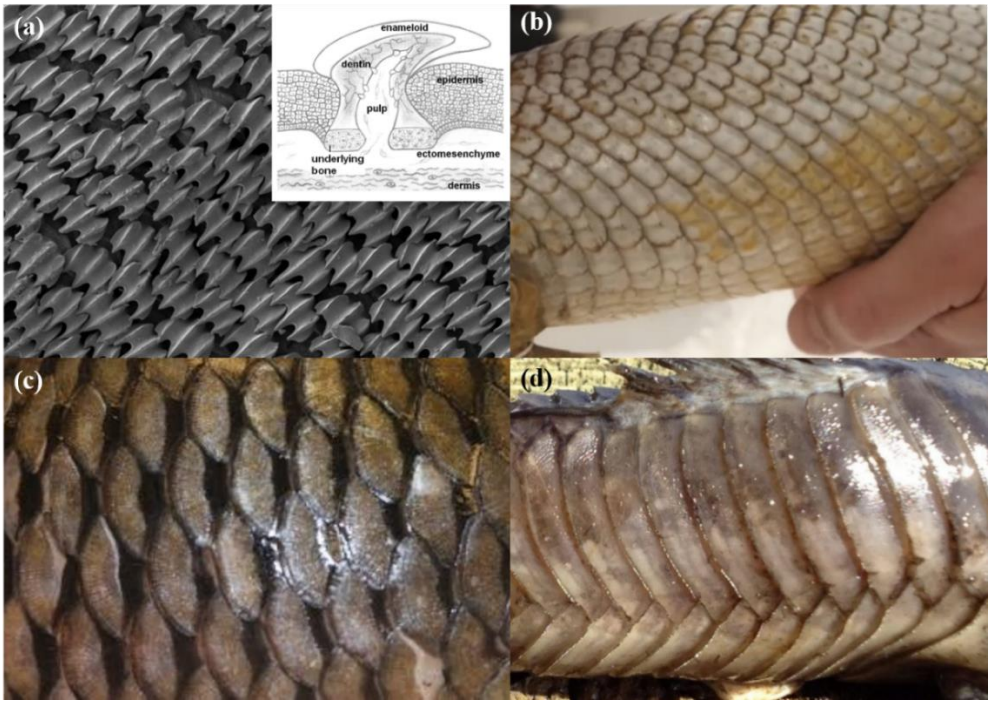

Figure 2-3 The representatives of four main categories of fish scales that currently exist. (a) Placoid scales of shark[70]; (b) Ganoid scales of alligator gar[57,69]; (c) Elasmoid scales of carp; (d) Dermal plates (scutes) of armored catfish.

2.2.5 Evolution of fish scales

The evolutionary trend of fish scales reflects how fish modified their dermal armor for protection to adapt to environment changes in past hundreds of million years; this can be a great source of inspiration for materials scientists to design advanced armor materials. The evolution of fish scales, without any doubt, is highly related to the evolution of fish[60]. Figure 2-4 (a) shows the simplified phylogenetic tree from the appearance of vertebrates all the way to the ancestors of terrestrial animals, tetrapods, which covers the evolution of fish[71]. It reflects the interrelationships of all the lineages of fish but the terminologies are very unfriendly to materials science researchers. The more simplified phylogenetic tree of the representative fish with common names is illustrated in Figure 2-4 (b) and some members whose scales have been widely studied are circled with dot lines. The cartilaginous fish including sharks, rays, sawfish, etc., are quite primitive with poorly-mineralized skeleton system and they possess placoid scales with simple teeth-like structure (odontode), which play a more important role on the hydrodynamic mechanics rather than in protection. All the protective scales existing currently are on the bony fish, which have more mineralized skeleton system. Figure 2-5 provides the evolutionary trend of fish scales and it perfectly matches the evolution of fish in Figure 2-4 (b). Combining these two figures, three interesting findings are revealed as following:

i. Evolutionary scenario of fish scales. The quad-layered ganoid scales, scales of bichir, are the most ancient scales in all the currently existing scales. The double-layered ganoid scales in alligator gars and all the elasmoid scales, scutes and dermal plates in teleosts are descendants of them with loss of some structural components.

ii. Evolutionary convergence. Cosmoid scales are evolved from the putative ancestral rhombic scales (the most primitive integumentary skeleton in non-tetrapods which is completely

extinct) in parallel with quad-layered ganoid scales and they are identified in some fossils of primitive lobe-finned fish. This corresponds to the parallel evolution between lobe-finned fish and ray-finned fish (Figure 2-5). However, the original cosmoid scales are completely extinct now and the current lobe-finned fish, coelacanth and lungfish, possess simplified cosmoid scales which structurally and morphologically resemble more the elasmoid scales in teleosts, thereby being classified as elasmoid scales. Thus, most teleosts and current lobe-finned fish, although evolving in parallel, developed elasmoid scales with excellent protective function. This is an example of evolutionary convergence.

iii. Structural simplification and mineralization reduction. From the evolutionary scenario presented in Figure 2-5, the more evolved fish scales have simpler structures and less mineralization than the ancient ones[60]. For example, the modern elasmoid scales are developed from quad-layered ganoid scales with loss of osteogenic component (bone) along with reduction and modification of odontogenic component (ganoid/enamel and dentine). All other component loss, reduction and modification are provided in Figure 2-5. More than structural simplification, the loss or reduction of hypermineral tissue (ganoid/enamel) and the increase of collagen-rich tissues (e.g. elasmodine) are also very clear in the scenario, resulting in the reduction trend of mineralization in fish scale evolution[60]. The scutes and dermal plates may not perfectly fit it this trend but the fish possessing them account for a relatively low ratio comparing with all the other types of scales. Such modification significantly improves the flexibility and toughness of the scales which may be more favorable for surviving in the current environment.

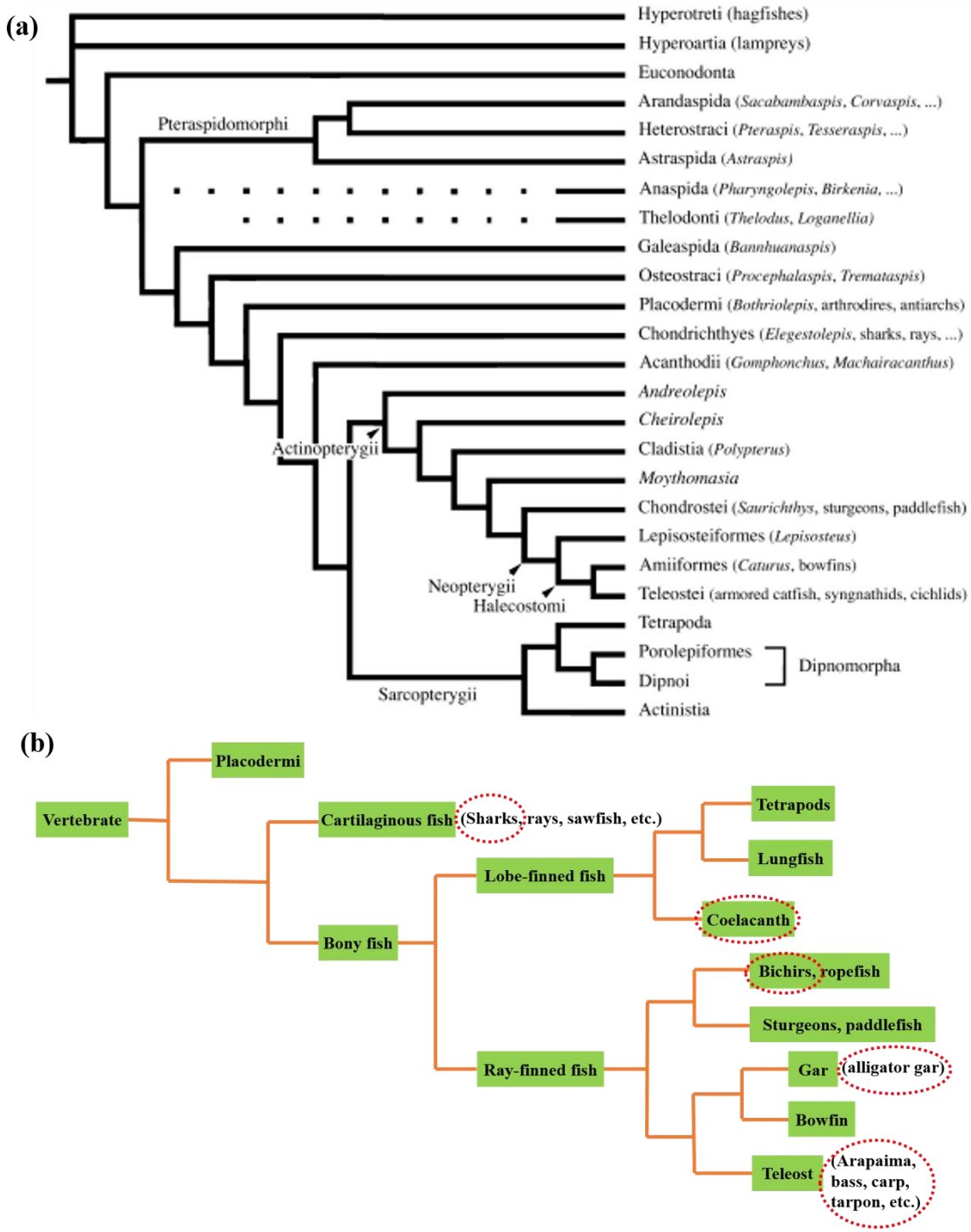

Figure 2-4 The evolution of fish. (a) Simplified Phylogenetic tree of the vertebrates[71]. (b) More simplified phylogenetic tree of selected fish with commonly used names. The circled ones are the fish whose scales were well-studied as biological materials.

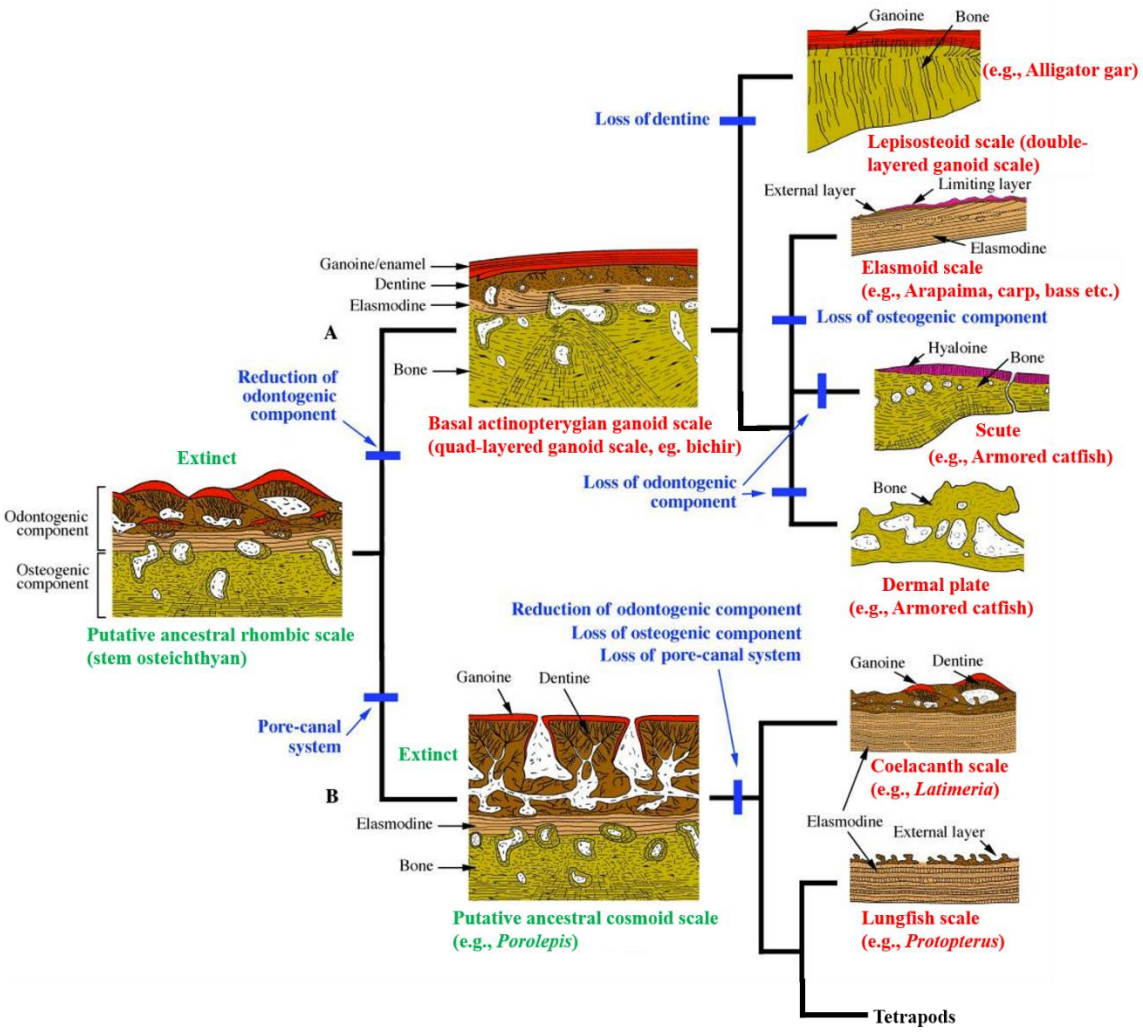

Figure 2-5 The evolution of fish scales. The extinct types of fish scales are shown in green and the currently existing scales are shown in red[60].

2.3 Structure of mechanical behavior of fish scales

Fish scales have many functions like protection, thermal isolation, camouflage, and hydrodynamic optimization. Among them, the protective function as dermal armor is the most distinctive one for most of the existing types of scales and their outstanding mechanical properties such as strength, penetration resistance and toughness are truly impressive for materials scientists, generating inspiration for synthetic armor materials[72]. To figure out how the scales protect the fish in different environments and further obtain inspired ideas for designing novel armor materials, investigation of the connection between the structure and mechanical behavior of various fish scales is strictly necessary. The following subsection reviews the previous research on the structure and mechanical behavior of three types of fish scales: ganoid scales, elasmoid scales, and scutes and dermal plates.

2.3.1 Ganoid scales

Ganoid scales, as introduced previously, are the primitive type of fish scales typical of ancient fish. Currently there are two groups of ganoid scales: the quad-layered ones, which appear on bichirs, and double-layered ones, which grow on gars.

The quad-layered ganoid scale is identified on Polypterus senegalus (*P. senegalus*), a species of Polypteridae (bichir) that has existed on earth for almost 100 million years. The entire fish body is covered by imbricated rigid ganoid scales (Figure 2-6a) and they have a rhombus-like shape (Figure 2-6b)[69]. Bruet et al.[69] characterized the structure of this quad-layered ganoid scale and applied multiscale experimental and computational methods to reveal how the scales provide protection. Figure 2-6 (c) shows the distinct four layers in the ganoid scale of bichir, which are ganoine, dentine, isopedine and bone. Ganoine layer is the thinnest layer comprised of hydroxyapatite nanocrystals aligned along thickness direction, providing desirable penetration

resistance. The dentine layer and isopedine layer (referred as lamellar bone in anatomic research) have similar thickness and they are both collagenous layers with different mineralization; dentine is more mineralized. The basal plate is bone which is the thickest layer and has similar structure with human cortical bone.

These four layers all have distinct structure, composition, mechanical properties and deformation mechanisms, but their juxtaposition generates a synergetic effect. The hardest ganoine layer is the first barrier for the external load, which can resist the deformation by its sufficient hardness and transfer the applied load to the more compliant dentine layer, which can dissipate a great amount of energy via plastic deformation. The isopedine layer with collagen-rich plywood-like structure can serve as second defense line, which has larger deformability to arrest the catastrophic crack propagation, resulting in significantly increased toughness. The thickest layer, the basal layer of bone provides physical support for the entire complex architecture. The tough nature of bone confers the basal layer with outstanding damage tolerance through various toughening mechanisms (see Section 1.2). These four layers juxtaposed in a well-designed sequence forms a gradient structure with hardness/stiffness gradually decreasing from the outer layer to the inner base (Figure 2-7a), promoting load transfer and stress redistribution, thereby suppressing plasticity, arresting cracks, improving adhesion and preventing delamination between dissimilar material layers. A clear evidence of crack arresting is shown at the junction between ganoine and dentine layers (Figure 2-7b). Last but not the least, the corrugated junction between the layers (Figure 2-7c) forming a suture-like structure which leads to spatially heterogeneous stresses and a higher net interfacial compression. In summary, this interlocking, quad-layered and functionally graded ganoid scales provide fascinating protection for the P. senegalus, which could be incorporated into the design of advanced engineered biomimetic armor materials[69].

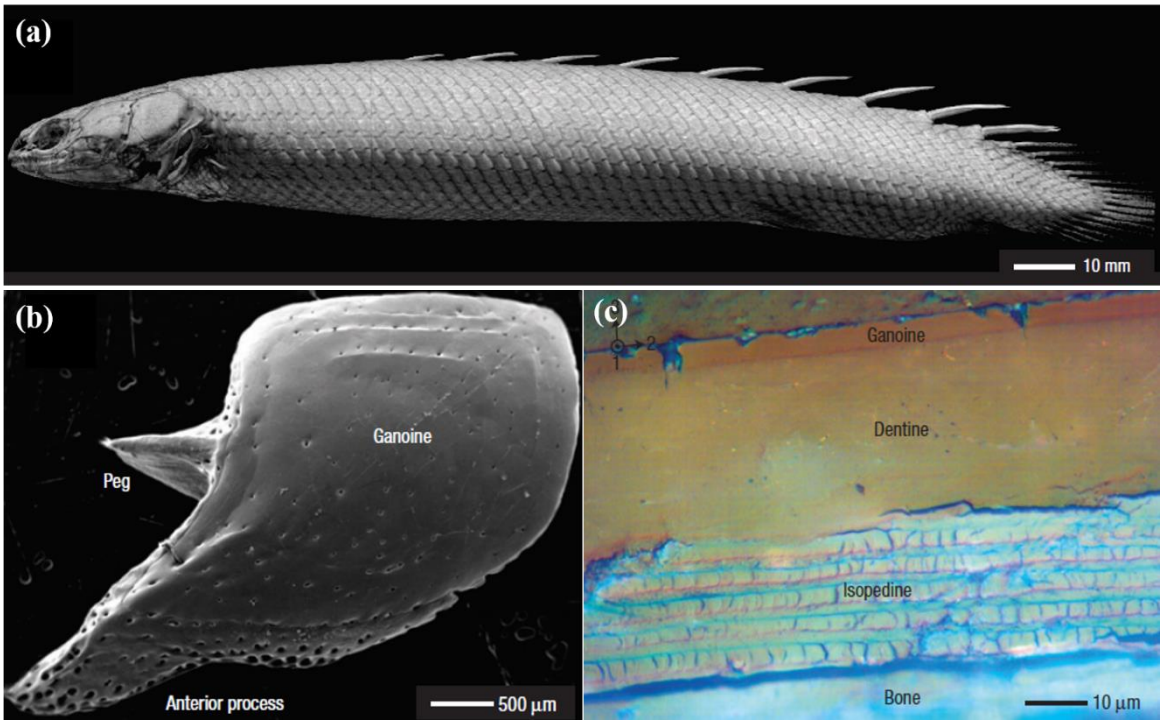

Figure 2-6 Structure and mechanical properties of quad-layered ganoid scales[69]. (a) P. senegalus is covered by imbricated ganoid scales. (b) SEM of an individual scale. (c) Optical micrograph of the cross-section showing distinct four layers; bony layer is partially shown.

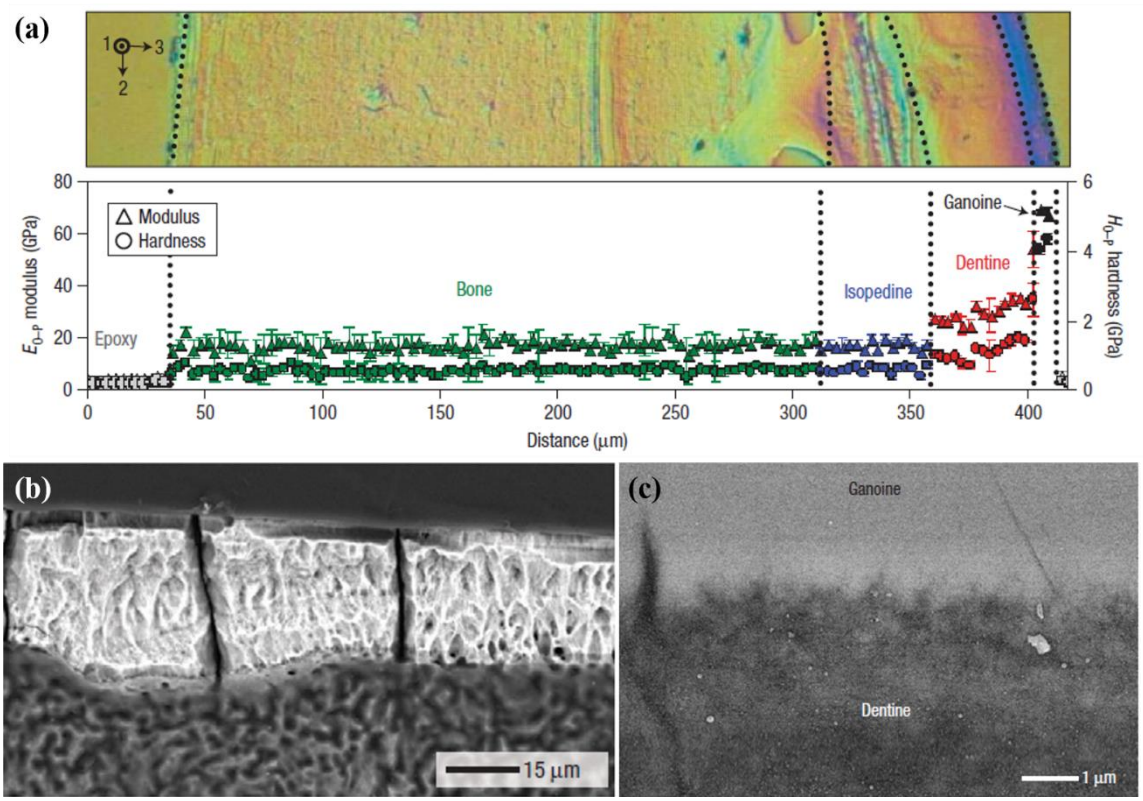

Figure 2-7 The nanoindentiaon mapping and failure mechanism of bichir scale[69]. (a) With 500 μN maximum load; average indentation modulus, E_{O-P}, and hardness, H_{O-P}, both obtained from Oliver–Pharr analysis as a function of distance from inner layer to most superficial layer. Epoxy is used for embedding. (b,c) Backscattered electron micrographs of junction and dentine junction.

The double-layered ganoid scale in alligator gar (Atractosteus spatula) is a more evolved one with simplified structure but still provides sufficient protection to survive from the predation of alligators. This type of ganoid scale is characterized by a hard ganoine layer and a bony base. In the living fish, the scales are not exposed but are covered by a layer of skin. Figure 2-8a shows the scales without the outer skin layer[57]. The ganoine layer (white in image, green in micro-computed tomography (μ-CT) scan in Figure 2-8b) covers most of the scale surface, while the overlapped region is the bony foundation (yellow in image, red in μ-CT)[57]. Figure 2-8a shows the shapes and organization of the gar scales, where three types of scales (Type I, Type II and Type III) are required to provide full coverage of the fish. These scales on the fish form an imbricated

array but the degree of imbrication is much smaller than that of elasmoid scales. This highlights a major difference between the gar and most other fish: it is protected principally by only one layer of scales, although this is also the case for the ganoid scales of the Senegal bichir introduced previously. In the overlap regions the thickness of the scale is reduced so that adjacent scales fit to produce a constant thickness. These chamfered overlapping edges provide protection against penetration when the tooth tip impinges on the boundary. The ganoine, shown in Figure 2-8c, consists of distinct layers of decussated mineral in a crossed pattern, while in the bony layer, shown in Figure 2-8d, hollow tubules and fibrils (the head of a single fibril is shown in the inserted picture) are present, which run throughout the thickness direction of the scale (Figure 2-8e)[57].

The principal function of the rigid scales is to resist the large biting force by delocalizing the stress[57]. Figure 2-9 (a) and (b) present the compressive and tensile stress-strain curves for the bony region of the gar scale[57]. Results for the orientation perpendicular to the scale surface (orientation A) are in black; blue lines indicate the orientation parallel to the surface plane of the scale, but perpendicular (orientation B); the red lines are the orientation parallel to the serrated edge (orientation C). Due to the running direction of the tubules and fibrils, the gar scales manifest significant mechanical anisotropy (Figure 2-9a) and the hydration is also very important for the deformability of the scales. In tension, the dry scales do not exhibit significant plasticity. Figure 2-9b shows the curves in tension, with the absence of plasticity. Dry and wet fish scales are toughened by differing mechanisms which are addressed in the following section[73].

The double-layered ganoid scale also has a wide variety of toughening mechanisms, which are vital for protecting gar from predatory attack[57]. First, the outer mineral layer has an arrangement of crystals which greatly contributes to the toughness of the ganoine. Figure 2-9c shows cracks which initiate in the ganoine layer under compressive load yet arrest within the layer;

this prevents cracks from propagating into the bony layer to cause failure of the scale. The mineral bundles in ganoine, observed from both the fractured (Figure 2-9d) and polished surfaces (Figure 2-9e), are shown to be twisted and interlocked with other bundles, in a manner similar to that seen in tooth enamel[57]. This decussation, or cross-plied arrangement of crystals, guides the cracks along a tortuous path which requires significantly more energy to propagate. Another important feature of the alligator gar scales are the tubules in the inner layer that are oriented nearly perpendicular to the scale surface. The tubules can cause crack meandering when the scale is dry (Figure 2-10b). However, the fish scales are always hydrated and this effect does not appear to occur when the wet scales (Figure 2-10a). This begs the question as to whether the tubules contribute to the in vivo fracture resistance of the alligator gar scale. The water molecules can act as a plasticizer and enhance plastic deformation and ductility in the wet scale, which we believe is the principal toughening mechanism in the presence of water; this is shown in Figure 2-9b. To mimic how the fish scales resist the penetration from biting of the alligator, a real alligator tooth was mounted on Instron machine and the real-time force vs displacement was measured, with a foam pad underlying the scale simulating the flesh of fish (Figure 2-10c). Application of pressure caused adjacent scales to hinge on one another in order to resist from penetration (Figure 2-10d). Small concentric cracks occurred in the ganoine layer but were arrested and did not propagate or cause failure[74]. Eventually, at a force of ~500 N, the alligator tooth failed (Figure 2-10d), illustrating the capability of the gar scale to withstand the huge biting force from the predatory action of an alligator.

The ganoid scales, no matter the quad-layered ones from bichir or the double-layered ones from alligator gar, are all composed of highly mineralized tissues making the individual scale extreme rigid. They are overlapped by small degree of imbrication to confer the fish certain extent

of flexibility. Although it sacrifices overall maneuverability for the fish, these ganoid scales provide excellent penetration resistance. The ganoid scales are typically possessed by 'living fossil fish that still retain many prehistorical characteristics. These ancient fish usually live in shallow confined water, where they co-exist with ferocious predators who have extremely large biting force. Therefore, the protective function against the huge penetration grossly overweights the flexibility, resulting in this fascinating efficient dermal armor. The intricate complex hierarchical structure maximizes the protection with minimal weight gaining and confers the scales excellent strength and toughness.

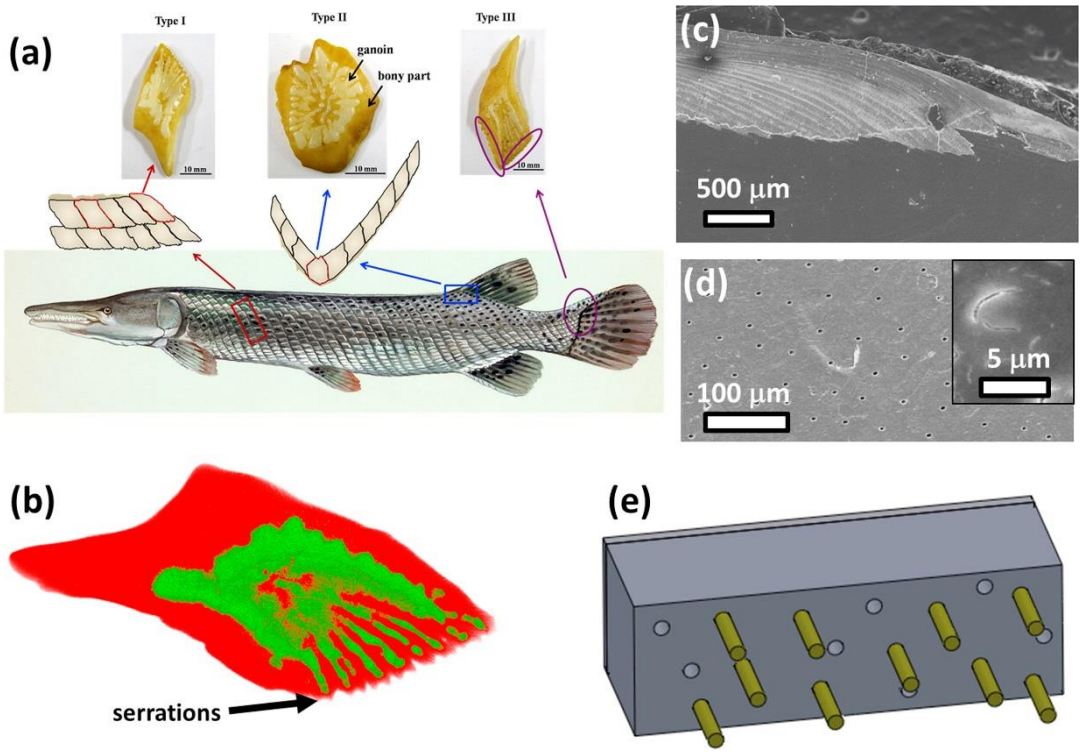

Figure 2-8 Structure of the scales of Atractosteus spatula[57]. (a) The protective armor is formed of three principal types of scales, shown as type I, II, III. Some portions of the scale are covered with white shiny ganoine; the darker areas around the ganoine are the bony base. (b) Micro-computed tomography(μ-CT): the green region is indicative of the dense ganoine mineral, while the red one indicates the bony composite. (c) The conjugated junction between two layers. (d) The bony region of the scale has hollow tubules and collagen fibrils which run throughout. (e) The scheme illustrating the arrangement of the ganoine (outer layer) and the bony inner layer with tubules (hollow) and collagen (green).

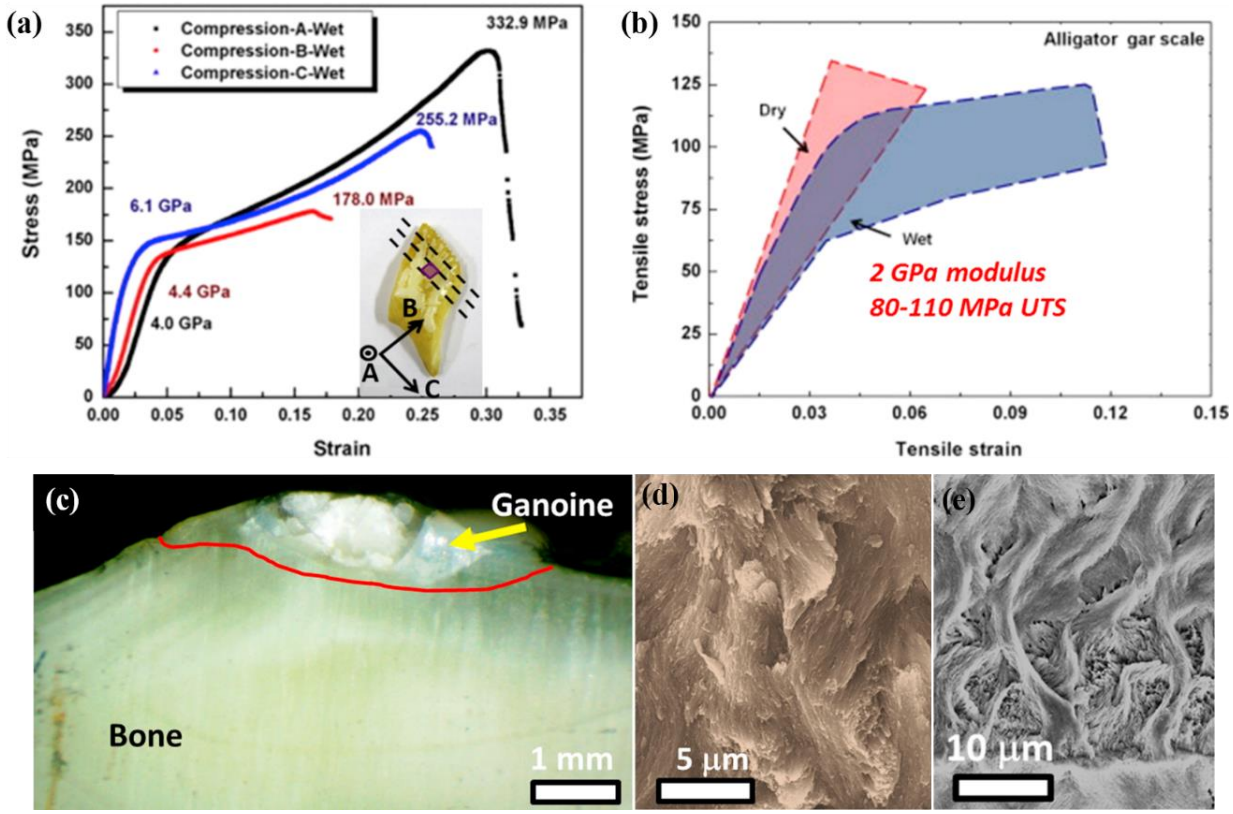

Figure 2-9 Mechanical response of alligator gar scale[57]. (a) The compressive response of the bony region of the alligator gar scale. Differences between orientations are due to the orientation of mineral and tubules in the scale. (b) The tensile response of the alligator gar scale[57]. (c) Compressive failure of the mineral layer (the separation between mineral and bone is shown by the red line). (d,e) The arrest of incipient cracking is due in part to the enamel-like weaving of the mineral, called decussation. This decussation is observed on a mineral fracture surface (d) and by use of an etchant (e).

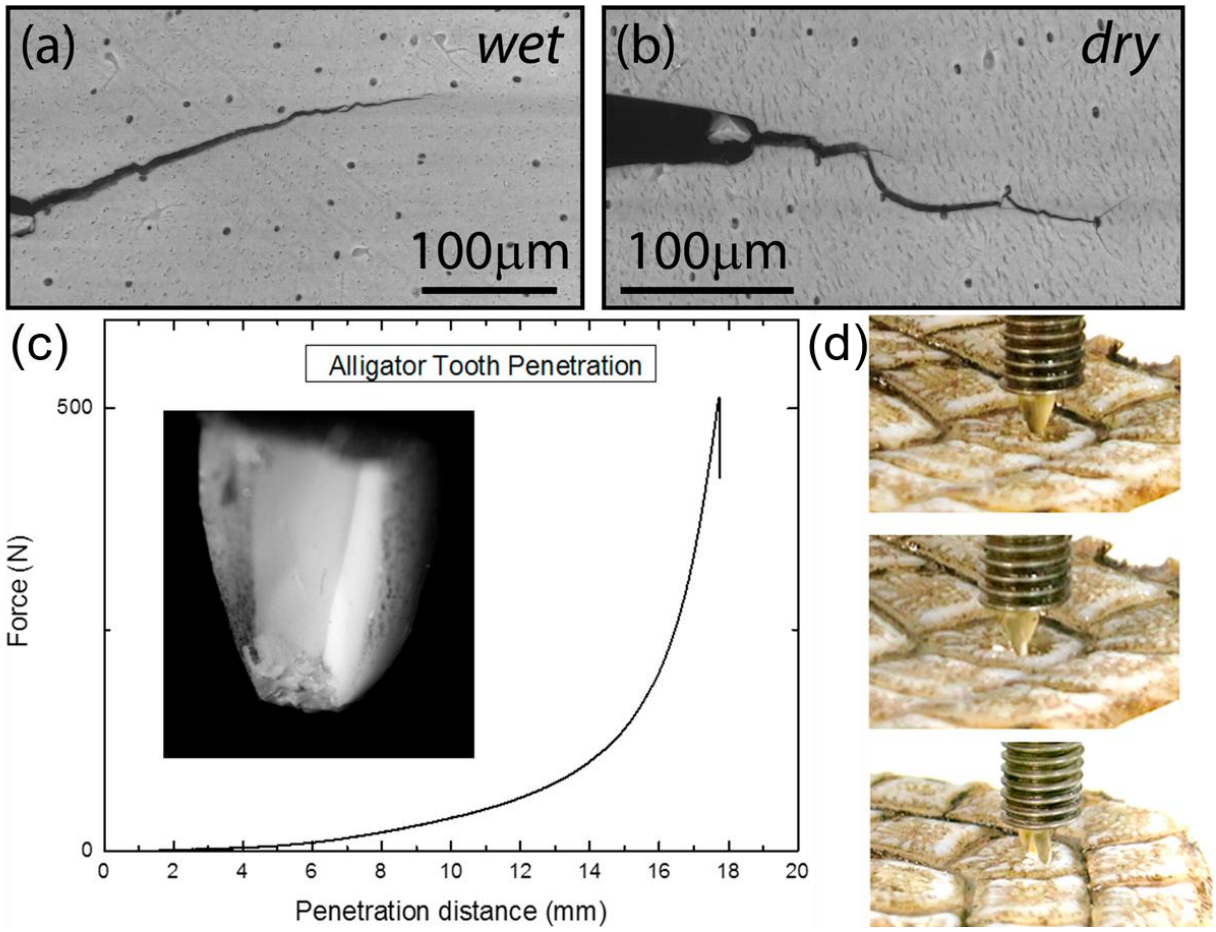

Figure 2-10 Crack propagation in ganoid scale and penetration test with real alligator tooth[57]. (a) Crack propagation in wet sample. (b) Crack propagation in dry sample. (c,d) Penetration of an alligator gar scale array by an alligator tooth and three stages during the test[74]. As pressure is applied, the scales hinge at their interfaces in order to absorb and conform to the flexing (overlapped scales redistribute penetration load over a larger area). As the test continues, the tooth breaks at 500 N, which corresponds to the maximum force in the plot. The scales are sufficiently strong to resist the high applied and defeat the attempted penetration by an alligator tooth. The inset in (c) shows the fractured tooth after an "attempted attack".

2.3.2 Elasmoid scales

Among all the living vertebrates, elasmoid scale is the most prevailing type of dermal armor, which covers body of 26000 species of teleosts, current lobe-finned fish (coelacanth and lungfish) and some amphibians like caecilians[60]. They are thin, slightly mineralized collagenous plates assembled together with a large degree of imbrication which significantly improves the overall flexibility. Most of elasmoid scales have two shapes: the cycloid and ctenoid ones. Cycloid scales are composed of concentric rings and ctenoid scales are composed of fringed projections. Despite the varied geometric morphology, the inner structure of all elasmoid scales is quite uniform, consisting of three layers: the limiting layer, external layer and collagenous layer. The general architecture of these three layers are introduced in Section 2.2.4.

Elasmoid scales provide protection for fish living in various environments. Zhu et al.[75] penetrated single scales of striped bass (*Morone saxatilis*) with a sharp indenter, and analyzed the sequence of events, dividing them into three stages: elastic deflection of the scale, fracture of the mineralized layer and penetration of the collagen lamellae. They also found that overlapping three scales essentially multiplies the puncture resistance by three. Friction between the scales is negligible. The redistributed stress prevents unstable localized deformation of the skin and protects the underlying tissues. Barthelat et al.[76] tested the fracture toughness of the elasmoid scales from striped bass and their results show the elasmoid scales from striped bass have toughness about 15 to 18 kJ m^{-2}, which is one of the toughest flexible biological materials.

Numerous types of elasmoid scales have been studied by many research groups and among them the elasmoid scale from arapaima gigas is a representative with most thorough investigation. As shown in Figure 2-11, the arapaima fish has elasmoid scales with cycloid shape and are composed of a hard and stiff outer mineral layer and a deformable plywood-like collagenous

lamellae in the base (also referred as Bouligand structure)[56]. The scales are overlapped and arranged with a degree of imbrication (exposed length/total length) equal to 0.4 and aspect ratio (length/thickness) of 50[56]. The darker region of the scale are the exposed part while the white regions are overlapped by surrounding scales (Figure 2-11). The exposed scale is covered by a thick mineral layer (~ 1 mm in adults) with ridges on the surface; in the embedded portion of the scale the mineral layer is thinner (~ 0.5 mm). Beneath the mineral, collagenous lamellae display a Bouligand-type structure. Individual lamella consists of parallel and straight collagen fibrils, while the orientation of fibrils are off-set by certain angle in adjacent lamellae. Fibrils can be imaged by transmission electron microscopy (TEM), as shown in Figure 2-11, where the misorientation between the two visible lamellae is visible. The cross-section of fibrils in layer 1 of collagen is elliptical and the periodicity of the banding in collagen fibrils in layer 2 is ~ 50 nm, i.e., less than the 67 nm characteristic d period of collagen. This indicates that the fibrils are at an angle to the surface, which can be calculated as $\theta = \arccos(50/67) = \sim 40°$.

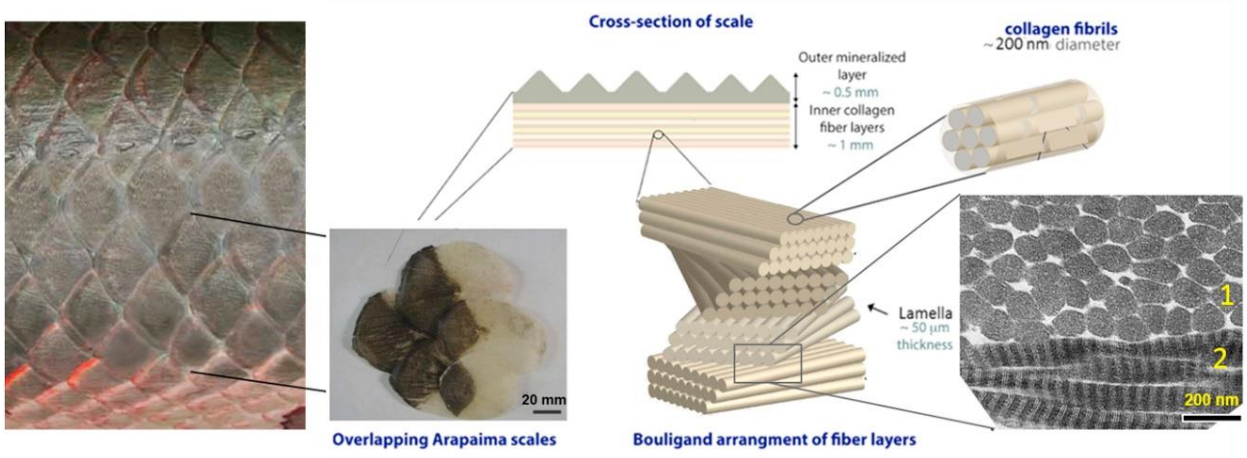

Figure 2-11 Hierarchical structure of the scale of Arapaima gigas[56].

The scales of arapaima have a great strength in tension. Figure 2-12 (a) shows the tensile behavior of arapaima scales in both longitudinal and transverse directions. With the mineral layer removed, there is a substantial increase in the tensile strength, indicating that the mineral is poor

for carrying tensile load due to its brittle nature. Although the arapaima fish scale is flexible in all directions, the scale in the longitudinal direction, i.e., along its length, is stiffer and stronger than in the transverse direction[56]. The stronger and stiffer direction of the scale aligns with a possible exotendon function of the scales, where scales store energy for more efficient swimming[76]. The more compliant direction allows the scales to accommodate movement as they can adapts to the curvature of the fish body. However, as previously addressed, the specific location of the scales on the fish is unknown and this effect may vary throughout the fish. SEM images in Figure 2-12b shows that the lamellar angles vary in the different layers of the plywood-like lamella tissue, which is highly resistant to crack propagation. Under tensile loading, some lamellae reorient as the deformation is applied so that the lamellae close to the tensile axis can more effectively carry the applied load. This reorientation has been estimated theoretically by considering the elastic stretching, strain-rate sensitivity and interfibrillar sliding of the lamellae[77]:

$$\Psi_1 - \Psi_0 = \arccos\left[\frac{\cos\Psi_0(\varepsilon_t + 2)}{2 + C\left(\frac{\dot{\varepsilon}}{\dot{\varepsilon}_0}\right)\frac{\varepsilon_t}{E_f}}\right] \quad (1)$$

where Ψ_1 is the predicted angle between the lamella and the tensile axis (positive values correspond to rotation towards the tensile axis), Ψ_0 is the initial value of Ψ at unstressed state, ε_t is tissue strain, the overall tensile strain of bulk scale sample, $\dot{\varepsilon}$ is the strain rate, $\dot{\varepsilon}_0$ is a reference strain rate, E_f is the modulus of a fibril, and C is an experimentally measured constant. Predictions from Eq. (1) for the angular rotation shown in Figure 2-12c indicate that all orientations will rotate towards the tensile axis, with the most significant rotation occurring between Ψ = 10° and Ψ = 30°. Corresponding experimental measurements of the scales, under tensile loading with real time small angle x-ray scattering (SAXS) technique, provide a detailed observation and analysis of the

mechanisms in Figure 2-12d. It unraveled that under tensile loading, the fibrils oriented within ~ 15 – 30° of the loading direction tend to rotate towards the tensile axis, whereas fibrils in the 61–90° rotate away. Moreover, as the lamellae rotate towards loading axis, the adjacent layers, which are far from the tensile axis are subjected to tension perpendicular to the fibrils, causing gaps to open. In addition, interfacial shear and sympathetic lamellar rotation by adjacent layers contribute to these reorientations, on average, rotating away from the tensile direction.

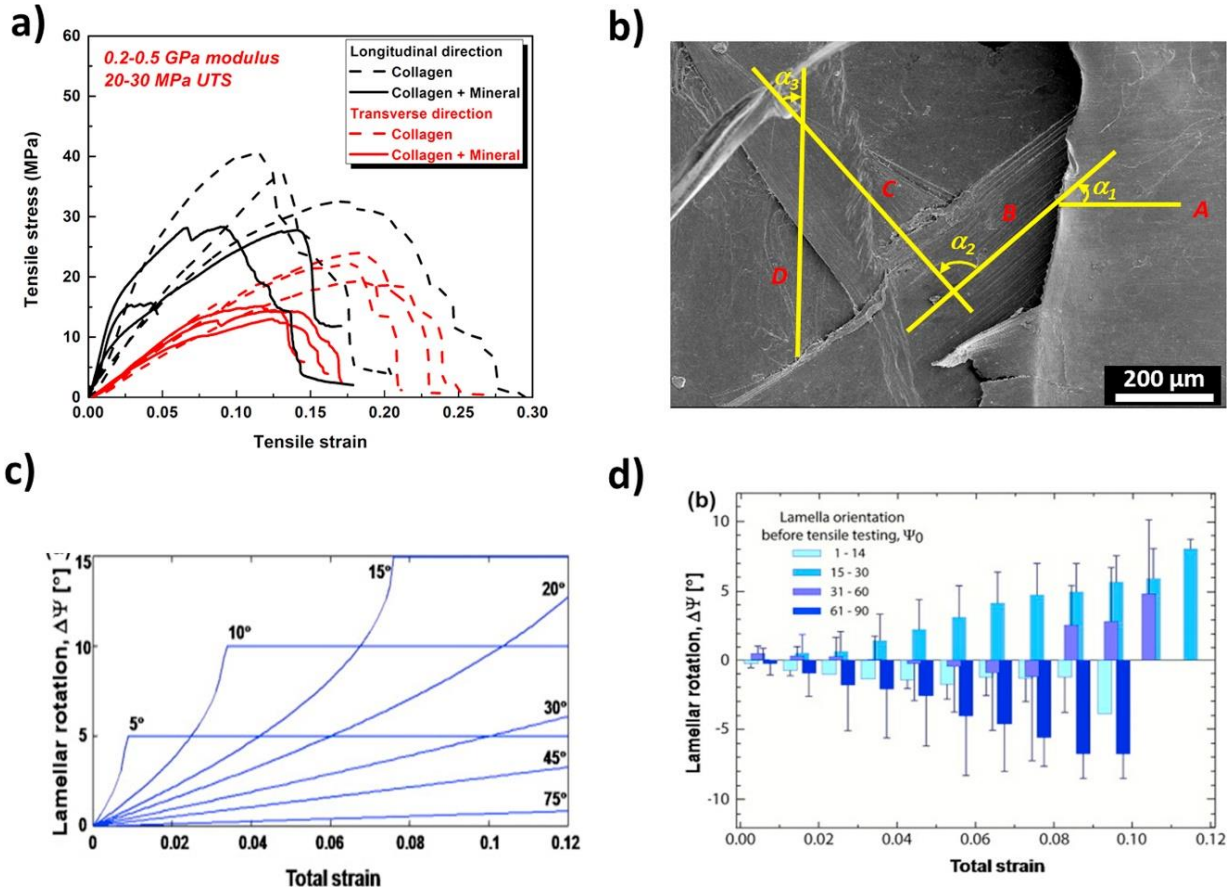

Figure 2-12 Mechanical response and lamellar rotation of the arapaima scale[56]. (a) The tensile response of the arapaima scale. (b) The variation in lamellar orientation is not consistent between layers. Three orientations of adjacent layers are shown; two at acute angles and one at an obtuse angle. (c) The lamellar reorientation predicted mathematically based on their initial orientation using Eq. (1). (d) The lamellar reorientation predicted from (c) is measured by SAXS[56,77].

The damage evolution in the scale has been examined by tensile testing on notched specimens with *in situ* observation by SEM[56]. Figure 2-13 shows a sequence of images captured during this test: at the beginning of the tensile test, fibrils at the notch tip start to delaminate in the vicinity of the notch tip (Figure 2-13a). Under increasing load, the collagen fibrils become stretched, with some fracturing close to the notch tip. The fibrils further from the tip become curved due to the geometry of notch-opening and the rotation from the layers beneath (Figure 2-13 b). Before fracture, more collagen fibrils delaminate (labeled as 1 in Figure 2-13c); some fracture (labeled as 2), bend or buckle (labeled as 3); but other layers remain intact and carry the load (labeled as 4 in Figure 2-13c,d). The scales negate the effect of cracks as they effectively delocalize into wide process zones with the partially detached collagen fibers engulfing the crack front. To further assess the effectiveness of arapaima scales, Meyers et al.[78] examined how an actual piranha tooth can penetrate the arapaima scale. With the tooth mounted on the upper fixture of the testing machine, it fractured before complete perforation of the scales occurred (Figure 2-14). The images show the sequence of events (for the tooth and the scale) during the test, with a picture of the failed tooth as an inset in the force-displacement plot. Microscopically, the lamellar base of the scales was observed and shown to serve as a resilient and tough base which acts synergistically with the hard and stiff outer mineral layer to prevent penetration from the tooth. Hence, this highly effective armor allows the passive arapaima to cohabitate peacefully with the piranha, one of the most vicious and feared fish in the Amazonian waters.

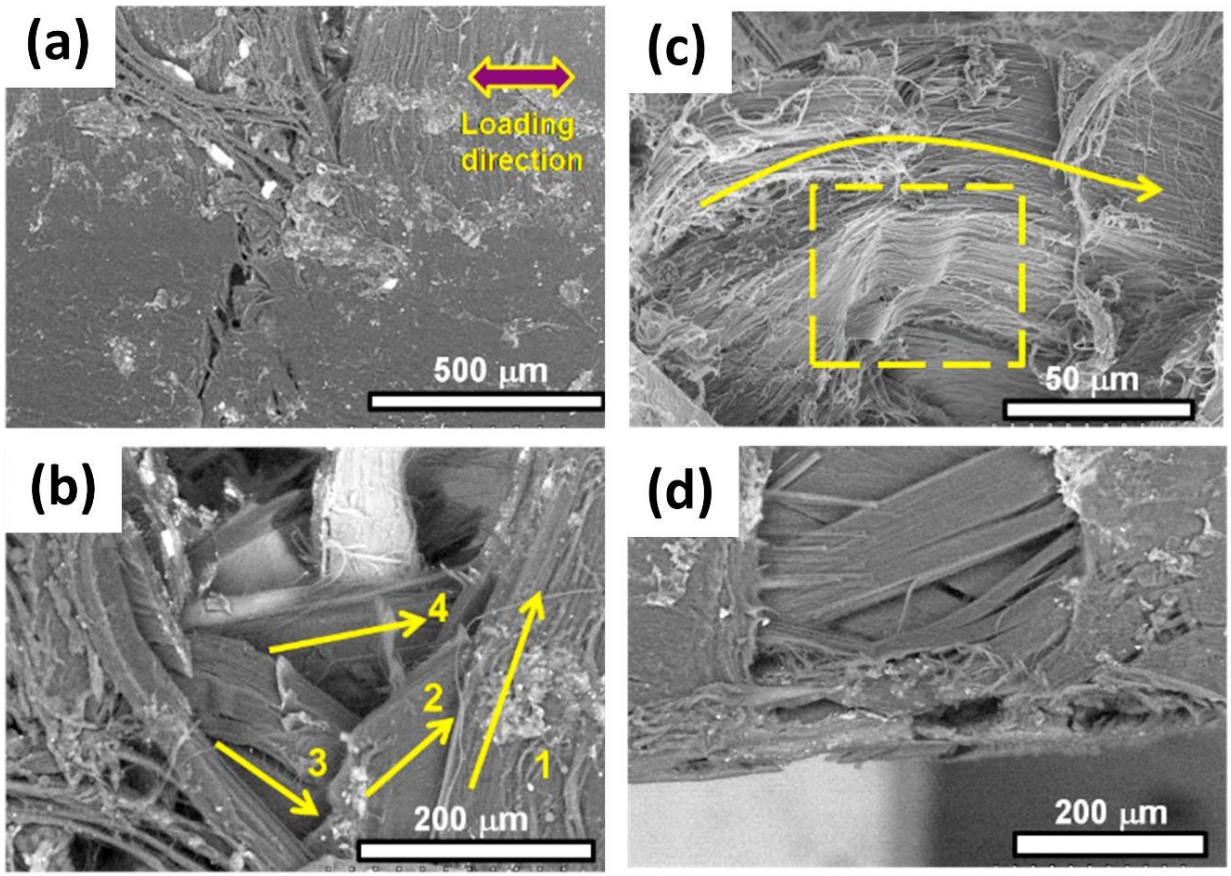

Figure 2-13 In situ SEM of a crack arrested in arapaima scales under tensile loading[50]. (a) An initially notched scale is loaded in tension in the direction indicated. (b) As stretching continues, multiple layers become apparent as lamellae stretch, reorient, bend, and buckle. (c) Lamellar delamination occurs as an energy absorbing mechanism. (d) The crack is fully arrested by reorientation, bending and stretching of the layers.

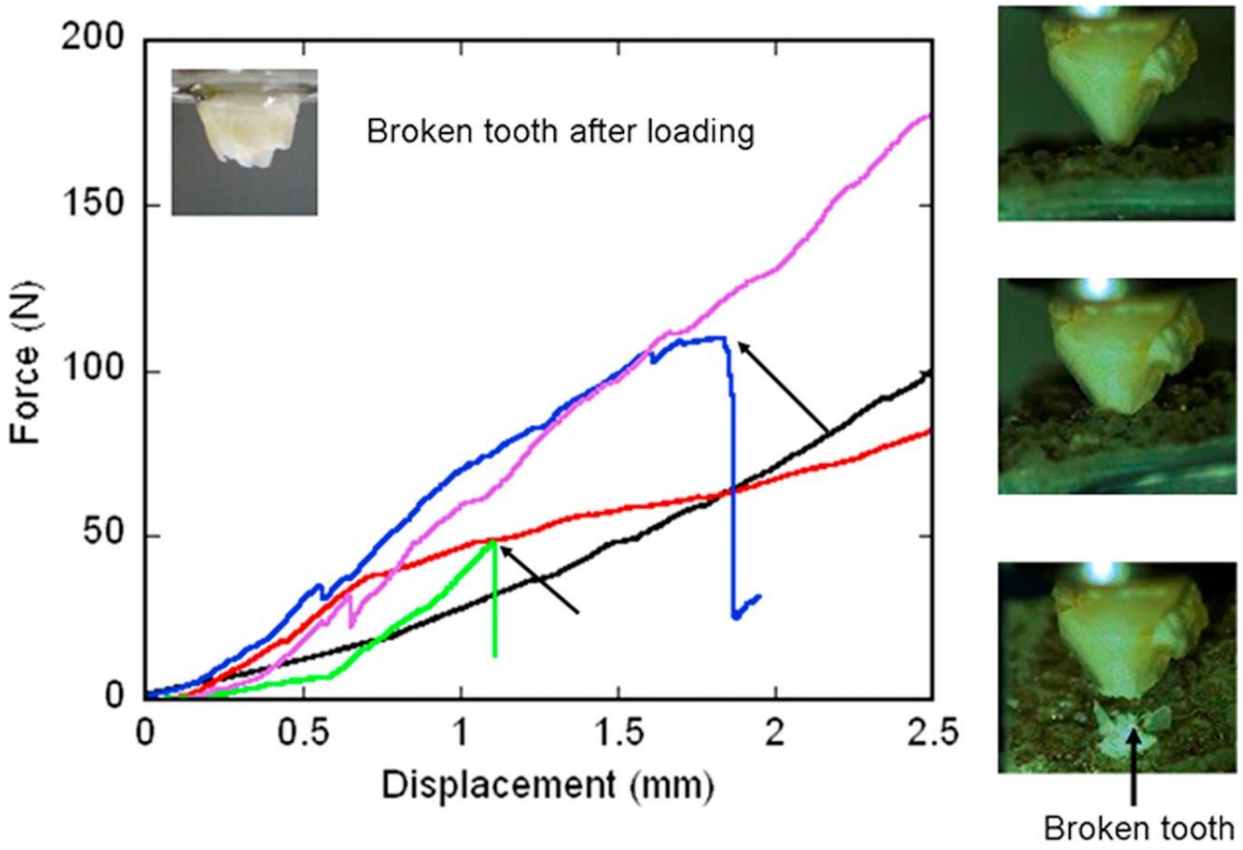

Figure 2-14 Piranha tooth penetration of the arapaima scale[78]. During an indentation experiment, the piranha tooth attempts to fully penetrate a single arapaima scale. A sequence of images on the right shows a time evolution of the penetration. The protective mineral and lamellar Bouligand structure base cause tooth fracture before the scale can be fully penetrated. The fracture of the tooth is indicated by the drop in force as seen in the force vs. displacement measurement (identified by black arrows) and the broken tooth is pictured as an inset within the graph[78].

2.3.3 Bioinspired flexible armor

Inspiration from nature in the design of armor has existed since the days of the Roman Empire. The lorica squamata mimicked lizard skin and provided protection to the soldiers while ensuring mobility. Indeed, the name squama signifies “scales” in Latin, referring the current elasmoid scales. These scales provided the best protection, superior to Lorica segmentatata (metal lamellar hoops associated with Roman legionnaires in movies), and Lorica hamata (chain mail), resulting from the majority of the body covered by two plates in which the kinetic energy of projectiles was transferred laterally. Researchers are currently using new techniques to mimic the overlap system of the fish scales as well as specification of the aspect ratio and imbrication in order to tune the flexibility and protection function of future bioinspired armor. Rudykh et al investigated the resistance to penetration of a microstructured elasmoid scale-inspired armor[56]. Indentation and bending tests on bioinspired 3-D printed structures (Figure 2-15a,b) indicate the optimized protection against penetration and flexibility as well as amplified penetration resistance by a factor of 50 while reducing flexibility by less than a factor of 5. This was achieved by identifying and separately analyzing the mechanisms which govern flexibility and penetration resistance. Similar efforts by Funk et al. have led to the creation of a synthetic “fish skin” for the production of soft materials through a combination of a mesh or dermis-like layer and rigid scales[56]. The assembled product is not specific to any particular classification of fish scale, but incorporates components that are key to the armors mechanical response (Figure 2-15c,d). It is claimed to have a potential application as a thin protective coating for soft materials and also important to understand how a stiff plate performs on a soft substrate; Martini et al. showed that small plates may fail by tilting due to a localized force, and emphasized the importance of avoiding this dangerous failure mode which drastically reduces the effectiveness of stiff armor plates[78]. Additionally, they produce a

bioinspired armor shown in Figure 2-15 (e) and (f), made of ceramic tiles and a soft substrate and capable of a large degree of flexibility and also resistant to penetration.

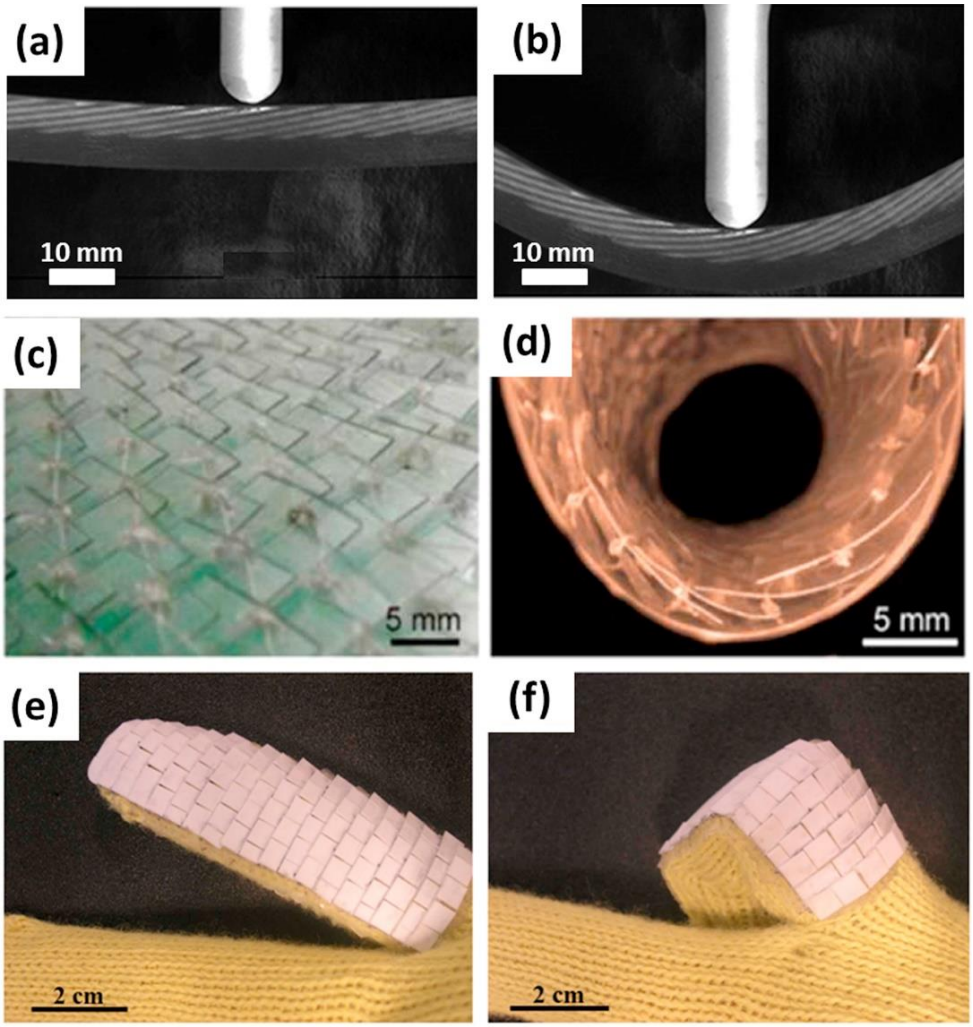

Figure 2-15 Bioinspired armor designs[79]. (a) and (b) Microstructured elasmoid scale armor amplifies penetration resistance with minimal loss of flexibility[80]. (c) and (d) A synthetic "fish skin" combines a mesh or dermis-like layer and rigid protective scales[81]. (e) and (f) The fish scale inspired armor by stretching a soft substrate and affixing ceramic tiles, which leads to imbrication upon release.

In summary, each type of scale has undergone million years of evolution and been structurally and functionally optimized for providing most efficient protection in their specific environment. Same as other biological materials, these scales are composed by very limited primary building blocks, mainly collagen, hydroxyapatite and calcium carbonate, but their unique and fascinating combinations in the nano-, micro-, and meso-levels lead to its capacity to prevent failure when under attack by either sharp teeth or crushing force of predators. The understanding of these dermal armors and their effectiveness in protecting these three fish may inspire the production of novel designs for flexible body armor, which provides superior safety and protection from physical threats.

2.4 Hydro-actuated reversible deformation of biological materials

2.4.1 Plant movement

As one of the dominant life forms on earth, plants produce a large variety of multifunctional biological materials to ensure survival. It is our general impression that plants are not as active as animals. They may stay statically for a long time without any detectable mobility. However, if we time-lapse their activities and view them in an accelerated way, their life is as vivid and lively as other organisms. Skotheim and Mahadevan[82] summarized some typical movements in plants and fungi, providing a brief but insightful perspective on their physical basis. As presented in Figure 2-16 (a), they classified the plant and fungal movements based on the smallest dimension, L (from microns to meters) and time scale, τ (from microseconds to days) of the moving unit. The absolute speed limit for all the movements, which is defined by the solid line in Figure 2-16 (a), is determined by the velocity of the elastic waves in the plant organs. All existing plant movements are slower than this speed limit and they are divided into two groups by the dashed line in Figure 2-16 (a). The movements to the right of the dashed line are significantly faster and are achieved by elastic instabilities. Some of them are dominated by a snap-buckling instability, which is circled in green. The most famous example is the rapid closure of the Venus flytrap (Figure 2-16b)[83], which can capture its prey (i.e., insects) within 0.1 s. A similar mechanism is found in the Aldrovanda, whose snapping speed is even faster due to its thinner leaf (in comparison with that of the Venus flytrap). Another type of fast movement is enabled by explosive fracture (circled in blue, Figure 2-16a). Here, the elastic energy stored in the intensively deformed organs is suddenly released when its tissue is fractured due to dehydration, which provides a large kinetic energy to disperse the seeds with an impressive initial speed (~10 m/s)[84]. Three representatives are presented

in Figure 2-16 (c), including *Polypodium aureum* (Figure 2-16c_1)[85], *Erodium cicutarium* (Figure 2-16c_2)[86] and *Cardamine hirsuta* (Figure 2-16c_3)[84].

To the left of the dashed line in Figure 2-16 (a), the movements circled in purple are actuated by the anisotropic swelling/shrinking of plant organs caused by differential hydration. Since the physical basis underlying the actuation mechanism for these movements is limited by fluid transport, they are usually relatively slow and undetectable to the human eye. Nonetheless, they are vital for plant growth, prey and sunlight capture, seed dispersal, and self-defense. Figure 2-16 (d) presents three well-studied examples: the pine cone (Figure 2-16d_1)[45], ice plant seed capsule (Figure 2-16d_2)[46] and a resurrection plant (*Selaginella lepidophylla*)[87]. They can actuate their characteristic structures by hydration, which plays a significant role in their seed dispersal and self-protection in different environments. Different from the movements relying on elastic instability, the actuation mechanism based on hydro-actuated anisotropic swelling/shrinking is purely passive and highly reversible, which may provide value to materials scientists developing robust self-shaping materials. Consequently, they are also the main focus of this section.

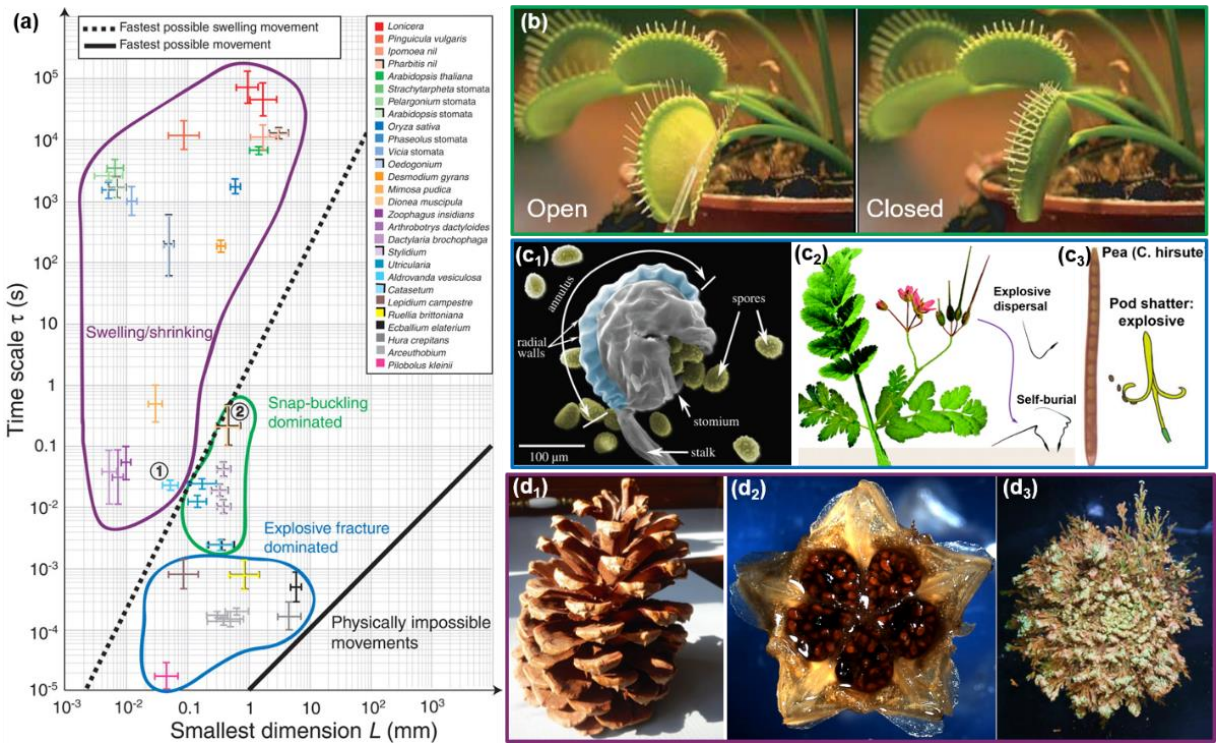

Figure 2-16 Various plant movements in nature. (a) Stockhein-Mahadevan classification of plant and fungal movements based on motion duration τ versus dimension (L) of the moving unit[82]. The solid line indicates the inertial time and the dash line characterizes poro-elastic time. (b) The reversible opening and closure of Venus fly trap as a representative of snap-buckling dominated plant movement[83]. (c) Examples of explosive fracture dominated movements. (c_1) A partially opened sporangium of *Polypodium aureum*[85]. (c_2) *Erodium cicutarium* launches seeds up to half a meter using energy stored elastically in a coil-shaped awn that is held straight before dehiscence[86]. (c_3) The explosive fruit of *Cardamine hirsuta*[84]. (d) Examples of swelling/shrinking dominated passive reversible deformation in plants (d_1) A pine cone opens its scales to release seeds in dry condition. (d_2) An ice plant seed capsule opens valves when they are fully hydrated[46]. (d_3) A resurrection plant *Selaginella lepidophylla* opens in water.

2.4.1.1 The anisotropic swelling of plant organs directed by cellulose microfibril angel (MFA) in the cell wall

The hydro-actuated deformation/movement of plant organs is also called hygroscopic movement; it is a passive humidity-driven actuation and completely independent of any control or energy input from metabolism[88]. The plant organs or tissues deform due to the restriction of the internal stress generated by the expansion/shrinkage of thick and rigid cell walls, even in dead cells[89].

Compared with animal cells, plant cells have a distinct characteristic with respect to morphology and functionality: they have a cell wall, an extracellular structural material that acts as a supportive framework and provides mechanical stability to the cell, maintaining turgor pressure and protecting inner organs. However, the walls of living and dead cells are different. Living turgid plant cells contain a plasma membrane, a unique structure that is semipermeable and separates the cell organs and cytoplasm from the external fluid. When the cell is immersed in a solution that has a different solute concentration from that within the cell, it will allow the water to pass through to equilibrate the osmotic pressure between the outside and inside of the cell, leading to a volumetric change (positive or negative, depending on whether water is flowing into or out of the cell, respectively). Once the cells are fully mature and dead, they become structural extracellular materials, the inner organs of plant cell and the plasma membrane disappear, and the center of the cell forms a hollow lumen. Figure 2-17 (a) shows a schematic of the structure of the dead plant cell wall. The dead cells are connected by middle lamellae and the outermost layer is the primary wall, which has cellulosic microfibrils embedded randomly. The major component of the dead plant cell wall is the secondary cell wall, which has three layers, denoted by S1, S2 and S3. They all consist of a specific array of cellulosic microfibrils embedded in a compliant and

amorphous matrix which is composed of lignin and hemicellulose. The cellulose microfibrils are assembled by several cellulose molecular chains interconnected to each other, forming alternating crystalline and amorphous phases[90,91]. Due to their crystallinity, the cellulose microfibrils are much stiffer than their matrix and consequently the mechanical properties of the entire plant cell wall are highly dominated by the arrangement of the cellulose microfibrils. The orientation of cellulose microfibrils within each layer are unidirectional, but subsequent layers are twisted relative to each other, forming a helical pattern. Since S2 is the thickest layer in the secondary cell wall, the mechanical properties of entire cell wall are dominated by the arrangement of its cellulose microfibrils.

Fratzl et al.[89] proposed a simplified model to quantitatively connect the hydroelasticity of the plant cell wall and the orientation of its cellulose microfibrils. Figure 2-17 (b) their thin-walled hollow cylindrical model; the angle between the microfibril orientation and the cell wall axis is defined as microfibril angle (MFA) and is denoted by μ. Fratzl et al.[89] assume that the matrix in which the cellulose microfibrils are embedded, can bear elastic swelling isotropically with increased humidity. This is analogous to the mechanism for shape recovery for keratin proposed by Sullivan et al.[51] and presented in Figure 2-23f: the amorphous phase absorbs the humidity and swells, whereas the crystalline filaments remain unchanged.

Furthermore, Fratzl et al.[89] also assumes that the swelling strain remains uniform in the (x,y)- plane and that there is no torsion of the cylinder due to confinement within a thicker tissue. Based on this model, the theoretical hydro-elastic performance for the plant cell wall as a function of the microfibril angle, μ, is plotted in Figure 2-17 (c). Plot I shows the normalized swelling stress σ_x/E_η (E is Youngs modulus, η is the isotropic volume strain due to swelling of the matrix)produced by the cell wall when its change in length is restricted; when $\mu \leq 45^0$, the stress is positive and tensile

for and plot II is the normalized swelling strain, ε/η, of the cell wall when it is free of applied stress. The positive values of ε/η represent tensile deformation and the negative ones correspond to compression. Plot III, Yeff, is the effective Young's modulus in the axial direction. Three curves are shown for each plot, representing three values of fibrils' relative modulus, which are 4, 20 and 100. The fibrils' relative modulus is the ratio between the Young's modulus of cellulose microfibrils and that of the matrix, namely, $(1-\nu^2)E_F/E$, where E_F, E and ν are the Young's moduli of fibrils, matrix and the Poisson coefficient, respectively. The horizontal straight lines, denoted by R, indicate values of stress, strain and Young's modulus with a random orientation of cellulose fibrils and a fibril's relative modulus of 20. The two vertical lines indicate the values of the microfibril angle where both stress and strain change from tension to compression where the relative modulus is equal to 20. Based on the information in the three plots, the following conclusions can be drawn:

- When the microfibril angle is relatively small ($\mu<45^o$), the stiff cellulose microfibrils can restrain the swelling and the cell wall tends to resist the expansion along the longitudinal axis, as indicated by the upper scheme in Figure 2-17 (d) (the hydrated cell wall expands radially, and longitudinal dimension shrinks);
- When the microfibril angle is relatively large ($45^o<\mu<90^o$), the restraining effect caused by the stiff fibrils is reduced with the increase the microfibril angle, and the cell wall is freer to swell along its longitudinal axis, as indicated by the lower scheme in Figure 2-17 (d) (the hydrated cell wall expands longitudinally and the radial dimension shrinks);
- With larger fibril's relative modulus, this anisotropic swelling effect is more obvious.

Figure 2-17 Mechanisms of hygroscopically-induced movement. (a) Schematic hierarchical structure of secondary cell wall in plant tissue. Cells are connected by middle lamellae and each cell wall is compromised of the primary wall and the secondary wall, the later consisting of three layers: S1, S2 and S3. The layer S2 is the major component, with largest thickness. The orientation of the cellulose microfibrils in these three layers twisted, forming a helical pattern, and the center of the cell is the hollow lumen. The cellulose microfibrils in the secondary wall is embedded in a matrix which is composed of hemicellulose and lignin, working as cross-links and filling interfibrillar spaces. The cellulose microfibril is composed of cellulose chains organized into alternative amorphous and crystalline phases. (b) Schematic of the S2 layer, the major component of the secondary cell wall in plant cell, which has the stiff cellulose microfibrils embedded in the swellable matrix[89]. The microfibril angle (MFA), μ, is defined in the presented coordinate system, as the angle of the cellulose microfibril with respect to the longitudinal axis of the cell (x axis). (**c**) Swelling behavior as a function of microfibril angle μ[89]. (i) The stress generated by swelling at fixed cell length; (ii) the swelling strain without applied external stress; (iii effective Young's modulus of the the secondary cell wall as a function of microfibril angle. (d) Dependence of dimensional changes on orientation of cellulose microfibril angle with cylinder axis: top: $\mu \leq 45^0$resulting in shrinking in longitudinal direction; bottom: $\mu \geq 45°$, resulting in expansion in longitudinal direction

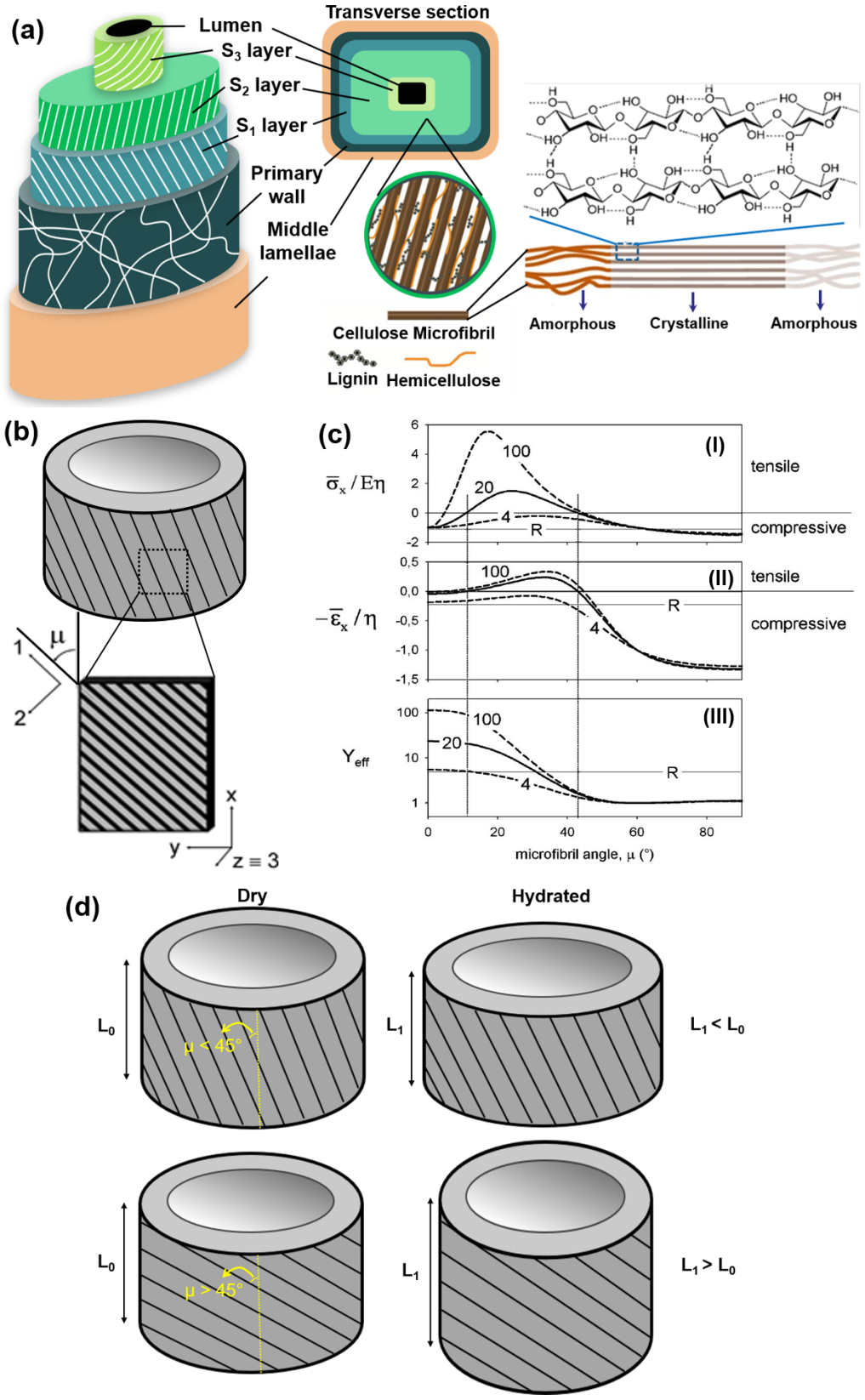
(a)
Lumen
S3 layer
S2 layer
S1 layer
Primary wall
Middle lamellae
Transverse section
Cellulose Microfibril
Lignin
Hemicellulose
Amorphous
Crystalline
Amorphous
(b)
μ
1
2
x
y
z ≡ 3
(c)
(I)
tensile
compressive
100
20
4
R
(II)
tensile
compressive
(III)
microfibril angle, μ (°)
(d)
Dry
Hydrated
L0
L1
μ < 45°
L1 < L0
μ > 45°
L1 > L0

The model by Fratzl et al.[89] provides a theoretical mechanistic insight for the origin of anisotropic swelling in various plant tissues. Manipulating assorted structures and anisotropy, nature creates many intricate hygroscopic movements, like bending, twisting, and coiling (also called helical twisting). In the following section, we provide some examples of this actuation mechanism. Moreover, from a biomimetic viewpoint, this mechanism also provides an inspiration for complex actuation that might be achieved by enforcing the compliant gels with stiff nanofibrils or nanotubes. Here we introduce several selected examples.

The most common humidity-driven reversible movements in many well-known plants are actuated based on the anisotropic swelling caused by varied microfibril angle (MFA). Here we introduce three types of well-investigated movements: bending, twisting and coiling, an provide specific examples of each. They all provide significant aid in seed-dispersal and germination.

Bending:

Bending is the most common movement since it is easy to achieve, as long as there is a noticeable strain mismatch in a well-integrated bi-layered structure[92]. The most well-studied example is from the pine cone[45,93] In the dry season, dehydration drives the pine cone to open, and then the seeds are released and carried by wind to travel long distances. On rainy days, the weather is not favorable for the seed dispersal, so the cones are closed to protect the seeds. This strategy of seed release and protection is achieved through the highly reversible bending deformation of the cone scales. Figures 2-18 (a_1) and (a_2) show pictures of an opened and closed pine cone in their dry and wet states, respectively. The scales of the cone bend outward with the reduction of hydration to release their seeds. The inset in Figure 2-18 (a_2) shows a broken scale, revealing the network of diverging fibers within it. The polished longitudinal section of a whole cone and an isolated scale presented in Figure 2-18 (a_3) clearly reveal the bi-layered structure of the pine cone

scale: the upper part is thinner but much brighter (called sclerenchyma fibers), while the lower part is relatively darker and is composed of sclereid tissue. Scanning electron micrographs (SEM) of the cell wall for these two parts (Figure 2-18a_4 and Figure 2-18a_5) demonstrate that the cellulose microfibrils are almost parallel to the cell's axis in the upper part (sclerenchyma fibers), resulting in a low microfibril angle (MFA ~ 30°), which restrains the hygroscopic swelling in the fiber direction. In contrast, the sclereid tissue (Figure 2-18a_5) in the bottom part has a much higher microfibril angle (MFA ~ 90°), leading to a free swelling of this region with increased humidity. The combined material response of the two components with different swelling response leads to the bending of the scale upon humidity changes.

A similar mechanism is identified in wild wheat awns[48]. Figure 2-18 (b_1) shows the closed and opened awn at relative humidities (r.h.) of 0.9 and 0.4, respectively. This bending is also produced by the heterogenous architecture inside the stem of the awn (Figure 2-18b_2), implying two distinct compositional regions: the cap, which is brighter, and the ridge, which is darker. The corresponding small angle x-ray scattering pattern indicates that the cellulose microfibrils in the cap region are laid almost parallel to the cell axis, restricting the swelling/shrinkage along the cell axis, while the tissue in the ridge region has multi-layered cell walls with randomly arranged microfibrils, which leads to a more isotropic shrinkage/swelling of the tissue upon humidity changes. As a result, the difference in the swelling/shrinkage of the inner and outer part of the awns results in a slow bending movement of the awns upon ambient humidity change. The cyclic changes between the relatively dry air during the day and higher humidity at night, as shown in Figure 2-18 (b_3), can lead to a slow crawling-like movement of the seed dispersal unit, while small spike-like silica hairs on the outside of the awns ensure a progressive forward movement by preventing the unit from moving backwards and out of the soil.

Twisting:

Twisting is another common passive hygroscopic movement which is usually identified in the seed pods of some plants such as the legume family, Fabaceae. For instance, bauhinia pods, also called chiral seed pods, can open and close their seed pods through a twisting movement upon humidity change (Figure 2-18c_1)[47]. Applying similar structural designs as pine cone and wheat awns, each valve of bauhinia pod consists of two layers of stiff cells with cellulose microfibrils oriented roughly at ± 45° with respect to the pod's longitudinal axis (Figure 2-18c_2). As illustrated with the scheme in Figure 2-18 (c_2), the preferential swelling/shrinking direction (indicated by arrows) in each layer is almost perpendicular. It turns out that the mere presence of two layers that shrink in perpendicular directions is sufficient to generate the flat to helical transition observed in pod opening. To prove this mechanism, two planar latex sheets are stretched uniaxially along two perpendicular directions and then glued together, forming a residually stressed compound sheet. The elongated strips cut out from the composite sheets were found to curl into helical configurations, confirming that the twisting movement of the pea pods are actuated by the mechanisms above.

Coiling:

Different from the Bauhinia pods, which twist around the long axis of the unit, the stork's bill (*Erodium gruinum*) separates from its fruit by coiling its awn when it is fully mature and dehydrated (Figure 2-18$d_{1,2}$). By the same coiling and uncoiling movement upon the humidity change in daily cycles, the awn can reversibly coil and uncoil (Figure 2-18d_3)[86], providing a propulsion to helps its seeds drill into the soil. Abraham et al.[49] found that the cellulose microfibril angle in the cell wall of the stork's bill awn is very unique. Unlike the common elongated cells in which the cellulose fibrils are wound in a helix around the cell wall (left side in Figure 2-18d_4),),

the stork's bill awn has a tilted helical arrangement of cellulose microfibrils within the cell wall, (model on the right side of Figure 2-18d_4), resulting in a varied threading angle of the microfibril along the cell wall. A simplified mechanical analogue made with swellable sponges and stiff threads proves that the normal helical (on the left in Figure 2-18d_5) winding produces the normal twisting, while the tilted helix can generate coiling, which directs the seed to a safe germination site.

Figure 2-18 Selected plant tissues that disperse their seeds or enable them self-burial through various passive hygroscopic movements. (a) The bending movement of pine cone scales. (a_1) The opened pine cone in dry season for releasing seeds. (a_2) The closed cone in wet state to protect seeds. Inset is a broken scale revealing sclerenchyma fibers inside. (a_3) Polished cross-section of an entire cone and a portion of isolated scale, showing double-layered inner structure. The bright upper layer is composed of sclerenchyma fibers and the dark lower region primally consists of sclereids. (a_4, a_5) SEM images of cell walls in sclerenchyma fibers and sclereids, respectively. (b) The bending movement of wild wheat awns driven by daily humidity change[48]. (b_1) The opening and closure of two awns at a relative humidity (RH) of 0.4 and 0.9. (b_2) The SEM image of the cross-section of an awn stem and the wide-angle x-ray scattering patterns of the crystalline cellulose at the cap and ridge regions, respectively. (b_3) Scheme of how one cycle of daily humidity alternation drives the awns to draw the seeds down into the soil. (c) The twisting movement of the pod opening in *Bauhinia variegate*[47]. (c_1) The flat valves of the closed pod curls into helical trips when it is open in dry state. (c_2) The inner layer (sclerenchymatous stratum) and outer layer of the pod valve are presented on the left and right sides, respectively, and the cell walls of them are both oriented approximately at 45° to the axis but pointing to opposite directions. The scale bar is 5 μm. (c_3) Schematic drawing of the cell wall orientations. (c_4) Demonstration of the twisting mechanisms: two pre-stretched thin latex sheets with anisotropic response (stiff direction indicated) are glued perpendicularly and a narrow strip (width of w) is then cut along a direction of θ as indicated; twisting deformation occurs when θ = 45°,135°, which exactly mimics the opening of the pods[47]. (d) The hygroscopic coiling in the stork's bill awn[49,86]. (d_1) The fresh fruit of stork's bill (*Erodium gruinum*) containing the seeds. (d_2) A ripened (dry) seed with coiled awn is peeling off from the fruit. (d_3) The passive hygroscopic coiling and uncoiling movements of the awn. (d_4) Schematic drawing of a normal helical arrangement of cellulose microfibril on a common plant cell wall (left) and a tilted helical arrangement of the cellulose microfibrils on the coiling cell wall of the stork's bill awn. (d_5) Drying sponge demonstrates the different hygroscopic behavior in plant cell walls with cellulose fibrils aligned in normal helix (left) and titled helix (right).

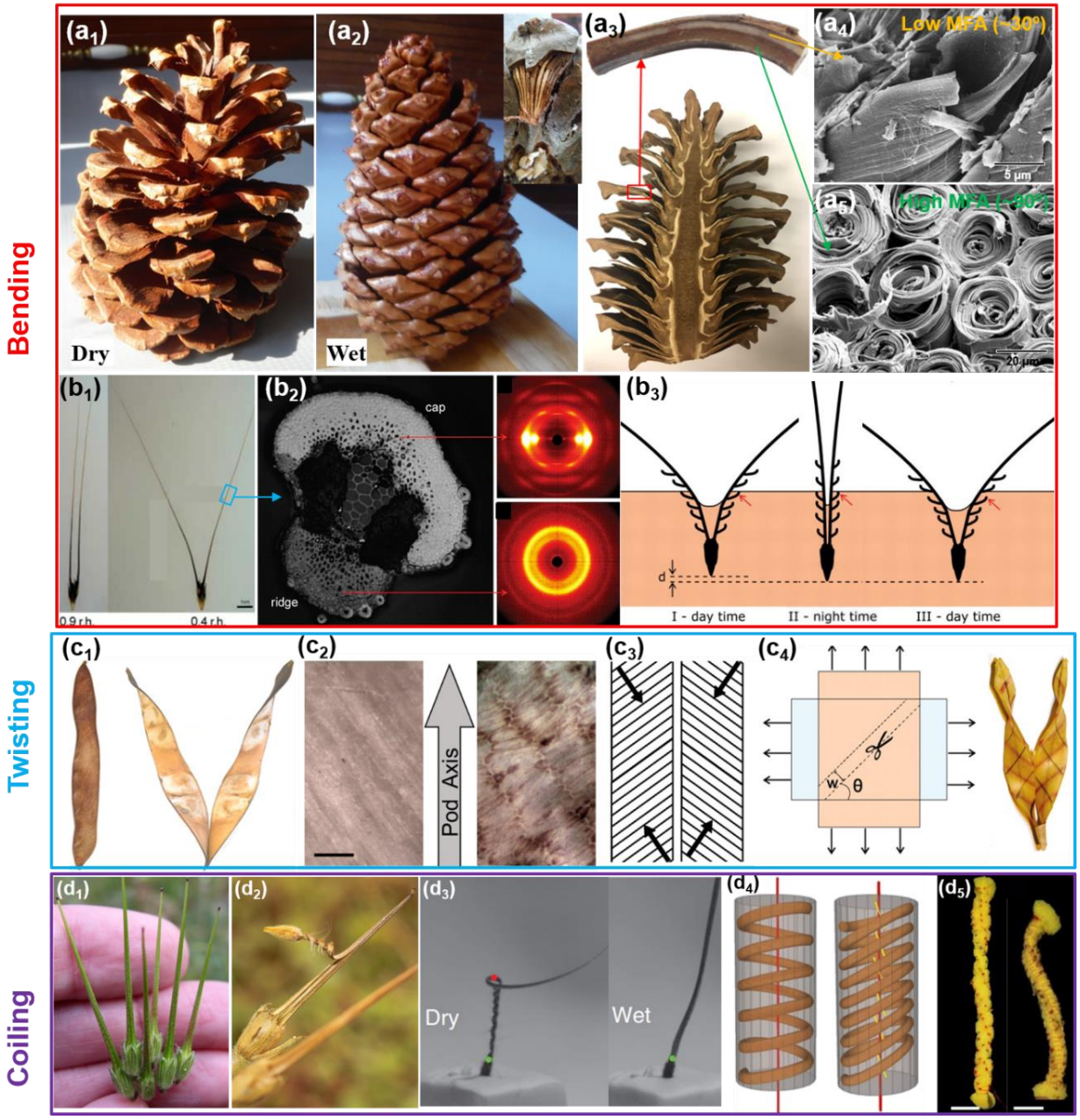
Bending
Twisting
Coiling
(a1)
Dry
(a2)
Wet
(a3)
(a4)
Low MFA (~30°)
5 µm
(a5)
High MFA (~80°)
20 µm
(b1)
0.9 r.h.
0.4 r.h.
(b2)
cap
ridge
(b3)
d
I - day time
II - night time
III - day time
(c1)
(c2)
Pod Axis
(c3)
(c4)
w
θ
(d1)
(d2)
(d3)
Dry
Wet
(d4)
(d5)

2.4.1.2 Anisotropic swelling/shrinking generated by gradient lignification

There are additional examples of simple hygroscopic movements that are also caused by the anisotropic deformation of plant tissue, but where the anisotropy is not based on the cellulose microfibril angle (MFA), but rather on gradients in lignin within different regions of the plant cell wall. Such is the case of structures found in resurrection plants.

Resurrection plants such as *Selaginella lepidophylla* flourish in desert regions and have an extraordinary capability to resist desiccation[87]. As shown in Figure 2-19 (a), their branches are able to contract with drying, curling the plant into a tight ball. Incredibly, it can hibernate for up to a century. After it curls, it can be transported large distances by the wind, rolling on the ground, making them obligatory travelers passing through enormous deserts, even crossing the borders of continents[94]. This is similar to the tumble weeds common to the Western United States. Within the curled plant, the inner fresh tissue remains attached and closed, protecting the fruits and seeds from being dispersed in extreme droughts. If there is a rare rainy season, the ball absorbs the water and uncurls itself within several hours (Figure 2-19b), waking up the plant from its dormant state and causing the capsular fruits to open and disperse the seeds. Figure 2-19 (c) and (d) depict the curling process of an isolated stem from the outer and inner regions upon desiccation. The curling curvature of the outer stem is much smaller than that of the inner one, which aids the branches from different regions to work synergistically to retract the plant into an integrated ball, providing optimal protection. This hygro-actuated process of curling and uncurling is completely reversible over multiple cycles. The ability of the plant to do this is attributed to the presence of a lignin gradient within the stem tissue. Since the higher degree of lignification can increase the stiffness of the tissue and consequently reduce the ability to swell, the lignin gradient within the stem in two directions produces a curling of the branch. Figures 2-19 (e,f) show the stained cross-sections

of an inner stem from the apical (top) region to the basal (bottom) section, indicating that the lignification on the same portion of the stem gradually decreases from the abaxial (outer) side to the adaxial (inner) one, while among different stem sections, there is a graded increase of lignification from the basal section to the apical section. This gradient generates the anisotropic swelling/shrinking of the plant branches and produces the highly reversible hydro-actuated deformation for the resurrection plants to protect themselves.

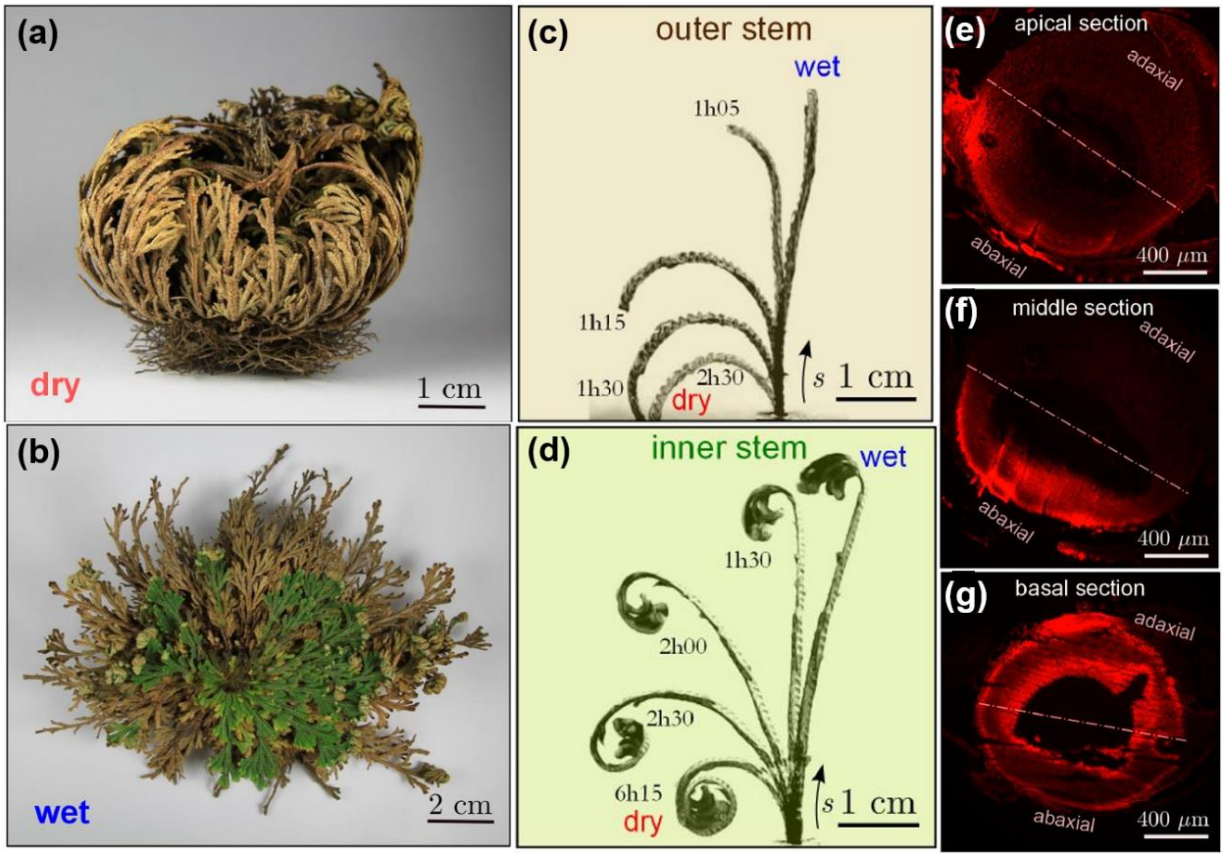

Figure 2-19 Hygroscopic movements induced by gradient lignification in resurrection plant *Selaginella Lepidophylla*[87]. A resurrection plant (*S. lepidophylla*) in dry (a) and (b) wet states. Its outer layer contains (c) older stems which curls with less curvature during the dehydration process than its inner layer stem (d). The cross-sections of a stained inner layer stem at (e) apical, (f) middle and (g) basal sections shows a gradient reduction of lignification (bright red) from stem base to tip.

2.4.1.3 Actuation or shape recovery by hierarchical foam-like structure

Another prevailing type of hygroscopic material is enabled by foam-like structures, including cleaning sponges, such as a luffa sponge[95], that we use on a daily basis. Figure 2-20 (a_1) shows the fresh and fully dried luffa; Figure 2-20 (a_2) reveals its inner foam structure. The hydrophilic foam structure absorbs or loses the water upon humidity change, resulting in a reversible change in the overall shape. The hierarchical foam structure is presented in Figure 2-20 (a_2), consisting of the struts which are in turn porous, confirming that the luffa sponge has a cellular structure at smaller length scales. Figure 2-20 (b_1) shows the compression of the luffa sponge and its subsequent dehydration. Numerous locally buckled and compressed struts are seen at the micrometer scale (Figure 2-20b_2). Since the plant tissue is highly hydrophilic, the deformed sponge can rapidly recover its original shape within less than 10 minutes (Figure 2-20c_1) by absorbing water to expand the cellular structure of the sponge (Figure 2-20c_2). The three central orifices in the luffa (seen in Figure 2-20a_2) contain the seeds, which are thus, well protected. This porous architecture is thought to provide a vehicle for the seeds to travel far from the source, serving as a dispersal medium.

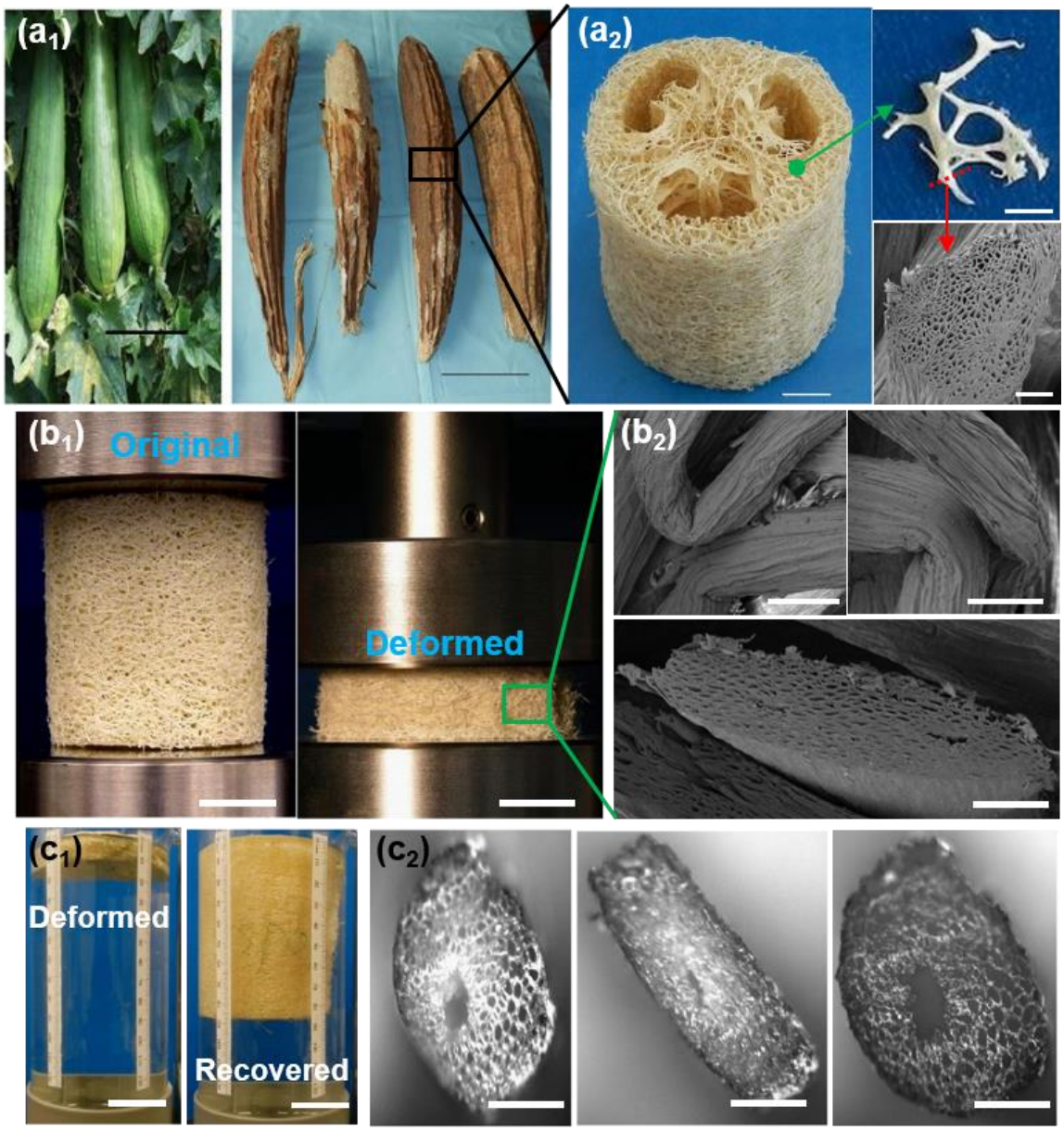

Figure 2-20 The rapid water-driven shape recovery of luffa sponge[95]. (a) The hierarchical foam structure of luffa sponge. (a_1) The matured and desiccated luffa fruit[95] (scale bar, 10 cm). (a_2) The luffa sponge has an open-cell foam structure and the struts are composed of dead plant cells with hollow tubular structure; seeds are carried in three internal channels (scale bar: left, 10 cm; right top: 2mm; right bottom: 100 μm). (b) Shape deformation of luffa sponge. (b_1) A luffa sponge permanently deformed after axial compression (scale bar, 2 cm). (b_2) SEM images of locally buckled foam struts and compressed stent cross-section compression (scale bar: top, 200 μm; bottom, 100 μm). (c) Water-driven shape recovery produced by lateral swelling of struts, which retain their original length. (c_1) The deformed luffa sponge recovers to its original shape after being immersed in water within 2 mins (scale bar, 5 cm). (c_2) Recovery of a single foam strut with micro-tunnels (scale bar, 1mm).

Another hygroscopic biological device actuated by a hydrophilic foam structure is found in the ice plant (*Delosperma nakurense*) seed capsule[46] and the carrotwood (*Cupaniopsis anacardioides*) seed pods. Since the habitat of ice plants is the desert, they only releases seeds in moist weather, which may increase their chance to successfully germinate in the most favorable environment. During their dormancy in drought season, the seeds are protected in compartments by five sealed valves in the capsule (Figure 2-21a_1). As the surrounding moisture content increases, the active hinge absorbs water and the valves straighten and bend outwards (Figure 2-21a_2), reopening the capsule (Figure 2-21a_3). This mechanism relies on the cellular structure in the inner side of the valve. Here, the compact cellular tissue is originally arranged as a collapsed honeycomb under dry conditions (Figure 2-21b_1), and can absorb water during the hydration process (Figure 2-21b_2) enabling the cells to expand and form a deployed honeycomb structure (Figure 2-21b_3), macroscopically generating the opening of the valves of the seed capsule. A similar mechanism is also identified in carrotwood seed pods. In contrast to the ice plant seed capsule, the seed pod of carrotwood opens upon dehydration and closes with increased humidity (Figure 2-21c). The inner surface of each pod valve is covered by a fluffy fibrous layer acting as a cushion to provide protection for the seeds (Figure 2-21d,e). The cross-sections of a pod valve in their dry and wet state are presented in Figure 2-21 (e), indicating that beneath the fibrous cushion, there are two distinct layers constructing the valve tissue. The two images in Figure 6e are taken from the same specimen at the same length scale. They clearly show the different potential to swell in each layer. Due to the swelling caused by hydration, the thickness of the upper layer, the bright one highlighted with a red box in Figure 2-21 (e), increases about 300 μm, while the thickness of the bottom layer, the sponge-like tissue, increases by approximately 500 μm. The mismatch of the swelling strain generates the retraction movement of the pod valve, causing the closure of the seed pod upon

hydration. This swelling mismatch is conferred by the distinct structural features within these two layers, and is revealed by SEM images (Figure 2-21f). The upper layer is composed of fibers aligned along the thickness direction (Figure 2-21f_1), whereas the bottom layer has a sponge-like porous structure with a pore size gradient. Figure 2-21 (f_2) the transitional region has a smaller pore size (10 ~ 20 μm), while the pore size at the bottom region, as presented in Figure 2-21 (f_3), is about 20 to 50 μm. Compared with the well-aligned fibers in the upper layer, the porous structure in the bottom region exhibits a larger expansion upon hydration, producing the anisotropic swelling in the pod valve tissue.

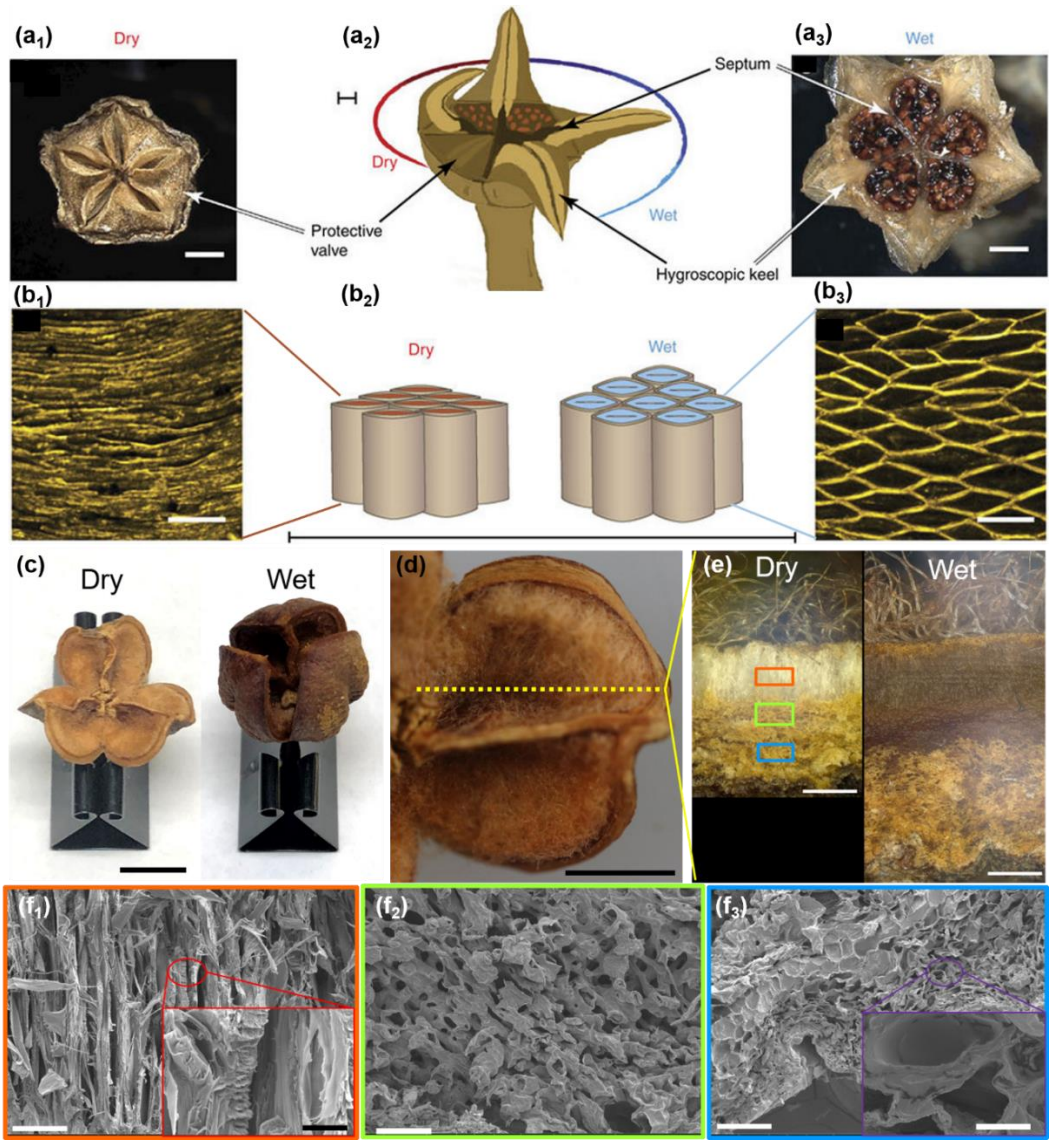

Figure 2-21 Hydro-actuated opening and closure of ice plant seed capsule and carrotwood seed pod. (a) The hydration-induced opening of the ice plant seed capsule (scale bar, 2mm). Schematic showing the opening of protective valve during hydration process[46]. (b) The hydration-induced swelling and collapsing of plant cell wall in the upper layer of the honey-comb like structure in the valve tissue causing deployment of recreation of the entire capsule, as the schematic drawing represents (scale bar, 0.1mm)[46]. (c) The hydration-induced closure of the carrotwood (*Cupaniopsis anacardioides*) seed pod (scale bar, 1cm). (d) The magnified image of one valve on the pod (scale bar, 1cm). (e) The cross-sections of one pod valve at the position indicated in (d) at dry and wet conditions with same magnification (scale bar, 500 μm). (f) The SEM images of the three regions shown in (e). (f_1) The upper layer is composed of well-aligned fibers (scale bar, 50 μm; scale bar in the inset, 5 μm). (f_2, f_3) The lower layer has porous structure, the pore size being larger in the bottom region (scale bar in f_2, 50 μm; scale bar in f_3, 100 μm; scale bar in the inset of f_3, 20 μm).

2.4.2 Shape recoverable natural polymeric materials produced by animals

Some biological materials produced by animals also have similar self-shaping properties due to hydration, but their recovery mechanism is different from that of plant tissue. Figure 2-22[53] provides a schematic that describes a general mechanism for the hydro-induced shape recovery in animal tissues, which is based on dual-phase composition in natural biopolymers[53]. Figure 2-22 (a) shows the simplified structural frame of the materials that posses the shape recovery effect. Typically, there are two phases: one is the crystalline phase, chemically cross-linked to determine the permanent structure for the material; the other phase is amorphous, consisting of randomly organized molecular chains and branches which have abundant hydrogen bonds connecting them, forming switches to enable the tunable temporary shape. The scheme for the cycle of the shape recovery process is displayed in Figure 2-22 (b). When the material is hydrated, the free water molecules enter the space between the polymer chains and branches, disrupting the original hydrogen bonds in the amorphous phase, turning on the switches to make the material compliant for deformation. With an applied external force, the hydrated material deforms and the polymer chains and branches relocate. During the dehyration process, the free water evaporates, leaving the relocated chains and branches to form new hydrogen bonds between them, turning off the switch and fixing the material into a temporary shape. Once the material absorbs water again, the new formed hydrogen bonds break again and, driven by entropic forces, the material recovers its original shape. Sullivan et al.[51] also developed a recovery model (Figure 2-23f), which provides a complete description atthe mesocopic level, incorporating both crystalline and amorphous components.

Based on the mechanisms proposed here, the former (crystalline phase) is not affected by hydration, whereas the amorphous phase absorbs water and plasticizes. The material can be

'trained' into a position upon drying by the formation of new hydrogen bonds in the amorhous phase. The complete model, incorporating the interplay between the two phases, was developed by Sullivan et al.[51]. Its mesoscale level representation, incorporating both crystalline and amorphous components (the latter developing permanent deformation) will be presented later (Section 2.4.2.1) It should be also noticed that a similar mechanism operates in wood and was modeled by Fratzl et al.[89] (Section 2.4.1.1).

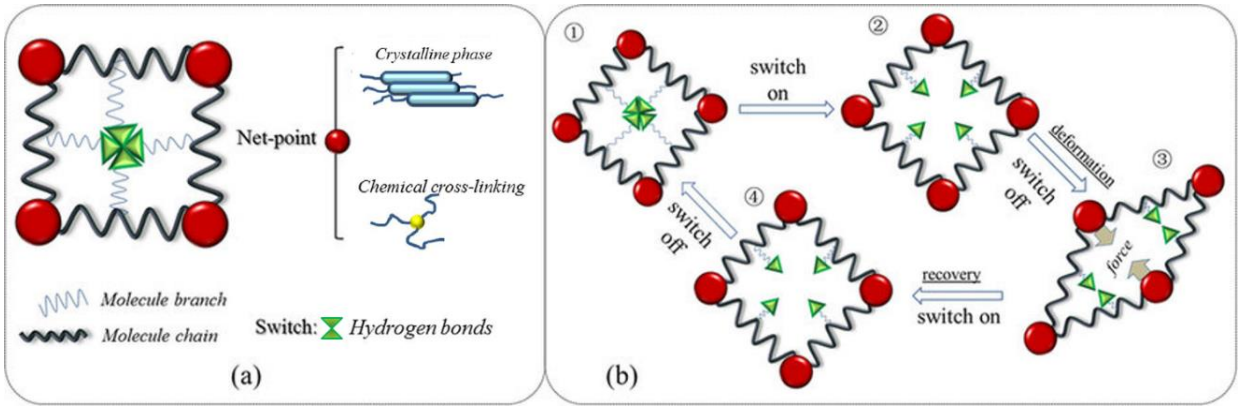

Figure 2-22 General mechanism for the passive shape recovery effect driven by water in the biopolymers produced by animals according to Xiao et al[53]. (a) A structural model of hydro-actuated shape memory biopolymers which consists of two key components: net point and switch. The net-point, which determines the permanent shape, could be crystalline phase in most cases or some other stable chemical cross-linking. The switch, which determines temporary shape, is usually hydrogen bonds. (b) The cycle of a representative shape recovery process. ① The structural model at original state. ② The switch (hydrogen bonds) is turned on (break) by the stimulus of water. ③ The applied external force deforms and dehydration turns off the switch (new temporary hydrogen bonds formed) to fix the structure into temporary shape. Once the stimulus (water) is applied again, the switch is reopened (temporary hydrogen bonds break) and driven by entropic force, the temporary shape returns the original one. ④ Dehydration turns off the switch (original hydrogen bonds reform) and the original shape is fixed.

2.4.2.1 Keratinous materials: bird feather, sheep horn and animal hair

Keratin is a ubiquitous biological material, representing a group of impermeable filament-forming proteins with a high sulfur content[96]. It is used in constructing the bulk of epidermal appendages such as nails, claws, hair, horns, whelk egg capsule, whale baleen, bird beaks, and feathers[96]. These keratinous materials are produced by specialized cells filled with keratin and not associated with metabolism once they are formed; thus, these materials are usually considered as "dead" tissue. Combining strength, toughness, and light-weight, keratin serves as a superior structural material for many functions, such as armor (pangolin scales), weapons (nails, claws, and horns), thermal insulator (hair and feathers) and transportation enablers (hoof and feathers)[96]. Since keratinous materials are usually located at the most superficial layer on an animal's body, their intricate hierarchical structure confers them an excellent capability to recover their shape and strength by hydration, which significantly improves their durability. Here we provide three examples for illustration: the bird feather, sheep horn, and animal hair. As imperative appendages to the wings of birds, feathers are an evolutionary marvel that is not only lightweight, but is also able to endure the intense aerodynamic loads during flight, perfectly meeting all the requirements of aerial locomotion[97]. However, after flying for thousands of miles, fighting, and other forms of environmental damage, structural deterioration is inevitable. In addition to preening, birds have developed a relaxing, yet highly effective strategy to recover their damaged feathers: bathing (Figure 2-23a). Figure 2-23 (b)[51] shows that the shaft of a feather is divided into two parts: the calamus, which is purely composed of cortex, and the rachis, which includes a foam-filled cortex. Figure 2-23 (c, d) show that after severe plastic deformation, both the cortex and rachis can rapidly recover their original shape in less than 30 minutes exposure to water. With the aid from the inner foam, the rachis can recover even faster. Liu et al.[50] pioneered and Sullivan et al.[51] further

improved on the shape and strength recovery of feather. Sullivan et al.[51] proposed the following mechanism for explaining the impressive recovery effect: since the cortex of the feather is composed of hierarchically arranged keratin fibrils and filaments embedded in an amorphous matrix (Figure 8e), the preferential permeation of water into the amorphous phase can break the hydrogen bonds between polymer chains and make the matrix swell, straightening the crystalline keratin filaments and consequently recovering the overall shape and mechanical properties (Figure 2-23f).

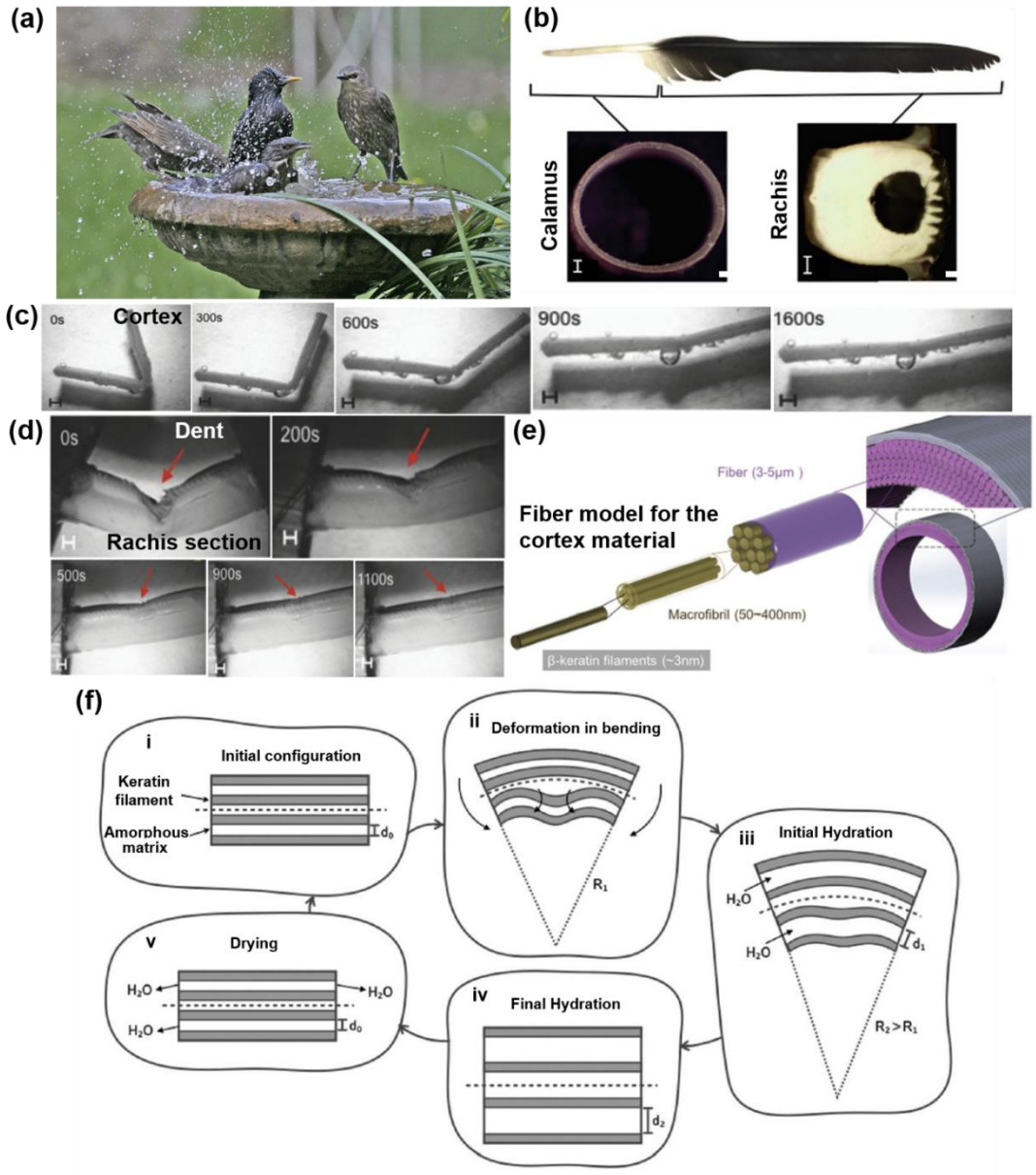

Figure 2-23 Hydration-induced shape and strength recovery of bird feathers[51]. Birds take bath for recovering their feathers (scale bar is 0.5 mm). (b) An isolated bird feather (scale bar is 0.5 mm). The calamus only has cortex while the rachis region has cortex filled with foam. The shape of both the shaft cortex (c) and rachis section (d) can be recovered in water after severe mechanical deformation (scale bar is 1 mm). (e) The hierarchical structure of the keratin fibers in bird feathers. (scale bar is 1 mm). (f) Schematic showing the mechanism for hydration-induced structural recovery in bird feathers according to Sullivan et al.[51]. i: initial configuration showing crystalline fibers embedded in amorphous matrix; ii, bending of feather producing buckling of lower (below neutral axis) fibers; iii hydration producing swelling of amorphous matrix; iv since matrix is constrained by fibers, swelling produces straightening of feather shaft; v. shrinking of amorphous matrix by drying.

Horn is another common keratinous-based tool possessed by many mammals including cattle, goats, sheep, antelope, and rhinoceroses, serving as a powerful weapon to help these animals defend themselves from predators and fight members of their own species (horn fighting) for territory, dominance, or mating priority. As a highly effective energy absorbent material[98], the horn inevitably suffers damage during fighting, yet it can repair itself via hydration[52]. Figure 2-24 (a) presents the hierarchical structure of the bighorn sheep horn. Unlike the well-aligned fibrous structure in feathers, the horn is assembled by lamellae of keratinized cells. The building blocks of these keratin cells, the microfibrils, are composed crystalline intermediate filaments that are embedded in an amorphous matrix. Huang et al.[52] discovered that hydration can effectively recover the morphology of horn in all three dimensions (Figure 2-24b) and that the underlying mechanism is also due to its dual-phase structure: the crystalline phase determines the permanent shape while the amorphous phase contributes the temporary deformation due to the abundant hydrogen bonds in it. Interestingly, they also found that since the impact occurs mostly along the radial direction during horn fighting of bighorn sheep, the strength recovery in the radial direction is the most efficient among all three directions (Figure 2-24c). In the first three cycles, the radial specimens exhibit minimum mechanical deterioration. After three cycles, the specimens loaded in longitudinal and transverse directions have completely failed, while the radial specimens still maintain sufficient mechanical strength. They attribute this performance to the tubular structure inside the sheep's horn. At the mesoscopic level, numerous tubules are aligned along the longitudinal direction (Figure 2-24a), which not only contributes to the energy absorption capability during the impact loading[98], but also facilitates the hydration-driven recovery in the radial direction. Figure 2-24 (d) provides the evidence: in the normal radial specimen, the collapsed tubules recovered with hydration, while the cracks remain in the radial specimen without tubules.

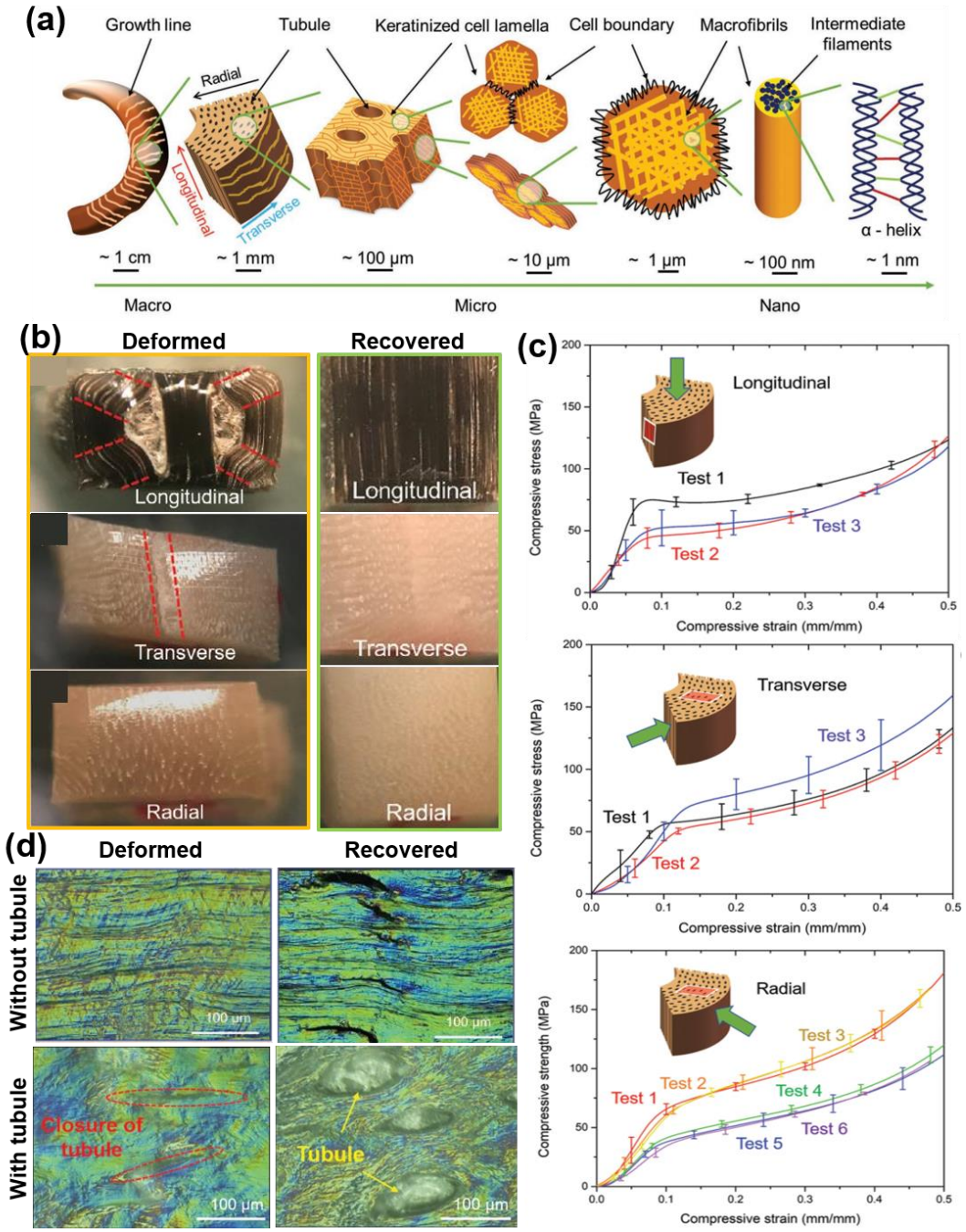

Figure 2-24 Hydration-driven recovery of bighorn sheep (*Ovis Canadensis*) horns[52]. (a) The hierarchical structure of sheep horns. (b) The photographs of the deformed and recovered horn specimens in different loading directions. (c) Compression tests on hydration recovered horn specimens along different directions. Test 1 is on the original specimens. The specimens along longitudinal and transverse directions failed after 3 tests. (d). The microscopy images of the deformed and recovered radial specimens with and without tubule structures. The cracks remain in the specimens without tubules.

The most familiar recovery phenomenon on keratinous tissue and observed almost everyday is the hydration-induced shape recovery of hair. One may notice that no matter how messy their hair, a quick hair wash will enable recovery of the original form. The shape recovery mechanism of hair is similar to other keratinous materials. Figure 2-25 (a) shows the intricate structure of human hair: the hierarchical crystalline elements at different length scales (i.e., α-helices, intermediate filaments, macrofibrils, cortical cells) are all embedded in the amorphous matrix[99]. Based on the general mechanisms proposed in Figure 2-22, animal hair also has two phases: the net-points (indicated in Figure 2-22), are composed of the crystalline elements and the disulfide bonds between polypetide chains (Figure 2-25b)[53]. Upon deformatio, hydrogen bonds in the amorphouas phase are broken and reforming at different positions. Upon the reversible hydration and dehydration process, the switches turn on and off accordingly, making geometrical and mechanical recovery possible (Figure 2-25c,d), which shows camel hair which trained into a circular shape and then dried, acquiring this shape. Upon rehydration, the elastic energy stored in the crystalline phase restores the original shape, since the amorthous phase is 'softened' by water. Once dried, hair regains its original straight shape. Such a behavior is at the root of the multi-billion dolllar hair-care indusstry. There is an additional effect: a strain-induced alpha to beta keratin transformation[100].

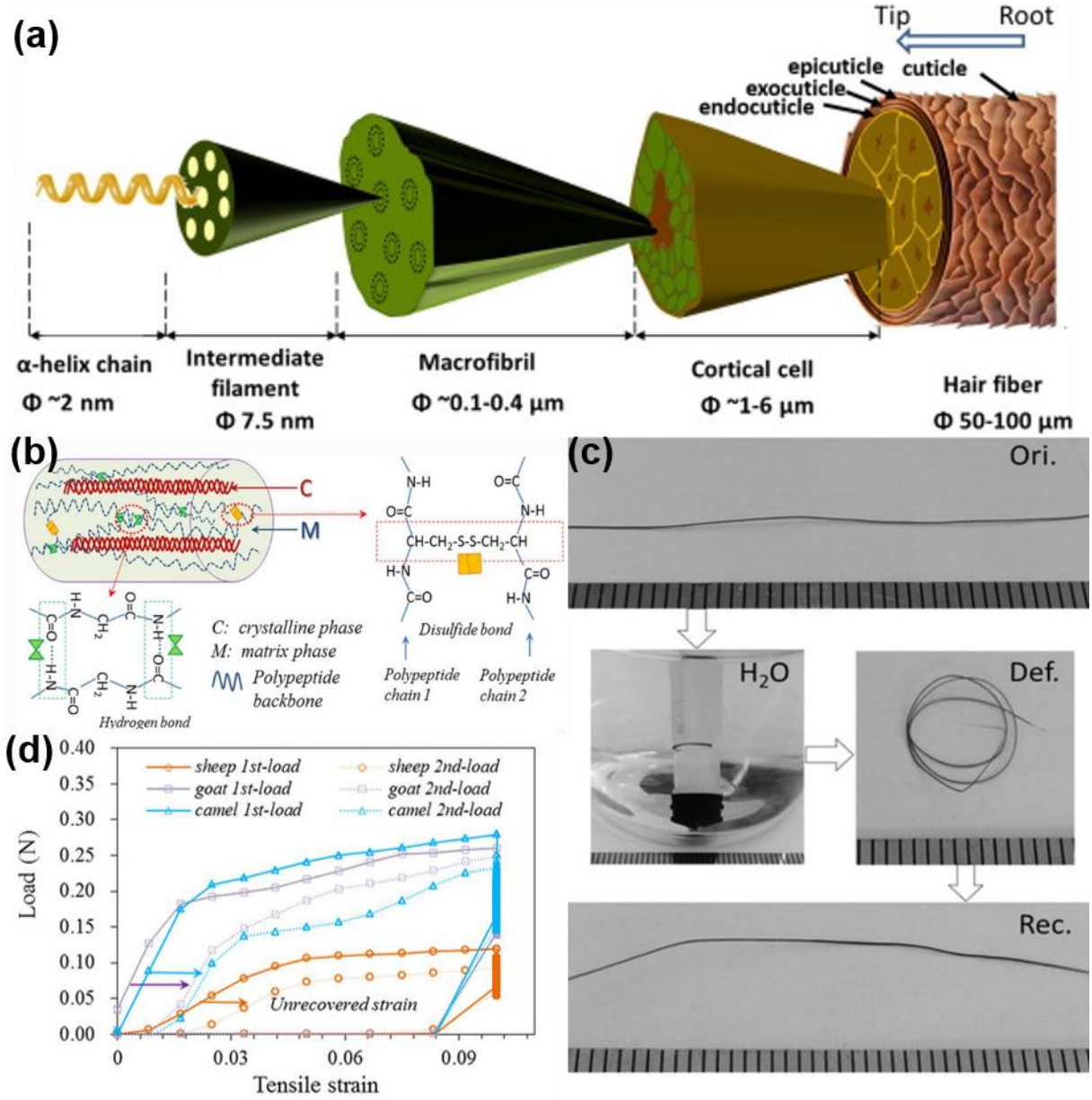

Figure 2-25 Water-stimulated shape memory effect in animal hairs[53,99]. (a) The hierarchical structure of a hair (human hair)[55]. (b) Structural model represents the crystalline α-helix (marked c) embedded in amorphous matrix (marked m). (c) The shape recovery process induced by water for a camel guard hair. An originally straight hair is immersed in water and curled after fully hydrated. The curled hair is dried to fix its temporary shape. After re-immersed in water, the curled hair returns to its original straight shape. (d) Mechanical strength recovery of hairs from three animals (sheep, goat and camel) after 2 cycles of load.

2.4.2.2 Other biopolymers: spider silk

Spider silks are extraordinary structural materials, which possess a combination of strength and extensibility that are superior, by weight, to most man-made fibers. In addition, it has been proposed that the spider dragline silk can also generate supercontraction induced by wetting, which plays an important role on taking up slack in webs, restoring web shape and tension after prey capture, and opposing extensional forces exerted by the weight of precipitation on webs. Figure 2-26 (a) shows the highly reversible change in the length of a spider silk strand upon the cyclic variation of relative humidity (from 10% to 90%)[54]. Similar to the keratinous fibers, spider silk is also hierarchically constructed from crystalline domains embedded in an amorphous matrix. Each domain is assembled by the β-sheet nanocrystals connected with semi-amorphous phase (Figure 2-26b)[7]. As the scheme in Figure 2-26 (c)[101] simply implies, the crystalline phase has a permanent shape and the humidity-driven length tunability is conferred by the activation of the switch (hydrogen bonds) in the amorphous phase[101,102].

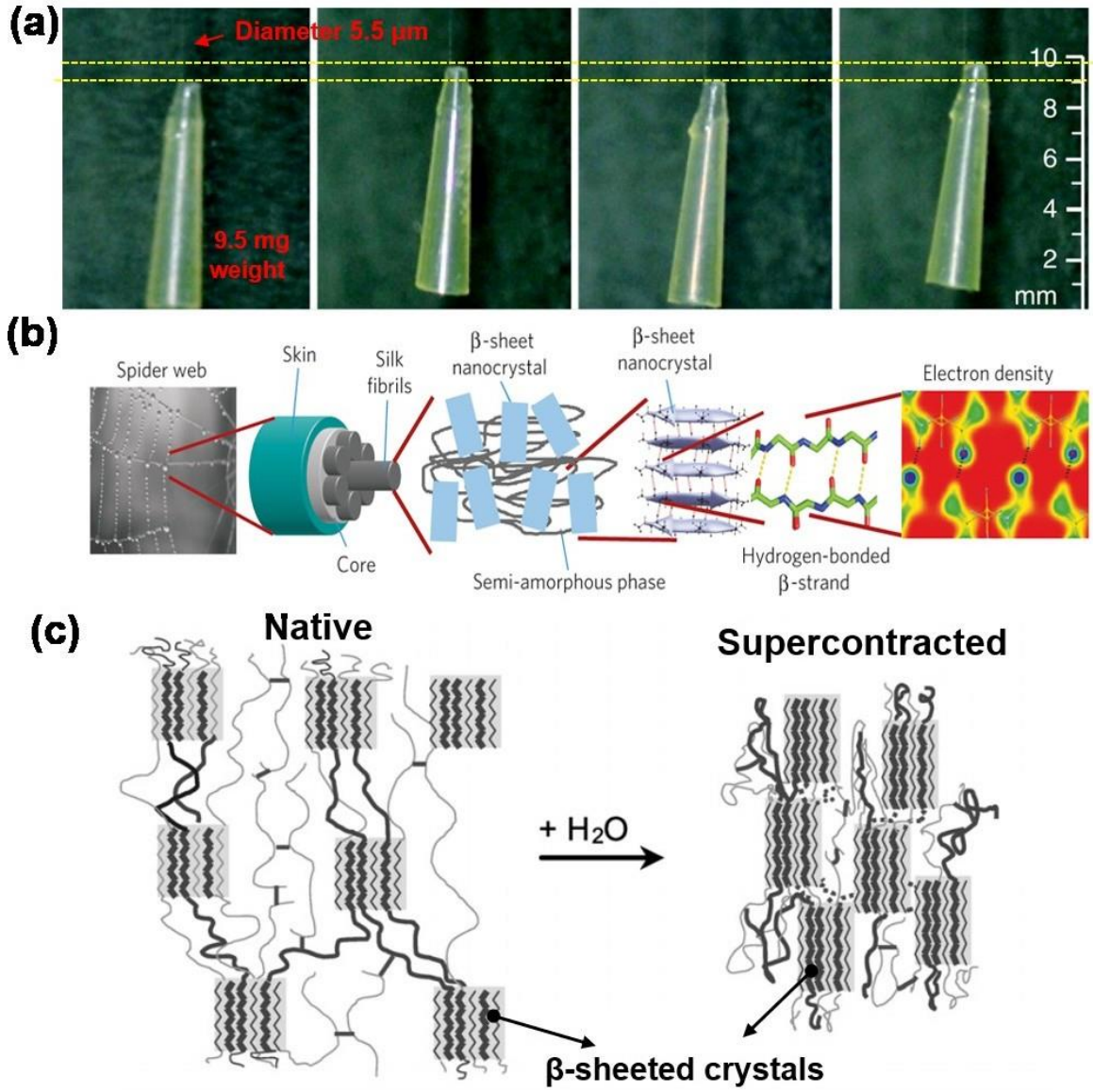

Figure 2-26 Moisture-driven reversible supercontraction of spider silk. (a) Several cycles of humidity-driven highly reversible contraction and relaxation for a spider silk containing an elongated weight at its bottom[56]. (b) The hierarchical structure of spider silk[57]. (c) Structural model of native and supercontracted spider silk[101]. The native spider silk has highly oriented β-sheeted crystals interlinked by the glycine-rich chains, forming the crystalline and amorphous dual phase structure. In the amorphous phase, there is a Gaussian distribution of pre- strains which can be described by the worm-like chain model[103]. As the humidity increases, the hydrogen bonds in the amorphous phase are broken by water molecules, releasing the pre-strain and generating entropy-induced supercontraction.

2.4.3 Bioinspired applications

Inspired by the various hydro-actuated reversible deformation mechanisms in a diverse set of natural structures, many smart materials, like programmable self-shaping materials and artificial muscles, are being developed based on different actuation mechanisms discussed in the previous sections. Here we provide four examples inspired by plant organs and two that mimic animal tissue.

Inspired by the anisotropic swelling of plant organs directed by the cellulose microfibril angle (MFA) in the cell wall, Erb et al.[25] fabricated several types of programmable self-shaping materials which can be driven by humidity or thermal change. As illustrated in Figure 2-27(a), they first developed discontinuous, anisotropic Al_2O_3 micro-platelets coated with superparamagnetic iron oxide nanoparticles, which make them manifest a magnetic response. Based upon the remote control of the orientation of the magnetic alumina platelets in different layers of a hydrogel composite using a weak external magnetic field, a multi-layered swellable/shrinkable polymer matrix with stiff inorganic reinforcements oriented along different directions was fabricated. This structure mimicked the structural design of self-shaping plant organs. By controlling the hydration or temperature, various programmable passive movements, including bending (Figure 2-27b, c) and twisting (Figure 2-27d) were achieved.

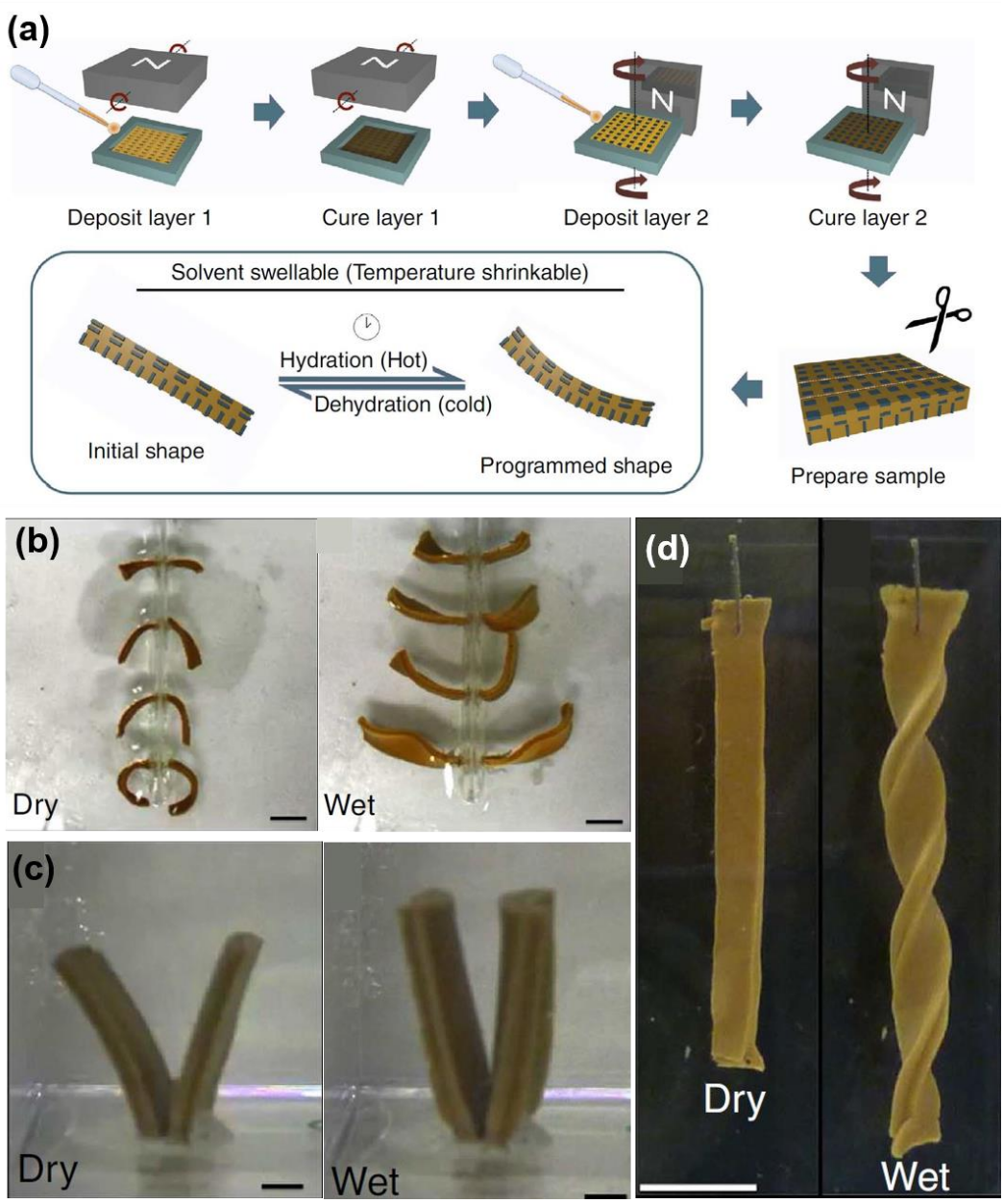

Figure 2-27 Bioinspired self-shaping composites manufactured by magnetic field controlled reinforcement[25]. (a) The scheme of manufacture technique. Multi-layered hydrogel matrix mixed with ultra-high magnetic response (UHMR) alumina plates is fabricated in a Teflon mold under a weak magnetic field generated by a rotating permanent magnet. The UHMR is produced by coating Al_2O_3 with iron oxide nanoparticles and the orientation of this reinforcement in each layer is determined by the applied magnetic field. (b) The hydro-actuated bending movement of the self-shaping hydrogel composites mimicking the reversible bending of pine cone scales and (c) wild wheat awns. (d) The hygroscopic twisting deformation mimicking the twisting opening of Bauhinia pod. All scale bars are 1 cm.

Additive manufacturing, also known as 3D printing, is a powerful technique for creating composites with complex structures. It has been widely utilized to fabricate bioinspired structures and devices having hierarchical structures. More recently, a new technique, called 4D printing, was developed and is very promising for creating smart materials with complex structures. 4D printing extends 3D printing by incorporating the dimension of transformation over time. The 4D printed materials can change to other structures upon the input of external energy such as temperature, light or other environmental stimuli. Gladman et al.[52] developed 4D printed biomimetic hydrogel composites with bilayer structures programmed into various patterns. Figure 2-28 (a) presents a hydrogel composite reinforced with cellulose microfibrils. The printing ink can be aligned by the shear force acting on the filament during direct ink writing. The subsequent anisotropy of the stiffness, E, and swelling strain, α, are shown on the right. Applying the same strategy identified in the movement of plant organs directed by cellulose microfibril angle, the printed hydrogel composites can localize swelling anisotropy and produce many complex shape changes once immersed in water. Figure 2-28 (b-d) show assorted movements generated by the 4D printed materials, including bending, curling, twisting and even more complex origami that mimic various floral patterns.

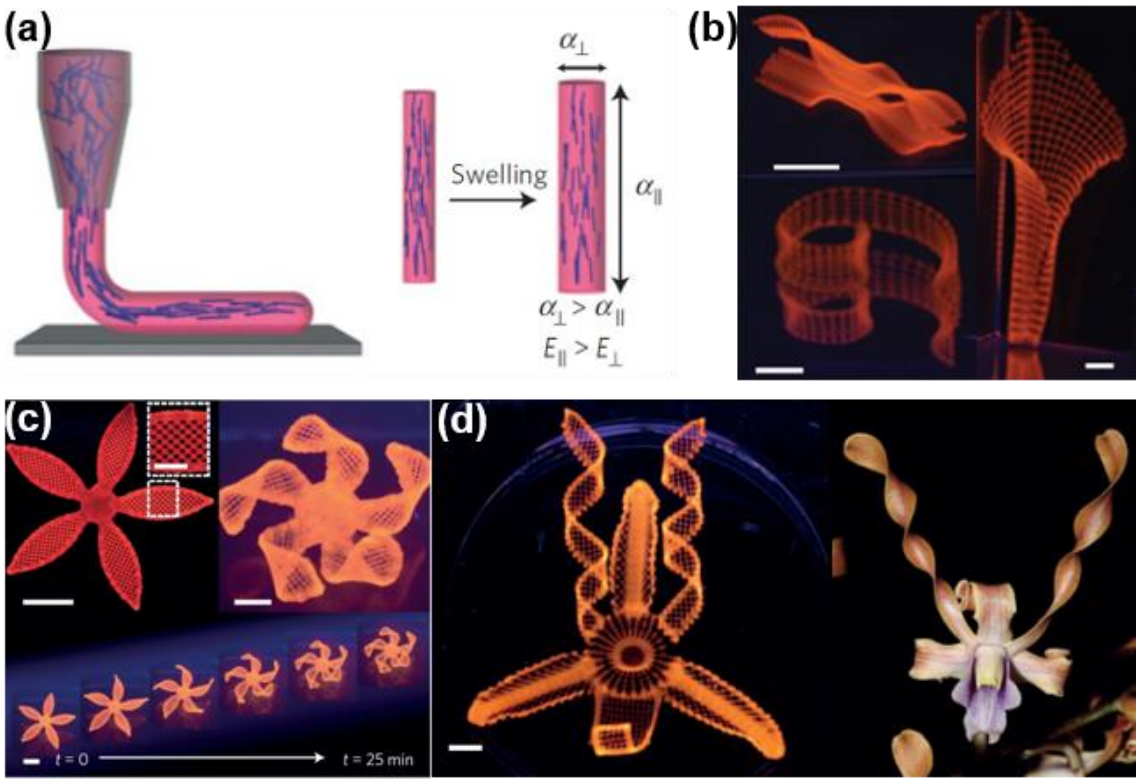

Figure 2-28 4D printed bioinspired self-morphing hydrogel material[104]. (a) Schematic of the printer nozzle and shear-induced one-step alignment of the cellulose fibril reinforcement (blue) in the hydrogel matrix (pink). The anisotropic swelling strain α (define: $=(a_1-a_0)/a_0$) and material stiffness E are denoted on the right. (b) Simple hygroscopic deformation generated by this 4D-printed hydrogel composite such as twisting (left top, scale bar = 10 mm), and curling (left bottom and right, scale bars = 5mm). (c,d) More complex flower morphologies generated by this biomimetic architecture. (scale bars, 5mm and the scale bar of inset is 2.5mm).

Self-assembly is another effective synthetic method to produce complex structures through bottom-up processes, similar to the intricate pathways used for formation of hierarchical structures in biological materials. Inspired by the morphogenesis in plant leaves (Figure 2-29a)[105], Huang et al. developed a self-shaping hydrogel by controlled molecular self-assembly[105,106]. They first investigated how the morphology of a growing leaf is determined by both the maximum value and the spatial distribution of growth strain quantitatively through experiments and simulations. Then, based on the parameters obtained from the plant organs, they fabricated a novel hydrogel using graded polymerization to replicate various morphogenesis processes in plant leaves. Due to the inhibitive effect caused by oxygen on the polymerization of hydrogels, a graded gel from the outer layer to the inner region via controlled diffusion of air into the hydrogel solution (Figure 2-29b) could be generated. With the aid of embedded stiff wires in the soft hydrogels, which also contribute to the anisotropic swelling strain, the hydrogels not only achieved common leaf morphogenesis (e.g., twisting and helical twisting, saddle bending, and edge waving, Figure 2-29c-e, respectively), but also can create even more complex 3D structures (Figure 2-29f).

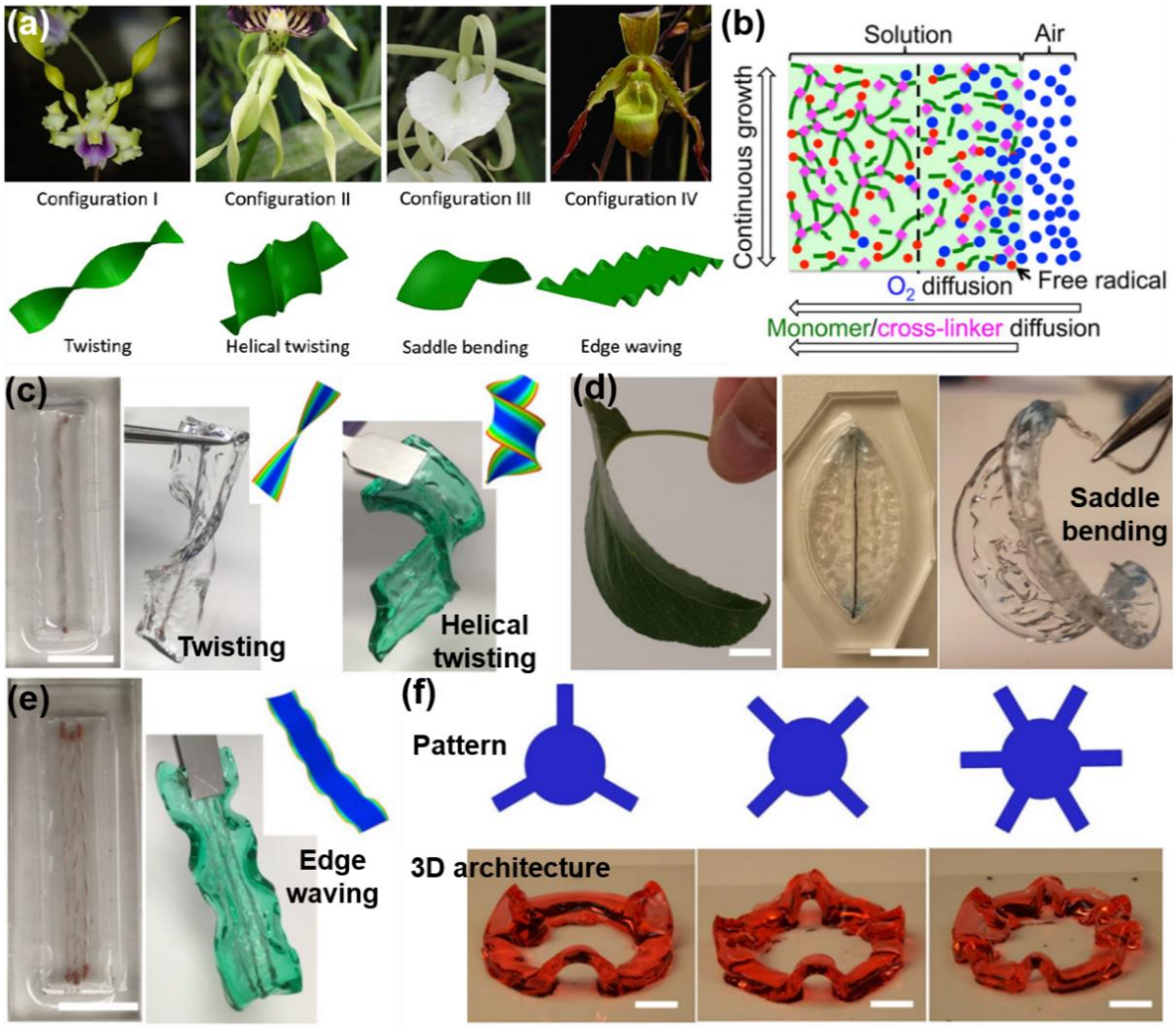

Figure 2-29 Plant inspired soft responsive materials fabricated by the controlled molecular self-assembly[105,106]. (a) Four types of differential growth and shape formation in plant organs: twisting, helical twisting (coiling), saddle bending and edge waving. The different morphology of these leaves is determined by both the maximum value and the spatial distribution of growth strain of the living leaf. (b) Schematic drawing of the self-assembly polymerization process induced by the diffusion of oxygen. The polymerization of hydrogels can be inhibited by the oxygen molecules and the gradient concentration of oxygen caused by the diffusion generates a gradience of gelation from outer layer to the inner region. The anisotropic swelling conferred by the gradient gelation with aid of embedding the stiff wire in the hydrogel matrix making the hydrogels able to achieve assorted responsive deformations including twisting and helical twisting (c), saddle bending (d), edging waving (e) and even more complex 3D structures (f). All scale bars are 1 cm.

These hydro-actuated self-shaping materials have not only been manufactured on a small scale but already been utilized as biomimetic building skins on meteoro-sensitive architectures at a large scale. Reichert et al.[107] fabricated a simple programmable veneer-composite system. They used the quarter cut veneer of maple wood to make a semi-synthetic bilayer structure: a climate responsive thin sheet combined with a climate independent layer. Manipulating with various geometrical calibrations, the fabricated programmable veneer can tune its shape driven by humidity changes to achieve simple (Figure 2-30a) and complex (Figure 2-30b) passive self-shaping. This ingenious design has already been utilized as smart building skins to tune the permeability of the real-scale architectures based on climate change (Figure 2-30c).

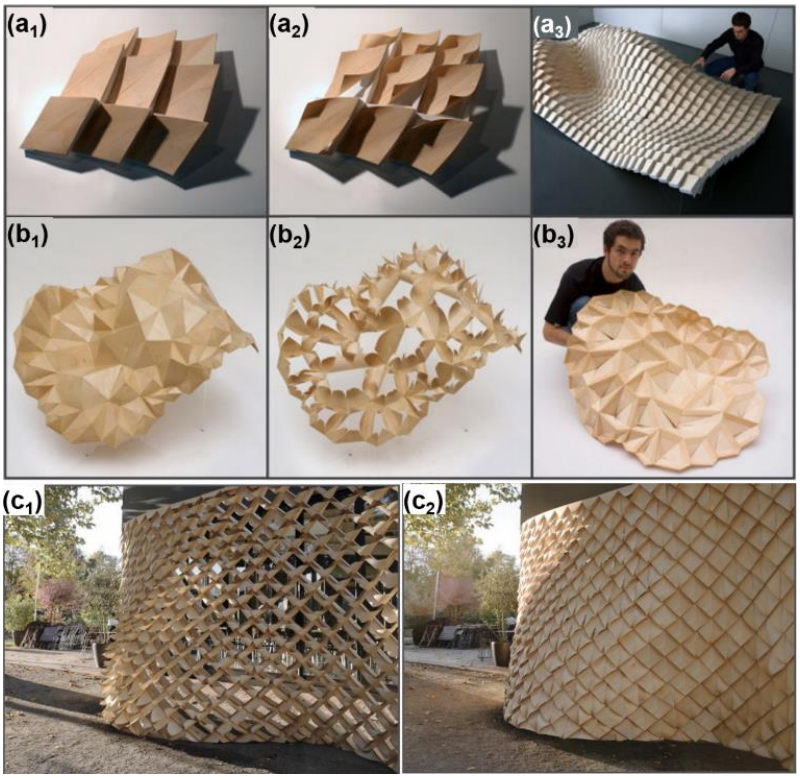

Figure 2-30 Large-scale fabricated bioinspired architectural building skin[107]. (a) Array of several square components with hygroscopic veneer layer on top. (a_1), (a_2) and (a_3) show the closed state, open state and overall display configuration, respectively. (b) More complex responsive surface structure; (b_1), (b_2) and (b_3) are closed, open and rear view, respectively. (c) Real-scale plant-inspired architecture skin in warm shiny days (c_1) and more humid weather (c_2).

Several types of hydro-actuated shape memory polymers have also been developed based on the inspiration from animal tissues. Applying the dual-phase strategy widely identified in shape memory animal tissues, Han et al. [54] fabricated an artificial skin with water-responsive shape memory materials. The major components of the mammal dermis are collagen fibers connected by elastin (Figure 2-31a). They interpenetrated waterborne polyurethane (PU) into an entangling and sticking collagen network, which was recycled from animal skin (Figure 2-31b_1). The fabricated skin composite has two structural phases (Figure 2-31b_2): the type I collagen fibers (Figure 2-31b_3) and the PU chains composed of a soft and hard segment (Figure 2-31b_4). The interruption and regeneration of the hydrogen bonds within the collagen fibers act as the "switch" to fix the temporary shape and recover the original geometry. Figure 2-31 (c) demonstrates one cycle of the shape memory effect within only 10 minutes, proving the success of this shape memory biocompatible synthetic polymers.

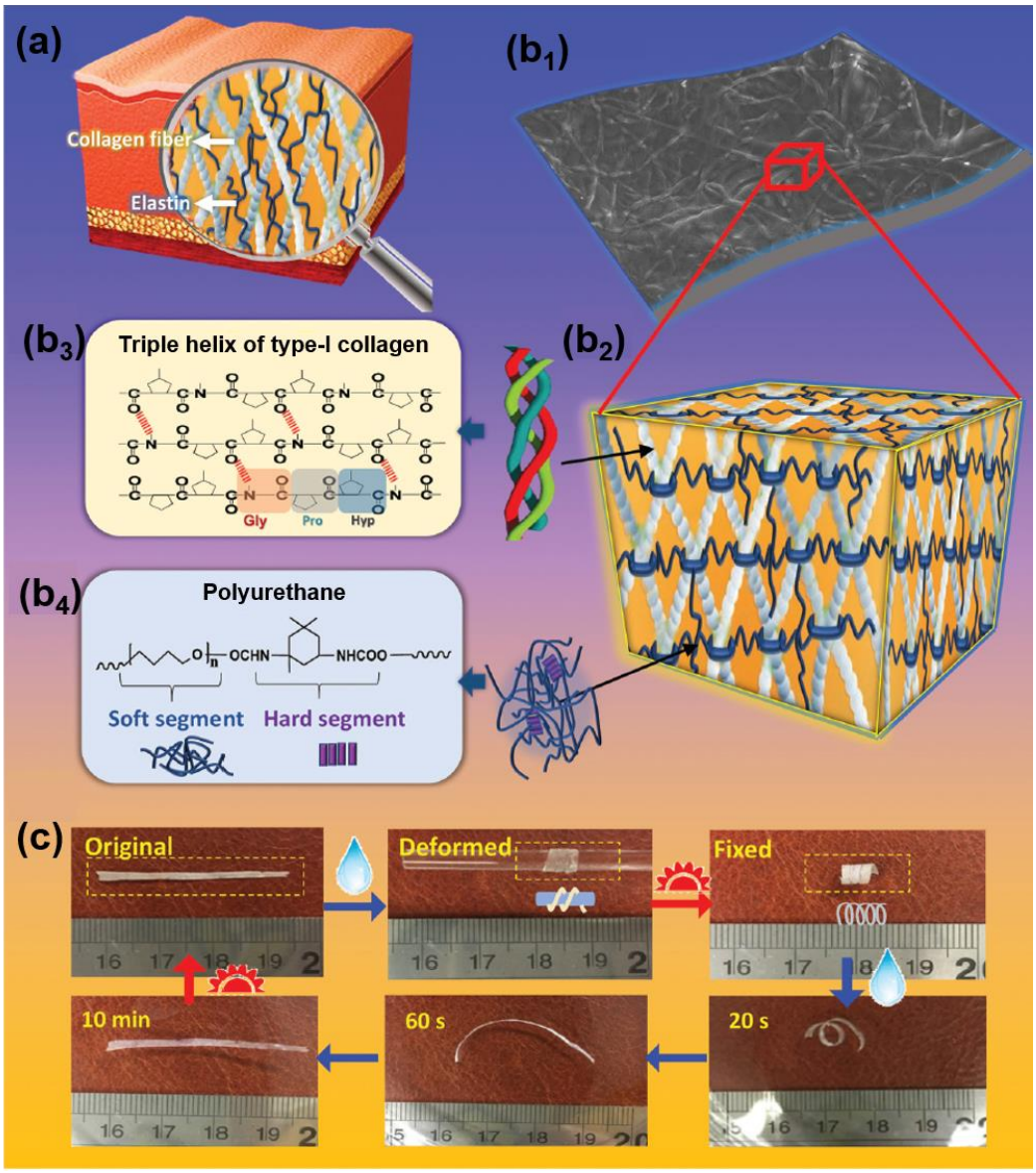

Figure 2-31 An artificial skin with water-responsive shape memory effect[108]. (a) Schematic of a simplified collagen–elastin dual network model for the structure of mammal skin. (b) The artificial skin fabricated based on skin collagen fiber/polyurethane composite. (b_1) The SEM image of the artificial skin showing the collagen fibrils embedded in polyurethane. (b_2) The structural model of the fabricated collagen-polyurethane composites. (b_3) The triple helix of collagen is composed of three amino acid chains interconnected by hydrogen bonds (red short lines). (b_4) The reinforcement.

Spider silk is a popular source of natural inspiration due to its superb mechanical properties. Inspired by its reversible supercontraction induced by water, Wu et al.[55] utilized a two-step synthesis to successfully fabricate a smart fiber which can also produce water-induced reversible contraction up to 50%. As shown in Figure 2-32 (a), they first drew the fibers from a hydrogel composite and then treated them with UV light at room-temperature. The initial hydrogel is built by two components: the major one is the complex cucurbit[8]uril (CB[8]), which is composed of silica nanoparticles with methyl viologen (MV)-functionalized polymer (P1) as branches, napthol (Np) functionalized hydroxyethyl cellulose (P2) and CB[8]; the other one is the necessary photo-initiator. As a supramolecular macrocycle, CB[8] can crosslink P1 and P2 in water, inducing the desired viscoelastic properties, and the functional group methacrylic anhydride (MA) on P2 facilitates the formation of UV crosslinks. The fibers drawn from this hydrogel have a double network: one is the physical interactions between P1 and P2 and the other is the covalent crosslinks within P2. The morphology of fabricated fiber is shown in Figure 2-32 (b). Based on this unique double network structure, the fiber can reversibly contract and relax for many cycles (Figure 2-32c) and work competently as a robust artificial muscle for lifting a weight of 5 mg (Figure 2-32d).

*Cucurbiturils are macrocyclic molecules made of glycoluril (=C4H2N4O2=) monomers linked by methylene bridges (-CH2-).

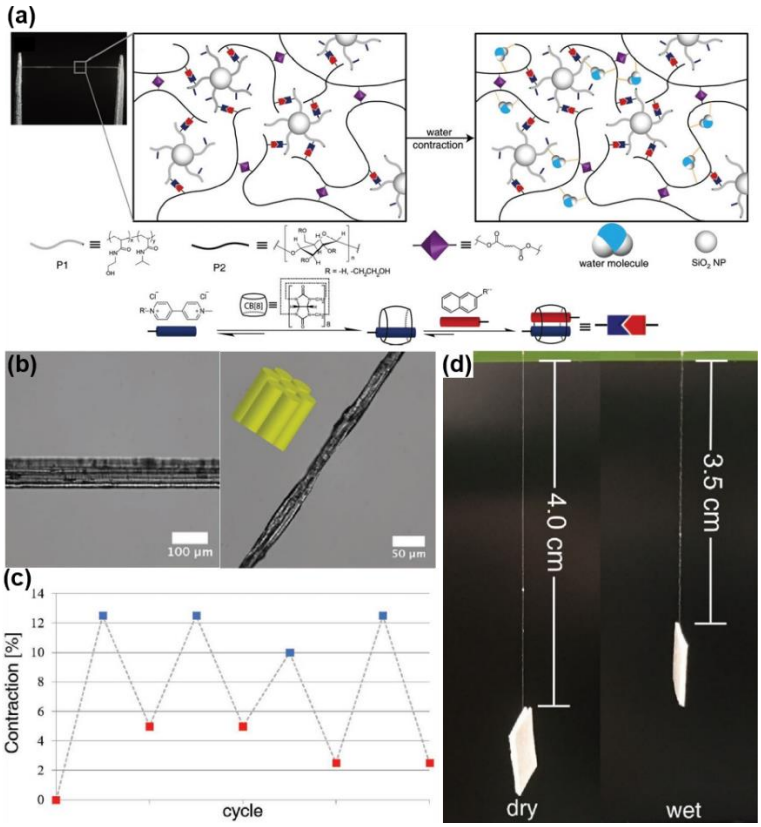

Figure 2-32 Spider silk-inspired polymer as artificial muscle[109]. (a) The synthetic silk with humidity-driven supercontraction effect. The stable configuration is determined by covalent crosslinks, while the contraction effect is caused by the breakage of hydrogen bonds. Water molecules interact with hydrophilic groups and serve as plasticizer to lubricate the mobility of the polymer chains. Driven by entropic force, the length of the synthetic silk shrinks, exhibiting the supercontraction effect. (b) Optical microscopic image of synthetic silk bundles. (c) Multiple cycles of weightlifting generated by the silk bundle. (d) A representative humidity-driven supercontraction process showing that the silk can act as artificial muscle to lift weight (5 mg).

Section 2.3 in Chapter 2, in part, is a reprint of the material as it appears in "A comparative study of piscine defense: The scales of *Arapaima gigas*, *Latimeria chalumnae* and *Atractosteus spatula*" Journal of the Mechanical Behavior of Biomedical Materials, vol 73, pp 1-16, 2017. This work was coauthored by V. Sherman, W. Yang, R. O. Ritchie and M. A. Meyers. The dissertation author is the second author of this work.

Section 2.4 in Chapter 2, in part, is in preparation for publication with coauthors D. Kisailus and M. A. Meyers. The dissertation author is the first author of this work.

CHAPTER 3: STRUCTURE AND MECHANICAL BEHAVIOR OF COELACANTH FISH SCALES

3.1 Introduction

Through the intricate and ingenious manipulation of structures consisting of primarily minerals and biopolymers organized hierarchically, many natural materials manifest a combination of strength, toughness, and light weight that are invariably mutually exclusive in synthetic materials a dynamic selection process, evolution drives all the living organisms to develop various biological materials[5,13]. The integumentary skeletons of fish, in the form of their fish scales, represent an excellent example of how nature evolves to afford an effective protection for the fish in its living environments[11,60,110]. Ancient fish were armored with large juxtaposed plates which provided a protective shield but also impeded their movement and locomotion[12,69]. Further evolution led to these large plates separating into imbricated smaller ones; a representative that still exists today is the ganoid scale[60]. It possesses very thick mineral layers that can provide outstanding penetration resistance but the rigid individual units and small degree of imbrication severely compromise the flexibility of the fish body[57,69,72,74,79]. With the further evolution, the elasmoid scales appeared, which are the prevailing type of scales today[60]. Much more compliant, they possess a dramatically reduced mineral layer and laminate inner core composed of non-mineralized or slightly mineralized collagen fibrils[76,111,112]. All the well-studied elasmoid scales exhibit an arrangement of the collagen fibrils that follows an orthogonal or twisted plywood structure (also called the 'Bouligand-type' structure), which can accommodate the imparted deformation through fibrous lamellae rotation, fibril straining and interfibrillar sliding[56,75,77,113-115]. Here we present a primitive type of elasmoid scale with a unique structure that is quite distinct from the prevailing current elasmoid fish scales. We show that this scale can adapt to the loads

associated with predator attacks through a suite of novel deformation mechanisms. Such a primitive type of scale is from a legendary fish, the coelacanth.

The coelacanth, one of the two living groups of lobe-finned fish (sarcopterygians), was thought to be extinct since the Late Cretaceous period (70 Myr), yet was discovered again in South Africa in 1938[116-118]. The discovery of a living coelacanth was considered one of the most important zoological findings of the 20th century, since it is thought to belong to the transitional group in the evolution from aquatic creatures to terrestrial tetropods[119]. The coelacanth fish live in the Indian Ocean at a depth of typically ~180 m, where fish are usually not as heavily armored as the ones inhabiting shallower fresh water[120-123]. However, since it was first discovered by the South African museum official Margorie Courtenay-Latimer, its shiny hard armor-like scale has attracted considerable attention[124]. In this chapter, we characterized its intricate and ingenious structure, that of bundled collagen fibrils which follow a unique form of the Bouligand-type pattern comprised of orthogonal bilayers embedded in a through-the-thickness collagenous matrix. Our tensile tests of intact and notched samples indicate that this fibrous hierarchical structure can not only accommodate the excessive deformation by delocalizing an imposed load and dissipating any excessive energy, but also can effectively arrest any local fractures, thereby enhancing the toughness of the scale both intrinsically and extrinsically. Various toughening mechanisms including crack deflection, fiber reorientation, twisting, stretching, delamination and the deformation of fibrous matrix are identified by in situ and ex situ (i.e., post-mortem) SEM observation. We also applied in situ synchrotron small-angle x-ray scattering techniques for real-time analysis of mechanical tensile tests on bulk scale samples to reveal the novel deformation and toughening mechanisms for the collagenous inner core in the scale of this ancient legendary creature.

3.2 Methods

3.2.1 Materials

The scale samples were collected from a coelacanth (Latimeria chalumnae) with a size of 950.0 mm in the Marine Vertebrate Collection of Scripps Institution of Oceanography, University of California San Diego; the fish specimen was collected from Grand Comore Island in 1973. The size of scales varied from 20 mm to 40 mm in length; they were peeled off from the linea lateralis below anterior dorsal fin, caudal peduncle region and caudal region on the fish body. All the scales were preserved in 80% isopropanol.

3.2.2 Structural characterization

The structure of the scales, the fracture surfaces after tensile testing, the crack propagation tests and the penetration area were all characterized in an FEI SFEG ultrahigh-resolution scanning electron microscope (SEM; FEI, Hillsboro, OR). The samples are first immersed in the 2.5% glutaraldehyde for 1 h to fix the structure and then dehydrated with an ascending series of ethanols (30, 50, 70, 90, 95 and 100 vol.% twice). To obtain the oblique fracture surface, the scale was immersed in liquid nitrogen for 30 s and fractured using forceps immediately. All dried samples were then sputter coated with iridium using an Emitech K575X sputter coater (Quorum Technoloties Ltd.) before observation. Micro-CT scans were conducted on air-dried samples in a Zeiss Versa 510 X-ray microscope (Zeiss, German). TEM images were taken on FEI Technai 12 (Spirit, 120-kV) transmission electron microscope (FEI, Hillsboro, OR).

3.2.3 Preparation of TEM specimens

The coelacanth scales were first cut into small strips, with a length of 4 mm and a width of 2 mm, and then immersed into 2.5% glutaraldehyde in 0.15 M sodium cacodylate buffer (pH 7.4) for 50 mins to fix the structure. The fixed specimens were stained with 1% OsO_4 solution with 8%

potassium ferrocyanide in 0.5 M sodium cacodylate buffer for 12 h at room temperature. The scales were then stained with 2% aqueous uranyl acetate for 12 h and subsequently dehydrated with an ascending ethanol series (50, 70, 90, 100% twice), followed by a 1:1 ratio of 100% ethanol and 100% acetone, and finally 100% acetone. The fully dehydrated specimens were embedded in Spurr's low viscosity resin and polymerized at 60°C for 48 h. The obtained blocks were then sectioned parallel to the vertical cross-section before ultrathin slices with thickness of 80 to 100 nm were generated using a Leica Ultracut UCT ultramicrotome (Leica) and a Diatome diamond knife (Diatome). Ultramicrotomed sections were then placed on copper grids for TEM observation, and post stained with Sato lead for 1 min before final examination.

3.2.4 Nanoindentation and EDX analysis

Scales were mounted in epoxy and polished to generate flat surface prior to indentation. By using a TI-950 nanoindenter (Hysitron, USA), the hardness mapping (5 s load, 2 s hold at displacement of 500 nm, 5 s unload) was performed on a cross-section of the laminate inner layer of the scale; additionally, 7 single indents with same loading conditions were made on the mineral layer. Energy-dispersive X-ray spectroscopy (EDX) was performed on the junction between the mineral layer and the collagenous inner layer using a FEI Scios DualBeam SEM (FEI, FEI, Hillsboro, OR).

3.2.5 Uniaxial tensile behavior

Dog-bone shaped tensile specimens with dimension of 15 × 3 mm were cut along longitudinal and transverse directions from the scale with thickness of 0.3 – 0.5 mm. The outer layers of some samples were removed using silicon carbide polishing paper of 180 # - 2500 #, leading to final thickness between 0.2 and 0.4 mm. To prevent sliding during the tensile test, the ends of the samples were glued between sand paper sheets using cyanoacrylate glue, resulting in

a gauge length of ~ 7 mm. Uniaxial tensile tests were performed on an Instron 3342 mechanical testing machine (Instron Corp., Norwich, MA) with a load cell of 500 N at a strain rate of 10^{-3} s^{-1} immediately following taking out the samples from deionized water, where they were kept prior to testing. The energy dissipation before failure was measured by the area beneath the stress-strain curves.

3.2.6 Crack propagation observations

A notch of width 1.5 mm was cut using a surgical blade on a 3-mm wide dog-bone shaped tensile test sample. Uniaxial tensile tests were carried out on these notched samples using the same strain rate with the same Instron testing machine described above. Engineering stress-strain curves were obtained before the test was stopped at a maximum strain of 0.143. The test sample were then removed from the Instron machine and immediately immersed into 2.5% glutaraldehyde solution to fix the morphology of the cracked region. The same dehydration procedure as the SEM sample preparation was performed on the fixed cracked samples prior to sputtering with iridium before final observation using FEI SFEG ultrahigh-resolution scanning electron microscope (SEM; FEI, Hillsboro, OR).

3.2.7 Penetration by shark tooth

Two fully hydrated scales were overlapped in the same manner in the real fish body and a piece of grouper meat was put under the scales to mimic the coelacanth flesh. A shark tooth removed from the fish's head was mounted on an Instron 3367 mechanical testing machine (Instron Corp., Norwich, MA) with a load cell of 30 kN and the penetration test was performed in the compressive test mode with strain rate of 1 min^{-1}. The damaged scale was dehydrated with the same procedure as described for SEM sample preparation, described above, and sputtered with

iridium before final imaging with an FEI SFEG ultrahigh-resolution scanning electron microscope (SEM; FEI, Hillsboro, OR).

3.2.8 *In situ* small-angle x-ray scattering (SAXS) during mechanical testing

With same specimen preparation procedure as for the uniaxial tensile tests, specimens comprising complete scales and those where the mineral layer had been removed were cut from the full hydrated coelacanth scales in both longitudinal and transverse directions. The tensile specimens were loaded in tension, while simultaneously exposing the samples to synchrotron x-rays at beamline 7.3.3 at the Advanced Light Source synchrotron radiation facility (Lawrence Berkeley National Laboratory, Berkeley, CA, USA). The tensile tests were performed with a customized rig using a displacement stage and a 45-N capacity load cell (Omega, LC703-10) to measure the force. Such an experimental set-up allows for SAXS data collection to be recorded in real time with the measurement of the load–displacement curve. The mechanical tests were performed at room temperature and a displacement rate of 1.4×10^{-2} mm s^{-1}.

A Pilatus 1M detector (Dectris Ltd., Baden, Switzerland) was used to collect the SAXS data. The detector was located at the largest allowable distance, around 4 m, to detect fine changes in the collagen peak's position. The sample was exposed to x-rays for 0.5 s with intervals of ~ 5s during the mechanical test; this radiation dosage was sufficiently low so as not to affect the structure and properties of the scales.

Since the collagenous lamellae have numerous orientations in the coelacanth scale, it is hard to separate the diffraction arcs in the SAXS data. Instead, 360 of even sectors were made on the Debye rings with the span of 1°, starting from $\Psi = 0°$ to $\Psi = 360°$ and then the sector graph was generated by the polar transformation of the 2-D diffraction pattern using the software IGOR Pro (Wavemetrics) in conjunction with the custom macro NIKA (Jan Ilavsky, Argonne National

Laboratory, IL, USA). Based on the obtained square map of intensity *vs*. pixel, the 1-D graphs, specifically, the plots of the integrated intensity as a function of azimuthal angle, were created by using the 'Image line profile' tool in NIKA.

The strain of the collagen fibrils in the lamellae was measured from the x-ray data in terms of the change in 1-D peak position determined from the plot of integrated diffraction intensity as a function of *d*-spacing. By using the same software used in the quantification of fibril orientation, the sample detector distance and beam center was calibrated with the 2-D diffraction pattern of a silver behenate standard. In order to convert the 2-D SAXS data to 1-D peaks, 17 sectors were evenly made on the upper half of the Debye rings, starting from $\Psi = -5°$ to $\Psi = 165°$, with a span of 10° in each sector, and then the integrated intensity over the diffraction arc in each sector was radially averaged to obtain the relationship between the intensity peaks and the radial distance of the arc, q. Based on the numerical relationship between q and the d-spacing, plots of integrated intensity as a function of the d-spacing for all 17 sectors were generated by the software; intensity peaks were fit to an exponential Gaussian function and a linear background to precisely locate the peak positions. The strain in the collagen fibrils was measured as the change in position of the first-order collagen peak's center normalized by the strain at unstressed state.

3.3 Results

3.3.1 Structure of the scale of coelacanth (*Latimeria chalumnae*)

The entire body of the coelacanth (*Latimeria chalumnae*) is covered by armor-like scales with a bright metallic blue color when the fish is alive but fades to brown color with the preservation, as shown in Figure 3-1(a)[116,120,125]. A close-up view in Figure 3-1(b) shows that numerous scales are imbricated and that their surface is very rough. Their posterior portion, which is exposed to the environment, occupies around one third of the entire scale, as shown in the inset in Figure 3-1(b); their anterior part, which is overlapped by the neighboring scales, is deeply inserted in the fish skin. The shapes of the scales vary significantly in different parts of the body but most of them are oval Figure 3-1(c). All previous research has indicated that the exposed part is more mineralized than the overlapped part and this is confirmed in the current work by the micro-computed tomography (micro-CT) scan shown in Figure 3-1(d). However, even in the overlapped part, the mineralization distribution is not homogeneous; for example, the micro-CT scan shows the lateral part to have a higher mineralization than the middle part. On the exposed part (Figure 3-1e), there are numerous denticle spines, which are anatomically called odontodes[126]; these comprise a tooth-like tissue which are scattered on the radial ridges and which significantly vary in number in the scales on different parts of the body. A micro-CT scan of an isolated odontode in Figure 3-1(f) reveals that it is composed of denticle on top of a star-like basis, which anchors the odontode to the radial ridges. The cross-sectional view of the scan in Figure 3-1(g) shows the odontode to have a hollow structure with the shell being highly mineralized. Based on previous anatomic research on the coelacanth scale, the detailed structure of the odontode is presented by the schematic in Figure 3-1(h)[126,127]. It is made of dental tissue (dentin) with a pulp cavity inside and with the dental tissue on the top of a bony basis. The surface is covered by a thin

layer of enamel and the entire odontode is built on the mineral ridges. All the odontodes are partially embedded in the dermis, which indicates their prime function is to anchor the scales in the integument[126]. The overlapped region of the scale is far smoother than the exposed part. Annuli ridges centered on the apex of the scale, which are associated with its growth, can be clearly observed in the overlapped part shown in Figure 3-1(i). There is another type of mineral ridges, which are also observed beneath the odontodes in the exposed part, radiate from the apex of the scale Figure 3-1(j). These radial ridges are much more regularly arranged with almost equivalent separated space. The direction of them runs almost perpendicular to the annuli ridges. A close-up view in Figure 3-1(k) reveals the regions between the mineral ridges that are located just above the inner layer and could be regarded as the head of the mineralization of the inner layer; they are covered by spherical mineralized corpuscles[126]. Several holes can be observed; these represent the openings of the vascular canals on the regions between the ridges, consistent with the previous observations[126,127].

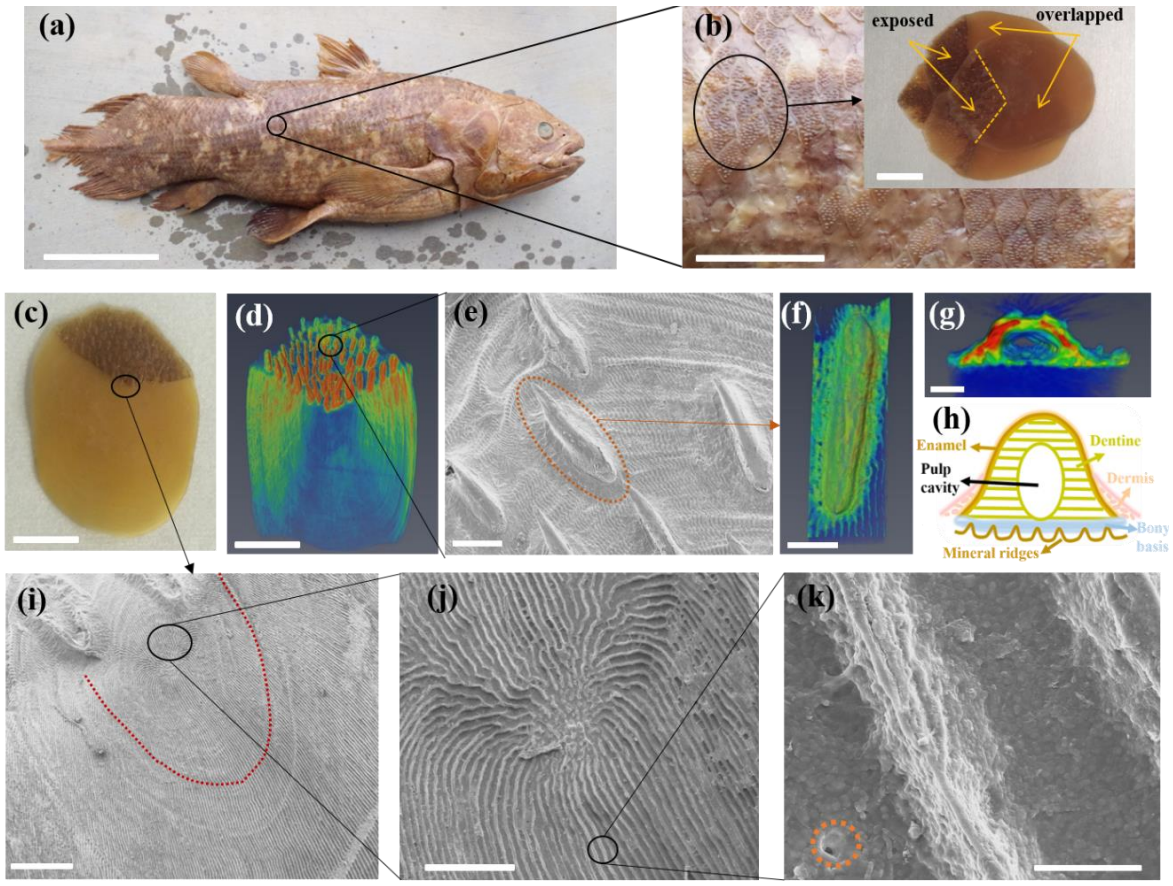

Figure 3-1 Surface morphology of the scale. (a) The entire coelacanth fish body is armored with scales. They are shinny dark blue when the fish is alive and the color fades after the fish is dead (scale bar 20 mm). (b) Scales are imbricated: the posterior part, which is around 1/3 of the whole scale, has very rough surface and is exposed to the environment. (scale bar, 5 cm). The anterior part is overlapped by the neighboring scales and inserted deeply in the fish skin (see inset, scale bar, 1cm). (c) Most of the scales have an oval shape (scale bar, 1cm). (d) Micro-CT scan of a scale. The mineralization of the exposed part is much higher than the overlapped part. Even within the overlapped part, the lateral area has higher mineralization than the center area (scale bar, 1 cm). (e) SEM image of the exposed part (scale bar, 500 μm). Odontodes are scattered on the radial ridges on the surface of exposed part. (f) Micro-CT scan of an isolated odontode. (scale bar, 200 μm). The odontode is composed of two parts: a denticle on the top and a star-like base. (g) The cross section of the micro-CT scan of an isolated odontode shows the highly mineralized outer layer and a pulp cavity inside (scale bar, 100 μm). (h) Schematic of the structure of the odontode: the central pulp is surrounded by a layer of dentine and outer surface is covered by a very thin layer of enamel. Beneath the denticle is a bony basal plate built on the mineral ridges and the entire structure is embedded in the dermis. (i) SEM of the scale center shows the scale surface has annular ridges centered on the apex of the scale and one of them was marked with red dot line (scale bar, 500 μm). (j) The close-up view reveals that radial ridges are arranged more regularly (scale bar, 200 μm). (k) Higher magnification SEM shows abundant Mandl's corpuscles and a few openings of vascular canals (circled with dot line) between the mineral ridges (scale bar, 10 μm).

Beneath the thin surface layer is the major component of the scale, the isopedine[127], comprising a laminated collagenous tissue with a twisted 'plywood' structure (Figure 3-2a). Different from the common elasmoid scales of other modern teleosts such as carps, in which each lamella is directly composed of individual collagen fibrils (Figure 3-2c), the collagen fibrils in the coelacanth scale are tightly packed into distinct bundles and the fiber bundles are aligned parallel in each lamella (Figure 3-2b,c). Additionally, the arrangement of the collagenous lamellae does not simply follow the stair-case pattern of a typical 'Bouligand-type' structure, which commonly appears in other elasmoid scales. In the coelacanth scale, the fiber bundles in the adjacent two lamellae, whose orientations are marked with arrows in Figure 3-2d, form an orthogonal bilayer, as shown in the inset; the units of orthogonal bilayers progressively rotate through the whole thickness in stair-case pattern, forming what is known as a double-twisted 'Bouligand-type' structure[116]. The spaces between the fiber bundles (FB) are filled with fibrils perpendicular to the laminate structure, along the thickness direction (Figure 3-2e), which are referred here as interbundle fibrils (IBF). They are much more loosely packed yet are aligned more randomly than the fibrils in the fiber bundles. We performed transmission electron microscopy (TEM) on the scale to confirm that the orthogonal arrangement of adjacent lamellae in one bilayer and the penetration of the interbundle fibrils through several layers provides a wrap for the fiber bundles, thereby forming a matrix that is the binding material (Figure 3-2f). The interbundle fibrils are also collagen, as shown by characteristic banded patterns (Figure 3-2g). Using this detailed characterization of the outer and inner layers of the scale, a complete structure of the coelacanth scale can be revealed in terms of three principal components:

(a) The collagen fibrils form bundles that organize into orthogonal bilayers, the bilayer arrangement following a 'Bouligand-type' pattern (Figure 3-2h);

(b) Loosely packed interbundle fibrils form perpendicular to the Bouligand layers and extend through the thickness of inner layer (Figure 3-2i); they wind around these bundles to act as a binding material to confine the fiber bundles in the lamellae;

(c) The surface is covered by a ridged thin mineral layer (Figure 3-2j).

Figure 3-2 Structure of the inner layer of the coelacanth scale. (a) The oblique fractured surface reveals the ‘plywood’ arrangement of laminate inner layer (scale bar, 100 μm). (b) Each lamella is composed of collagen fiber bundles arranged in parallel (scale bar, 5 μm). (c) The bundle is formed by the tightly packed collagen fibrils (scale bar, 200 nm). (d) The close-up view of oblique fractured surface. The orientations of the collagen fiber bundles in three successive layers are marked with arrows. The orientations in adjacent two layers are almost perpendicular to each other and the schematic of such arrangement is shown in the inset (scale bar, 50 μm). (e) Vertical cross-sectional view shows that the spaces between the fiber bundles (FBs) are filled with interbundle fibrils (IBFs), which go through the whole thickness of the inner layer, binding the lamellae (scale bar, 10 μm). (f) TEM image of two adjacent collagenous lamellae showing that the loosely packed interbundle fibrils wrap the collagen bundles (scale bar, 2 μm). (g) The characteristic band pattern of collagen fibril is clearly shown in the high magnification TEM (scale bar, 200 nm). (h-j) Schematics of the structure of the coelacanth scale, (h) the double twisted Bouligand structure with orthogonal bilayers progressively rotating throughout the whole thickness, (i) the matrix composed of interbundle fibrils to hold such a system with (j) the top covered by a mineralized outer layer.

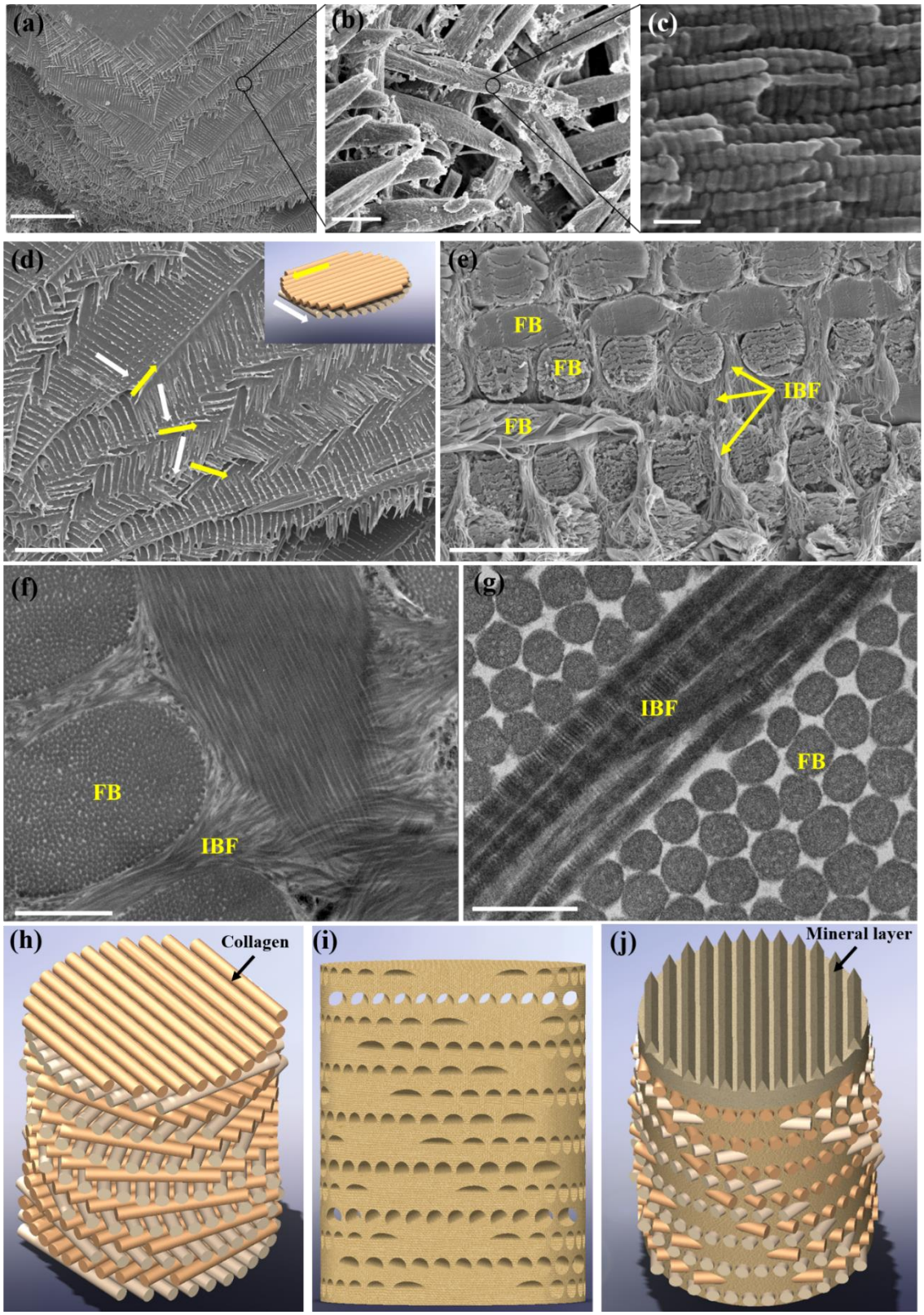
(a)
(b)
(c)
(d)
(e)
FB
FB
FB
IBF
(f)
FB
IBF
(g)
IBF
FB
(h)
Collagen
(i)
(j)
Mineral layer

3.3.2 Mechanical behavior of coelacanth scale

This complex yet fascinating hierarchical structure significantly enhances the toughness, *i.e.*, resistance to penetration and fracture, of the coelacanth scale, which is vital for protecting the body of the fish from predators. In order to verify this, a penetration test using a shark tooth was performed on two unattached but overlapped coelacanth fish scales located on a base of a slab of fresh fish flesh. The resulting force *vs*. displacement curve, shown in Figure 3-3 (a), indicates periodic drops in the curve which are associated with the penetration of different layers of the scale. The tooth penetrated through the top scale and lifted it up but left the bottom scale largely undamaged. When the test was performed several times, it was clear that the actual penetration damage avoided the actual location of the odontodes and always occurred between them (Figure 3-3b). Though a large penetration displacement was involved in the scale with the small thickness of 0.5 mm, the damage was localized with the remaining area left undamaged. Within a single scale, cracks initiated in the outer layer propagated but were arrested by other cracks, as shown by the circles in Figure 3-3b. The inner layer was damaged locally and became exposed from the damage to the outer layer. However, with SEM examination, it was apparent that the collagen fibrils in this inner layer were indeed stretched and some were delaminated, but with little other overt damage (Figure 3-3c,d). Under extreme penetration displacements into the scale, the inner collagenous layer played a role of tough base under the tension force. Using the concept of a harder outer layer to resist penetration with a more ductile lower layer to accommodate the excessive strain, the tough collagenous lower layer served to localize the outer layer cracking and avoid catastrophic separation.

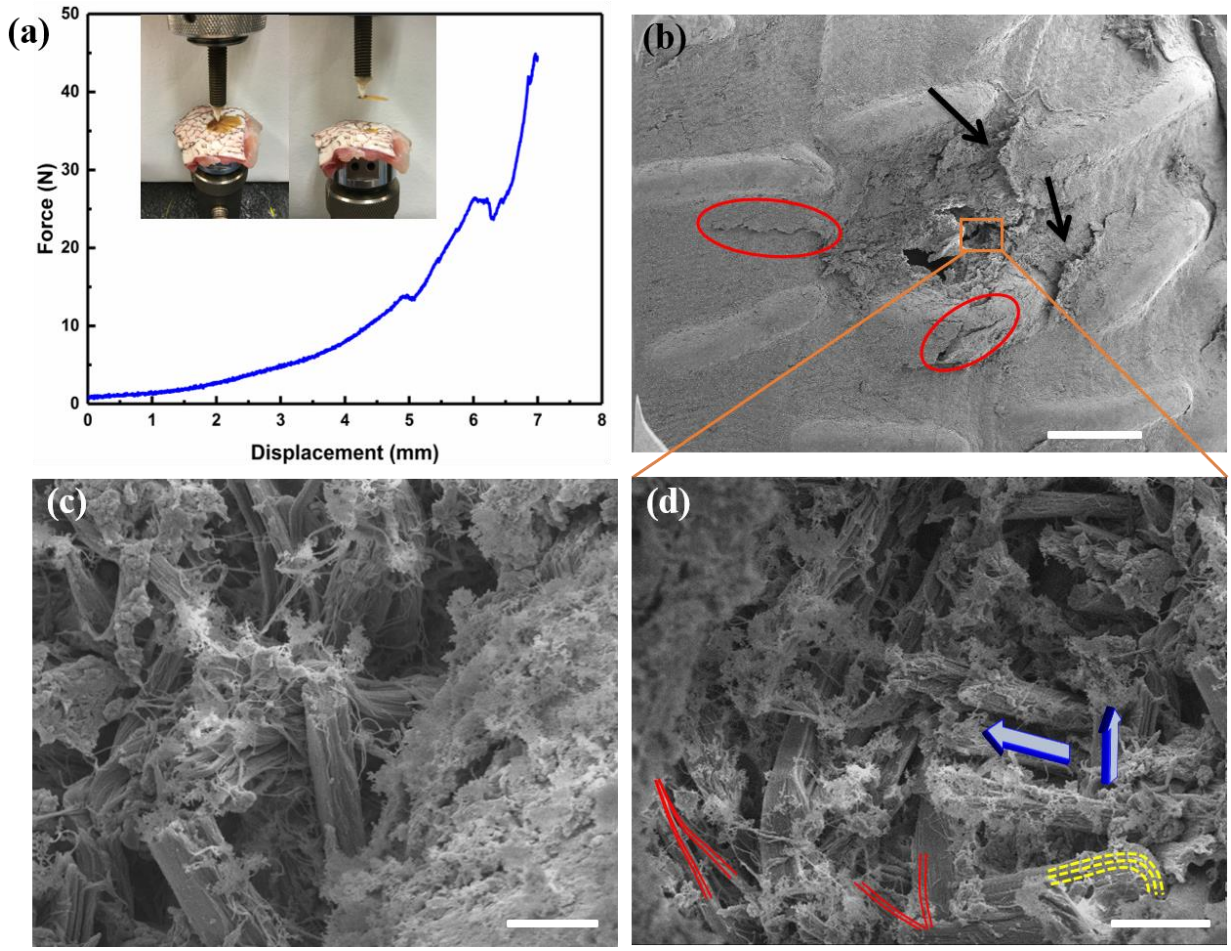

Figure 3-3 Penetration of the coelacanth scale by a shark tooth. (a) Force *vs*. displacement plot with the images of loading and unloading. The experiment set-up is presented in the inset. The shark tooth was mounted on the Instron testing machine and the two overlapped scales were located on the grouper meat. The top scale was completely penetrated. (b-d) The SEM images of the scale after penetration. (b) the top scale with the penetration damage. Note that the damage is localized among the odontodes (scale bar, 500 μm). (c) The collagen fibrils were stretched, delaminated and curled after fracture (scale bar, 20 μm). (d) Close-up view of the inner layer shows the bending, rotation and delamination (marked with dot lines, arrows and solid lines, respectively) of the fiber bundles (scale bar, 10 μm).

Nanoindentation mapping of the boxed region in the Figure 3-4(a) indicates that the hardness gradually decreases from the external surface to the lamellae in the deep inner layer (Figure 3-4b). Such a hardness profile, which was averaged and plotted as a function of the normalized distance from the outer surface (Figure 3-4c), clearly demonstrates the gradient structure of progressively decreasing mineralization as one moves inward from the outer surface.

The creation of such a gradient serves to mitigate interface failure by enhancing the interfacial toughness which results in an improved resistance to penetration[69]. Energy-dispersive x-ray spectroscopy (EDX) analysis of the junction region in Figure 3-4(d) shows the element mappings of carbon, phosphorus and calcium in that area (Figure 3-4(e), (f), (g), respectively. The larger amount of the phosphorous and calcium and smaller amount of carbon is consistent with the higher mineralization of the outer layer, resulting in the increased hardness in that location. The element density of calcium and phosphorous in the inner layers is much lower, which indicates the slight mineralization of the collagenous lamellae that close to the mineral layer.

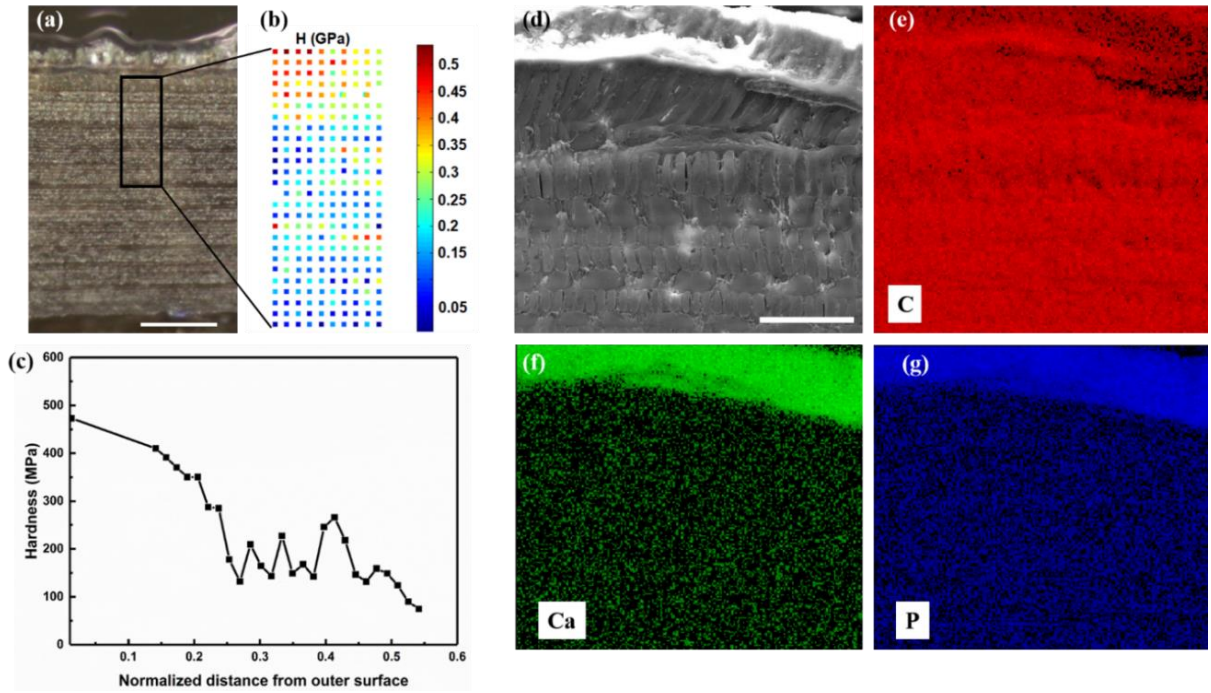

Figure 3-4 Nanoindentation and EDX analysis of coelacanth scales. (a) Optical microscopy image of the polished vertical cross-section (scale bar, 100 μm). The boxed region is the nanoindentation area. (b) Hardness mapping on the boxed region in (a). (c) The average hardness is plotted against the normalized distance from the outer surface. The hardness value of the outer surface is obtained from several single indents on the outer layer. (d-g) SEM image of the connecting region between the outer layer and the inner layer and the element mapping of carbon, phosphorus and calcium, respectively (scale bar 40 μm).

To re-evaluate the effect of the collagenous layer, the fracture toughness was estimated using pre-cracked compact-tension specimens loaded between anti-buckling plates. Extension of the fully hydrated and pre-cracked specimen resulted in the crack-tip opening and blunting. This was followed by distinct fiber bridging as the crack started to propagate (Figure 3-5a-c). The estimated fracture toughness K_{Ic} of coelacanth scales was found to be 4.9 ± 1.5 MPa·m$^{1/2}$, which is not particularly impressive yet is still comparable to the toughness of other elasmoid scales (see, for example, Dastjerdi *et al.*[76]). Nevertheless, this value is high compared to many biological materials. The fracture toughness value is not as large as we expected from this complicated structure; however, one must recognize that the tested coelacanth specimens have been preserved in isopropanol for 45 years, which clearly resulted in some deterioration in their mechanical properties. Such an effect is consistent with the noticeable variation in strength of common carp scales after two years of preservation (as described in Figure 3-6). In other words, fresh coelacanth scales likely had a somewhat higher toughness.

The *in situ* SEM sequence of images during the loading of a pre-cracked specimen in Figures 3-5 (d-f, g-i) reveals the details of the toughening mechanisms. The crack deflects as soon as it starts to propagate (Figure 3-5d) with the collagen fibers bridging across the crack surfaces (Figure 3-5e). The fiber bundles tend to rotate and deform as a unit; bundles firstly separate from their neighboring bundles and then delamination of the internal fibrils occurs within each bundle (shown by the arrow in Figure 3-5f). With further extension, fibers/fibrils along the propagating direction of the crack delaminate and pull-out, with associated necking prior to their fracture (shown by arrows in Figure 3-5h). Most of the fibers fractured in a brittle fashion, possibly aided by dehydration from the vacuum inside the *in situ* SEM.

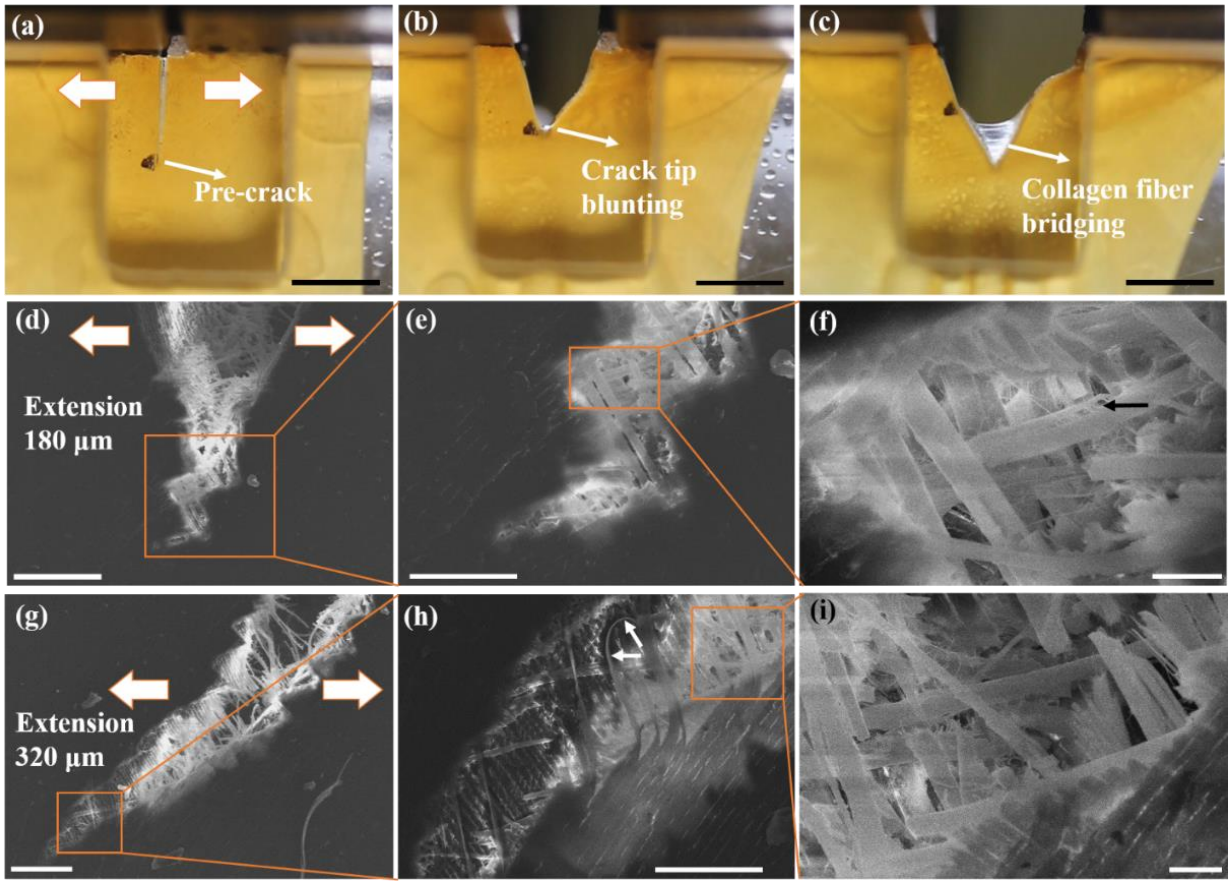

Figure 3-5 Fracture toughness test and crack propagation process. (a) The set-up of the fracture toughness test with anti-buckle plates (scale bar, 3 mm). (b,c) The images at different stages during the fracture toughness test (scale bar, 3 mm). (b) The crack tip opens and becomes blunt first; (c) with further extension, the collagen fibrils are pulled out and form bridging behind the crack tip. (d-i) *In situ* observation of crack propagation of a dehydrated coelacanth scale under tension load. (d-f) The crack-tip region when the scale has been tensile extended by 180 µm (scale bar, 100 µm, 50 µm and 10 µm, respectively). After the initiation of cracking, the crack deflects in a zig-zag pattern, with collagen fiber bundles being stretched and bridging behind the crack tip. Some fibers were delaminated (shown by the arrow). (g-i) The crack-tip region when the scale is extended by 320 µm (scale bar, 100 µm, 50 µm and 10 µm, respectively). (g) More fibers are pulled out and fractured, (h) fibers aligned along the crack propagation direction are delaminated with necking prior to fracture (shown by arrows), (i) behind the crack tip, more fibers in different orientations are fractured.

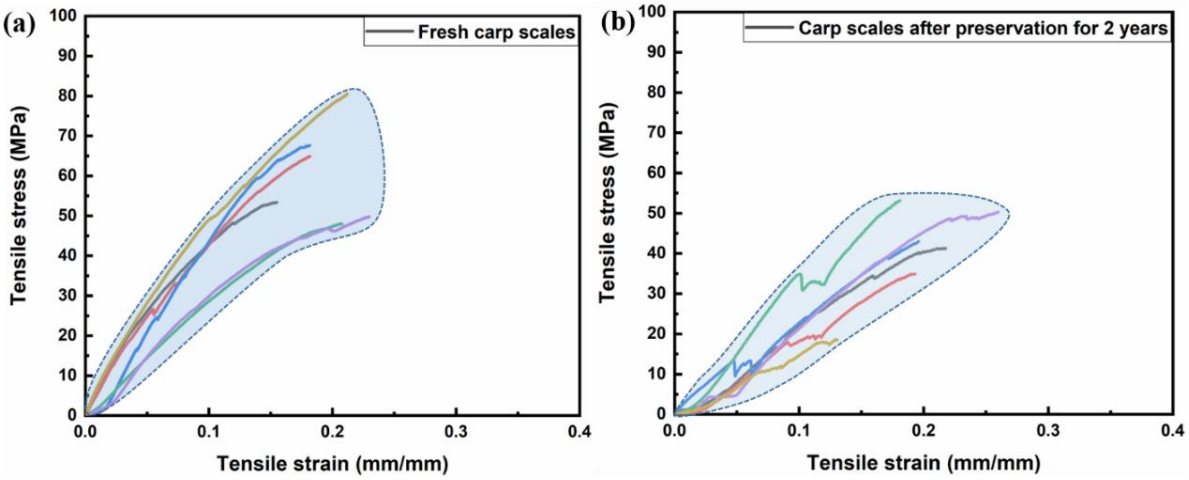

Figure 3-6 The effect of preservation in isopropanol on the mechanical properties of Carp fish scales. (a,b) The uniaxial tensile behavior of fresh and preserved carp scales, respectively. After being preserved in isopropanol for two years, the tensile mechanical properties of carp scales significantly decreased.

Most biological materials lose some degree of their deformability in the dehydrated state. Collagen-based materials, such as the fish scales, are no exception and sacrifice their ductility when they are not fully hydrated. Due to dehydration of the samples (~50% dehydration from the preserved samples) in the *in situ* SEM tests, there was no clear observation of crack blunting and fiber bridging before the initiation of cracking, although these features were clearly evident in the *ex situ* tensile tests (Figure 3.5a-c). Consequently, to further demonstrate the tough nature of the coelacanth scales, we also performed uniaxial tensile tests on 3-mm wide dog-bone shaped specimens containing each a 1.5-mm deep notch, as indicated in the inset of Figure 3-7a. The average measured tensile strengths (and their variation) of coelacanth scales in the longitudinal and transverse directions were 45.5 ± 4.9 MPa and 46.9 ± 12.7 MPa, respectively. The slight variation in the thickness of the samples along the gauge length of the test samples had little effect on the measured strength – indeed, strength values were quite consistent; however, since the coelacanth scale has a shorter transverse length with relatively small thickness close to the edge, the thickness of the samples had a little larger variation on the transverse samples where strength

values were found to have a higher standard deviation (21.7% of the average value, 12.7 MPa). Figure 3-7 (g) shows the tensile behavior of intact specimens along longitudinal and transverse directions. Specifically, there is no particular difference between the stress-strain response of samples cut along longitudinal direction and transverse directions, both for the whole scale and for the collagenous layers. This is confirmed by the quantitative results shown in Table 3-1 in which the tensile strength, failure strain, Young's moduli and energy dissipation all have very similar values in longitudinal and transverse directions. Removing the mineral layer causes no significant changes in the tensile stress-strain curves of coelacanth scales in the two directions. Results in Table 3-1 also show that by removing the mineral layer, there is a ~20% increase in the tensile strength, failure strain and energy dissipation; this can be compared with the more mineralized arapaima scales[56] where removal of the mineralized layer also significantly elevated the strength, by roughly 50%. Compared with the tensile results of the unnotched samples (Figure 3-7g), the pre-notched samples (Figure 3-7a) showed very little notch-sensitivity, *i.e.*, the strength and ductility do not decrease dramatically with the presence of crack; rather, the notched scales displayed similar tensile mechanical properties to the unnotched specimens. As more mechanistic information can be gleaned from such tension tests of pre-cracked hydrated samples, we loaded fully hydrated samples in tension to cause propagation (without a final failure) of a crack, prior to *ex situ* SEM observation. Based on the SEM imaging of the crack-tip region (Figure 3-7b-f), we identified several mechanisms associated with deformation and fracture in these scales:

(a) shear failure of the mineral (Figure 3-7e);

(b) deformation of the fiber bundles which become twisted, distorted/bent and delaminated with the stretching and reorientation of the fibrils (Figure 3-7d);

(c) crack bridging by the stretched fiber bundles (Figure 3-7d,f);

(d) delamination and relaxation of the fractured fiber bundles further away from the crack-tip region (Figure 3-7f);

(e) the matrix of interbundle fibrils acts to constrain the fiber bundles, as shown in Figure 3-7(h,i), although the interbundle fibrils delaminate after the fiber bundles are pulled out from the matrix.

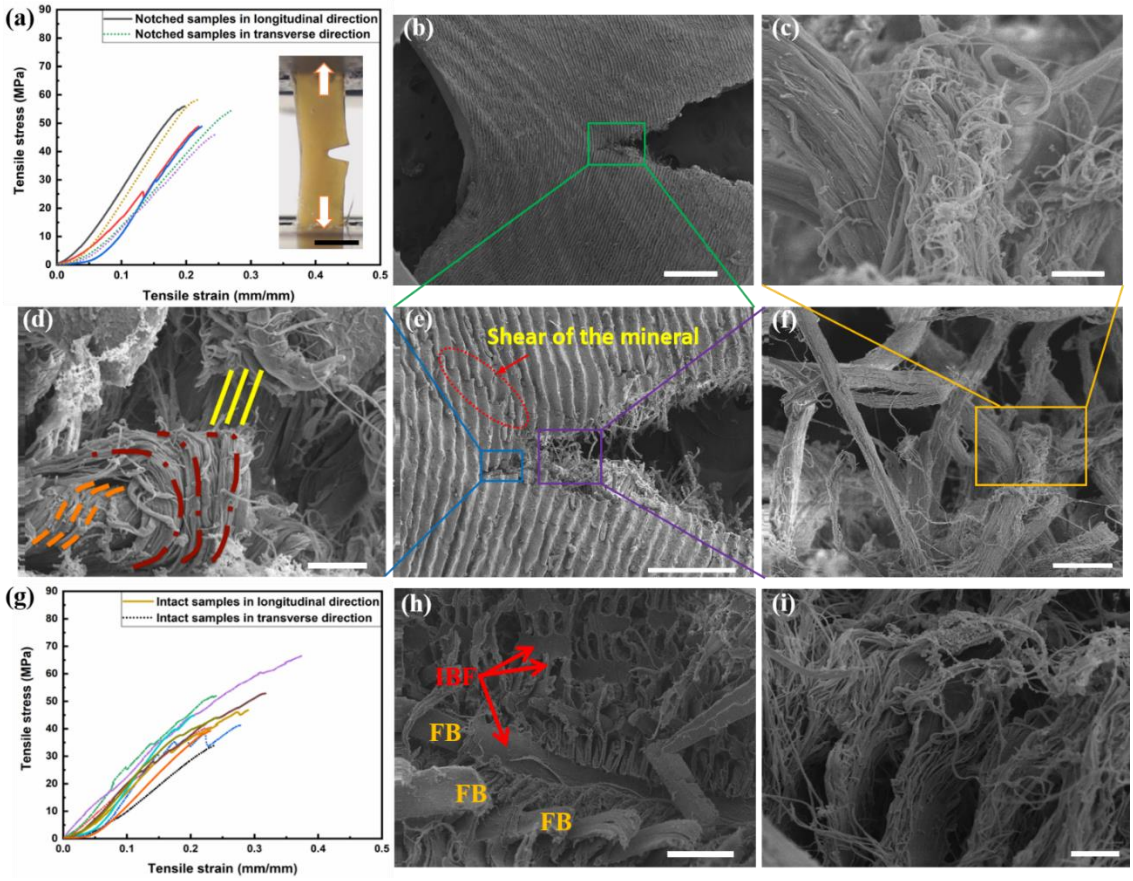

Figure 3-7 Mechanisms of retardation of crack formation in scale. (a) The tensile stress-strain curve of notched samples. The inset shows the blunted notch in the hydrated scale when the sample is being tensile tested (scale bar, 3 mm). (b-f) The SEM images of the regions around the crack tip. (b) Overview of crack propagation; region around the crack tip is boxed (scale bar, 500 µm). (c) Severe stretching, delamination and relaxation of the fibrils in the fiber bundle (scale bar, 2 µm). (d) Fiber bundles close to the crack tip are bent, buckled, twisted while being stretched partially around the head of the crack. (scale bar, 5 µm). (e) Close-up view of the region around the crack tip reveals secondary cracks (shear of the mineral) in the mineral layer and fibril stretching, delamination and relaxation behind the crack tip (scale bar, 200 µm). (f) Close-up view of the region behind the crack tip also showing severe stretching, bending, buckling, rotation, and delamination of the bundles (scale bar, 10 µm). (g) Tensile stress-strain curve of intact samples. (h) Typical fracture surface after tensile failure indicates the extensive deformation of fiber bundles (FBs) and interbundle fibrils (IBFs) (scale bar, 20 µm). (i) SEM image at higher magnification shows the squeezing, stretching and delamination of IBF matrix (2 µm).

Table 3-1 Uniaxial tensile tests result in both longitudinal and transverse directions for the entire coelacanth scale and for the collagen layer only.

Scale	Coelacanth			
	Longitudinal		Transverse	
	Entire scale	Collagen layer	Entire scale	Collagen layer
Young's Modulus (GPa)	0.26 ± 0.04	0.26 ± 0.02	0.25 ± 0.06	0.25 ± 0.05
Ultimate (engineering) tensile stress (MPa)	45.5 ± 4.9	55.5 ± 5.6	46.9 ±12.7	58.7 ± 12.1
Ultimate (engineering) tensile strain (mm/mm)	0.26 ± 0.05	0.29 ± 0.04	0.27 ± 0.06	0.32 ± 0.06
Energy dissipation (MJ/m^3)	5.99 ± 2.21	8.04 ± 2.32	7.23 ± 4.27	9.57 ± 2.62

.

Accordingly, based on these observations, we conclude that the double Bouligand structure and the matrix of interbundle fibrils are the keys to generating the toughness of the scales. The mineral and collagen utilize different mechanisms to avoid catastrophic failure; while the external load is increasing, the collagen fibrils are continuously stretched but the mineral stops shearing and any cracks are arrested by the resultant bridging. More micro-deformation mechanisms are involved in this procedure, including crack deflection in the mineral layer, delamination between collagen bundles, and separation at the relatively weak interfaces between the collagen bundles and the interbundle fibrils. Note that some of the interbundle fibrils extend directly into a collagen lamella, all of which serve to confer toughness to the coelacanth scales. At relatively low tensile strains, the IBFs deform, due to the Poisson effect, and function to hold the collagen fibrils together to prevent delamination; at larger strains, it is possible that they could generate stress concentrations, although without the constraining effect of the IBFs, the collagen lamellae would

delaminate and be largely separated at an early stage; in another way, the relatively weak interfaces can lead to enhanced toughness by enabling sliding between the matrix (IBFs) and collagenous lamellae which increases the deformability of the entire scale. Additionally, intense deformation at the nano-scale, associated with the bending, twisting, stretching and delamination of the fibrils in the fiber bundles, coupled with the deformation of the collagen matrix and some degree of secondary cracking and crack deflection in the mineral layer, act *in concert* to further enhance the fracture toughness of these scales.

3.3.3 In situ characterization of deformation

Similar to the protective function of other elasmoid scales, the coelacanth scale is comprised of a hard mineralized outer shell, graded properties through the scale thickness, which transfer the most deformation to the tougher inner layer, and the soft collagenous inner core, which dissipates the excessive energy through plastic deformation. However, the coelacanth scale is a primitive elasmoid scale and its inner layer has a unique structure, different from other 'modern' elasmoid scales. To discern the precise deformation mechanisms of the collagenous inner layer, *in situ* synchrotron small-angle x-ray scattering (SAXS) was applied during uniaxial tensile testing of the scales (Figure 3-8a). Similar to the regular tensile tests described above, the scales were cut into a dog-bone shape, but along both the longitudinal direction (shown in the figure) and the transverse direction (not shown). Due to the periodical structure inside of the collagen fibril, the high flux x-ray was scattered by the collagen fibrils in the inner layer and left the diffraction pattern, which is composed of numerous sets of concentric arcs, on the screen (Figure 3-8b)[77,128-130]. In each set of concentric arcs, the arc closest to the beam center, the first-order arc, represents the distance q from the beam center which has a reciprocal relationship with the d-spacing of the collagen fibrils, whereas the rest of the concentric arcs are high-order arcs, corresponding to the

harmonics of the *d*-period. The azimuthal angle of each set of arcs, referred as Ψ, indicates one distinct orientation of the collagen fibrils in the scale, as illustrated in the inset of Figure 3-8 (b). Therefore, based on the change of the diffraction pattern, particular the change of *q* and Ψ of all sets of the first-order arcs, the rotation of the collagenous lamellae and the deformation of the collagen fibrils can be tracked in real time during uniaxial tensile tests on the scale, which in the present experiments were performed with the tensile loading applied along Ψ = 0°.

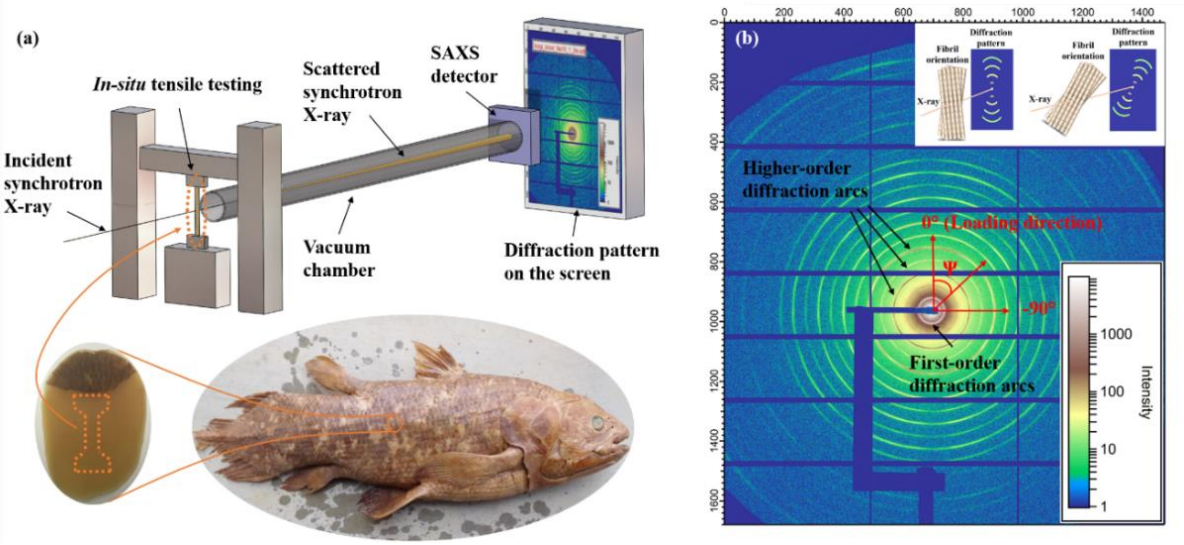

Figure 3-8 Experimental set-up for the *in situ* synchrotron small angle x-ray scattering (SAXS) during tensile tests. (a) Dog-bone shaped tensile test specimens are cut from the overlapped parts of the scales along both longitudinal and transverse directions. Synchrotron x-rays from the beamline at the Advanced Light Source successively hit the scale sample during the tensile tests and the scattering patterns are recorded for different deformation stages. (b) A representative diffraction pattern of the unstressed sample shows the several sets of concentric arcs which result from the x-rays being diffracted by the collagen fibrils in the scale. These concentric arcs are generated by the periodic structure in the collagen fibrils and the orientation of each set is parallel to the alignment of one group of the fibrils. The coordinates of each set of arcs are termed as q, the radial distance from the beam center to the first-order arc, and Ψ, the azimuthal angle, which is defined as 0° at the loading direction.

Figure 3-9(a) shows a representative diffraction pattern of an entire scale, cut along the longitudinal direction, in the unstressed state. In comparison to the scale after removing the outer mineral layer, shown in Figure 3-9 (b), (c), the diffraction pattern of the entire scale is blurrier with

the lower order arcs almost invisible, indicative of the mineral causing significant diffuse scattering to mask the diffraction from the collagen fibrils. The diffraction pattern of the inner layer has much more well-defined concentric arcs and the immediate visibility of high-order arcs reveals that the mineralization level of the inner layer is not very high[77]. Due to the double twisted arrangement, the diffraction patterns of the longitudinal sample, shown in Figure 3-9 (b), and transverse sample, shown in Figure 3-9 (c), are very similar; both do not display distinct regular preferential orientations for the diffraction arcs. This is quite different from the diffraction patterns from a typical Bouliand-type scale, for example, the carp scale, which shows the distinct five preferential orientations of the arcs (marked with arrows) equally separated by 36° in the diffraction pattern in Figure 3-9 (d), indicating the strictly ordered lamellae rotation. For comparison, the integrated intensity distribution along the Debye ring for the carp scale is shown in Figure 3-9 (e) and the equally separated five peaks with similar height confirmed the arrangement of collagen fibrils in successive lamellae form a highly ordered twist with rotation angle of 36° and the number of the lamellae in each orientation is almost same. However, the same plot for the coelacanth scale in Figure 3-9 (f) shows many more peaks with different heights which are distributed with unequal separation along the azimuthal angle, suggesting that due to the double twisted arrangement, the scheme of which is shown in the inset, collagen fibrils in coelacanth scale have many more orientations. The different intensities for the different orientations of fibrils may result from the uneven thickness of different lamellae, shown in Figure 3-10 (a). The collagen fiber bundles in the lamellae closer to the outer layer have a larger size than the corresponding lamellae in the deeper inner layer; the larger the size of the bundle, the more the collagen fibrils are packed together, which leads to the higher diffraction intensity at that orientation.

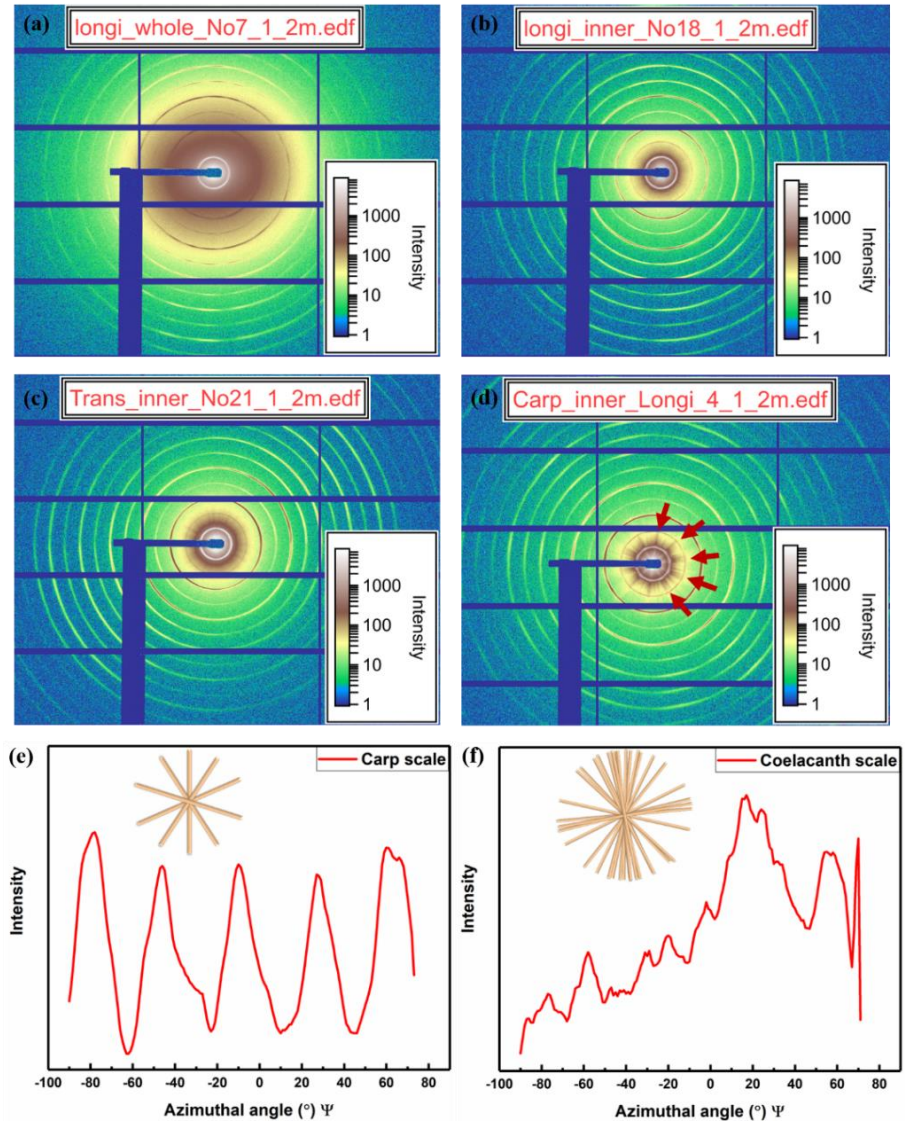

Figure 3-9 Diffraction patterns of the unstressed samples and orientations of the collagen fibrils in the coelacanth scales. (a) The diffraction pattern of an unstressed entire coelacanth scale is blurred, which indicates that the mineral layer impedes the diffraction. (b) and (c) are the diffraction patterns of the collagenous inner layers of coelacanth scale along longitudinal and transverse directions, respectively. These patterns are much more distinct than (a), which clearly show the concentric arcs but with no preferential angular orientation, compared with other elasmoid scales with typical Bouligand-type structures, such as carp scales. (d) For comparison, the diffraction pattern of the collagen layer in carp scale shows distinct five sets of symmetric concentric arcs equally separated by 36°, marked by arrows. (e) Diffraction intensity as a function of azimuthal angle for the carp scale confirms the five preferential orientations of the collagen fibrils in the inner layer and the schematic of the fibrillar orientation is presented in the inset. (f) Diffraction intensity as a function of azimuthal angle for the coelacanth scale indicates that the collagen fiber bundles in the inner layer have many more orientations than that in carp scale, with scheme in the inset.

To investigate how the complex orientations of collagen lamellae rotate and how the collagen fibrils deform within a matrix consisting of loosely packed interbundle fibrils in the coelacanth scales, real time diffraction patterns of the inner layer at five stages during tensile deformation are presented in Figure 3.10(a). In the unstressed state – stage 1 – because of the widely distributed orientation of the collagen fibrils in coelacanth scale, the numerous concentric arcs almost form concentric circles, indicating that the characteristic *d*-spacing of the collagen fibrils in all lamellae are almost same, *i.e.*, 63.5 ± 0.2 nm, as quantified from the diffraction pattern. However, with increasing applied tensile loading, the scale become stretched, causing the diffraction patterns to change from a 'round' to a 'square-oval-like' shape.

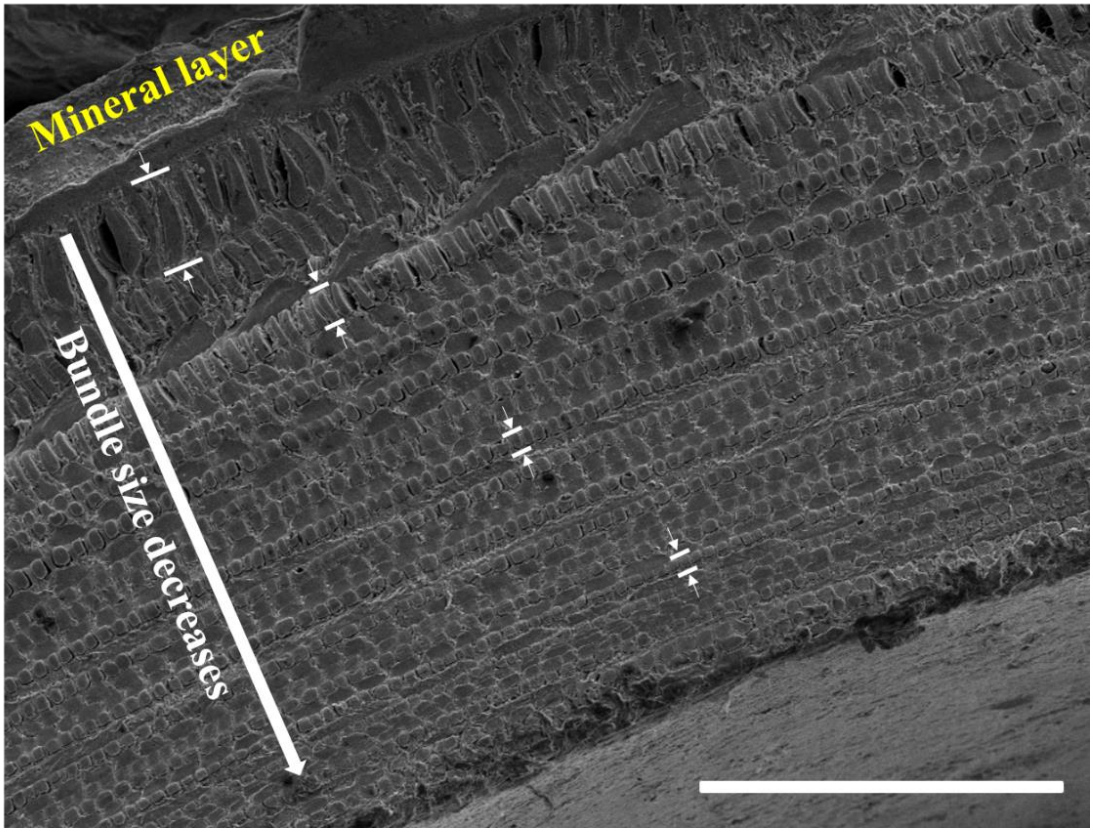

Figure 3-10 SEM image of the cross-section of the coelacanth scale. The bundle size gradually decreases from the outer (close to the mineral layer) to the inner regions of the scale with the larger bundles containing more collagen fibrils. (scale bar, 100 μm).

To quantitatively analyze the rotation of the collagenous lamellae during the elongation of the scale sample, the integrated diffraction intensity as a function of the azimuthal angle on the first-order Debye ring at the successive five stages (Figure 3-11a) is plotted in Figure 3-11 (b). In the unstressed state, the numerous peaks indicate the widely distributed orientation of the collagen fibrils. As the load is applied, the peaks between ± 40° are gradually merged into a high broad peak located at the loading direction, indicating that the lamellae with orientations in this range are gradually rotated towards the loading direction. Meanwhile, the peaks between Ψ = - 90° and Ψ = - 40° and the peaks between Ψ = 40° and Ψ = 90° are gradually moved far away from the loading direction, suggesting that the lamellae with orientation in these two ranges gradually rotate towards the horizontal direction, far away from the loading direction. Moreover, it is observed that one peak at the low azimuthal angle are split into two peaks, as circled in the plot, revealing that some lamellae may be separated during the deformation. The signal between Ψ = 70° and Ψ = 90° is not detectable due to the experiment set-up. The more surprising finding is the integrated intensity at the vicinity of Ψ = ± 40° (± 40° ~ 50°) are almost same during the whole process of the mechanical test, which indicates that no matter how the lamellae rotate, the number of the collage fibrils with these two specific orientations remains same. This phenomenon is very consistent in all the tested samples, both in longitudinal direction and transverse direction, as shown in Figure 3-12.

In order to quantify the deformation of the collagen fibrils different orientations, the diffraction pattern from Ψ = - 90° to Ψ = 70° was evenly divided into 17 sectors with a span of 10° and the averaged q of the arc in each sector was calculated. Based on the reciprocal relationship between q and the characteristic d-spacing, the d-spacing of the collagen fibrils in each sector was derived. For the successive five stages during the tensile test, the change in d-spacing in each sector

was normalized by its original length to define as the collagen fibril strain, which is plotted as a function of the azimuthal angle Figure 3-11 (c). Within the same range that the lamellae rotate towards the loading direction, the collagen fibrils with orientations between $\Psi = -40°$ and $\Psi = 40°$ are deformed in tension; the maximum tensile strain in the fibrils, which we measured as 0.12, was located at $\Psi = 0°$, *i.e.*, along the loading direction. These observations indicate that with the lamellae rotating towards the loading direction, the collagen fibrils in these lamellae are also being stretched. Within the ranges in which the lamellae rotate away from the loading direction (Ψ between - 90° and - 40° and Ψ between 40° and 70°), the deformations of the collagen fibrils are not in the same form. Fibrils with orientation between - 70° and - 40° and with orientation between 40° and 60° are deformed in compression, while the fibrils oriented almost horizontally (Ψ between - 90° and - 70° and Ψ between 60° and 70°) are still in tension but the tensile strain is almost negligible. This phenomenon is also observed at the two specific orientations, $\Psi = \pm 40°$, in which the strain in the collagen fibrils remains unchanged during the entire process of the mechanical tensile test. In other words, when the scale is pulled in tension, the collagenous lamellae rotate and the collagen fibrils are deformed, either in tension of in compression, but fibrils oriented in two specific directions, $\Psi = \pm 40°$, neither rotate nor are stretched or compressed. This phenomenon was very consistent in all the tested samples, as shown by the plots of the variation in fibril strain with azimuthal angle in Figure 3-13.

Figure 3-11 The adaptive mechanisms of collagen fibrils in the coelacanth scales. (a) The SAXS diffraction patterns of the scale at five stages during the uniaxial tensile test are selected to represent the in situ structural change. The diffraction pattern changing from ‘round’ to ‘square’ indicates the inhomogeneous deformation of the fibrils in different orientations. (b) Plots of diffraction intensity as a function of the azimuthal angle at the successive five deformation stages show the peaks approximately at ± 40° are merged to one broad peak with higher intensity located at loading direction and the peaks located ahead of 40° and behind - 40° move towards the direction perpendicular to the loading direction, with decreasing intensity. The relocation of the peaks with the intensity change indicates that most of the fibrils are rotated towards the loading direction during the tensile test but some of them rotate away from the loading direction. (c) The fibril strain is calculated from the d-space change during the tensile test and normalized by the d-space of collagen fibrils in the original state. The plots of fibril strain as a function of the azimuthal angle reveal that the fibrils oriented close to loading direction (within the range from - 40° to 40°) are in tension and the fibrils oriented far from loading direction, namely in <- 90°, 40°> and <40°, 90°> are in compression.

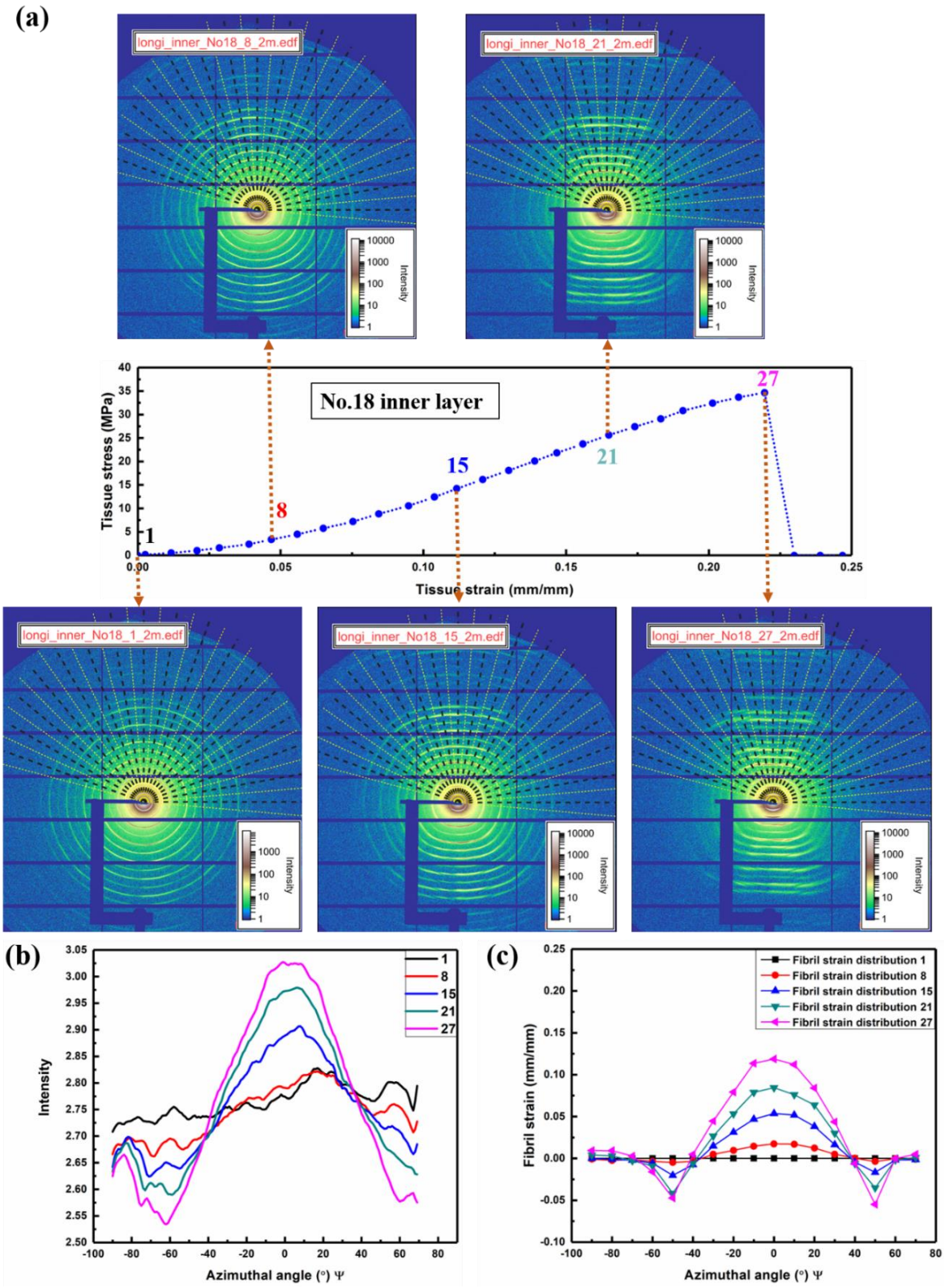
(a)
longi_inner_No18_8_2m.edf
longi_inner_No18_21_2m.edf
Intensity
No.18 inner layer
Tissue stress (MPa)
Tissue strain (mm/mm)
1
8
15
21
27
longi_inner_No18_1_2m.edf
longi_inner_No18_15_2m.edf
longi_inner_No18_27_2m.edf
(b)
Intensity
Azimuthal angle (°) Ψ
(c)
Fibril strain distribution 1
Fibril strain distribution 8
Fibril strain distribution 15
Fibril strain distribution 21
Fibril strain distribution 27
Fibril strain (mm/mm)
Azimuthal angle (°) Ψ

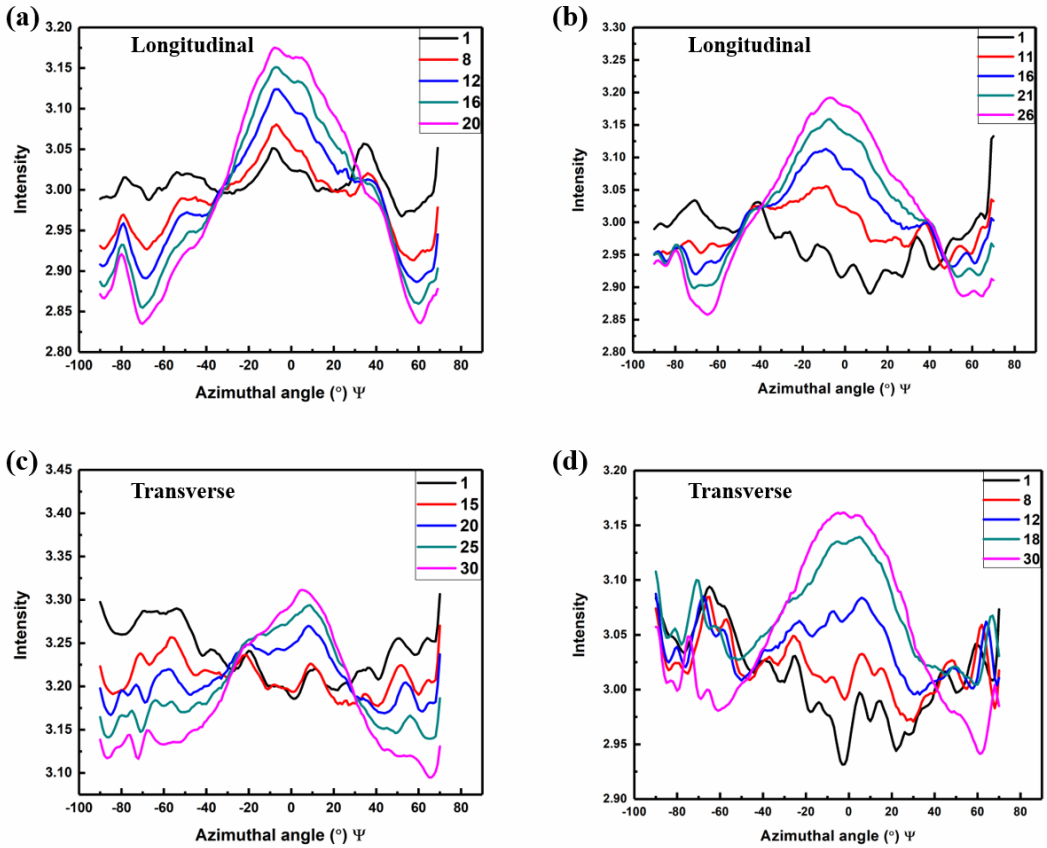

Figure 3-12 Plots of integrated diffraction intensity as a function of azimuthal angle in the coelacanth scales. (a-d) The plots of diffraction intensity vs. azimuthal angle at the successive five deformation stages in two samples cut in the longitudinal direction and two samples cut in the transverse direction are presented, respectively.

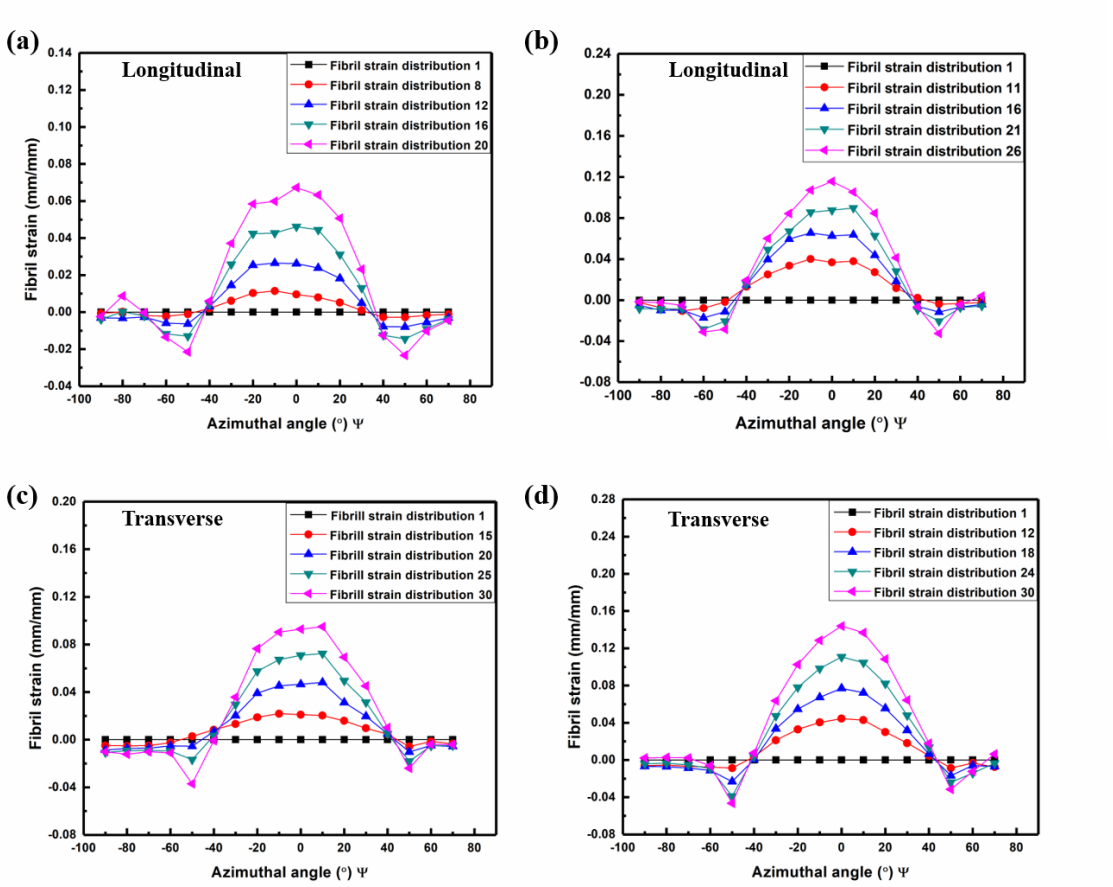

Figure 3-13 Plots of collagen fibril strain as a function of azimuthal angle in the coelacanth scales. (a-d) The plot of fibril strain vs. the azimuthal angle at the successive five deformation stages in two samples cut in longitudinal direction and two samples cut in transverse direction are presented, respectively.

3.3.4 Modeling of the evolution of fibril strain as a function of orientation

In order to predict the strain of collagen fibrils oriented at any given azimuthal angle at any stage during the deformation of the bulk scale sample, a mathematical model was proposed to quantify the relationship between the tissue strain (ε_t), the azimuthal angle (Ψ) and the fibril strain at a given angle (ε_f^{ψ}). Based on the quantitative analysis of collagen fibril deformation during the mechanical tensile test in the *in situ* SAXS experiment, the fibrils oriented at $\Psi = \pm 40°$ are neither stretched or compressed. Accordingly, during the evolution of the diffraction pattern from a 'round' to a 'square-oval-like' shape, two points at $\Psi = \pm 40°$ are also fixed (Figure 3-14). We assume that the path for the change of the diffraction patterns between - 40° and + 40° follows a set of concentric ellipses intersecting at $\Psi = \pm 40°$, which is shown in Figure 3-15 (a). The strain of collagen fibril at any given angle Ψ, denoted as ε_f^{ψ}, is defined as $(d - d_0)/d_0$, where d and d_0 are the instantaneous and initial *d*-spacing in collagen fibril, respectively. Due to the reciprocal relationship between the radius of the first-order diffraction pattern and the *d*-spacing of the collagen fibril, the strain of the fibril at any angle Ψ can be expressed as

$$\varepsilon_f^{\psi} = \left(\frac{r_0}{r_i} - 1\right) \tag{2}$$

where r_0 is the radius of the first-order diffraction pattern at the unstressed state and r_i is the radial distance between the beam center and the point at angle Ψ on the elliptical diffraction pattern when the tissue is in tension. Since the ellipses intersect at $\Psi = \pm 40°$, the equation of such set of ellipses can be expressed as

$$\frac{r_i^2 \sin^2\psi (b^2 - 0.59 r_0^2)}{0.41 r_0^2 b^2} + \frac{r_i^2 \cos^2\psi}{b^2} = 1 \tag{3}$$

where b is the minor axis of the ellipse. Substituting r_i in Eq. (3) with Eq. (2), the ellipse equation as a function of fibril strain ε_f^{Ψ} can be obtained as

$$[2.44-1.44(\frac{r_0}{b})^2]\sin^2\psi+(\frac{r_0}{b})^2\cos^2\psi=(\varepsilon_f^{\psi}+1)^2 \quad (4)$$

The fibril strain at $\Psi = 0°$, denoted as ε_f^0, has a reciprocal relationship with the minor axis of the ellipses b, namely $r_0/b = \varepsilon_f^0 + 1$. Moreover, based on the measurement from the *in situ* SAXS experiment, which is shown in Figure 3-16, the fibril strain at $\Psi = 0°$, the loading direction, is linear to the tissue strain ε_t, namely $\varepsilon_f^0 = \beta\varepsilon_t$, and β can be considered as a material constant that depends on different samples. Therefore, the r_0/b in Eq. (4) can be substituted by $r_0/b = \beta\varepsilon_t + 1$, which leads to

$$[2.44-1.44(\beta\varepsilon_t+1)^2]\sin^2\psi+(\beta\varepsilon_t+1)^2\cos^2\psi=(\varepsilon_f^{\psi}+1)^2 \quad (5)$$

Finally, the relationship between the tissue strain ε_t, the azimuthal angle Ψ and the fibril strain at the given azimuthal angle ε_f^{Ψ}, is quantified as

$$\varepsilon_f^{\psi}=\sqrt{[2.44-1.44(\beta\varepsilon_t+1)^2]\sin^2\psi+(\beta\varepsilon_t+1)^2\cos^2\psi}-1 \quad (6)$$

Based on this model, at any stage during the tensile deformation of the bulk sample, the strain of collagen fibril at the given azimuthal angle can be predicted. Since we only considered the diffraction pattern change between - 40° and + 40°, such model also only can be applied in the same range. Figure 3-15 (b) shows the fibril strains as a function of azimuthal angle Ψ for different tissue strains ε_t = 0, 0.05, 0.11, 0.16 and 0.22. The agreement between the calculated and measured values is excellent, proving that the hypothesis in this evolution of strains is correct. For the fibrils oriented beyond the range from - 40° and + 40°, they are no longer in tension, which is shown in

Figure 3-11 (c) and Figure 3-13. Their stress state is more complicated and the simple model we proposed above can not be applied.

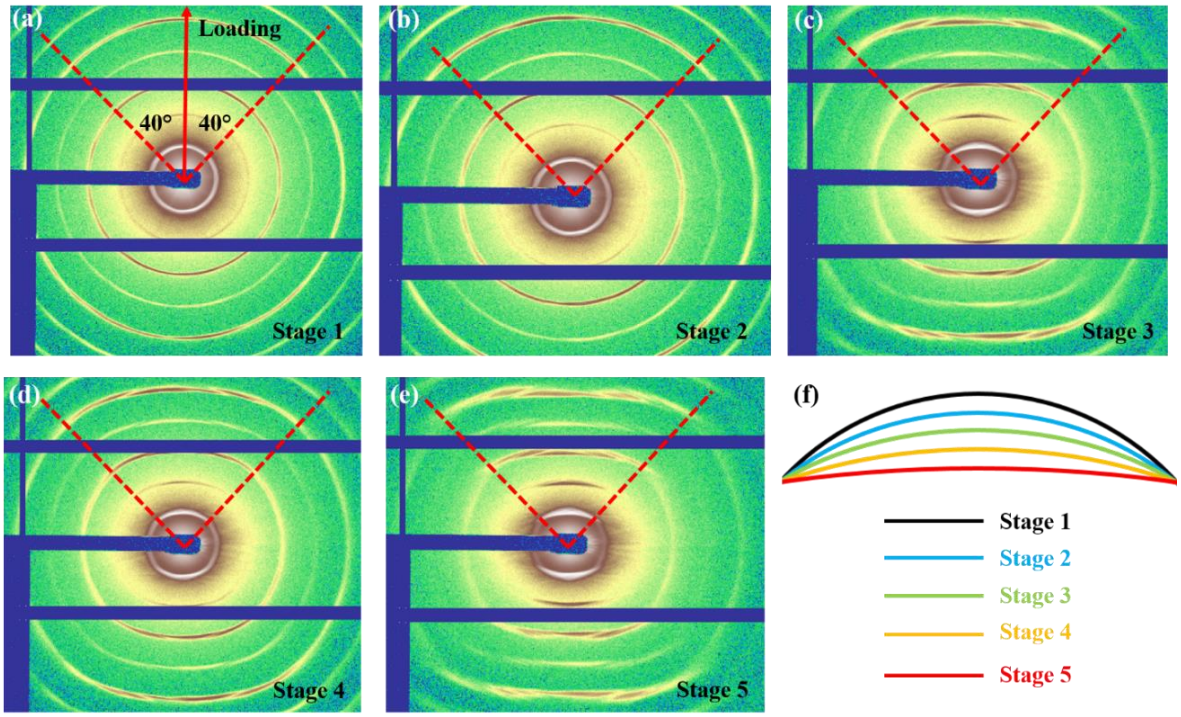

Figure 3-14 Diffraction pattern change between Ψ = ± 40°. (a-e) Magnified first-order diffraction pattern change between Ψ = ± 40° for successive 5 stages during the tensile deformation of the coelacanth scale. (f) The schematic of the first-order diffraction pattern change.

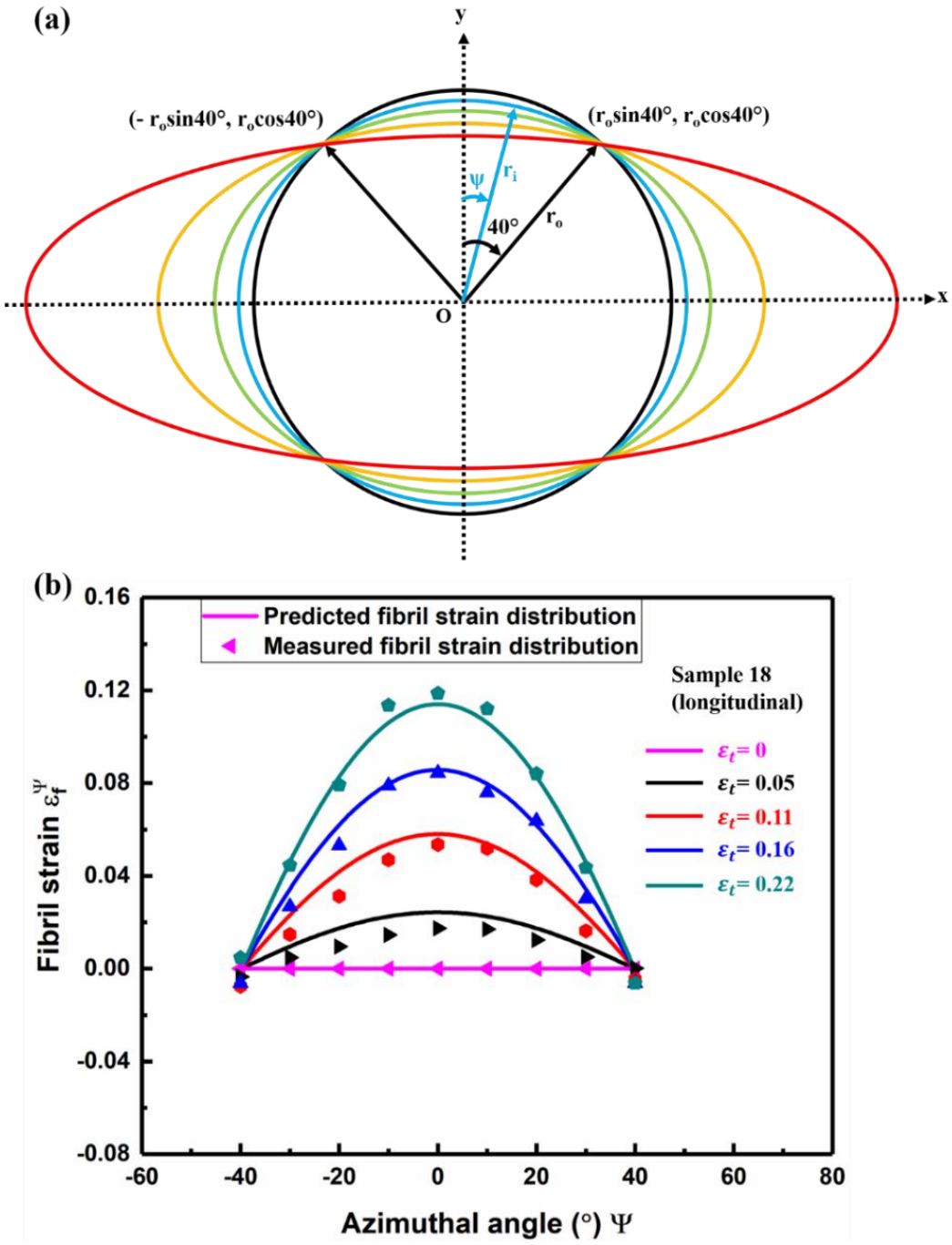

Figure 3-15 Modeling of the collagen fibrillar strain evolution as a function of orientation assuming that diffraction pattern evolves from circular to elliptical, with eccentricity increasing with applied load. (a) The elliptical model to present the diffraction pattern change. (b) Evolution of fibrillar strains with azimuthal angle Ψ at different loading stages (tissue strain ε_t is shown in figure). The predicted results based on the model (continuous curves) is compared with experimental results (points).

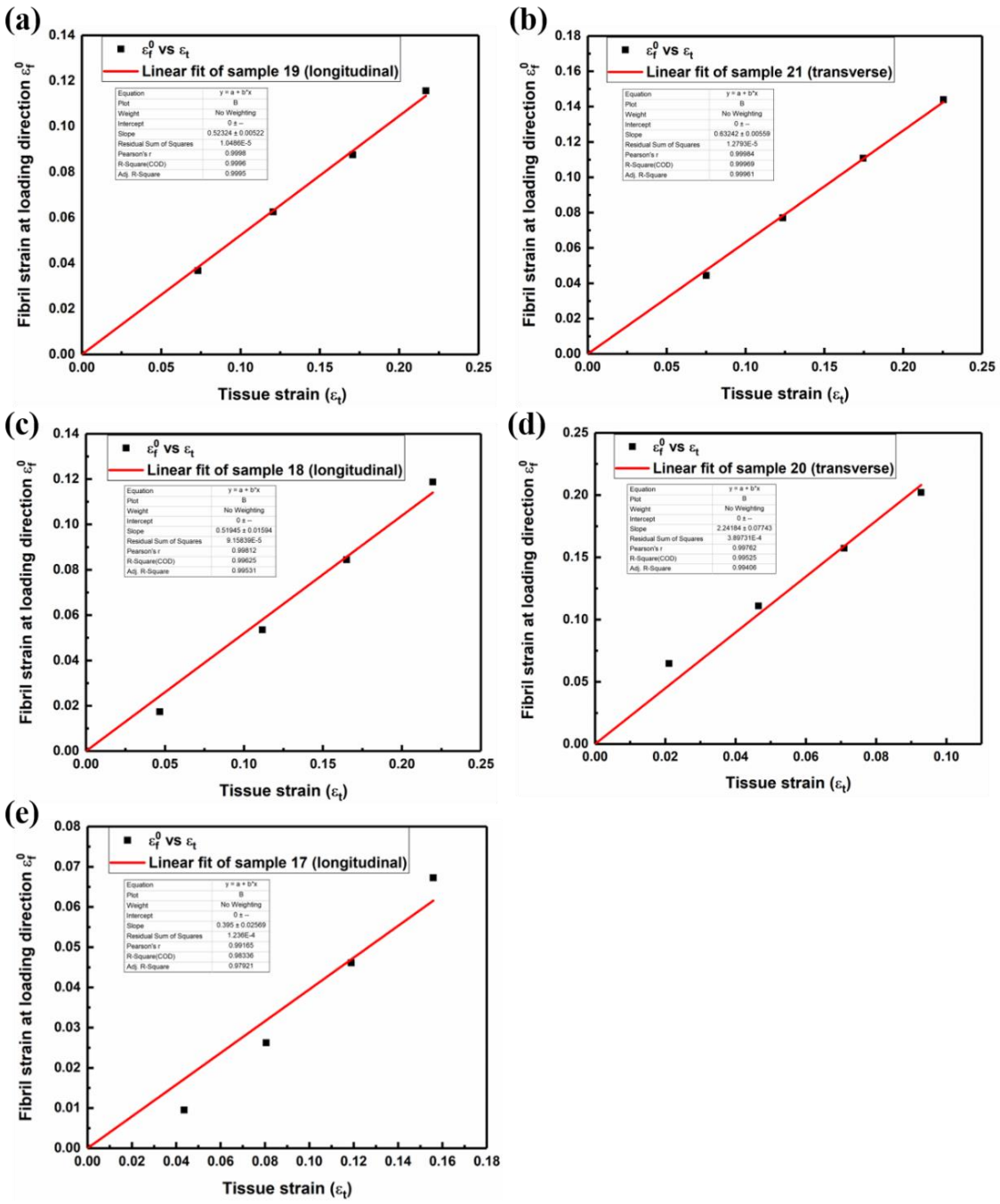

Figure 3-16 The local strain of collagen fibril at the loading direction as function of the tissue strain. (a-e) Based on the measure measurement from the in situ SAXS experiment, 5 points of fibril strain at $\Psi = 0°$ (the loading direction), ε_f^0, as function of the tissue strain ε_t, were plotted for each of 5 samples. Three of them are cut from longitudinal direction and two of them are cut from transverse direction. The linear fitting analysis fixed at (0,0) point was conducted for all 5 samples and they all show perfect linear relationship between ε_f^0 and ε_t.

3.3.5 Discussion

Fish scales are a prime example of dermal armor providing a protective function through their sophisticated hierarchical and graded structures which can deform and dissipate energy from different components and at differing length-scales. In simple terms, these scales possess a hard mineralized surface layer to resist penetration with graded and tougher inner layers to dissipate the excessive deformation and retain the structural integrity of the scale. The coelacanth's scales are no exception. As an extremely slowly evolved primitive fish, coelacanth has been well protected by its armor-like scales for more than 400 million years[116,118]. Their unique structures were once regarded as the only cosmoid scales in existence but the current research has established that that they are a primitive type of elasmoid scale[60]. Instead of a thick and continuous mineralized spongy tissue named as cosmine, the coelacanth scale is covered by a thinner mineralized outer layer with regularly spaced mineral ridges and the numerous tooth-like tissue odontodes are scattered on the exposed region. Such highly mineralized outer layer provides the hardness to minimize the local plasticity and the resistance to the penetration caused by the predator's teeth[78,131]. The degree of imbrication for the coelacanth scales is almost as same as the 'modern' types of elasmoid scales, which enhances the stress redistribution and improves the flexibility of the entire fish's body. The aspect ratio of the coelacanth scale is also close to 'modern' types of elasmoid scales, much smaller than other primitive fish scales, such as alligator gar scales, bichir scales and arapaima scales; the fact that the individual scales are thinner makes them more flexible which enhances the maneuverability of the entire fish, an important characteristic for a fish living in the open ocean. The distinct equally spaced ridges on the scale anchor the scale and enhance its bending ability, which also facilitates the stress transfer from the outer to the inner layer. The graded transition

between the hard outer layer and the soft inner layer leads to smoother stress gradients, which serve to improve the interfacial toughness and hence reduce the possibility of interfacial failure[69].

Underlying the thin mineral layer is the collagenous inner layer, isopedine, which constitutes a major part of the scale. The unique structure of the inner layer in the coelacanth scale differentiates itself from all the other well-studied fish scales by three distinct characteristics. First, the collagen fibrils form the well-defined bundles, which are arranged in parallel and form the lamellae. Second, the successive collagenous lamellae are arranged in a double-twisted plywood (Bouligand-type) pattern. Each adjacent two layers form orthogonal ply and these orthogonal plies rotate clockwise. Third, the collagen bundles are imbedded in a matrix formed by the loosely packed collagen fibrils, which play as a role of binding material to hold the double-twisted plywood structure. Such a unique architecture results in extremely effective mechanical adaptability for coelacanth scales through the unique deformation mechanisms of the fibrous core, which are the crucial to the toughening mechanisms of the entire scale.

The double twisted plywood arrangement enables the very wide distribution of fibril orientations and is the origin of the ‘in-plane’ isotropic tensile behavior of the scales. The loosely packed fibrils in the matrix and the weak interface between the fiber bundles and the matrix significantly improve the deformability of the scale, resulting in the significant energy dissipation before tensile failure. The complex hierarchical structure also develops mechanisms that act to inhibit crack propagation; specifically secondary cracks can form in the mineral layer to dissipate a relatively small amount of stored elastic energy with the larger dissipation of energy occurring via plastic deformations in the collagenous inner layer, including the rotation, twisting and delamination of the collage fibrils both within the bundles and in the matrix. Furthermore, stretched collagen fibrils behind the crack tip act to bridge the crack, thereby carrying load that

would otherwise be used to promote crack extension; such crack-tip shielding reduces the stress intensity at the crack tip that drives cracking. These damage tolerant mechanisms also enable the scale to dissipate the energy created by attacks from the predators, which is crucial to the protective function of the armored scale.

Using mechanical tests on the scale with simultaneous *in situ* SAXS, the fundamental deformation mechanisms in the collagenous inner layer were deduced, specifically involving the rotation and deformation of the lamellae. Similar to the deformation of collagen fibrils in Arapaima scales[15], the collagenous lamellae in coelacanth scale rotate in two directions, towards the loading direction and in the opposite direction, depending on the angle between their original orientation and the loading axis. The rotation of lamellae towards the loading direction may result from the interfibrillar shear in the bundles and the shear between the bundle and matrix. As the loading increases, simultaneous shear between all the bundles in a given lamellae within the matrix additionally will lead to significant deformation in the matrix. Since the matrix itself performs as a binding material that holds together the entire laminate structure, the rotation of one lamella will largely affect the rotation of the adjacent lamellae, which causes the 'sympathetic' rotation that could drive some lamellae to rotate away from the loading direction.

With the rotation of the collagenous lamellae, the collagen fibrils are also deformed to adapt the applied tensile load. The fibrils oriented closer to the loading axis, with an angle span of 80° (from Ψ = - 40° to Ψ = 40°), are stretched when the bulk scale is in tension. This range of the orientations in which the fibrils are in tension is larger than that for the Arapaima scale, which found to 60° in our previous study[15]. This may result from the collagenous matrix in coelacanth scale constraining the rotation of the lamellae such that they become stretched rather than rotating further. A very interesting phenomenon we observed is there are two specific directions around Ψ

= ± 40° that the fibrils located there are neither stretched nor compressed. Similar with the neutral axis in the beam, there are no fibril stresses or strains at these two specific directions and they are the transitions that the stress state of the fibrils changes from tensile to compressive. Therefore, the two orientations at Ψ = ± 40° can be regarded as the neutral axis for the deformation of collagen fibrils inside of the coelacanth scale when the tissue is in tension. Another interesting phenomenon that was observed in the *in situ* SAXS experiment is the compressive strain for the collagen fibrils in coelacanth scale reaches maximum around Ψ = ± 50° and it gradually decreases to almost zero from Ψ = ± 50° to the horizontal direction. This could also be the effect of the matrix. Beyond Ψ = ± 50°, as the azimuthal angle increase, the constraint effect of the matrix on the lamellae becomes more and more dominating, which leads to large deformation of matrix to adapt to the Poisson's effect and smaller deformation of fibrils in lamellae. Without the effect of matrix, such as Arapaima scales, the only way to adapt to the Poisson's effect is compressing the fibrils that oriented perpendicular to the loading direction. This could be the reason why the maximum compressive strain in Arapaima scales occurs at the direction that perpendicular to the loading direction, while in coelacanth scale the compressive strain reaches maximum at Ψ = ± 50°.

3.4 Summary

In summary, we have carefully characterized the detailed structure of the coelacanth scale: the loosely packed IBFs generate a matrix that acts as a binding material to confine the FBs in the lamellae into a double-twisted Bouligand arrangement with the external surface covered by a ridged thin mineral layer. Such a hierarchical fibrous structure can effectively arrest crack propagation, constrain the delamination of the collagen fibrils, and enhance the stretching and sliding along the tension direction with large strain, which renders the coelacanth scale a tough material to resist predatory attacks. Mechanical tensile testing coupled with SEM and in situ synchrotron SAXS revealed its unique deformation mechanisms. The lamellae with orientations close to the tensile axis rotate towards the loading direction along with stretching and sliding of the fibrils to adapt to the applied load, as described by the constitutive equation developed in the Supporting Information. The fibrils oriented far from the tensile axis (beyond Ψ = • } 40°) rotate away from the loading direction. Within this range, they are non-uniformly deformed in compression as they are affected by the constraint of the matrix which forces the collagen FBs to bend and twist; this represents a manifestation of the Poisson's ratio effect (lateral contraction). The sophisticated hierarchical structure of the coelacanth scale, with its double-twisted Bouligand structure, is quite unique, as compared with the modern elasmoid scales in teleosts, and provides an excellent protective function for this "living fossil" fish. Such a unique structure may well inspire innovative designs for new high-performance structural materials.

Chapter 3, in full, is published as "Novel Defense Mechanisms in the Armor of the Scales of the "Living Fossil" Coelacanth Fish", Advanced Functional Materials, vol 28, pp1804237, 2018. This work was coauthored by W. Yang, E. Schaible, R. O. Ritchie and M. A. Meyers. The dissertation author is the first author of this work.

CHAPTER 4: STRUCTURE AND MECHANICAL ADAPTABILITY OF CARP SCALES

4.1 Introduction

The integument of vertebrates is a continuous, heterogeneous layer covering the body surface. It consists of two distinct strata: the epidermis and the dermis[60]. The epidermis is mainly composed of keratin with a stratified structure, playing a crucial role in permeability barrier and mechanical protection[60,96]. Within it, many specialized cells are also able to develop non-skeletal epidermal scales, such as the ones in pangolin, and appendages like feathers, hoofs, hairs, claws, beak and nails, serving as multifunctional structural materials (armors, weapons, transportation tools, and thermal protection) to carry out assorted functions for organisms surviving in diverse environments[96,132]. The deep counterpart to the epidermis is the dermis, which is collagen-based[60]. The ability to mineralize the dermis layer is a major innovation for many lower vertebrates, and enabled them to develop an efficient protective shelter, also called "dermal armor", to prevent tissue damage caused by predatory attack[11,133]. The fish scale is the most common one, providing effective protection for the overwhelming majority of fish species living from the tropical to the polar regions.

Based on the histological and histochemical characteristics, the scales of the current existing fish are mainly grouped into placoid, ganoid, elasmoid, dermal plates, and scutes [60]. The placoid scale is characteristic to cartilaginous fish like sharks and rays. The ganoid scale is another primitive category, and also called rhombic scale because it has a diamond shape. There are mainly two types of ganoid scales existing currently: the quad-layered one, which is unique to *polypteriformes* (bichirs and reedfish) and the double-layered one, which is commonly found on *lepisosteiformes* (gars)[57,69] . The scutes and dermal plates are also rigid fish scales, which are modified from ganoid scales[60]. The scutes are composed of a thick bony base capped by a layer of

non-collagenous hypermineralized tissue called “hyaloine”, while the dermal plates are composed exclusively of bone. The most common representative possessing scutes is the armored catfish (*callichthyids, loricariids and doradids*); the dermal plates are usually found in sturgeons, paddlefish, sticklebacks, boxfish, pufferfish and seahorses[60]. Due to their rigidity, scutes and dermal plates are only able to provide protection for limited fish species, compared with the most evolved type, the elasmoid scale.

The elasmoid scale, without any question, is the most prevailing dermal armor among living vertebrates, including most of current fish species and some gymnophionan amphibians[60,134]. They are thin collagenous plates embedded in the dermal pocket with roughly two thirds of posterior surface overlapped by neighboring scales. Notwithstanding considerably diverse in morphology and ornamentation (including both ctenoid and cycloid shapes), all elasmoid scales have a similar fundamental structure, which consists of three layers[60,65,135]. By the developmental sequence, the first one formed is the external layer, which is an ornamented thin layer comprised of minerals (mainly hydroxyapatites) and well-mineralized, randomly-oriented collagen fibrils (woven fibrils). The second one formed is the tissue beneath external layer, which is a thick basal plate composed of larger collagen fibrils forming a laminated plywood structure called “elasmodine”, where the name of elasmoid scale originates from. This plywood tissue (elasmodine) is slightly mineralized or completely unmineralized, resulting in great deformability for the scales. The last formed component is an extremely thin layer sitting on the very top surface which is composed of pure mineral and called “limiting layer” in some literatures. Based on previous investigation on the structure and mechanical behavior of elasmoid scales in various fish species, including arapaima[56,77,78,114,131,136-138], red seabream[139], bass[76,113] and tarpons[140], the protection mechanisms of elamsoid scales are unraveled: the well-mineralized outer layer,

including the external layer and limiting layer, provides hardness against the bite from predators' attack; the soft collagenous laminated base enables great deformability to dissipate the stored elastic energy through assorted mechanisms, such as lamellar rotation and separation, collagen fibril stretching/compression, fibrillar delamination and bridging, etc., leading to outstanding toughness. By using primarily biopolymers and minerals in an intricate and ingenious hierarchical architecture, the elasmoid scales can combine sufficient strength with excellent damage tolerance, properties that are commonly exclusive in synthetic materials, making them a high-performance structural material[11,13].

Here, we cast our interest on the elasmoid scales of the common carp (*Cyprinus carpio*). As a typical dermal armor, the scales protect carps to survive in various environments worldwide and make them one of the most flourishing species. Although the structure and some mechanical properties of carp scale have already been studied previously [141-147], the ultrafine structure of its collagenous lamellae is not well investigated, and the deformation mechanisms are not quantified[141,143-147]. In this chapter, we fully unravel the detailed structure of the carp scale, especially using transmission electron microscope (TEM) to characterize the ultrafine structure of the collagen fibrils in the laminated inner core. We found that there are two collagenous frames comprising the plywood base of carp scale. The first one is composed of the collagenous lamellae made of isolated collagen fibrils; the arrangement of their orientations follows a helical pattern. The second one is a set of several layers composed of thinner collagen fibrils and forming a "sheet-like" structure oriented from the basal part towards the superficial layer. In addition to conventional tensile testing, in-situ synchrotron small angle X-ray scattering was applied during the tensile deformation to quantify the lamellar rotation and collagen fibril stretching/compression. In comparison with the primitive elasmoid scale from the living fossil coelacanth, the deformation

mechanisms of this well-evolved elasmoid scale are identified, which may bring up some critical thinking on the design of new synthetic structural materials.

4.2 Methods

4.2.1 Materials

The scale samples were collected from a common carp (Cyprinus carpio) fish with a size of 670 mm, which was purchased from Ranch 99 Market (7330 Clairemont Mesa Blvd, San Diego, CA, USA). The scales were extracted from their pocket with tweezers and preserved in deionized water. They varied from 20 mm to 40 mm in length but the ones we used are all ~30 mm in length and extracted from the mid-lateral region. For comparison, coelacanth scales were obtained from a *Latimeria chalumnae* with a length of 950 mm in the Marine Vertebrate Collection of Scripps Institution of Oceanography, University of California, San Diego; the specimen was preserved in 80% isopropanol since it was collected from the Grand Comore Island in 1973. They were peeled off from the *linea lateralis* below the anterior dorsal fin.

4.2.2 Structural characterization

The structure of the scales and the fracture surfaces after tensile testing were all characterized in a FEI Quanta 250 and FEI Apero scanning electron microscope (SEM; FEI, Hillsboro, OR). To obtain oblique fracture surfaces, scales were immersed in liquid nitrogen for 30 s and immediately fractured using forceps. The samples were first immersed in the 2.5% glutaraldehyde for 1 h to fix the structure and then dehydrated with an ascending series of ethanols (30, 50, 70, 90, 95 and 100 vol.% twice), before being dried using an automatic critical point dryer (Tousimis AutoSamdri 815A, MD). All dried samples were then sputter coated with iridium using an Emitech K575X sputter coater (Quorum Technologies Ltd.) before observation. TEM images

were taken on FEI Technai 12 (Spirit, 120-kV) transmission electron microscope (FEI, Hillsboro, OR).

4.2.3 Preparation of TEM specimens

The carp scales were first cut into small strips, with a length of 5 mm and a width of 2 mm, and then immersed into 2.5% glutaraldehyde in 0.15 M sodium cacodylate buffer (pH 7.4) for 1 h to fix the structure. The fixed specimens were stained with 1% OsO_4 solution with 8% potassium ferrocyanide in 0.5 M sodium cacodylate buffer for overnight at room temperature. The scales were then stained with 2% aqueous uranyl acetate for 12 h and subsequently dehydrated with an ascending ethanol series (50, 70, 90, 100% twice), followed by a 1:1 ratio of 100% ethanol and 100% acetone, and finally 100% acetone. The fully dehydrated specimens were embedded in Spurr's low viscosity resin and polymerized at 60°C for 72 h. The obtained blocks were then sectioned parallel to the vertical cross-section before ultrathin slices with thickness of ~80 nm was generated using a Leica Ultracut UCT ultramicrotome (Leica) and a Diatome diamond knife (Diatome). Ultramicrotomed sections were then placed on copper grids for TEM observation and post stained with Sato lead for 1 min before final examination.

4.2.4 Uniaxial tensile testing

Dog-bone shaped tensile specimens of carp scales with dimensions of 20 × 3 mm were cut along longitudinal and transverse directions from carp scales with a thickness of between 0.2 and 0.3 mm. The outer layers of some samples were removed using silicon carbide polishing paper of 180 # - 2500 #, leading to final thickness around 0.1 mm. To prevent sliding during tensile testing, the ends of the samples were glued between sand paper sheets using cyanoacrylate glue, resulting in a gauge length of ~ 10 mm. Uniaxial tensile tests were performed on an Instron 3342 mechanical testing machine (Instron Corp., Norwich, MA) with a load cell of 500 N at a strain rate of 10^{-3} s^{-1};

samples were tested immediately after being removed from deionized water, where they had been kept prior to testing. The ultimate tensile stress, uniform elongation (strain at maximum stress) and the toughness, as measured by the area beneath the uniaxial stress–strain curves, were determined.

4.2.5 *In situ* small-angle x-ray scattering (SAXS) during mechanical testing

Using identical specimen preparation procedures as for the uniaxial tensile tests, specimens for *in situ* SAXS measurements were made in both longitudinal and transverse directions of complete carp scales and those where the mineral layer had been removed. The resulting specimens were loaded in tension, while simultaneously exposing them to synchrotron x-rays at beamline 7.3.3 at the Advanced Light Source synchrotron radiation facility (Lawrence Berkeley National Laboratory, Berkeley, CA, USA). The tensile tests were performed with a customized rig using a displacement stage and a 45-N capacity load cell (Omega, LC703-10) to measure the force. Such an experimental set-up allows for SAXS data collection to be recorded in real time with the measurement of the load–displacement curve. The mechanical tests were performed at room temperature and a displacement rate of 2.0×10^{-2} mm s^{-1}.

A Pilatus 1M detector (Dectris Ltd., Baden, Switzerland) was used to collect the SAXS data. The detector was located at the largest allowable distance, around 4 m, to detect fine changes in the collagen peak's position. The sample was exposed to x-rays for 0.5 s with intervals of ~5 s during the mechanical test; this radiation dosage was sufficiently low so as not to affect the structure and properties of the scales.

Quantification of fibril orientation using SAXS: On examining the SAXS spectra patterns, 360 of even sectors were made on the Debye rings with a span of 1°, starting from $\Psi = 0°$ to $\Psi = 360°$ (Ψ, the azimuthal angle, which is defined as 0° at the loading direction); as such, a

sector graph was generated by the polar transformation of the 2-D diffraction pattern using the software IGOR Pro (Wavemetrics) in conjunction with the custom macro NIKA (Jan Ilavsky, Argonne National Laboratory, IL, USA). Based on the obtained square map of intensity *vs.* pixel, the 1-D graphs, specifically, the plots of the integrated intensity as a function of azimuthal angle, were created by using the 'Image line profile' tool in NIKA.

Quantification of fibril strains: The strains in the collagen fibrils in the lamellae were measured from the x-ray data in terms of the change in 1-D peak position determined from the plot of integrated diffraction intensity as a function of *d*-spacing. By using the same software as in the quantification of fibril orientation, the sample detector distance and beam center was calibrated with the 2-D diffraction pattern of a silver behenate standard. In order to convert the 2-D SAXS data into 1-D peaks, 17 sectors were evenly made on the upper half of the Debye rings, starting from $\Psi = -5°$ to $\Psi = 165°$, with a span of 10° in each sector; then the integrated intensity over the diffraction arc in each sector was radially averaged to obtain the relationship between the intensity peaks and the radial distance of the arc, *q*. Based on the numerical relationship between *q* and the *d*-spacing, plots of integrated intensity as a function of the *d*-spacing for all 17 sectors were generated by the software; intensity peaks were fit to an exponential Gaussian function and a linear background to precisely locate the peak positions. The strain in the collagen fibrils was measured as the change in position of the center of the first-order collagen peak, normalized by the strain in the unstressed state.

4.3 Results

4.3.1 Structure of the scales of common carp (*Cyprinus carpio*)

The common carp (*Cyprinus carpio*) is a widespread freshwater teleost from the family *Cyprinidae* which originated from eutrophic waters in lakes and large rivers in Europe and Asia.

Their body is fully covered by imbricated/overlapped elasmoid scales anchored in the dermis pocket, as shown in Figure 4-1 (a). The individual scale has an oval-like shape and 2/3 of its surface, the white part shown in Figure 4-1 (b), is covered by neighboring scales, which distributes stresses from a bite across a large volume of material and provides penetration resistance at a reduced weight[148]. Figure 4-1 (c-i) manifest the surface characteristics of the scale's exterior surface (named the limiting or osseous layer due to its high degree of mineralization) and the external layer (~40 to 50 μm thick). The well mineralized limiting layer covers the external layer except at the periphery. The posterior region (dark region shown in Figure 4-1b) is the exposed part which has numerous mineral denticles scattered on it (Figure 4-1c). The close-up view of an isolated denticle, shown in Figure 4-1 (d), indicates that it is embedded in the dermis which is composed of randomly oriented collagen fibrils (Figure 4-1e). The overlapped surface presented in Figure 4-1 (f,g) with different magnifications shows two ornamentation characteristics: the *circuli*, as indicated by the dotted lines, and *radii*, indicated by the arrows. The *circuli* are concentric ridges or elevations on the superficial layer (dotted lines in Figure 4-1f,g); in some primitive fish species like coelacanth or bowfin fish, they are in a radial position[134,149] . The *radii*, as indicated by arrows in Figure 4-1 (f,g), are the linear grooves starting from the focal region of the scale and breaking off *circuli*. These features aid the anchoring of the scales in the dermis pocket and improve their stability. A close-up view of the *circuli* (Figure 4-1h) shows the regularity of their arrangement, with an approximately equal spacing. Mineralized thin woven fibrils (~30 - 50 nm in diameter) are observed in the space between *circuli* ridges (Figure 4-1i), forming a randomly oriented loose network; this indicates that the limiting layer is extremely thin and discontinuous, leading to the partially exposed external fibrous layer. We compare the mineral contents of three types of elasmoid scales (carp, coelacanth and arapaima) by performing

thermogravimetric analysis (TGA); the results, provided in Figure 4-2, show that the carp scale has the lowest mineral content. The thickness of each component in this layered structure is provided in the detailed cross-sectional images in Figure 4-3.

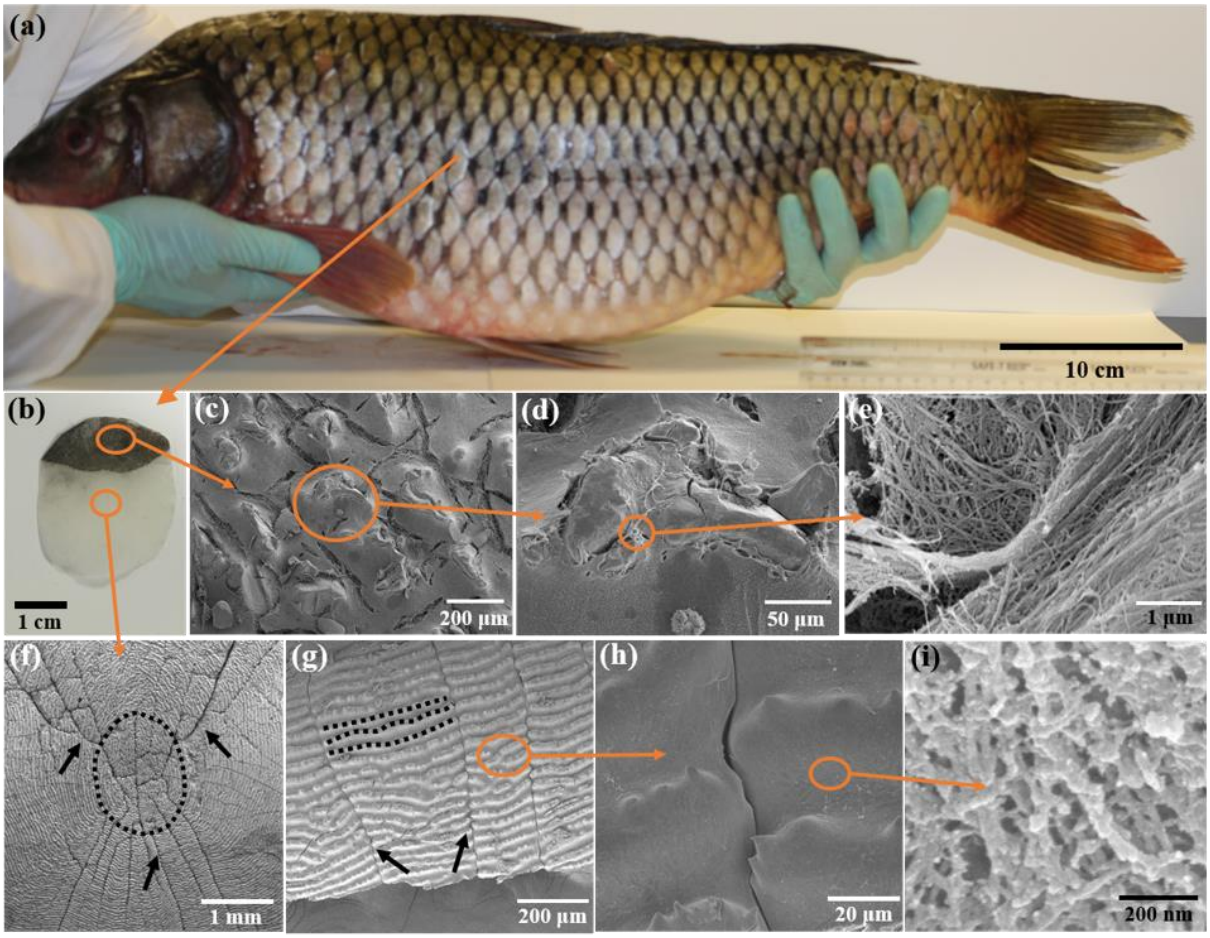

Figure 4-1 Surface morphology of carp scales. (a) The common carp (Cyprinus carpio) from which the scales are extracted. (b) The carp scale is a typical elasmoid scale with an oval shape; two thirds of surface (the white part) are overlapped by neighboring scales. (c-h) Scanning electron micrographs of the outer surface of the carp scale. (c) The mineralized denticles are scattered on the exposed part (dark region) and increase the surface roughness. (d) Most parts of the denticle are covered by the dermis and only the rounded tip is exposed. (e) The fibrous dermis tissue around the denticle tip. (f,g) The overlapped region of the carp scale suggests that the mineral ridges (*ciruli*), indicated as dotted lines, are interrupted by cracks (*radii*), as indicated by arrows. (h) A close-up view reveals that the mineral ridges which define the *circuli* are regularly spaced. (i) The external layer, which is comprised of woven mineralized fibrils (diameter ~30 to 50 nm), is exposed at the spaces between the ridges.

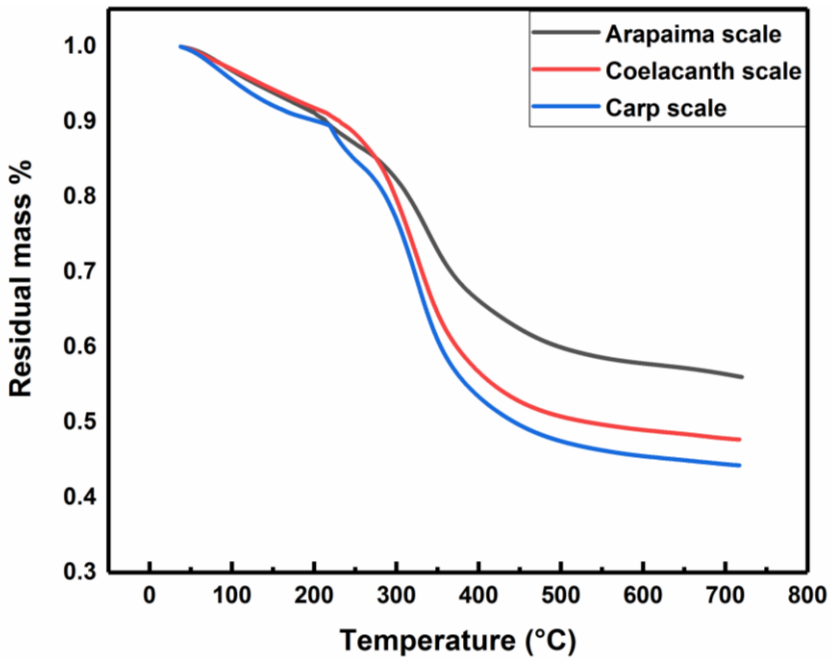

Figure 4-2 Thermogravimetric analysis (TGA) of three elasmoid fish scales from the carp, coelacanth and arapaima fish. The carp scale has lowest residual mass after the temperature is increased to 700°C, indicating it has the lowest mineral content compared with the coelacanth and arapaima scales.

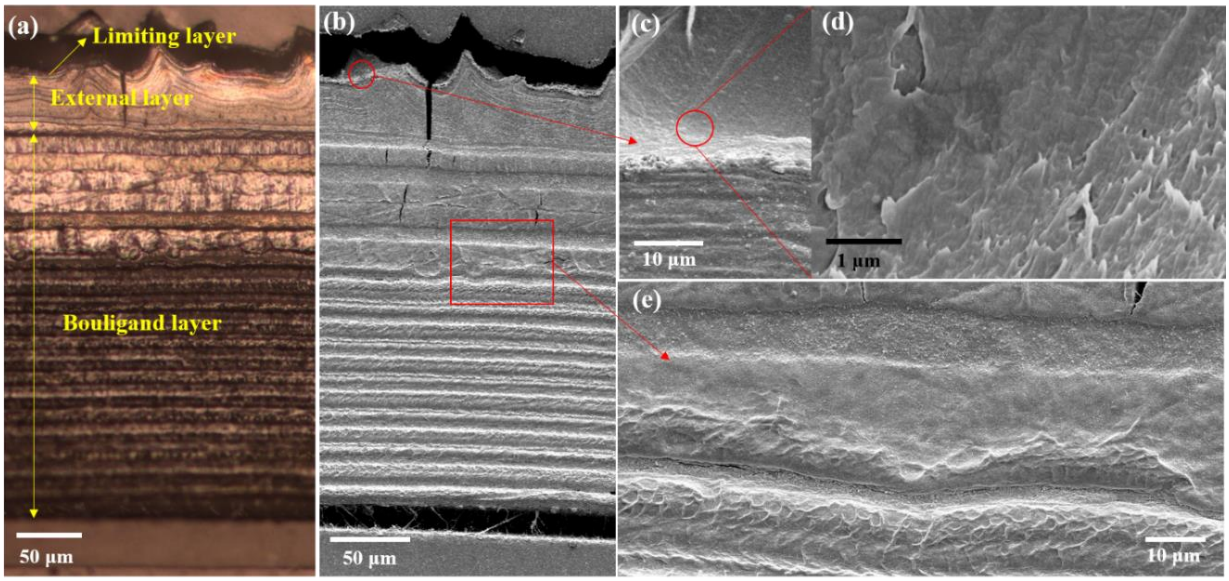

Figure 4-3 Three layers in the carp scale. (a) Optical microscopy image of the polished cross-section of the carp scale. (b) SEM images of the same area in (a). (c,d) Close-up view of the limiting layer reveals the fibrous structure is exposed on the surface. (e) Close-up view of the polished cross-section of the collagenous lamellae.

SEM images of the oblique fracture surface of frozen scales are provided in Figure 4-4 (a-c), disclosing structural characteristics of the inner layer. The basal layer of the scale is a stacking of collagenous lamellae, forming a plywood-like arrangement occupying a major volume fraction of the scale. The collagen fibrils in each lamella are assembled in parallel, but the orientations of successive lamellae are offset by a specific angle. For better understanding the uniqueness of the structure of carp sale, the structure of a primitive elasmoid scale from the coelacanth is compared, the SEM images of which are presented in Figure 4-4 (d-f). There are three distinct differences between these two types of scales:

1. The arrangement of lamellae orientations. As the arrows indicate in Figure 4-4 (a), the orientations of successive lamellae in the carp scale form a helicoidal pattern rotating counterclockwise; this is also called "Bouligand" structure. The rotation angle is about is about 36°, which is precisely determined by SAXS experiments and will be illustrated in a later section. A similar helical pattern is also observed in the basal plate of arapaima[56] and tarpon scales[140]. In contrast, the lamellae orientations in coelacanth scale form an alternative Bouligand type[149]. Figure 4-4 (d) shows that two adjacent lamellae forming successive orthogonal plies (marked in different colors); this bilayer system rotates clockwise, forming a double-twisted Bouligand structure. Some other elasmoid scales like red seabream [139], golden fish [135] or striped bass[75] have an orthogonal arrangement for their collagenous plies: the adjacent two lamellae are always perpendicular to each other.
2. The fibril arrangement in each lamella. The close-up view of the assembly of collagen fibrils in one lamella is provided in Figure 4-4 (b,c), which manifest that there is no group of bundles formed in carp scale. Each lamella is composed of isolated collagen fibrils connected by sacrificial bonds (arrows in Figure 4-4 c). A similar structure is also identified

on most other elasmoid scales, such as arapaima[131], red seabream[139], tarpon[140], golden fish[135], and striped bass[75]. However, the collagen fibrils in the coelacanth scale are distinctly grouped into round bundles, as circled with dotted line in Figure 4-4 (e), and the characteristic band pattern (Figure 4-4 f) is more well-defined[149].

3. The space between the lamella fibrils. In the carp scale, the isolated collagen fibrils in lamella are directly packed together and there is no noticeable substance between them, as presented in Figure 4-4 (b). Most of other elasmoid scales like arapaima, tarpon, striped bass, etc., share the same characteristic. In contrast, the space between the fiber bundles in coelacanth scale is filled with a fibrous structure as indicated in the inset of Figure 4-4 (e).

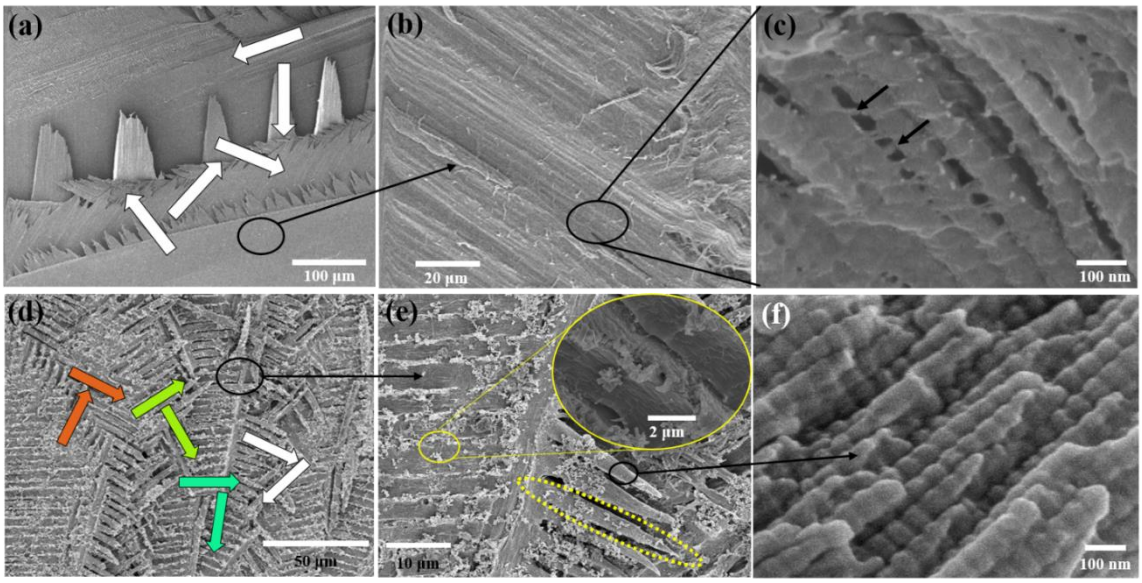

Figure 4-4 The Bouligand-type collagenous lamella in the carp, as compared to coelacanth scales. (a-c) The carp scale. (a) Fracture in the frozen carp scale reveals the layered twisted plywood structure of the inner layer. The arrows represent the orientations of each collagenous lamella, indicating the periodic alignments of the lamella; there are 5 orientations in each period (Layer 1 and Layer 6 are oriented at same direction). (b) There are no distinct fiber bundles formed in carp scale. Each lamella is directly comprised of collagen fibrils. (c) High magnification shows the characteristic band pattern of collagen fibrils and the sacrificial bonding connecting the fibrils, as indicated by the arrows. (d-f) The coelacanth scale. (d) The inner layer of coelacanth scale also has a laminated structure, but the arrangement of lamellae orientation is different. The adjacent two layers are almost perpendicular to each other (1&2; 3&4…) and the bi-layers form a twisted Bouligand pattern. (e) The collagen fibrils form distinct bundles circled by the dotted line and the space between bundles is filled by out-of-plane fibrils, as shown in the magnified inset. (f) A high magnification image shows the well-defined band (*d*-spacing) pattern of the collagen fibrils.

To further investigate the structural features of the collagenous lamellae at the nanoscale, the inner core of carp scales was characterized by transmission electron microscopy (TEM); the cross-sectional images are presented in Figure 4-5 (a-d). We found that there is a secondary collagenous array aligned with the thickness direction, which is very explicit and was barely reported in previous literature. Figure 4-5 (a) shows three adjacent collagenous lamellae of carp scale. Numerous wire-like structures with bifurcations are embedded in the cross-sectional view of lamellae and one of them is marked with a dotted line. The close-up view (Figure 4-5 b-d) shows that these lines are also collagen fibrils, with clear evidence of banded pattern revealed in Figure

4-5 (d). In these cross-sectional images, these collagen fibrils are completely isolated from each other and interspersed in the lamella fibrils (Figure 4-5c,d); they are not as grouped as those in the coelacanth scale (Figure 4-5f,g). One should keep in mind that the TEM image is a 2D projection of a 3D structure, which means each individual vertical fibril shown in Figure 4-5 (a-d) represents an entire plane of one-layer well-aligned fibrils that are normal to the observer's view, forming a "sheet-like" structure which is illustrated in the schematic drawing in Figure 4-5 (e). The diameter of such vertical fibrils in carp scale, which is denoted as d_2 in Figure 4-5 (d), is about 20 to 40 nm, as measured by normal cross-sectional TEM images, and is much smaller than the diameter of lamella fibrils, d_1 (~ 100 nm). In comparison, the interbundle fibrils in the coelacanth is much more bountiful in coelacanth scale (Figure 4-5f,g), and their diameter is about as same as the fibrils in fiber bundles. Except in the family of Cyprinidae (carp, golden fish, etc.) and Sarcopterygii (coelacanth and lungfish), all other elasmoid scales lack of this structural characteristic.

Figure 4-5 The secondary fibrous frame in the carp and coelacanth scales. (a-d) Transmission electron micrographs (TEMs) of carp scale with different magnifications. The cross-section of three neighboring layers indicates there are a few very thin vertical fibrils going through the thickness direction. One of them is marked with dot line. (b) Higher magnification image of the junction between two layers. (c) The close-up view of the cross-section reveals the delamination of the vertical fibril and that the collagen fibrils which comprise the lamella are tightly packed and squeezed into a polygonal shape. (d) The high magnification image shows the thin vertical fibril is collagen, as indicated by the arrow. The diameter of the lamella fibril and vertical fibril is denoted as d_1 and d_2, respectively. (e) Schematic illustration of the structure of the vertical fibrils interspersed in the lamellae. (f,g) TEM of a coelacanth scale. The space between the fiber bundles (FBs) are filled with abundant interbundle fibrils (IBFs) which forms a well-defined matrix to hold the Bouligand-type lamella. The inset in (e) shows that the packing of the fibrils in the fiber bundle is not as tight as that in carp scales and their cross-sections remain round shape.

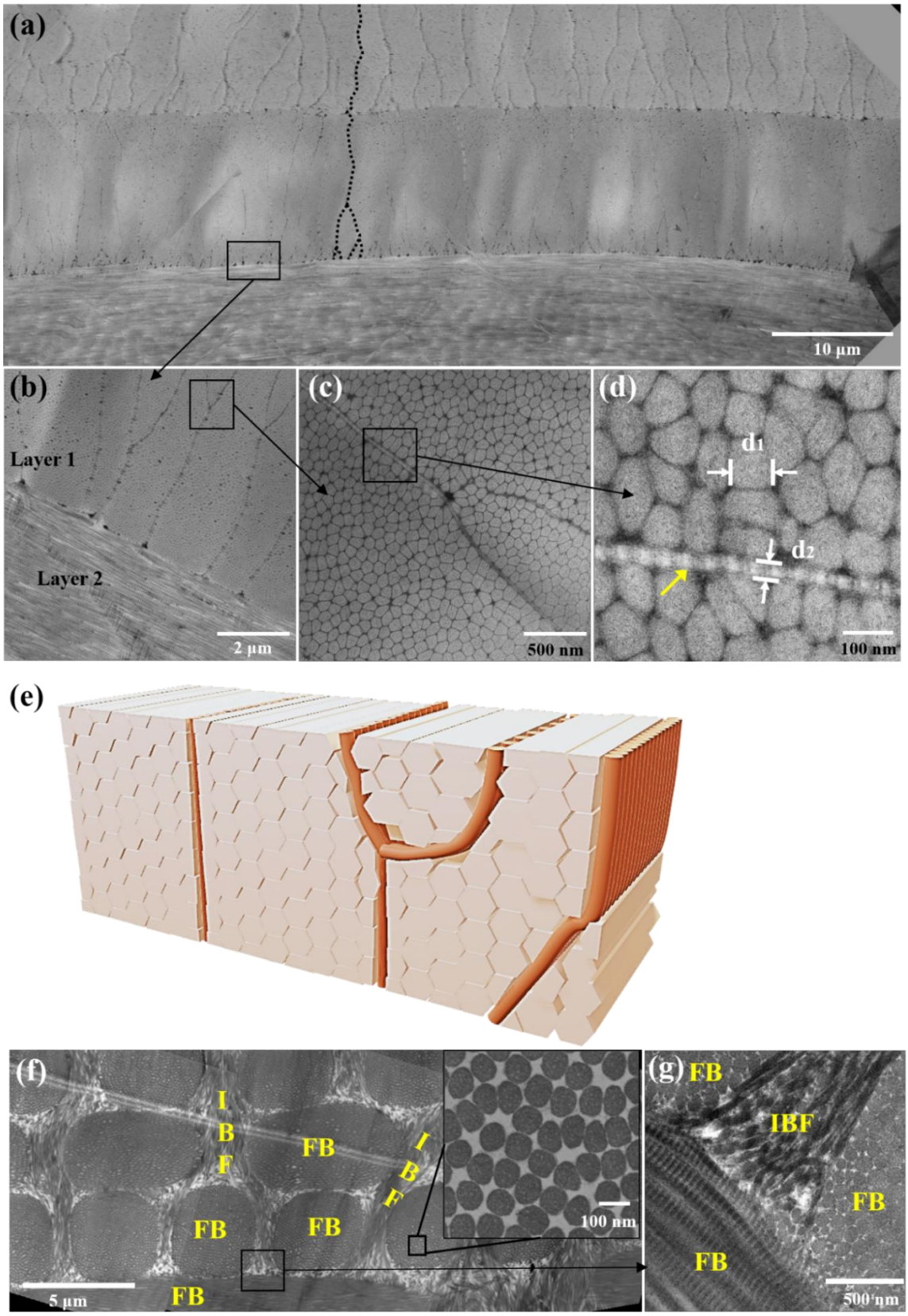
(a)
10 µm
(b)
Layer 1
Layer 2
2 µm
(c)
500 nm
(d)
d1
d2
100 nm
(e)
(f)
I
B
F
FB
I
B
F
FB
FB
FB
100 nm
5 µm
(g)
FB
IBF
FB
FB
500 nm

4.3.2 Tensile behavior of carp scale

Uniaxial tensile tests were performed on the carp scales that were extracted from mid-lateral region. A representative tensile stress-strain curve is presented in Figure 4-6 (a) and the inset indicates that this dog-bone shaped specimen is cut along the transverse direction. The longitudinal specimens were cut along the direction perpendicular to it. The video recording of the deformation of this specimen is provided in the Supplementary Information; several screenshots at ε_t = 0, 0.06, 0.11, 0.20, 0.22, 0.25, 0.27, 0.34 and 0.43 are shown in Figure 4-6 (b-j), respectively. In the elastic region, the scale is deformed uniformly, as shown in Figure 4-6 (b-d). At ε_t = 0.20, the external layer starts to crack, as circled in Figure 4-6 (e); after that point, the load is entirely taken by the collagenous inner core. At ε_t = 0.22, shown in Figure 4-6 (f), the stress reaches the maximum and the external layer starts to separate from the fully stretched collagenous lamellae. Right before the significant load drop, at ε_t = 0.25, the external layer is almost peeled off from the collagen layer, as indicated by the dotted line in Figure 4-6 (g). Beyond this point, although the collagen fibrils are still being stretched, as shown in Figure 4-6 (h-j), the engineering stress is almost 0, indicating that the lamellae are completely separated, and that the material is already failed.

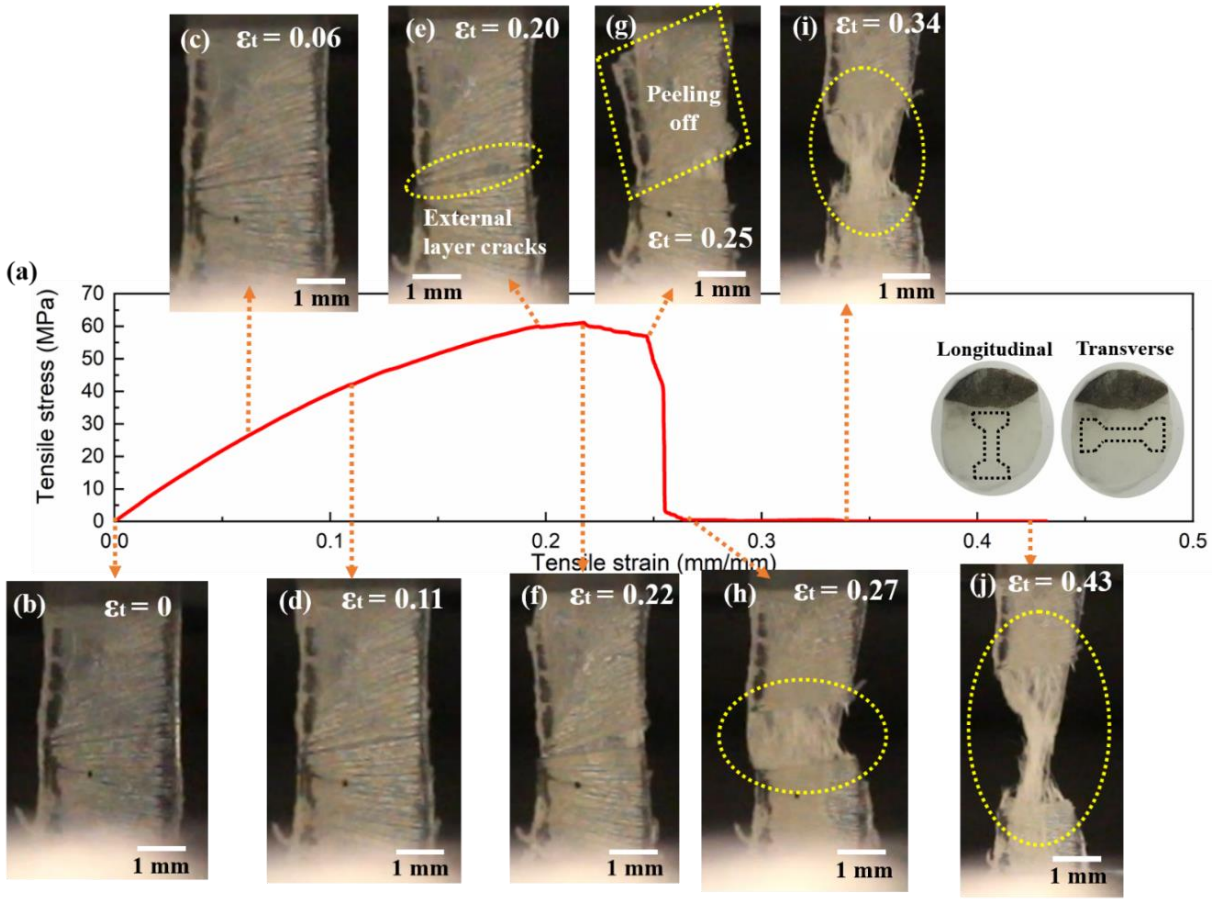

Figure 4-6 A representative uniaxial tensile stress-strain curve of carp scales with images at different tissue strains (ε_t). (a)The tensile stress-strain curve of a dog-bone shaped specimen cut along the transverse direction. The orientations of tensile testing specimens are indicated in the inset. (b-d) Tensile specimen is being stretched in the elastic region. **(**e) The external layer starts to crack. (f) The crack grows, and the external layer starts separation from the inner collagen layer. (g) The mineral layer peels off from the scale. (h-j) The tissue has already failed. Some collagen fibrils are still being stretched although the load has dropped to almost zero.

Figure 4-7 shows the seven stress strain curves obtained from each of four conditions: whole scales on longitudinal and transverse directions, and the collagen layers on these two directions. The collagen layer specimens were prepared by removing the external layer through mechanical polishing. The strength in longitudinal direction is slightly higher than the transverse one, notwithstanding the variation of longitudinal samples which is larger. The tensile results,

including Young's modulus, ultimate tensile stress, ultimate tensile strain and total energy dissipation, are listed in Table 4-1. Two conclusions can be obtained:

a) Regardless of whole scale or collagen layer only, except the ultimate tensile strain, all the Young's modulus, yield stress, and tensile stressare slightly higher in the longitudinal than transverse direction, indicating a modest anisotropic tensile behavior for the carp scale. Similar anisotropy is also observed in arapaima scales with more significant difference between orientations[56]. Striped bass also exhibits in-plane anisotropic tensile behavior but the trend is just opposite[75]; the strength in the transverse direction is higher and the variation between specimens also larger than in the longitudinal direction[75]. In comparison, the tensile behavior of the coelacanth scales is much more isotropic, due to their double twisted Bouligand pattern[149].

b) Since the superficial mineral layer in the carp scale is extremely thin and the mineral content is low, there is almost no difference between the tensile properties of the whole scale and collagen layer. In other elasmoid scales that possess well-defined mineral layer, such as coelacanth[149], arapaima[56], even striped bass[75], the collagen layer is stronger than the whole scale.

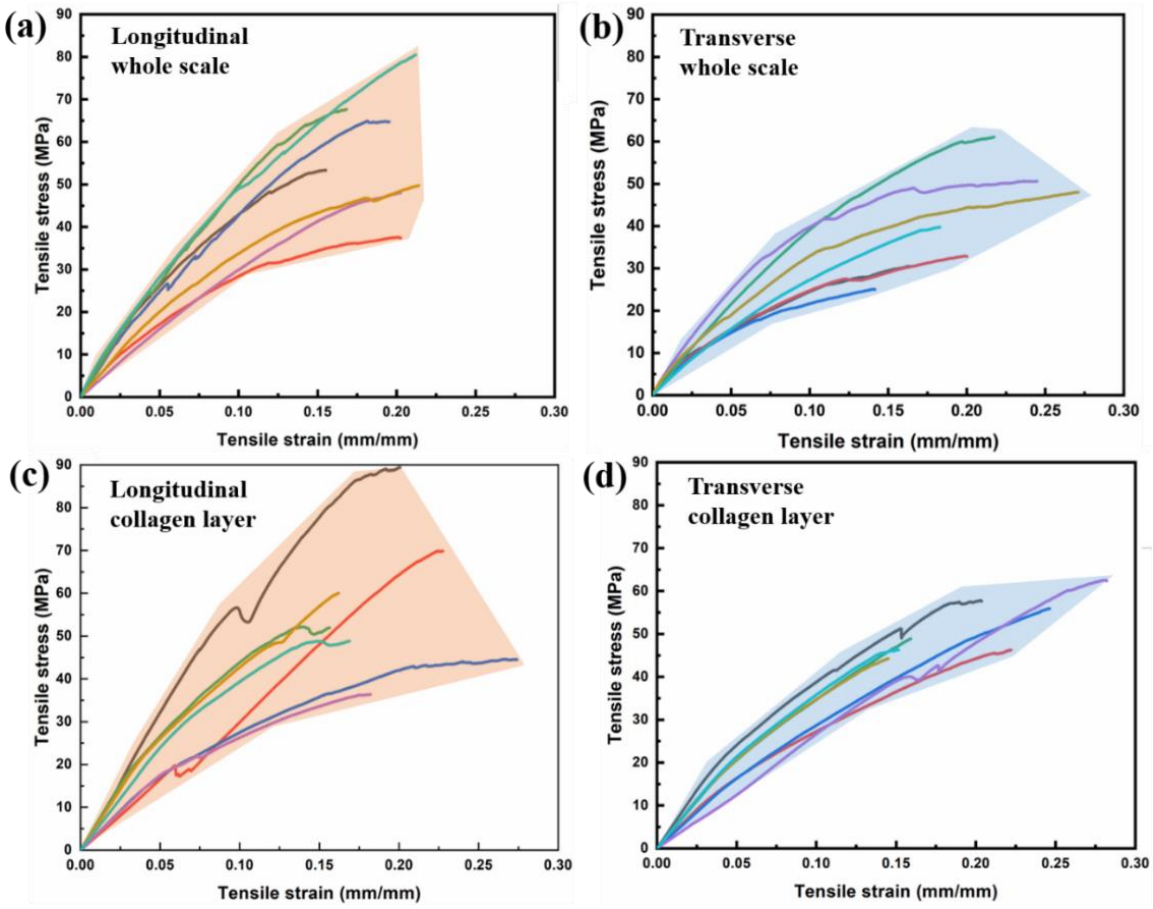

Figure 4-7 Tensile behavior of carp scales in different orientations and conditions. (a,b) The uniaxial engineering stress-strain curves of whole scales (mineralized external layer + inner collagen layer) along the longitudinal and transverse directions, respectively. (c,d) The stress-strain curves of collagen layers (the mineralized external layer was mechanically removed) along the longitudinal and transverse directions, respectively.

Table 4-1 Uniaxial tensile test results in both longitudinal and transverse directions for the whole carp scale and for the collagen layer only.

Carp scale	Whole scale		Collagen layer	
	Longitudinal	Transverse	Longitudinal	Transverse
Young's Modulus (MPa)	521.5 ± 125	463.5 ± 92.3	526.0 ± 126.1	406.4 ± 95.5
Ultimate tensile stress (MPa)	57.4 ± 14.5	41.4 ± 12.8	57.3 ± 17.8	51.7 ± 7.00
Ultimate tensile strain (mm/mm)	0.193 ± 0.023	0.206 ± 0.047	0.196 ± 0.043	0.201 ± 0.005
Energy dissipation (MJ/m^3)	6.79 ± 1.75	5.83 ± 2.90	6.8 ± 2.31	6.22 ± 2.23

SEM images of the fracture surface after tensile failure of the carp scales, presented in Figure 4-8, show typical ductile tearing of the collagen. Since the external layer is vulnerable to peeling off from the collagen lamellae, there is no remaining external layer on the fracture surface (Figure 4-8f). Numerous straight fiber lamellae are revealed around the break region, which are due to the failure of the "sheet-like" secondary network enabling the collagenous lamella to separate. The fracture surface of relaxed broken fibers and fibrils after tensile failure (Figure 4-8e) indicates their stretching during extension of the bulk specimen. In the region adjacent to the fracture, other mechanisms[56,7756,77] can be identified[56,77], including fiber twisting, delamination, and bridging between fibrils; these are shown in Figure 4-8 (a,b,d,h). The separation between the lamellae is shown in Figure 4-8c, together with their delamination due to the failure of the perpendicular sheets. Further evidence of inter-lamellar separation can be seen in Figure 4-8g in a region behind the fracture surface; groups of dotted lines in this image delineate the orientations of four adjacent lamellae. In general, these surfaces reveal that the lamellae fibrils are significantly stretched and delaminated when inter-lamellar separation occurs.

.

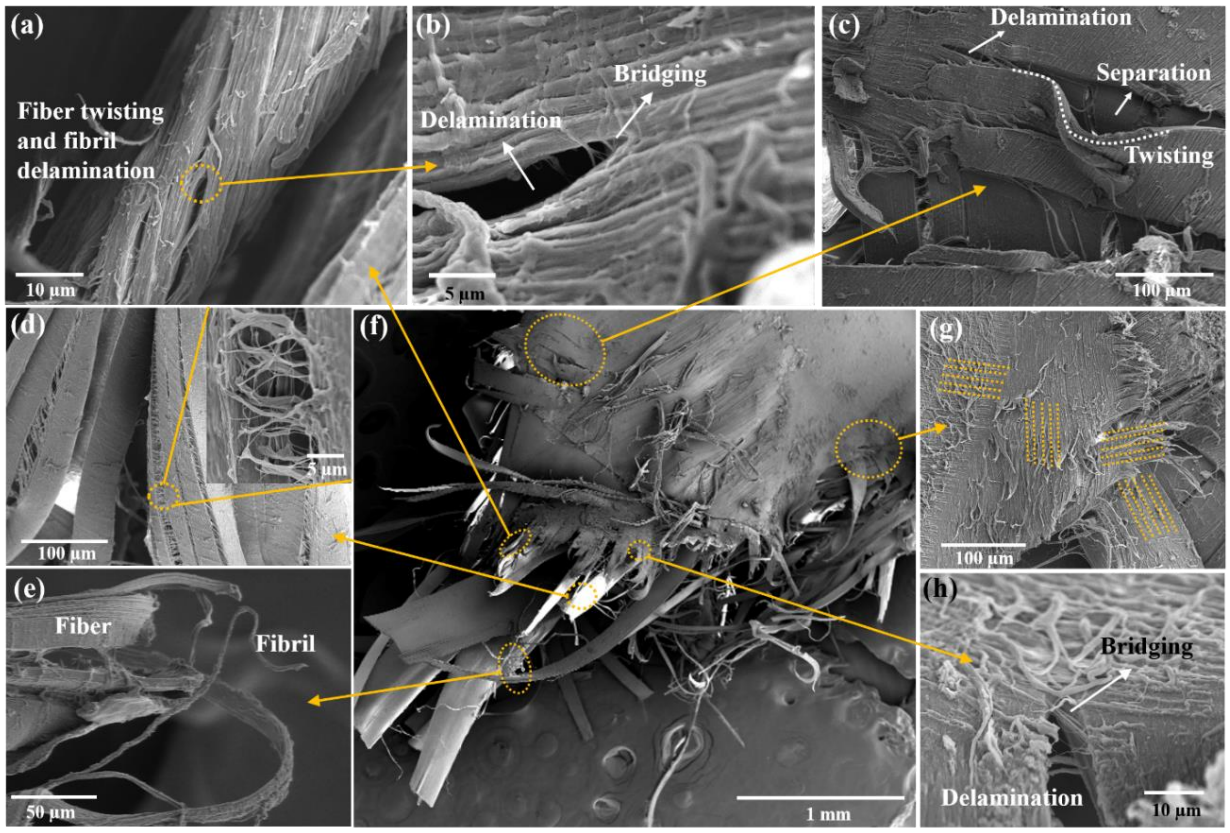

Figure 4-8 Fracture surfaces after tensile failure of the carp scale. (a-h) SEM images of a fractured tensile specimen in different regions reveals multiple failure mechanisms. (a) The collagen fibers become twisted and start to delaminate. (b) A close-up view of the delaminated fibrils shows crack bridging near the tip of the delamination. (c) Delamination occurring in the same lamella with layer separation between two adjacent lamellae; the collagen fiber in the top lamella becoming twisted after separation. (d) The delamination and fibrillar bridging between collagen fibers. (e) The fracture collagen fibers and fibrils. (f) An overall view of a fractured tensile specimen. (g) The four sets of dot lines indicate the orientations of four neighboring lamellae. The irregular fibrous surface reveals the ductile separation between these layers as the tissue was being deformed. (h) Fibrillar delamination and crack bridging in a single collagen lamella.

4.3.3 *In-situ* SAXS analysis of adaptive mechanisms

In total, toughening by adaptive structural reorientation, where the majority of the fibers or fibrils rotate in order to carry more of the load, is not uncommon in collagenous materials; notable examples are in arapaima fish scales[56] and particularly in skin[4]. Due to the periodicity of the molecular assembly in type I collagen and the highly ordered lamellar structure in the plywood tissue, in situ small angle x-ray scattering (SAXS) is a powerful tool to precisely characterize such deformation and movement of collagenous lamellae under load, having been successfully applied for such behavior in the scales of arapaima[77] and coelacanth[149] fish. Figure 4-9 (a) shows the experimental set-up that we used. Dog-bone shaped tensile specimens are were cut from the carp scales in both longitudinal (shown in figure) and transverse (not shown) directions, similar to the regular tensile tests described above. During the mechanical testing, a high flux of synchrotron x-rays is focused on the tensile specimen and scattered by the collagenous lamellae, generating a diffraction pattern composed of several concentric arcs on the screen, shown in Figure 4-9 (b). In each set of concentric arcs, the arc closest to the beam center (the first-order arc) represents the distance q from the beam center which has a reciprocal relationship with the d-spacing of the collagen fibrils, whereas the rest of the concentric arcs are higher order arcs, corresponding to the harmonics of the d-period. The azimuthal angle of each set of arcs, referred as Ψ, indicates one distinct orientation of the collagen fibrils in the scale, as illustrated in the inset of in Figure 4-9 (b). TheWith uniaxial tensile loading was applied along the $\Psi = 0°$. direction, Therefore, the change of in the value of q for all sets of the first-order arcs at different tissue strains can quantify, respectively, the rotation of the collagenous lamellae and the deformation of strain in the collagen fibrils in real time during uniaxial tensile extension.

Figure 4-9 (c) presents the real time diffraction patterns of a carp scale specimen cut from longitudinal direction for five stages during tensile deformation, at the tissue strains ε_t equal to 0, 0.06, 0.10, 0.14 and 0.18. The close-up view of the first-order Debye ring coupled with the real-time pictures at the initial state ($\varepsilon_t = 0$) and fully stressed state ($\varepsilon_t = 0.18$) are provided in the insets. When the scale is fully relaxed, the diffraction pattern is composed of 5 distinct sets of arcs equally distributed along the Debye ring, indicating there are 5 preferential lamellae orientations in the carp scale. This corresponds to the rotating angle in this single twisted Bouligand structure is about ~36˚: (i.e., $5 \times 36^{\circ} = 180^{\circ}$). As the applied tensile load increases, the diffraction pattern evolves accordingly. When the tensile stress reaches its maximum at $\varepsilon_t = 0.18$, the specimen is fully stretched, and the diffraction pattern turns into a 'hexagon-like' shape, indicating the dramatic structural evolution of the lamellae inner layer involving anisotropic strains.

Figure 4-9 *In situ* small-angle x-ray scattering (SAXS) patterns of carp scales taken in real time during a uniaxial tensile test. (a) Experimental set-up. Tensile specimens are extracted from the overlapped region of the scales along both longitudinal and transverse directions and the mineral layer is removed mechanically. The prepared specimen is exposed to the synchrotron x-rays in the beamline at the Advanced Light Source during *in situ* uniaxial tensile tests, with the scattering patterns recorded as a function of the tissue strain in real time. (b) A pattern of a fully relaxed tissue shows the several sets of concentric arcs, each of them caused by the diffraction of collagen fibrils well aligned in certain directions, which is the lamella orientation in the fish scale. The loading direction is at the azimuthal angle (Ψ) equals to 0°, as we defined. (c) *In situ* SAXS patterns at five different tissue strain states (ε_t = 0, 0.06, 0.10, 0.14, and 0.18) in the tensile test of a longitudinal sample. The insets in the patterns of fully relaxed state (ε_t = 0) and fully stressed state (ε_t = 0.18) are the close-up views of first several Debye rings with the real-time images of the tissue. The diffraction pattern changed from a round circle with 6 equal sectors to a hexagon-like shape, revealing the inhomogeneous deformation of the fibrils in different orientations.

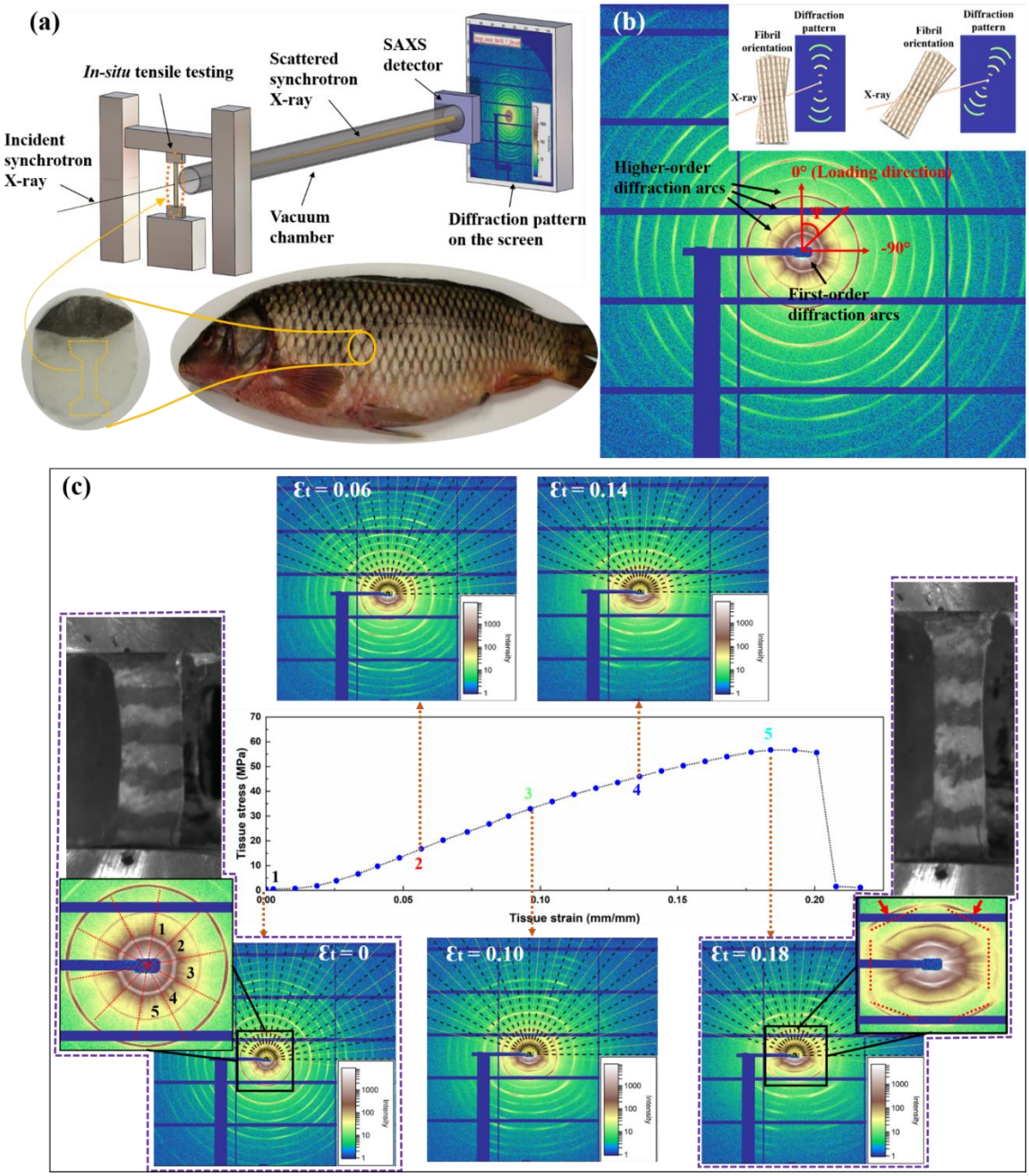
(a)
In-situ tensile testing
Scattered synchrotron X-ray
SAXS detector
Incident synchrotron X-ray
Vacuum chamber
Diffraction pattern on the screen
(b)
Fibril orientation
Diffraction pattern
X-ray
Higher-order diffraction arcs
0° (Loading direction)
90°
-90°
First-order diffraction arcs
(c)
εt = 0.06
εt = 0.14
εt = 0
εt = 0.10
εt = 0.18
Tissue stress (MPa)
Tissue strain (mm/mm)
Intensity

4.3.3.1 Quantification of the lamellae rotation

The integrated intensity distribution along the Debye ring can quantify the orientations of the lamellae due to the one-to-one correspondence between the intensity peak and the fibril orientation. Thus, to quantitatively analyze the rotation of the collagenous lamellae during the elongation of the scale, the integrated diffraction intensity as a function of Ψ on the first-order Debye ring are plotted in Figure 4-10 (a) at six successive stages of the deformation, from $\varepsilon_t = 0$ to the last stage where $\varepsilon_t = 0.22$ prior to the tissue completely breaking. For comparison, a similar plot for coelacanth scales is presented in Figure 4-10 (b).

In the unstressed state, due to its single-twisted 'Bouligand-type' structure, the carp scale shows the five peaks, equally separated with similar height, indicating that the arrangement of collagen fibrils in successive lamellae forms a highly ordered twist with a rotation angle of 36° and that the number of the collagen fibrils in each orientation is almost about the same. In contrast, the coelacanth scale shows many more peaks with different heights which are distributed with unequal separation along the azimuthal angle, suggesting that the lamellae thickness is not evenly distributed. Due to this double-twisted Bouligand arrangement in the coelacanth scale, the collagenous lamellae have many more orientations.

As the applied load is increased, the evolving location and height of peaks reveals the rotation of the lamellae; however, the nature of the rotation is quite different in these two fish scales. In the coelacanth scale, the lamellar rotation is much more uniform with two primary rotation mechanisms: lamellae with orientations near the tensile direction gradually rotate towards the loading direction, while the lamellae oriented closer to the perpendicular direction gradually rotate towards the horizontal direction, away from the loading direction. In contrast, the lamellar rotation in carp scale is much more complex. The lamellae oriented at $\Psi = -78^{\circ}$ and $\Psi = 61^{\circ}$, which

are far from the loading direction, rotate away with increased tissue strain ε_t, as indicated by the arrows in Fig. 8a. The peak at $\Psi = 27^\circ$ also moves away from the loading direction with reduced intensity, indicated by the black triangle, indicating that the lamellae oriented at $\Psi = 27^\circ$ also rotate away, but the number of fibrils keeps decreasing. The peak at $\Psi = -46^\circ$ initially moves away with a similar reduction in intensity, but then splits significantly (indicated by the circles in Fig. 8a) implying that fewer fibrils are rotating away from the tensile direction; the lamellae at $\Psi = -46^\circ$ are notably delaminated, which presumably is a result of the failure of the weak transverse "sheet-like" structure. The peak at $\Psi = 27^\circ$ represents the lamellae oriented closest to the loading direction. As the tissue strain εt increases, this peak also splits into several broad ones (as the stars denote), which indicates that some fibrils from other orientations have rotated into this range (approximately from $\Psi = -30^\circ$ to $\Psi = 10^\circ$); this also implies delamination of the lamellae. Compared with the initial state when $\varepsilon_t = 0$, after the scale is completely broken at $\varepsilon_t = 0.22$, there are more peaks distributed along the azimuthal angle, indicating that the significant lamellar delamination is not recoverable, i.e., the scale has experienced significant plastic deformation and the collagenous lamellae are no longer highly ordered.

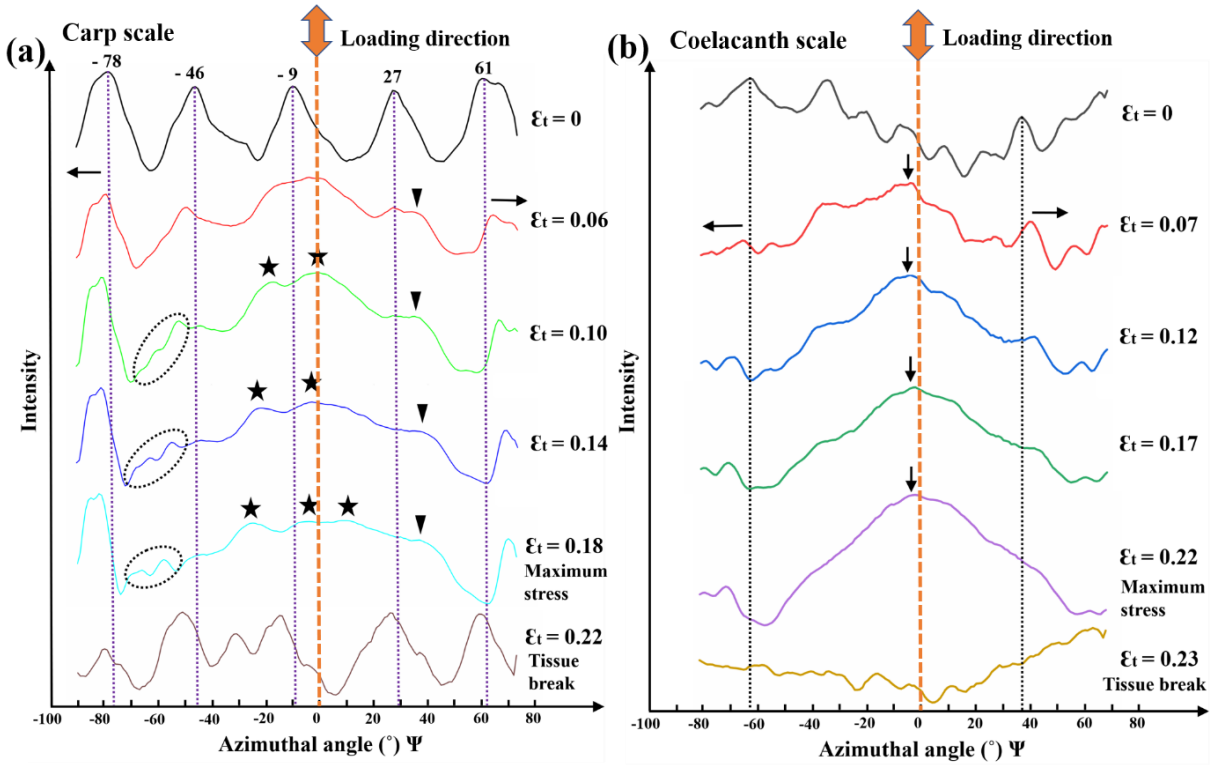

Figure 4-10 Quantification of the rotation of collagenous lamellae for the carp scale under tensile load in comparison with that for the coelacanth scale. (a) The curves of integrated diffraction intensity *vs.* azimuthal angle (Ψ) for the carp scale at different deformation states (ε_t = 0, 0.06, 0.10, 0.14, 0.18and 0.22). (b) Corresponding curves of integrated diffraction intensity *vs.* azimuthal angle (Ψ) for the coelacanth scale at different deformation states (ε_t = 0, 0.07, 0.12, 0.17, 0.22 and 0.13).

4.3.3.2 Quantification of the deformation of lamellae of collagen fibrils

In order to quantify the deformation of the collagen fibrils with different orientations, the diffraction pattern was evenly divided into 17 sectors with a span of 10° from Ψ = - 90° to Ψ = 70° and the averaged r of each sector was calculated. Based on the reciprocal relationship between r and the characteristic d-spacing, the d-spacing of the collagen fibrils in each sector was obtained. For the successive five stages during the tensile deformation, the change in d-spacing in each sector was normalized by its original length to define the collagen fibril strain ε_f^{Ψ} , plotted as a function of the azimuthal angle in Figure 4-11 (a). For comparison, a similar plot for the coelacanth scale is presented in Figure 4-11 (b)[149].

In the range in which the lamellae rotate towards the loading direction, the collagen fibrils with orientations between $\Psi = -40°$ and $\Psi = 40°$ in the carp scale are deformed in tension. This is the same for the deformation of the lamellae fibrils in the coelacanth scale. However, instead of reaching the global maximum tensile strain in the fibrils along the tensile direction as in coelacanth scale, the lamellae fibrils in carp scale reach two local strain maxima strains at $\Psi = -20°$ and $\Psi = 10°$. It causes that at the fully stressed state, which is shown in the inset of to Figure 4-9 (c) where $\varepsilon_t = 0.18$, there are two flat diffraction arcs on both sides of the loading direction ($\Psi = 0°$), as indicated by the red arrows, making the diffraction pattern a hexagon-like shape. The maximum tensile fibril strain, when the tissue is fully stretched, is about 0.1; this is considerably lower than the global tissue strain, 0.18, indicating that significant fibrillar sliding has taken place. The same mechanism was also identified in both coelacanth and arapaima scales, but the fibril extensibility of carp scale is higher than that of the arapaima scale (maximum fibril strain was $\varepsilon_f \sim 0.05$)[77], but lower than the coelacanth's scale , where the maximum fibril strain (maximum was $\varepsilon_f \sim 0.12$)[149]. For the lamellae oriented from $\Psi = \pm 40°$ to the direction perpendicular to the tensile axis, the fibrils in the carp scale are deformed in compression, and the strain is not uniform. The maximum compressive strain is located at $\Psi = \pm 60°$ and the for reasons behind it that are still needs exploration unclear. More interestingly, we found a transitional range where the fibril deformation changes from tension to compression, i.e., at initial fibril orientation from $\Psi = -30°$ to $\Psi = -40°$ and from $\Psi = 40°$ to $\Psi = 50°$. This indicates that exclusive deformation by shear takes place on some fibrils within these two ranges. When the tissue is stretched more than $\varepsilon_t = 0.10$, there is no diffraction peak detected beyond $\Psi = 50°$, implying that at this strain, although the bulk material can still carry load and undergoes deformation, the fibrils aligned closer to perpendicular to the loading direction are delaminated and not sufficiently well-aligned to form well-defined diffraction

peaks. The fibril strains at $\varepsilon_t = 0.22$, when the tissue completely breaks, are not recovered to the original fibril strains when $\varepsilon_t = 0$, indicating that plastic tensile and compressive deformation occur when the scale is being stretched to fracture.

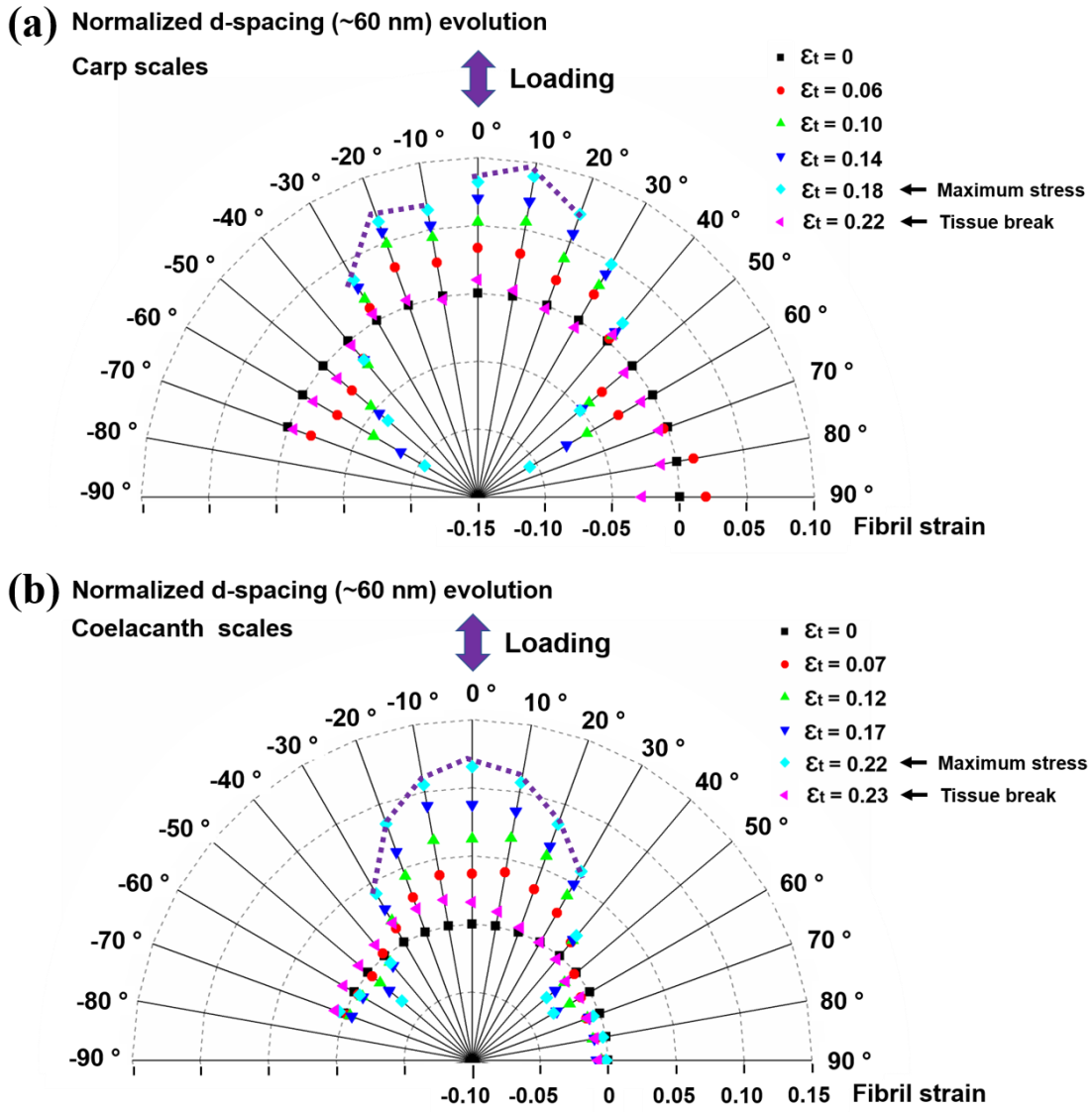

Figure 4-11 Quantification of the deformation of collagen fibrils under tensile load in carp scale as compared to coelacanth scale. (a) Plots of fibril strain as a function of the azimuthal angle Ψ for the carp scale at different tissue strains (ε_t = 0, 0.06, 0.10, 0.14, 0.18 and 0.22). (b) Corresponding plots of fibril strain as a function of the azimuthal angle for the coelacanth scale at different tissue strains (ε_t = 0, 0.07, 0.12, 0.17, 0.22 and 0.13). For each scale, the fibril strain is calculated from the change in *d*-spacing along the collagen fibril during the tensile test and normalized by the *d*-spacing of the fibrils in their original (unloaded) state.

These results presented in Figure 4-10 and Figure 4-11 can be summarized in the schematic drawing of Figure 4-12, which shows the sequence of mechanisms experienced by the collagenous lamellae in the carp scale based on both lamellar reorientation (quantified in Figure 4-10a) and deformation (Figure 4-11a). The first stage during tensile loading is the cracking and peeling off of the highly mineralized external layer (Figure 4-12a). The lamellae close to the loading axis ($-40° < \Psi < 40°$) are subjected to tensile strains, resulting in the increase in length with *d*-spacing increases ($d > d_0$, Figure 4-12b,c) and the reorientation towards the loading direction caused by interfibrillar shear (Figure 4-12c). There is some difference in the fibrillar strain distribution between the carp and coelacanth scale, shown in Figure 4-11 (a,b). Since the threading fibrils in carp scale are not as profuse as the ones in coelacanth scale, the lamellae are more vulnerable to failure by delamination as illustrated in Figure 4-12 (d). This delamination is characterized by SEM in Figure 4-8 (b,c). Interestingly, a transitional range exists where the fibril deformation changes from tension to compression, *i.e.*, the fibrils initially oriented from- 40° to -30° and from 40° to 50° ($d<d_0$, Figure 4-12d). This indicates that deformation takes place exclusively by shear on some fibrils within these two ranges. The fibril strained at $\varepsilon_t = 0.22$, when the tissue completely breaks, are not recovered to the original value ($\varepsilon_t = 0$), indicating that plastic tensile and compressive deformation are retained when the scale is being stretched to fracture.

By combining all the deformation mechanisms discussed above, the *Bouligand*-type lamellar inner base of the carp scale adapts to the applied load by lamellar rotation, fibrillar deformation and interlayer separation, as illustrated in Figure 4-12 (e), thereby being capable of dissipating stored elastic energy effectively and conferring to the carp scale its excellent toughness.

Figure 4-12 A schematic showing the mechanisms for the adaptive deformation of the carp scale under tensile load. The purple arrows indicate the loading direction. (a) The mineral layer cracks and separates from collagenous base. (b) The lamellae along the tensile direction are stretched ($d > d_0$) and finally break as the loading increases. (c) The interfibrillar sliding causes the lamellae rotate towards the loading direction (as the black arrow indicated) and the collagen fibrils are also stretched with increased d-spacing ($d > d_0$). (d) The lamellae initially oriented far from tensile axis are compressed ($d > d_0$) and rotate away (as the black arrow indicates). With further increase in loading, the lamellae fail by interfibrillar delamination. (e) The original collagenous lamellae form a highly ordered Bouligand-type structure with a rotation angle of 36°. (f) The overall deformed collagenous lamellae with applied tensile load. Combining all the adaptive mechanisms in (b-d) and the separation and shear between lamellae, the fibrous base confers the scale with significant deformability to adapt to the applied load.

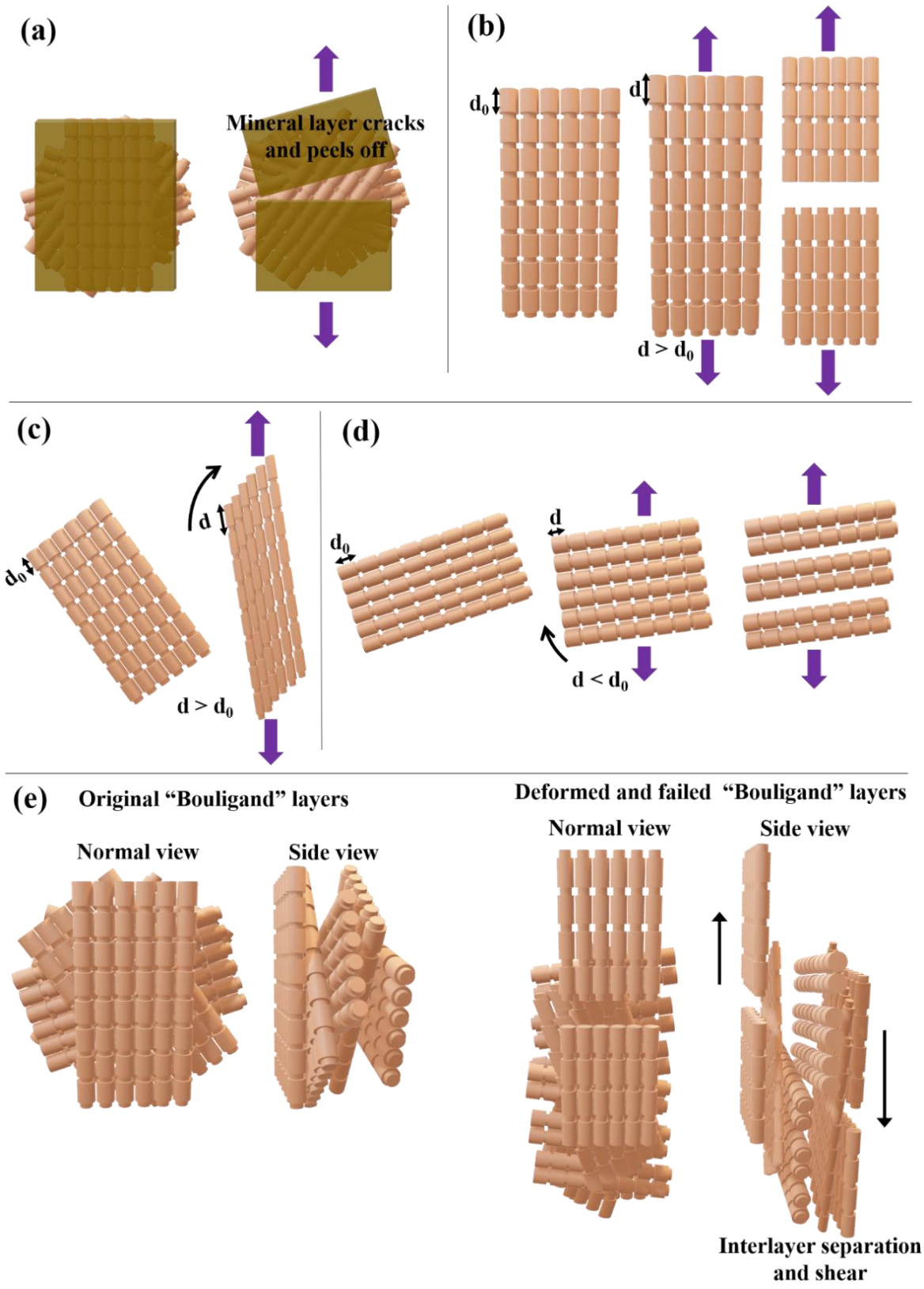
(a)
Mineral layer cracks and peels off
(b)
d_0
d
$d > d_0$
(c)
d_0
d
$d > d_0$
(d)
d_0
d
$d < d_0$
(e)
Original "Bouligand" layers
Normal view
Side view
Deformed and failed "Bouligand" layers
Normal view
Side view
Interlayer separation and shear

4.4 Summary

We have characterized the detailed structure of the modern elasmoid scales of the common carp and determined their mechanical properties. Using the synchrotron SAXS, the lamellar rotation and fibril deformation have been quantified in order to identify the salient toughening mechanisms. To improve our understanding of these prevailing mechanisms, we have further compared our results for the carp scale with those of the primitive elasmoid scales from the coelacanth fish. Based on this work, several conclusions on the prime structural components of this damage-tolerant natural material can be made:

- With respect to the structure of carp scales, the external portion is composed of highly mineralized woven fibrils covered by an extremely thin and discontinuous mineral layer.
- The inner core is comprised of highly ordered plywood-like tissue consisting of superimposed collagenous lamellae, successively rotating by 36°, forming a typical single-twisted *Bouligand* structure. Each lamella is made of thick tightly packed collagen fibrils with no evidence of the fiber bundles that are so prevalent in the primitive elasmoid scales of the coelacanth fish. The secondary 'threading' fibrils along the thickness direction, perpendicular to the lamellae, are less pronounced than that in coelacanth scales and are assumed to ensure the integrity of the scales by impeding the lamellae from separating when the scale is subjected to bending.
- The tensile behavior of the carp scale was found to be somewhat more anisotropic than the coelacanth scale, with the strength and toughness being both higher (by ~20%) in the longitudinal, compared to the transverse direction. A synergy of toughening mechanisms including external layer separation, inter-lamellae separation, fiber twisting and splitting, fibrillar delamination and bridging, and fibrillar reorientation, all act *in concert* to improve the damage tolerance of the scales.

- The lamellar fibrils in carp scale reach two local maxima strains at azimuthal angles of Ψ = -20° and Ψ = 10° to the tensile axis, instead of reaching a clear maximum fibrillar tensile strain in the tensile direction, as is the case for the coelacanth.
- With respect to adaptive structural reorientation within the carp scales under load, *in situ* SAXS measurements during mechanical straining of the scales demonstrate that the lamellae oriented closer to the tensile direction rotate towards it and the ones oriented far from the loading direction rotate away from it. This behavior has been previously observed for arapaima and coelacanth fish scales. Along with lamellar rotation, fibrils closer to the loading direction are stretched whereas those closer to perpendicular to the loading direction are deformed in compression. These deformation mechanisms operate together to render the carp scale an excellent dermal armor. They may well provide further inspiration for the design advanced synthetic structural materials with unprecedented toughness and penetration resistance.

Chapter 4, in part, is under peer review for publication with coauthors W. Yang, M. Lapeyriere, E. Schaible, R. O. Ritchie and M. A. Meyers. The dissertation author is the first author of this work.

CHAPTER 5: FRACTURE TOUGHNESS OF ARAPAIMA SCALES

5.1 Introduction

Hardness and strength are important material properties but only describe mechanical performance imperfectly. A fundamental parameter that bridges these two concepts is the fracture toughness, which is the ability of a material to resist the propagation of cracks and/or flaws when loaded[13]. This is especially true for structural materials where the toughness becomes the overriding property[150]. The same applies to biological materials that are subjected to extreme loads[151-156]. The dermal armor of fish is a splendid example where toughness is essential[69,76,147,148,157].

Arapaima gigas are a large Amazonian fish (weighing up to 150 kgf) living primarily in seasonal lakes infested with ferocious piranhas[78]. The fish is covered with elasmoid scales which are composed of a mineralized outer layer that provides penetration resistance through its hardness, and a more ductile inner collagenous lamellae layer, following a Bouligand-type pattern, that confers deformability to accommodate excessive deformation; the result is a tough scale with exceptional resistance to cracking from penetration by the teeth of predators. Figure 5-1 shows the structure of the arapaima scale[77]. The fish body of arapaima is fully covered by thick elasmoid scales (Figure 5-1a). Each scale has an elliptical geometry and they are overlapped to redistribute biting stress from predators, providing excellent protection while retaining great flexibility (Figure 5-1b). The outer layer is highly mineralized conferring the scale hardness and the inner layer is composed of laminated collagen fibrils to improve deformability (Figure 5-1c). The collagen fibrils in each lamella is arranged in parallel but the orientations of lamellae follow a helical pattern, which is also called ‘Bouligand’ structure (Figure 5-1d). The collagen fibril in arapaima scale is mineralized, containing hydroxyapatite interspersed in collagen molecules (Figure 5-1e). The

fibrils have characteristic diameters of ~100 nm and are organized in a quasi-hexagonal arrangement due to their tight packing, which comprise the lamellae, with a thickness of ~50 μm each. Although the structure of arapaima scales and their mechanical properties, notably hardness, modulus, strength, ductility and puncture resistance, have been established[56,77,131,136], their fracture toughness value, *i.e.*, the stress intensity or energy required to fracture them in the presence of a worst-case flaw, is still lacking quantitative analysis. Dastjerdi *et al*.[76] applied fracture mechanics measurements to estimate the toughness of elasmoid scales, specifically for the striped bass, and showed that these scales were among the toughest flexible biological materials. In this chapter, we report a new design for measuring a more realistic fracture toughness of the arapaima fish scale and confirm that it is among the toughest flexible biological materials. Our study may also bring inspiration for the process of the mechanical testing of other biological materials. We note here that there are two primary principal fracture-mechanics parameters which are used to measure the toughness, namely the linear-elastic 'crack-driving force', K_c, and corresponding nonlinear-elastic energy parameter, J_c. They can be related through the mode-I *J/K* equivalence relationship: $J_c = K^2_c/E'$, where $E' = E$ (Young's modulus) under plane-stress conditions and $E/(1 - \nu^2)$ in plane strain (ν is Poisson's ratio)[158]. However, because of the small size of the scales and their inherent plasticity, which tend to invalid a linear-elastic fracture-mechanics approach, our focus is on determining a nonlinear-elastic J_c fracture toughness which is a more appropriate methodology to evaluate the fracture resistance of these scales.

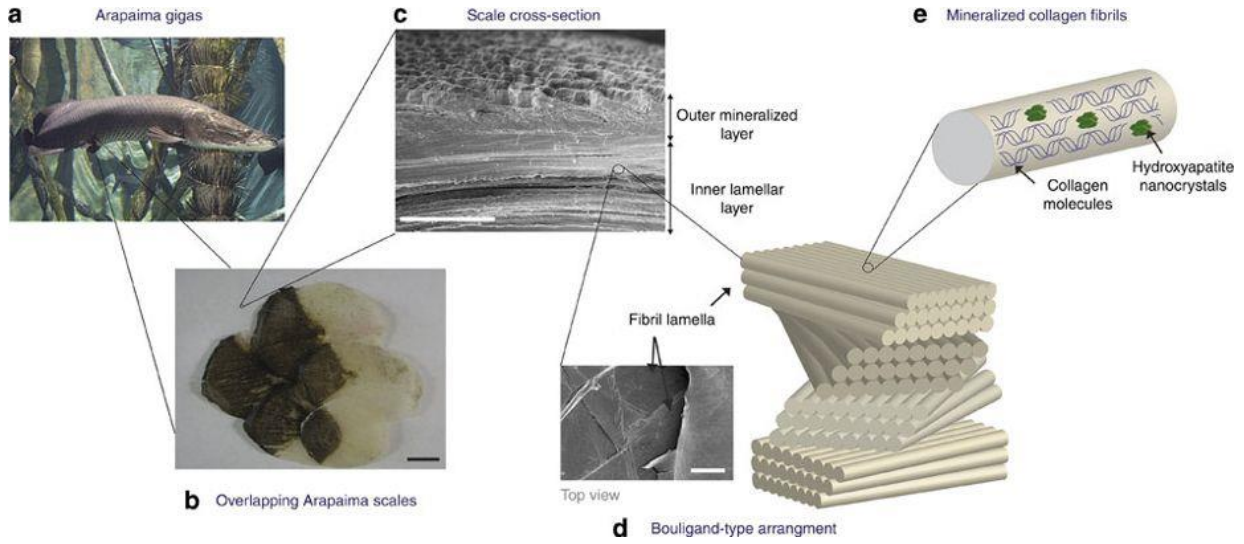

Figure 5-1 Hierarchical structure of arapaima scales[77]. (a) Arapaima is fully covered by elasmoid scales. (b) Each scale has an oval shape and they are overlapped to confer the flexibility (scale bar, 20 mm). (c) The outer surface is highly mineralized layer and the inner core is collagenous lamellae (scale bar, 0.5 mm). (d) The lamellae orientations follow a Bouligand-type (or twisted plywood) pattern (scale bar, 200 μm). (e) The mineralized collagen fibril is composed of collagen molecules hydroxyapatite nanocrystals.

The (mode-I) fracture toughness can be obtained by creating an artificial (worst-case) crack in a material and then loading it in tension. If the flaw resists further cracking, the material can be considered as tough. Despite the simplicity of this methodology, testing biological materials can be somewhat more problematic. As such, it was necessary to develop a new compact-tension testing fixture to evaluate the fracture toughness of the arapaima scales because of their specific geometry and related mechanical effects. Unlike that used by Dastjerdi *et al.*[76], our fixture was designed to not constrain the crack by enabling the two sides of the grips to rotate freely under increased loading but also to provide the bending plus tension loading characteristic of the natural fish scale's geometry. Figure 5-2 (a) shows the apparatus design; additional details as well as our methods of analysis are provided in Experimental Procedures below. Specifically, the testing of the scales presents two challenges: (i) the perforation of the scales to introduce the loading pins as well as the tears in scales during testing, and (ii) the scale is subjected to out-of-plane buckling

during the application of the external force, which causes combined mode-I (tensile) plus mode-III (anti-plane shear) loading of the crack. To avoid tearing at the pins during the test, the perforations on the scale to insert loading pins were replaced by an adaptor rigidly attached to the scales by two screws and having the ability to rotate freely upon loading, thus eliminating the need for constrained loading. To avoid mixed-mode loading, we employed two lateral plates to sandwich the sample in a manner that minimizes out-of-plane buckling. Both solutions are shown in Figure 5-2 (a,b).

There are two modes of loading which can cause damage to the fish scale:

a. Flexure with compression in the external surface and tension in the internal surface. It would be extremely difficult to prepare a toughness sample along thickness direction because the crack length has to be very small, a fraction of a millimeter, since the scale thickness is ~1.5 mm. In this geometry the crack propagation direction is perpendicular to the lamellae.

b. Tension loading of the scale with the crack propagation direction parallel to lamellae. This orientation simulates the damage produced by a tooth that penetrates through the scale and is pushed further in, creating a void that could be transformed into a crack if the toughness is not sufficient. This is the situation that we are addressing in the current loading configuration, similar to the one described Dastjerdi et al.[76].

Indeed, in our previous study[56], we determined the penetration effect on the arapaima fish scales and discovered that the Bouligand structure could develop similar toughening mechanisms to protect the scale against both penetration and tensile loads. Here, we aim to use a natural pre-cracked fish scale (mimicking the pre-damage created by predators) to illustrate how the damaged scales can still carry load and provide protection from predators. We show that the lamellae are powerful crack inhibitors because of their Bouligand arrangement.

5.2 Methods

Due to the thin-sheet like geometry of arapaima scale, the conventional compact-tension C(T) sample fracture toughness testing (ASTM E1820) is difficult to utilize. Instead, thin-sheet compact samples (modified 1T plan samples) were extracted from arapaima scales with the dimensions comparable to the size of the scale (Figure 5-2b). Since the thickness of these scales, which is on the order of 1 mm, is not uniform, measurement of the thickness, *B*, involved the average of taken at similar positions on each sample. The in-plane dimensions of the scales were between 50 and 120 mm; consequently, these dimensions followed the conventional 1T compact geometry provided in the ASTM standard,[18] specifically with $W \sim 50$ mm. To provide for a notch, a rough cut was firstly introduced along the longitudinal direction of the scale by a low speed diamond saw and then sharpened using sharp razor blade to a crack length-to-sample width ratio, a/W, of ~0.5. Four through-thickness holes were prepared using Dremel, with two on each side of the pre-notch, as indicated in Figure 5-2 (a,b), resulting a gauge length of 12.5 mm. The samples were tightened to the steel plates by screws which were connected to the Instron with pins to enable a free rotation. Testing was performed in displacement control on an Instron 3342 mechanical testing machine (Instron Corp. Norwood, MA, USA) applied to the transverse direction of the fish scales with a load cell of 500 N at a displacement rate of 0.06 mm/min. Before testing, the arapaima fish scale samples were stored in fresh water.

To fully quantify the crack-growth fracture toughness of the arapaima scales and to incorporate the important role of plasticity in generating the toughness, as noted above we used nonlinear-elastic fracture mechanics methods and performed measurements of the *J*-based fracture toughness, J_{max}, and the full J_R (Δa) R-curves, in accordance with ASTM Standard E1820. The *J*-

integral for sharply-notched test specimen can be determined in terms of the sample thickness, *B*, and uncracked ligament, *b*, ahead of the crack tip, *i.e.*, (*W* – *a*), from the following relationship:

$$J = \frac{\eta A_T}{Bb} \ ,$$

where A_T is the total area (elastic plus plastic) under the load *vs*. load-line displacement curve integrated from beginning (zero displacement) to a given displacement determined by a pertinent value of Δa), and η is the specimen geometry factor, given by $\eta = 2 + 0.522\ b/W$. This approach combines estimates of the contributions to the *J*-integral toughness from both elastic and plastic deformation, since separating them can be a more complicated issue for biological tissue.

Figure 5-4 (a) shows the resulting rising $J_R(\Delta a)$ curve toughness data for moist arapaima fish scales. Although these fracture toughness measurements were not in plane strain as they pertain to actual arapaima scales, *J*-field validity was assured as $b > 10\ J/\sigma_o$,[23] where σ_o (= 21.9 MPa) is the flow stress for the arapaima scales in the transverse direction,[19] perpendicular to the direction of crack propagation. Accordingly, the $J_R(\Delta a)$ curves in Figure 5-4 (a) can be regarded as an accurate representation of the nonlinear-elastic fracture toughness of these scales.

The *ex-situ* observation of the crack tip after testing were characterized in a FEI Quanta 250 scanning electron microscope (SEM; FEI, Hillsboro, OR). After the fracture test, the samples were first immersed in the 2.5% glutaraldehyde for 1 h to fix the structure and then dehydrated with an ascending series of ethanols (30, 50, 70, 90, 95 and 100 vol.% twice), before being dried using an automatic critical point dryer (Tousimis AutoSamdri 815A, MD). All dried samples were then sputter coated with iridium using an Emitech K575X sputter coater (Quorum Technologies Ltd.) before observation.

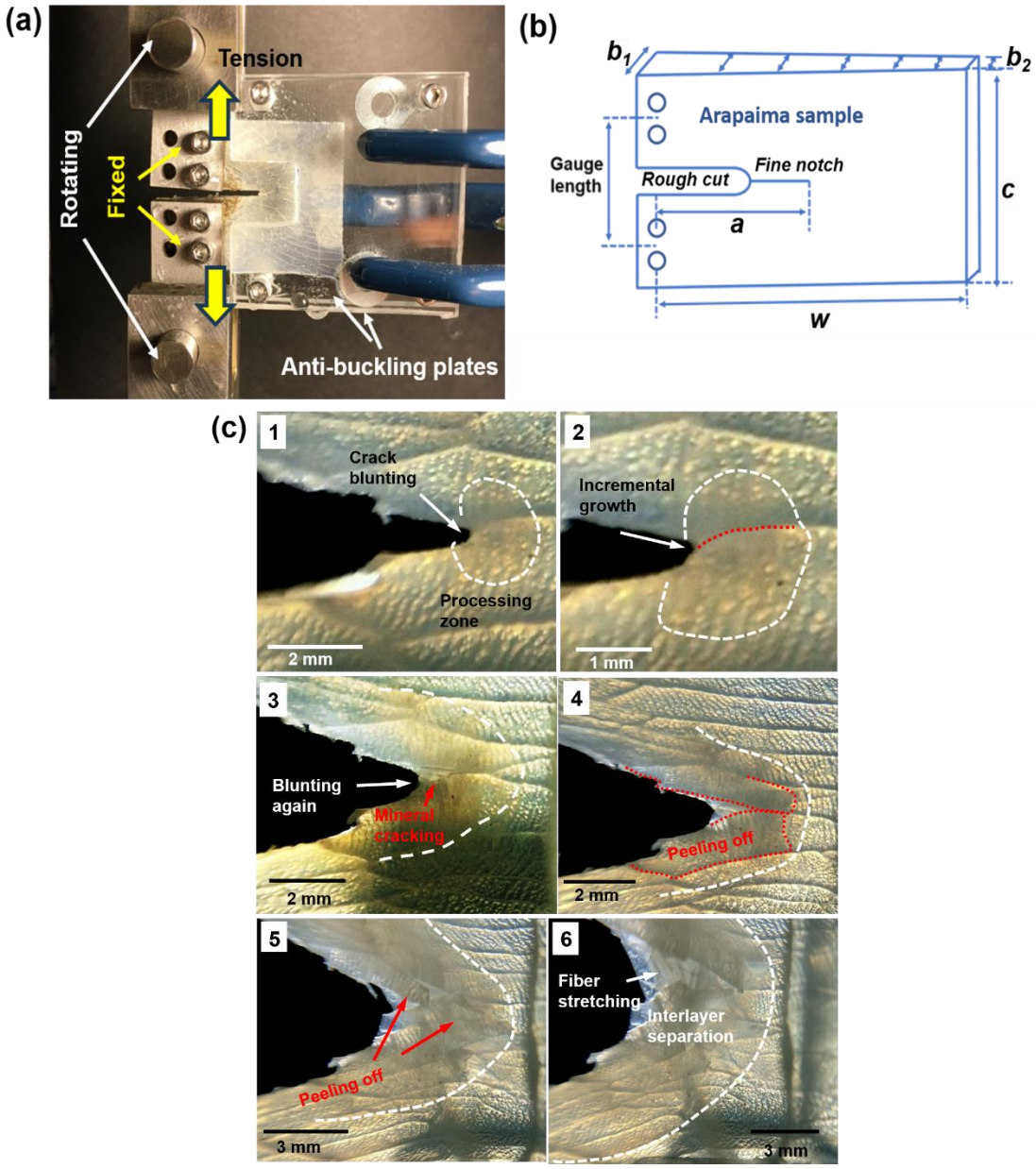

Figure 5-2 Experimental set-up and crack-tip behavior. (a) Fracture toughness measurement set-up showing platens with rotation pins attached to sample ends. The sample is attached to four steel plates by screws; the latter are connected by a loading pin attachement to the tensile testing machine, allowing for the free rotation as the arrow indicates. A pair of anti-buckling guide plates prevents the sample from bending out-of-plane during the test. (b) Sample design and dimensions. The white dashed line shows the process zone (see text). (c) Six successive views stages of crack-tip behavior during the fracture toughness test.

5.3 Results

Using this technique, the sequence of deformation, imaged using optical microscopy at the crack tip in a moist arapaima scale, is shown in Figure 5-2 (c). The white dashed line shows the boundary of the process zone, which was estimated by the change in coloration of the mineral layer, produced by the separation from the collagenous lamellae when the latter undergo substantial non-elastic deformation. As Dastjerdi and Barthelat[76] also remarked, the mineral undergoes whitening when this occurs. This region has a dimension of ~1-4 mm and expands with the evolution of loading. Because of its greater hardness and lesser ductility, the mineral first cracks at the surface and gradually peels off from the lamellar Bouligand layers. Further increase in the applied load causes an increase in the area of the separated mineral layer with more mineral fragments peeling off. The advanced design of divided areas in the mineral layers results in a local peeling-off with other areas remaining. The crack tip undergoes blunting, advance and re-blunting as the lamellar layers in different orientations deform and rotate; finally interlayer separation occurs in collagenous lamellae. The observation of crack-tip behavior suggests that the arapaima scale can undergo high loads and significant deformation without catastrophic failure. The fractured mineral layer and the exposed blunted lamellar layers are shown in greater detail in Figure 5-3, revealing the extrinsic toughening mechanisms for arapaima scales. The post-test specimen exhibits a well-defined triangle crack region around the crack tip, as shown in Figure 5-3 (a), which is a typical characteristic of ductile composites. The area right round crack tip, presented in Figure 5-3 (b), shows the crack occurs in the mineral layer while the beneath collagen layer undergoes tremendous irreversible deformation with evidence of delaminated collagen fibrils. The area a little bit behind crack tip, shown in Figure 5-3 (c), reveals the shearing between two adjacent layers which is caused by rotation of lamellae and collagen fibrils are bridging between

layers. With further away from crack tip, as shown in Figure 5-3 (d), the lamellae fibers start delamination and collagen fibrils are still bridging them. At the end of the cracked region, as shown in Figure 5-3 (e), some collagen fibers are still bridging the crack while some of them are already completely fractured (indicated by dash lines), with tremendous inter-fiber separation and fibrillar bridging, as indicated by arrows. Inside of the fractured collagen fibers, as shown in Figure 5-3 (f), collagen fibrils broke and curved due to the relaxation after tensile failure, indication significant tensile deformation before fracture. All these extrinsic toughening mechanisms we observed above, combined with the intrinsic toughening mechanisms identified by Zimmermann et al.[77], act in concert to resist fracture, the question that what magnitude of fracture toughness is actually induced in this excellent damage-tolerant material.

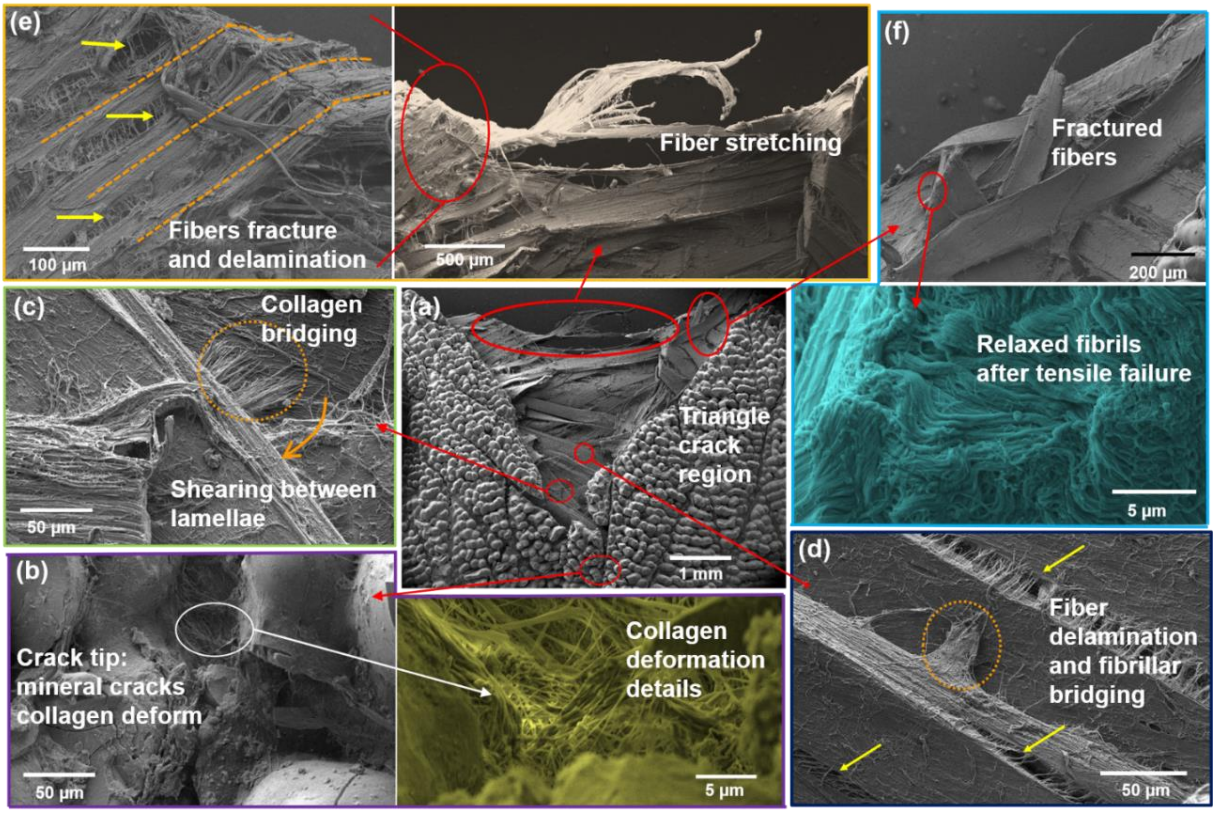

Figure 5-3 SEM characterization of the crack tip region. (a) The cracked region shows a triangle shape. Crack propagation into mineral surface region and blunting into collagenous lamellar core; (b-f) Detailed views of crack retardation mechanisms: (b) mineral cracks at the crack tip the beneath collagen fibrils deforms irreversibly; (c) collagen fibrillar bridging between adjacent lamellae caused by the rotation mismatch of different lamellae; (d) separation of collagen fibers and fibrillar bridging between them; (e) stretching of fibers behind the crack tip region and part of them fractured with delamination; (f) fibers fractured and fibrils relaxed and curved after the tensile failure.

This question is addressed by a nonlinear-elastic fracture-mechanics analysis method based on our *J*-integral fracture toughness testing of moist arapaima scales, the experimental and analysis details of which are provided in the method section of this chapter. Note that we elected to not present the simpler linear-elastic fracture-mechanics stress-intensity *K*-based toughness analysis as the scales were too small and displayed too much plasticity (flow stress of the scale in the transverse direction is $\sigma_o \sim 22$ MPa[56]) to satisfy the small-scale yielding criterion for the validity of *K*-based crack-tip stress and displacement fields accordingly to the ASTM Standard E1820 for

fracture toughness measurement[158]. Moreover, such linear-elastic measurements do not account for the important contribution of plastic deformation, which invariably plays a major role in enhancing the toughness of biological materials[159]. Further discussion on our toughness measurements are given in method section.

Figure 5-4a shows the results of our measurements of the crack-resistance curves in terms of J as a function of stable crack advance, Δa; the R-curve data for moist arapaima fish scales, so measured on five different samples, are plotted, where an increase in J is required to advance the crack stably. Based on these R-curves where stable cracking takes place for up to $\Delta a \sim 6$ mm, a maximum (plateau) J_{max} value of ~100 to 200 kJ·m^{-2} can be deduced for stable crack growth. This value does not satisfy a condition of plane strain but this is not relevant as it represents the toughness of actual ~1 mm thick scales. However, it definitively represents a valid J measurement, as discussed in the method section, and clearly demonstrates the exceptional crack-growth toughness of the arapaima scales. In energy terms, this toughness value is higher, by one order of magnitude, than that of Dastjerdi et al.[76]; however, they used a constrained testing configuration which, as they themselves state, can severely underestimate the toughness. In terms of a stress-intensity value, using the Young's modulus measured for the arapaima scale in the relevant transverse direction of $E \sim 210$ MPa[56], our measured J-based fracture toughness of 200 kJ·m^{-2} translates to an approximate K-based crack-growth fracture toughness of ~6.4 MPa·m^{½}.

With respect to comparisons to Dastjerdi *et al.*[76] measurements of the toughness of striped bass scales, another significant difference between these and the current arapaima fish scales is the thickness of the lamellae; the lamellae thickness for the arapaima fish is ~50 μm[56], whereas it is only 5 μm for the striped bass[76]. The thicker lamellae can not only provide higher strength due to

the larger number of collagen fibrils, but also involve the breakage of more interfaces during the plastic deformation, which is vital for toughening the materials.

The shape of the R-curves of the tougher arapaima scales displays a progressively increasing toughness over a range of stable crack extensions of Δa ~ 1.5 to 5 mm prior to reaching the ~100 to 200 kJ·m^{-2} "plateau" (Figure 5-4a). The initial toughness can be seen to be quite low, with some R-curves displaying an S-shape, that can be related to the rapid initial cracking of the brittle mineral surface layer (which can bias our crack length measurements as they are made at the surface). Once this surface layer fails, however, the resultant sequence of mechanisms of extensive plastic deformation in the collagen layers serves to increasingly resist crack extension with a consequent elevation in crack-growth toughness. Over ~ 5 - 6 mm of such crack extension, maximum (valid) crack extension capacity of our sample is exceeded; at this stage in some of the samples, some degree of out-of-plane buckling was detected (these invalid data points are delineated by open symbols on the relevant R-curves). Nevertheless, considering only the valid data points until this condition, we are able to measure a reliable value of the crack-growth toughness of moist arapaima fish scales of J_{max} values between ~100 to 200 kJ·m^{-2} in our five tested samples.

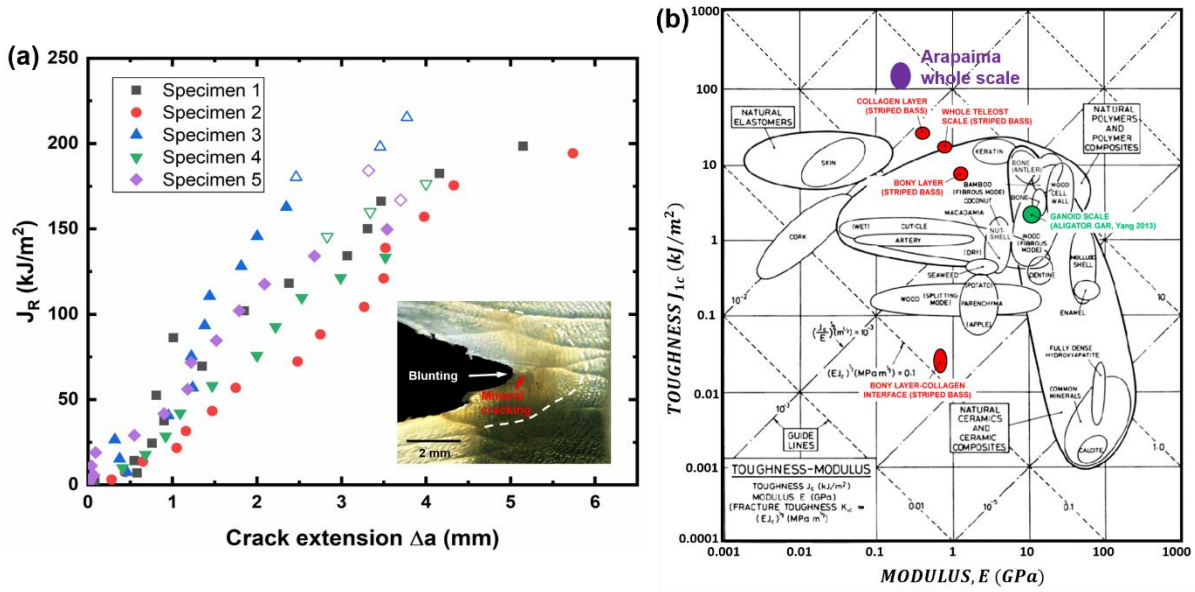

Figure 5-4 Fracture toughness of arapaima scales. (a) Nonlinear-elastic fracture-mechanics *J*-based measurements of the crack-resistance (R-curves) for wet arapaima scales in the form of J_R as a function of crack extension Δa for five representative samples. Inset shows the crack opening and associated crack blunting. (b) Ashby plot of fracture toughness (J_{Ic}) *vs.* elastic modulus (E) showing a comparison with other biological materials including striped bass[76] and ganoid scale.[57] The arapaima scales show one of the highest toughnesses of ~100-200 kJ·m^{-2}. (Note in (a) that the crack-initiation toughnesses, where $\Delta a \rightarrow 0$, can be extremely low; this is due to the fact that the highly mineralized layer at the surface of the scale (where our crack extension measurements are made) can sometimes break almost immediately on loading. Also, the open symbols on some of the R-curves at longer crack extensions were not considered for analysis as this is where we observed some degree of buckling as the longitudinal (load-line) displacements of the sample became too large (typically exceeding ~10 mm) for the anti-buckling plates to work effectively).

These results are plotted on an Ashby-Wegst map[160] for the *J*-based toughness as a function of modulus for a number of important biological materials including other fish scales such as those of the striped bass scale (Figure 5-4b). The ellipsis for the arapaima encompasses our measured crack-growth toughness values between 100 and 200 kJ·m^{-2}. The arapaima and striped bass fish scales are the toughest flexible biological materials in the plot. As noted above, the toughness of the striped bass scales was measured by Dastjerdi *et al.*[76] who correctly attributed the toughening mechanisms to their intricate and ingenious hierarchical structure. Such mechanisms are the result of accommodation and cooperation of the collagen lamellae which has been identified by previous

studies[56,77]. All these toughening mechanisms act *in concert* to provide for the outstanding deformability of arapaima scales and engender their remarkable toughness, making them highly damage-tolerant, armor, materials.

5.4 Summary

In summary, the R-curve toughness of arapaima fish scales was measured to be as high as 200 $kJ \cdot m^{-2}$ (equivalent to a stress intensity toughness of on the order of 6.4 $MPa \cdot m^{½}$), which represents an exceptional fracture toughness associated with a synergy of deformation mechanisms acting *in concert* in the layers of tightly packed parallel collagen fibrils. Specifically, the Bouligand-type organization of the collagen fibrils in the arapaima scales provides close to in-plane isotropy to the scale, whereas each lamella is strongly anisotropic; as such, the hierarchical toughening mechanisms dissipate energy within the sub-layers through collagen fibrillar lamellar separation, collagen fibrillar bridging, sliding, and delamination. Although similar mechanisms were observed in the fish scales of striped bass[76], the significantly higher toughness of the arapaima scales appears to be associated with the increased thickness of their lamellae layers and scale thickness itself, and to a higher degree of mineralization, a necessity for protection of the arapaima from piranha attacks in the Amazon basin.

Chapter 5, in part, is under peer review for publication with coauthors W. Yang, R. O. Ritchie and M. A. Meyers. The dissertation author is the joint first author of this work. The dissertation author is the first author of this work.

CHAPTER 6: ACTIVE DEFENSE MECHANISMS OF THORNY CATFISH

6.1 Introduction

Through billions of years of evolution, the complexity of living organisms keeps increasing; such development pattern is largely driven by predator-prey interaction[133]. In order to survive, maintain the population, and keep the ecological balance, preys developed various mechanisms of anti-predator adaptation. A variety of passive defense mechanisms such as camouflage, nocturnality, playing dead, protective armor and others are used with the purpose of avoiding detection or resisting attack. From the perspective of materials science, the natural flexible dermal/epidermal armors are an eloquent example. They were developed by convergent evolution in mammals, reptiles, and fish, and are extraordinary structural designs with performance exceeding many synthetic ones at the same scale[11,132]. For example, the pangolin possesses overlapped scales which are mainly composed of keratin and fully cover its body (in the retracted position) for protection[160]. Armadillo, turtle, and fish evolved collagen-based bony plates and leather shells and scales, respectively, serving as dermal armors which are not only strong enough to resist the penetration by the teeth and claws of predators, but also damage-tolerant through the deformability, enabled by the hierarchically assembled collagen[57-59,72,149] intermeshed with minerals. These natural materials with their intricate and ingenious structures provide inspiration for fabricating novel light-weight, strong, and tough high-performance armor.

However, organisms also adapt other defense mechanisms which are more active. Instead of waiting for attack by predators, they actively use their unique functional organs to help them escape or poison and threaten. Some of these active defense mechanisms are chemically based. For example, many marine mollusks, notably sea hares, cuttlefish, squid, and octopus, release thick black ink to scare and distract predators[161]. Skunks (*Mephitis*) generate and spray out a liquid with

very strong odor using their anal glands potent enough to discourage predators, and even cause temporary blindness[162]. Some small animals, like sea cucumbers (*Holothuria forskali*), when irritated, can expel a few toxic Cuvierian tubules which lengthen, instantly become sticky, and rapidly immobilize most predators with which they come into contact[163]. The hagfish[164] expels keratin filaments which form a hydrogel-like substance and engulf the predator's mouth. These active defense mechanisms rely mainly on the chemicals produced in glands by metabolism but cannot provide inspiration for load-bearing materials or novel structures.

There is another group of animals which have active defense mechanisms operating on mechanical principles. Hairy frogs (*Trichobatrachus robustus*) are compelling by their ability to break their erectile, terminal phalanges to inflict cuts in their antagonist's skin, forming sharp bony claws to fight against predators[165]. Similarly, the threatened Spanish ribbed newt (*Pleurodeles waltl*) can protrude its spear-shaped ribs through the body wall, forming sharp spines on the back to warn or stab the enemies[166]. More well-known examples are porcupines and hedgehogs, which possess sharp quills or spines covering their body. These quills and spines use the same design strategy: a thin keratinous cortex (shell) filled with closed-cell foam is detachable and penetrates the skin of the predators. The architecture of quills and spines improves the compressive and flexure/buckling resistance while maintaining the light-weight[167].

Here we cast our interest on two active anti-predatory mechanisms adapted by catfish (*Siluriformes*), which have been scarcely noticed by materials scientists or structural engineers. They evolved a pair of stout pectoral fin spines which can be deployed (adducted) and retracted (abducted) repeatedly, producing stridulation sounds for intraspecific communication or to warn predators[168]. When threatened, the pair of spines can also be rigidly locked in the abducted position, effectively increasing the cross-sectional circumference to provide protection from predators with

a limited gape, effectively making the catfish too big to swallow[169]. The cutting edges and hooks lining the spines add injury to the potential predator. Experimental evidence also proves that the presence of locked spines significantly increases the handling time, making preying on catfish an unfavorable choice[170]. There are reports of catfish spines being implicated in wounds or death of largemouth bass, water snakes, great egrets, and brown pelicans, proving that such sharp spines are able to cut the soft tissue inside the predators[169]. Some catfish even have venom glands in the pectoral fin spines, causing additional harm to predators[171]. In addition to the pectoral spines, thorny catfish (*Siluriformes Doradidae*), have two sets of mid-lateral scute rows on both sides of the body[172]. These bony thorns have a hooked shape and can also cause additional damage when catfish the flexes its body repeatedly, trying to escape from the predator. In this article, we reveal the dual friction based locking mechanism of the pectoral spines in a thorny catfish and characterize the structure and mechanical properties of the its spine and mid-lateral scutes. Our results uncovered the active mechanisms of the armored catfish and also provide inspiration for the materials science or structural engineering community to create novel structural materials or designs.

6.2 Methods

6.2.1 Materials

The thorny catfish (Doridiidae) was caught in the Paraguay River in Brazil and the channel catfish (Ictalurus punctatus) was purchased from Ranch 99 market in San Diego. The fish were decapitated after being euthanized in freezer until spontaneous movement ceased. Pectoral girdles with spines were skeletonized with boiling water and oven dried at 60°C. Scutes on thorny catfish were dissected with surgical blades and then air dried at room-temperature.

6.2.2 Structural characterization

Direct observation of the articulations and movements of the pectoral spine relative to the girdle are based on manual manipulations of these skeletal preparations. All photos are taken by cell phone (iPhone X) and digital camera (Canon 60D). The sectioning was performed with a diamond saw. Optical microscope characterization was conducted with Axio Fluorescence Microscope (Zeiss, German).

The micro-CT of the articulated spine with girdle and the dissected scutes for thorny catfish was performed by synchrotron X-ray computed micro-tomography at beamline 8.3.2 of the Advanced Light Source synchrotron (ALS, Lawrence Berkeley National Laboratory) with standard procedures. The spine located at fully abductive position and fully adductive position are both scanned with a 1x lens and the voxel size is 9 μm. The scan for the scutes used 2x lens with a voxel size of 4.5 μm. The micro-CT of the isolated spine shaft of thorny catfish and the articulated spine with girdle of channel catfish were conducted on air-dried samples in a Zeiss Versa 510 X-ray microscope (Zeiss, German) in National Center for Microscopy and Imaging Research (NCMIR). The voxel size for the scan of channel catfish is 3.6 μm and the scan for spine shaft of thorny catfish is 1.8 μm.

The SEM (scanning electron microscopy) characterization and EDX (energy-dispersive X-ray) analysis are conducted with FEI Quanta 250 (FEI, Hillsboro, OR). The samples for SEM characterization are first immersed in the 2.5% glutaraldehyde for 1 h to fix the structure and then dehydrated with an ascending series of ethanol (30, 50, 70, 90, 95 and 100 vol.% twice). To obtain the oblique fracture surface, the scale was immersed in liquid nitrogen for 30 s and fractured using forceps immediately. All samples were dried with Tousimis Autosamdri 815B ((Tousimis, Rockville, MD) and then sputter coated with iridium using an Emitech K575X sputter coater (Quorum Technoloties Ltd.) before observation.

6.2.3 Mechanical testing

Microhardness tests were performed on the polished cross-section of dentations on pectoral spine and midlateral scutes of thorny catfish, using a LECO M-400-H1 hardness testing machine equipped with a Vickers hardness indenter and the applied load is 200 grams. Indent positions are recorded manually and the color scale for the microhardness value is also created manually. The compression specimens were sectioned from the shell of spine shaft and tested in an Instron 3367 testing machine (Instron Corp., Norwich, MA) at a strain rate of 10^{-3} s^{-1}. The specimens all immersed in water for 24 h before testing to keep the hydration. The failed specimens were immediately immersed into 2.5% glutaraldehyde solution to fix the morphology of the cracked region. The same dehydration procedure as the SEM sample preparation was performed on the fixed cracked samples prior to sputtering with iridium before final observation using FEI Quanta 250 (FEI, Hillsboro, OR)**.**

6.2.4 3D printing

The artificial catfish spine and girdle were fabricated by a commercially available 3D printer (Stratasys Objet350 Connex3). The materials utilized for printing consist of a mixture of

three polymers: a translucent photopolymer (TangoPlus FLX930), a flexible black photopolymer (TangoBlackPlus FLX980), and a rigid, clear photopolymer (VeroClear RGD810). The mixture ratio of these three materials is tuned for creating different colors for the spine (black) and girdle (transparent white). A flexible, low-yield polymer (SUP705) was utilized as support material. After the artificial structure was fabricated, the remaining support materials are removed by careful mechanical cleaning and washing with alkali solution.

6.3 Results

The thorny catfish was caught in Paraguay River in southern Brazil, as shown Figure 6-1 (a). When the fish is taken out of water (threatened), a pair of lateral sharp fins, also called pectoral fin spines, are deployed to protect itself. In addition to the lateral spines, two arrays of sharp thorny scutes having hooked tips line both mid-lateral sides of fish body. These three active defense mechanisms will be analyzed in the sections below.

6.3.1 Pectoral spines: locking mechanism

After being sacrificed and skeletonized, the fish head with pectoral and dorsal fin spines was separated from the body. Figure 6-1 (b) shows the pectoral spines that could still be locked in several positions during the deploying (abductive) movement. Locking here is defined as: in certain position, a distinct resistance force is detected if further opening (abductive) or closing (adductive) motion is applied to the spines. This locking can only be released when appropriate torque applied. This locking phenomenon of the abduction/adduction motion occurs in the skeleton and the soft tissues (muscle and tendon) assist in the immobilization by bringing the components together and allowing friction to fully operate. The locking (or resistant) force is produced by pushing the components together and allowing the friction between bony surfaces to operate. It relies on the complex articulation formed by the spine base with the bones of the pectoral girdle

as shown in Figure 6-1 (c). The rotation of the spine occurs in a channel (also called fossa) in a cam-like mechanism. Figure 6-2 presents the detailed structure of the spine base and the pectoral girdle.

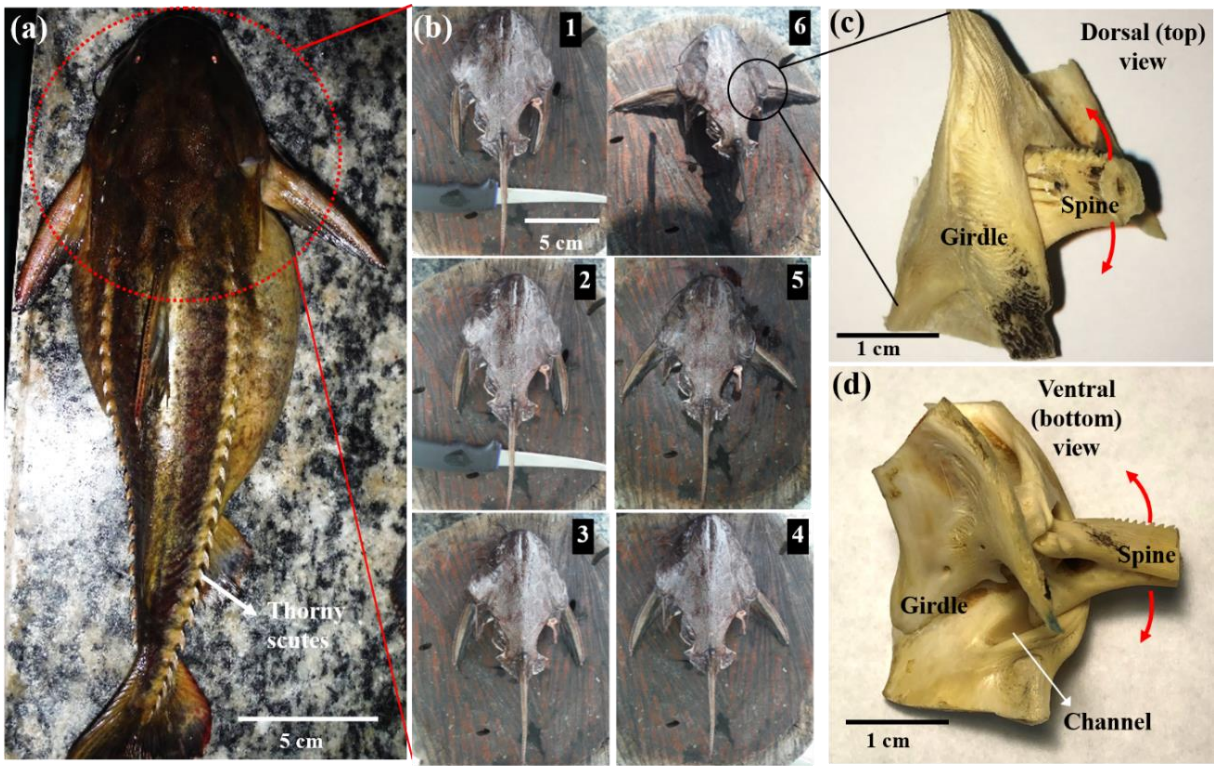

Figure 6-1 The locking phenomenon of pectoral spines on thorny catfish. (a) The thorny catfish (*Doradidae*) caught in Paraguay River, Brazil. The pectoral spines are partially abducted and two arrays of scutes with hooked tips located on both midlateral sides of the body. (b) Six locking positions of pectoral spines observed when the fish was just decapitated. (c, d) Dorsal (top) and ventral (bottom) views of the skeletonized joint part of the pectoral spine articulated with girdle in the locked position, respectively. Arrows indicate the rotation direction.

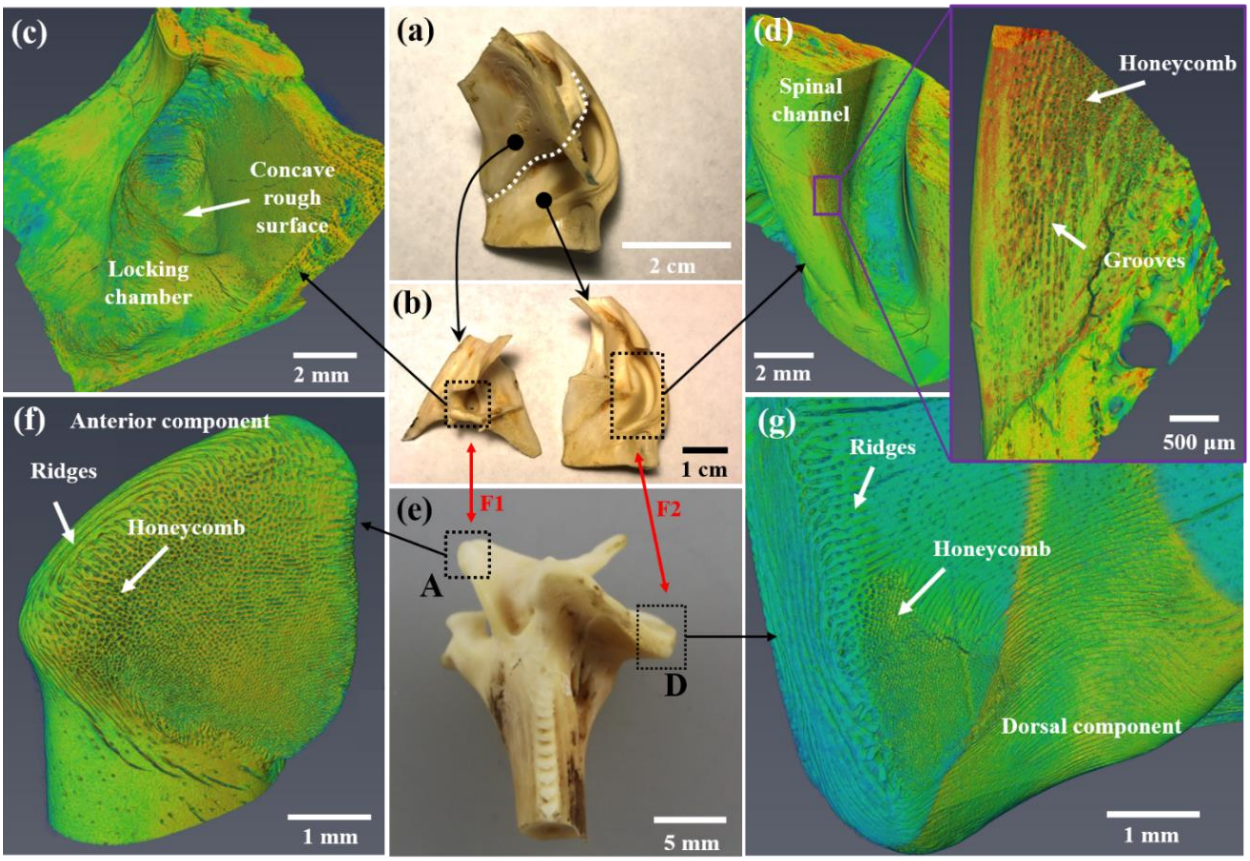

Figure 6-2 The structure of the girdle and spine base. (a) The isolated girdle part involved in the locking. The girdle is cracked along the dotted line and separated into two parts. (b) The separated two parts of the girdle. Two key structures are involved in the locking of pectoral spines: one is a locking chamber boxed with dotted line on the left; the other one is a spinal channel (fossa) boxed on the right. (c, d) The micro-computerized tomography (micro-CT) of the locking chamber and spinal fossa, respectively. The locking chamber has a convex structure and the inner surface is very rough. The spinal channel (fossa) is curved and the its width narrows down from posterior end to the anterior end. The inner lateral wall of the spinal channel, shown in the inset of (d), is highly mineralized (brighter red color indicates higher mineralization) and surrounded by groovess and honeycomb-like microstructures. (e) The basal part of the pectoral spine. There are several structural components on the base but two of them are the key components involved in the locking, which are the anterior component (A) boxed on the left, and the dorsal component (D) boxed on the right. The locking of the pectoral spine relies on two frictions (denoted as F1 and F2) generated between these two key components. (f, g) The micro-CT of anterior and dorsal components, respectively. (f) The anterior component has a triangle-like shape with ridges and honeycomb-like structures surrounding the surface. (g) The dorsal component is the largest component and outer surface also has distinct ridges and honeycomb-like structures to increase the roughness.

The isolated girdle, shown in Figure 6-2 (a), is split along the dotted line to display its inner structural features. The two separate parts of the girdle are shown in Figure 6-2 (b), revealing the two structural elements in the locking mechanism. A cavernous structure, also called locking chamber (fossa) in literature[173], is boxed on the left part. Figure 6-2 (c) presents the micro-computerized tomography (micro-CT) of the locking chamber, consisting of a concave channel having an internal rough surface. The other part of girdle shown on the right in Figure 6-2 (b), contains another key element: spinal channel (fossa), as boxed with black dotted line. Its detailed structure, as presented with micro-CT in Figure 6-2 (d), indicates that the inner lateral wall of the channel has numerous highly mineralized ridges (brighter red color indicates higher mineralization) and honeycomb-like structural components, which significantly increase the surface roughness.

The spine base is shown in Figure 6-2 (e). There are several structural components on the bony base of the spine and two of them are key: the anterior component (boxed and marked as A) and the dorsal component (boxed and marked as D). The detailed structure of these two key components are presented by the micro-CT in Figure 6-2 (f,g), respectively. The anterior component (Figure 6-2f) has a triangle-like overall geometry with numerous ridges and honeycomb-like structures on the surface. The dorsal component (Figure 6-2g) is the largest one among all the structural components on the spine base. Its outer surface is also very rough, with numerous similar ridges and honeycomb-like structural features. When the spine is fully deployed, the anterior and dorsal components on the spine base will tightly fit into the locking chamber and spinal channel, respectively, and their perfectly complementary geometry and tightly contacted rough surfaces will generate two frictions, denoted as F1 and F2 in Figure 6-2 (e). They work together to lock the spine firmly in the deployed position. The evidence of this dual-friction-based locking mechanism is provided in Figure 6-3.

Figure 6-3 shows the micro-CT of the entire joint part of the pectoral spine base with articulated girdle. For better demonstration, both the lateral view and ventral view of the joint at the fully retracted and deployed (locked) positions are presented in Figure 6-3 (a) and (b) respectively. It is clearly shown that the dorsal component slides in the spinal channel from the posterior to the anterior end and that the trajectory of the movement is determined by the curvature of the channel. When the spine is fully deployed, its basal part is firmly locked by the interaction of structural components on both spine base and girdle interior. Figure 6-3 (c) provides the close-up view of the anterior component. The triangle-like anterior component (A) perfectly fits into the cavernous locking chamber and the tightly contacted rough surfaces of both parts generate significant friction that dominates the locking of entire spine. A supplementary friction is generated by the dorsal component, as presented in Figure 6-3 (d). The cross-sectional view indicates that the anterior end of the spinal channel tightly surrounds the dorsal component (D), and the surface feature of these two parts as shown in Figure 6-2 (d) and (g) work synergistically to provide another friction to enhance the locking of the pectoral spine.

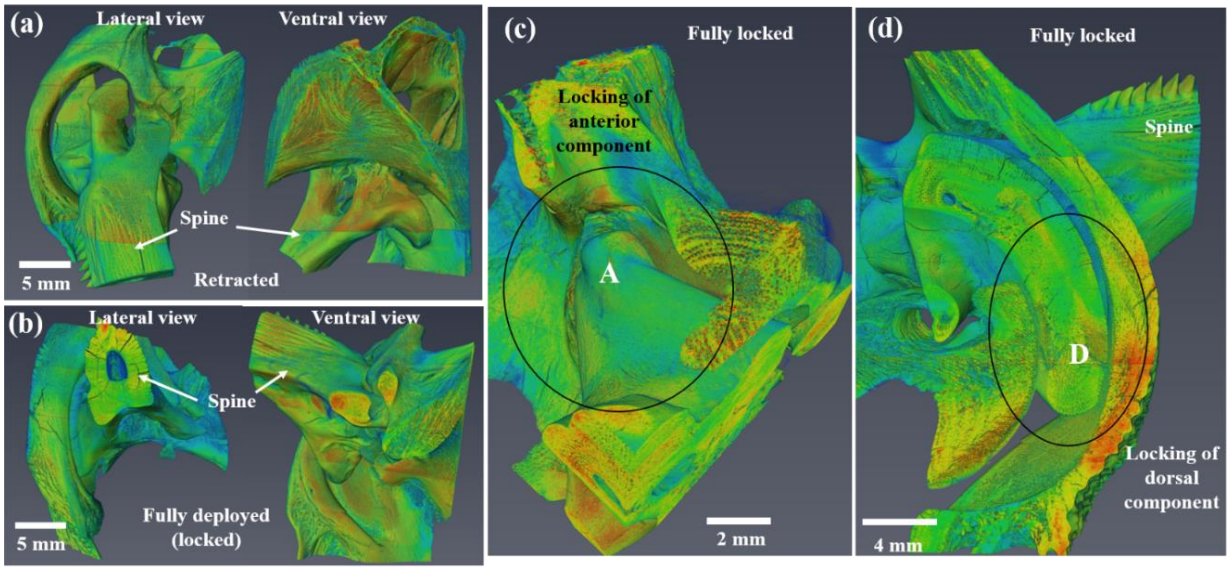

Figure 6-3 Micro-CT of the pectoral spine joint part revealing the locking mechanism. (a, b) The spine articulated with the girdle at retracted state and fully deployed (locked) state, respectively. The lateral and ventral view of the joint are shown at both states. The dorsal component slides in the spinal channel during the deploying movement. The curvature and gradient width of the channel guide the movement of the spine base. (c) The close-up view of the anterior component (A) at the fully locked position. When the spine is fully deployed and locked, the anterior component (A) tightly fit into the locking chamber on girdle. The complementary geometry and rough surface generate a strong friction leading to the firm lock of the spine. (d) The cross-section of the dorsal component (D) at the locked position. With the spine fully lifted, the dorsal component slides to the anterior end of the spinal channel, where the width of the channel is about the same size of the dorsal component, resulting in a tight contact between the channel wall and outer surface of the dorsal component. The surface features on both parts, presented in Figure 2 (d) and (g), generate another friction that supplements the locking of spine.

Based on the structural characterization above, the locking mechanism of the pectoral spine on thorny catfish is fully unraveled and illustrated in the schematic rendition in Figure 6-4. The spine is engaged and rotates in the circular segment of the spinal channel (fossa). Three positions are shown: retracted, Figure 6-4 (a); intermediate, Figure 6-4 (b); and deployed Figure 6-4 (c). The top rendition corresponds to the view from the top (dorsal view); the lower rendition corresponds from the view from the bottom (ventral view). When the spins are fully retracted (Figure 6-4a), the spine base is located at the posterior end of the spinal channel and possesses enough room for free movement, with no friction generated. When the spine is in the intermediate position (Figure

6-4b), the dorsal component is engaged with the grooves and rough internal surface of the spinal channel, generating a significant resistance force. When the spine is fully deployed (Figure 6-4c), in addition to the engagement by dorsal component and spinal channel, the anterior component (shown in the bottom part of Figure 6-4b) fits into the locking chamber, resulting in another locking mechanism also using friction to ensure immobilization for protection.

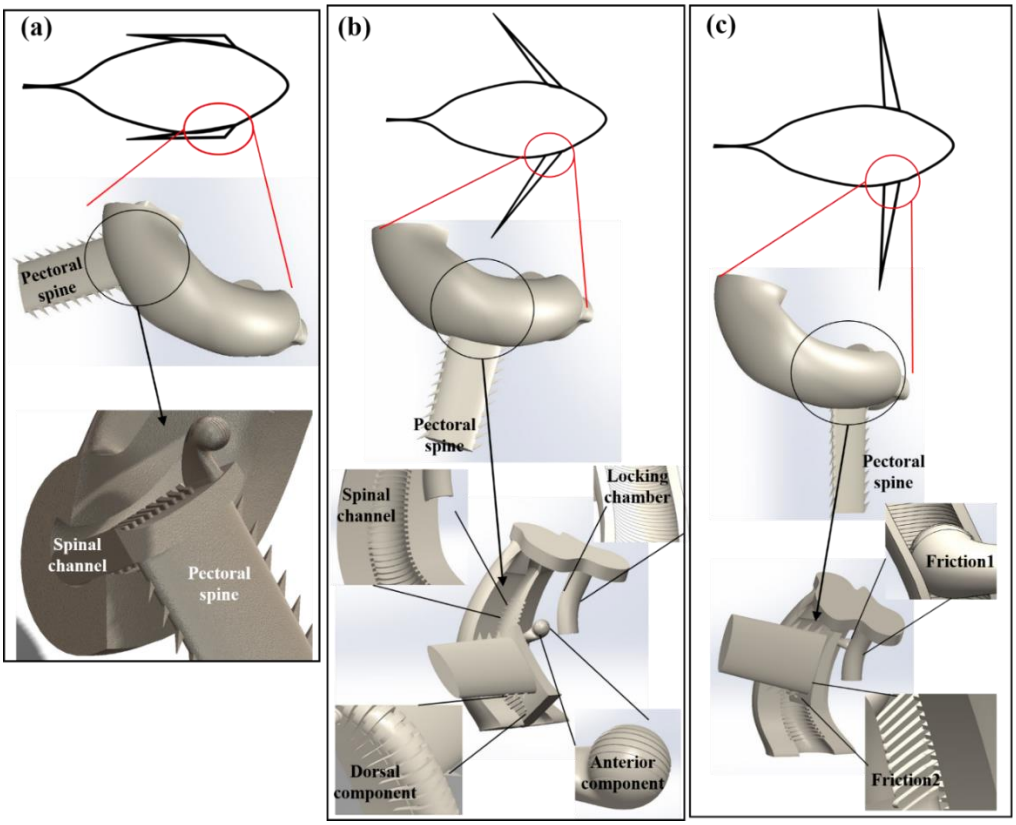

Figure 6-4 Schematic showing two-friction based locking mechanism. (a) The spines are fully retracted, aligned with the longitudinal direction. The ventral view shows the posterior end of the spinal channel is wide and there is no groove, causing no friction with the end of spine. (b) The spines are partially deployed. The ventral (bottom) view of this position reveals all the components which leads to the friction-based locking: spinal channel with grooves, dorsal component with ridges, locking chamber with rough inner surface and the anterior component with ridges. In such partially locking position, the friction is already generated by the engagement of spinal channel and dorsal component. (c) The spines are fully deployed and locked. The ventral view shows the two frictions which leads to the robust lock of spines. They are the friction generated by spinal channel and dorsal component; and the friction generated by locking chamber and locking tubercle on the anterior component. These two frictions are denoted as Friction1 and Friction 2, corresponding to F1 and F2 in Figure 2 (e).

The locking phenomenon of the pectoral spines is prevailing in most of catfish species. To confirm the two-friction locking mechanisms described above, the pectoral fin spines of common channel catfish were investigated with same techniques; the details are provided in Figure 6-5. Figure 6-5 (a) shows that the pectoral fin spines of channel catfish have the same locking phenomenon and the skeletonized pectoral joint part indicates the spine is articulated with girdle in a similar manner with thorny catfish (Figure 6-1c). The anterior (A) and dorsal components (D) are also the two key structural components responsible for the locking phenomenon. Micro-CT combined with SEM images reveals the locking mechanism for the channel catfish. The fully retracted and deployed states are presented in Figure 6-5 (b) and the ventral (bottom) view of the deployed spine joint is shown in Figure 6-5 (c). The locking is also due to the two frictions generated from anterior component with the locking chamber in girdle (Figure 6-5d), and the dorsal component with the ventrolateral wall of spinal fossa (Figure 6-5e). In summary, based on the previous literature and our current investigation, the locking phenomenon of pectoral fin spines for various catfish species is confirmed: it mainly results from the two-friction locking mechanism generated from the intricate articulation of spine base with the ingenious inner design of the girdle. We also 3D printed the spine and girdle parts based on our CT scan, as shown in Figure 6-6, demonstrating that the locking is purely based on the structural design and independent of the material composition. The video demonstrating the structure and locking mechanism of the 3D printed pectoral spine joint is provided in the supplementary information.

Figure 6-5 The locking mechanism of pectoral spines on channel catfish. (a) The channel catfish with the fully deployed pectoral spines. The skeletonized girdle articulated with spines is shown in dorsal view. The girdle is composed of two symmetric parts which are sutured together, as the red line indicates. The isolated spine base also contains the two key structural components causing the lock, which are the dorsal component (D) and anterior component (A). There are numerous dentations scattered on the posterior side of spines. (b-d) Micro-CT of the articulated spine and girdle. (b) The spine is fully retracted and deployed, respectively. (c) The joint at fully deployed state is viewed from ventral (bottom) side, which is the fully deployed state shown in (b) rotated for 90° clockwise, as the red arrow indicted. (d) The friction generated by anterior component (A). The anterior component (A) has numerous ridges scattered on the surface. The locking chamber (squared with dot line) has a concave and rough surface. When the spine is fully deployed, the the anterior component (A) engaged with the concave locking chamber and generate frictional force (Friction1). (e) The middle part is the micro-CT of dorsal component (D) sitting in spinal channel; the left and right parts are the SEM images of dorsal component and spinal channel, respectively. The spinal channel surrounds the dorsal component (D) and narrows anteriorly. Numerous ridges and honeycomb-like structures are on the surface of dorsal component (D) and the ventrolateral wall of the spinal channel are decorated with distinct grooves. The ridges on the dorsal component (D) tightly contact with the grooves of the channel wall, generating the supplementary friction (Friction2) to improve the overall locking of the entire spine.

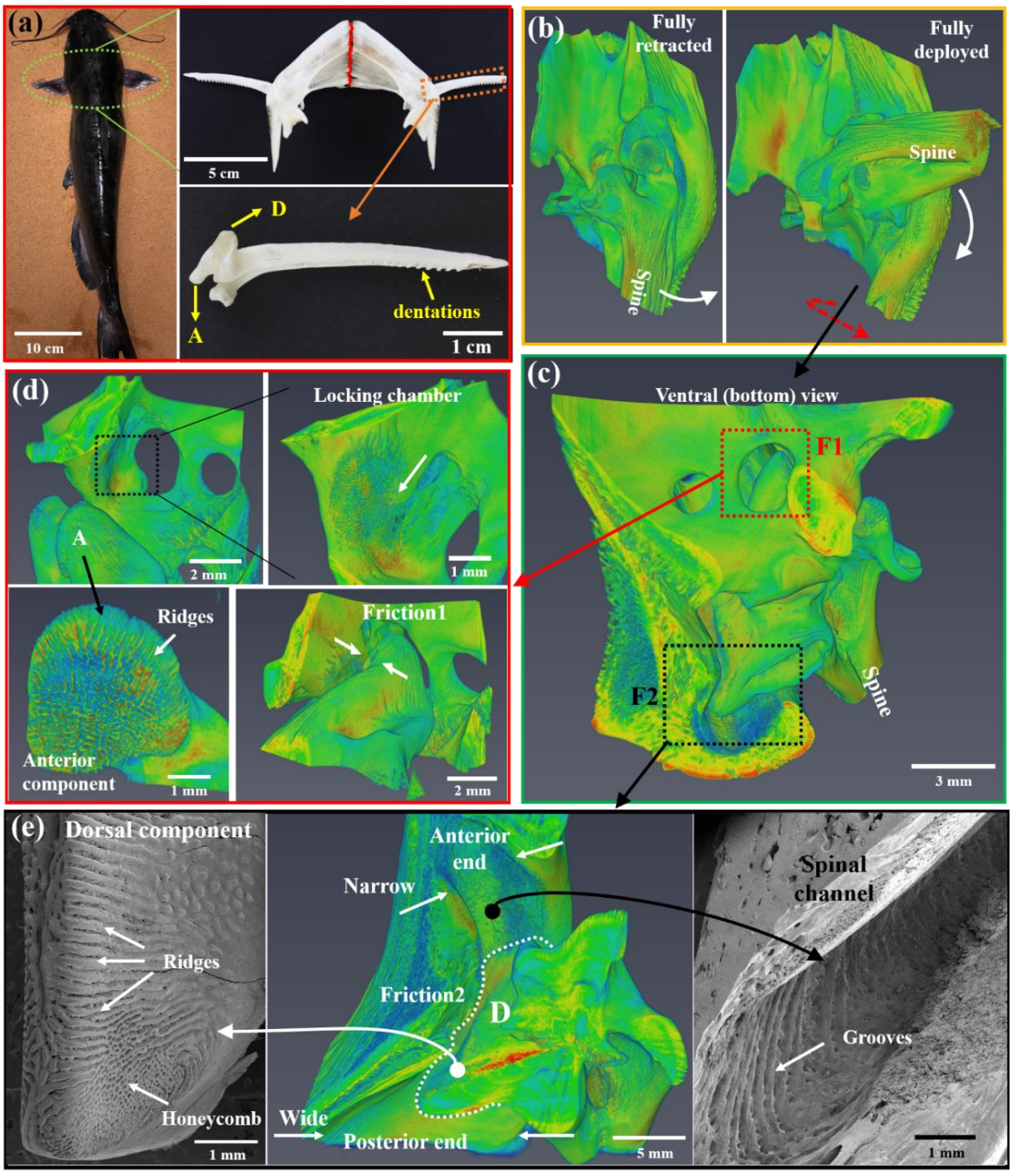
(a)
10 cm
5 cm
D
A
dentations
1 cm
(b)
Fully retracted
Fully deployed
Spine
Spine
(c)
Ventral (bottom) view
F1
F2
Spine
3 mm
(d)
A
2 mm
Locking chamber
1 mm
Ridges
Anterior component
1 mm
Friction1
2 mm
(e)
Dorsal component
Ridges
Honeycomb
1 mm
Anterior end
Narrow
Friction2
D
Wide
Posterior end
5 mm
Spinal channel
Grooves
1 mm

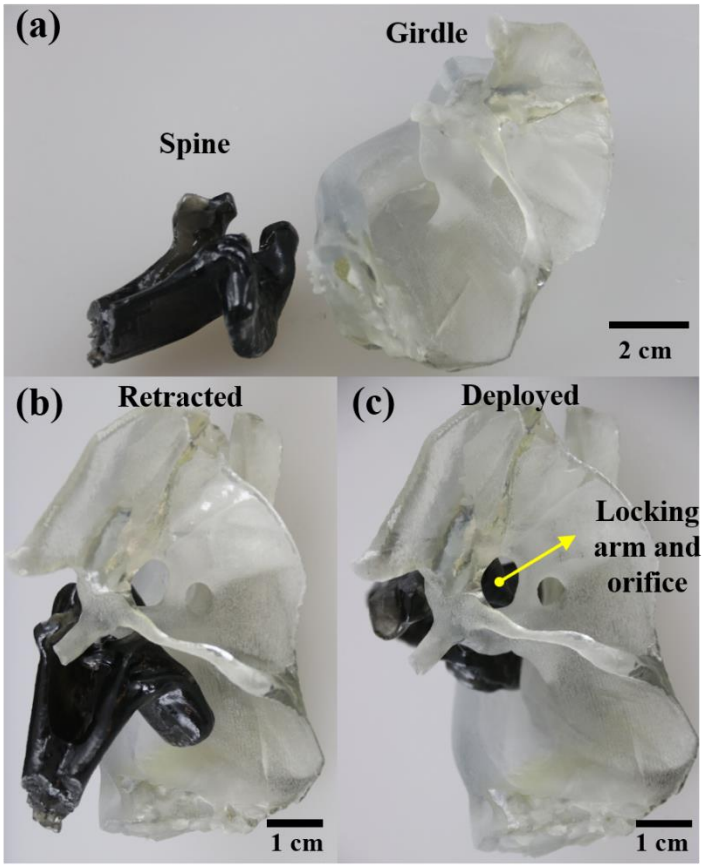

Figure 6-6 3D printed pectoral spine joint. (a) 3D printed basal part of the pectoral spine (black) and girdle part (white) based on the micro-CT scan. (b) The articulated spine in retracted and (c) deployed state.

With the locked spines in a fully or partially abducted (deployed) position, the effective circumferential size for the thorny catfish is significantly enlarged, increasing the handling time and making it an unfavorable prey choice; the long spines with numerous sharp dentations also can threaten the predators or cut their soft tissues if they try to swallow it.

There are also some noticeable differences between the fully deployed state (locking) and the partially deployed state (binding). In the partially deployed, or binding state, the dorsal component can contact the ventrolateral wall of spinal channel only with appropriate torque applied on the spine; thus, the anterior component can contact the locking chamber, resulting in the generation of noticeable friction. This is also why in the skeletonized specimens, the binding,

namely the resistant force to prevent further moving of the spine, can only be detected with slight torsion applied. However, when the spine is fully deployed, it can be locked firmly without applying torque. This is due to the fact that, at this position, the dorsal component is located at the anterior end, the narrowest end of the spinal channel, which does not need external force to ensure that the contact is sufficiently tight. As well, the anterior component in this position also fully squeezes into the locking chamber and these two strong frictional forces generated simultaneously and making the spine locked firmly without torsion needed. In the realistic case of living catfish, muscular force is needed to achieve binding, which is the spine is partially deployed. Once the spine is fully deployed, no more muscles are needed for locking it and the muscles only work when the threaten is gone and the slight torque needs to be applied on spine to release them back to the retracted position. Therefore, the locking phenomenon of the spines, including the binding, is generated by combination of ingenious design of the articulation and well-timed muscular work.

Another interesting finding is that, after repeated the deployment and retraction movement on the spine, the locking force gradually deteriorates, and it almost completely gone in the end. This is due to the wearing of the surface features of all the structural elements after several friction events. The evidence is provided in the supplementary information from Figure 6-7 to Figure 6-10, where the ridges and honey-comb structures that generate the surface roughness for dorsal component, anterior component, ventrolateral wall of spinal fossa and the apron region of locking fossa, are all worn out, which significantly reduces the frictional force and make the locking phenomenon disappear. Nevertheless, such wearing effect which causes the loss of locking also confirms that the spine locking is dominated by the two-friction mechanism. However, the living catfish are able to keep the locking ability for their spines after countless abductive and adductive motion. This is because in the living catfish, the spine base and girdle are fully hydrated, which

increases the deformability of the bones and reduces the wear of the surface structures. Moreover, bone keeps remodeling in living animals and the damaged surface structures can be repaired by osteoclasts and osteoblasts, making the locking of spines a very robust active defense mechanism in the entire life of catfish.

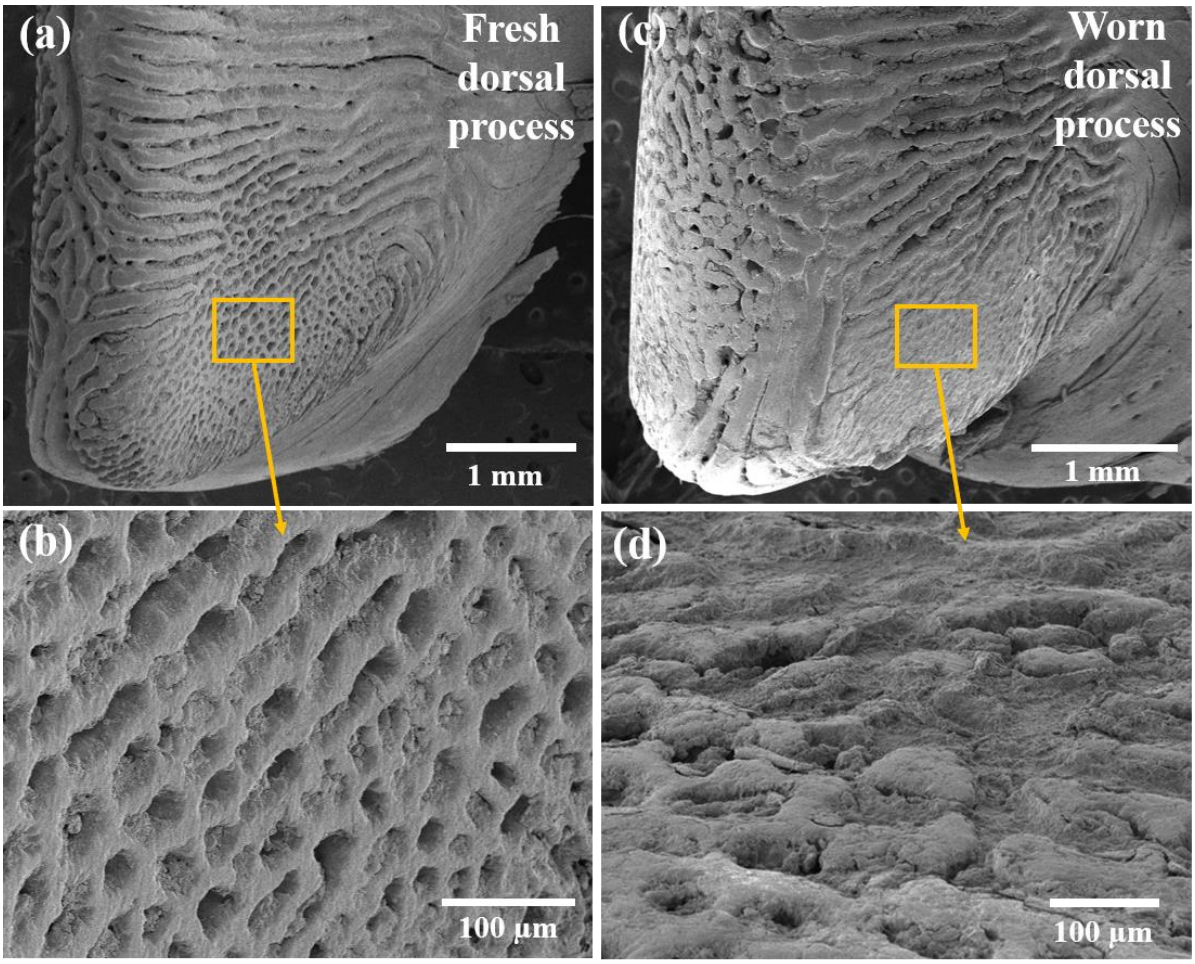

Figure 6-7 SEM images of the fresh and worn dorsal process of channel catfish. (a,b**)** The fresh dorsal process has well-defined ridges and honey-comb structures. (c,d**)** The ridges and honey-comb structures are damaged on the worn dorsal process.

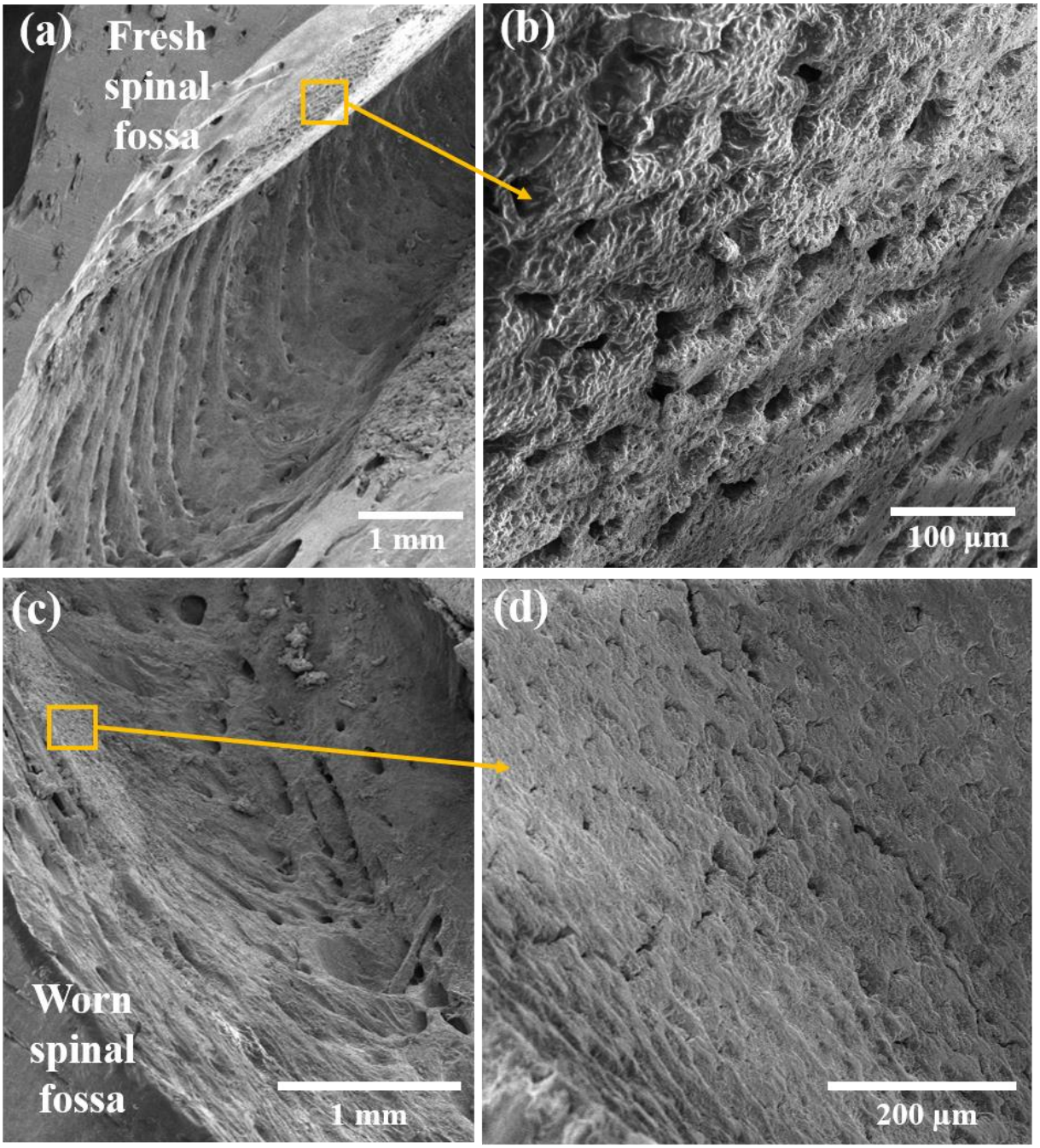

Figure 6-8 SEM images of the fresh and worn spinal fossa of channel catfish. (a,b**)** The fresh spinal fossa has well-defined ridges and honey-comb structures on the ventrolateral wall. (c,d**)** The structural elements are damaged on the worn spinal fossa.

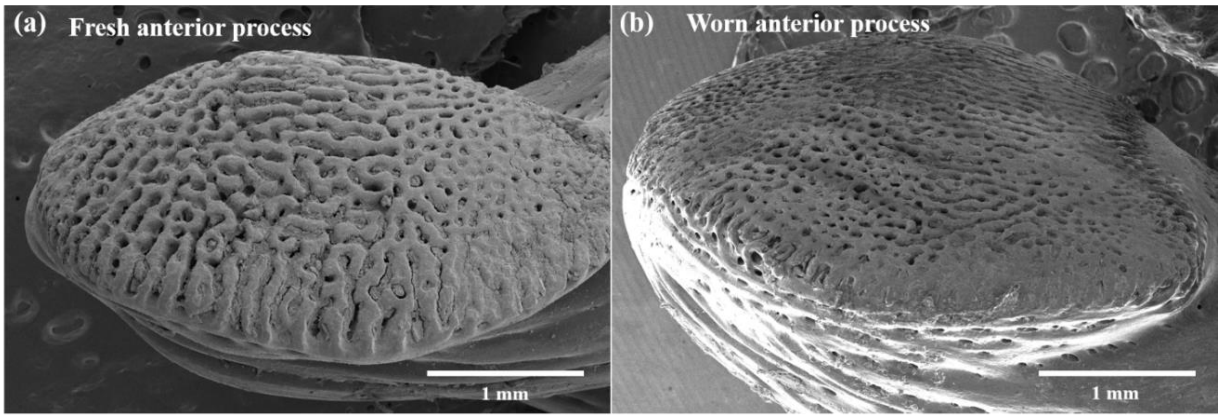

Figure 6-9 SEM images of the fresh and worn anterior process of channel catfish. (a**)** The locking tubercle on the fresh anterior process has well-defined ridges and honey-comb structures. (b**)** The structural elements are damaged on the worn anterior process.

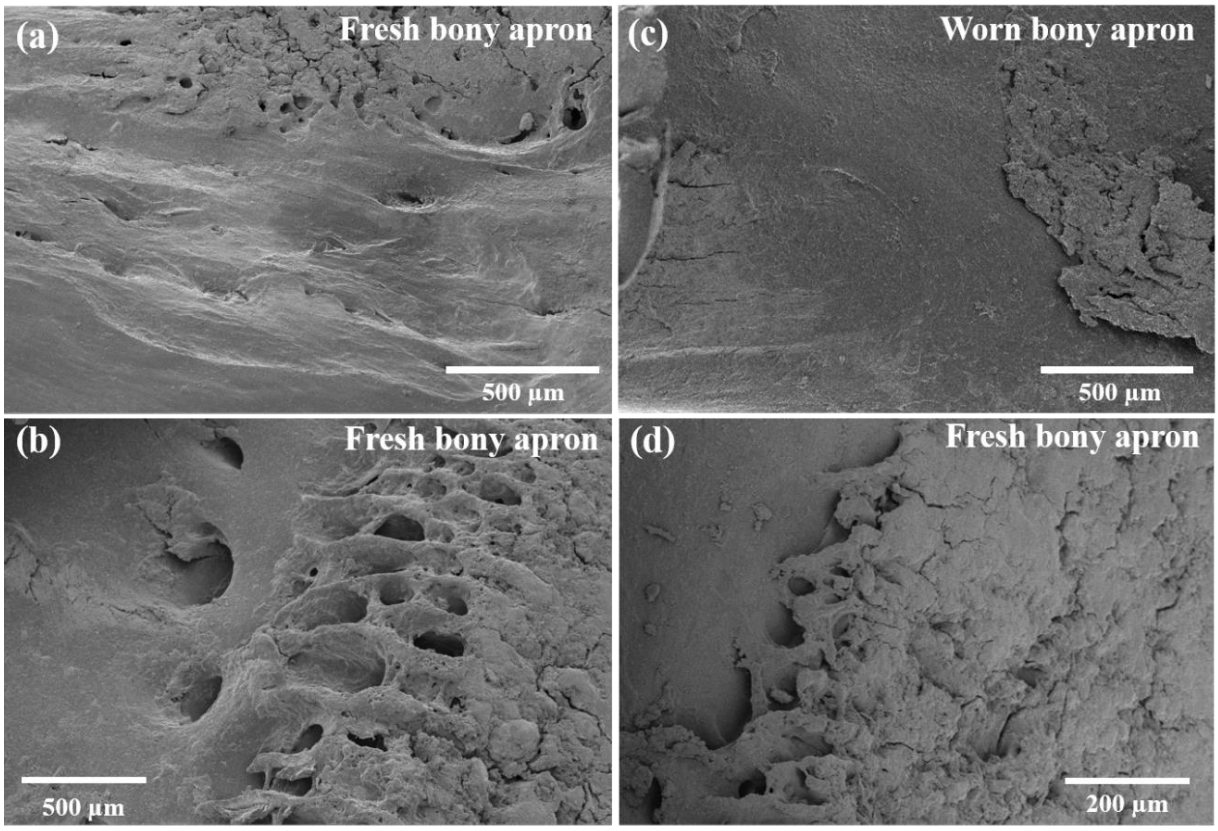

Figure 6-10 SEM images of the fresh and worn apron region of locking fossa of channel catfish. (a,b**)** Two regions on the bony apron of locking fossa show the well-defined rough surfaces with ridges and honey-comb structures. (c,d**)** The structural elements are damaged on the worn sample.

6.3.2 Pectoral spines: dentations

A dissected pectoral spine from the thorny catfish is shown in Figure 6-11 (a), with debris of dermis (dark) covering it. Unlike the channel catfish, whose dentations only grow on the posterior side (Figure 6-11b-d), the pectoral spines of thorny catfish have sharper and larger dentations (compared with ones in cultured channel catfish) rooted on both anterior and posterior sides of spine. The pointing orientations of the dentations on two sides are asymmetrical, which can improve the stabbing and cutting ability through double damage by penetration into and extraction from the predators' soft tissues. An interesting bifurcation of the pointing orientations of dentations is observed in the micro-CT around the spine tip region (close to the distal end), as circled in Figure 6-11 (b). Since the during the life of the fish, the spine grows distally (the distal end appears at first and the spine grows outward), such bifurcation demonstrates the asymmetry is developed during its maturing. The center region of the spine is hollow (Figure 6-11c, d) and the cavity is completely enclosed in a bony shell, forming a tubular structure along the longitudinal direction. The diameter of the central cavity gradually decreases from the proximal to the distal end, as the circles with dotted line indicate in Figure 6-11(d) and (c), respectively. Such central hollow structure is adopted by many other biological materials like bird feathers, beaks, and whale baleens. It significantly reduces the weight while maintaining the flexure and buckling resistance. The sharp dentations on the spines are highly mineralized with two distinct characteristics. First, the mineralization gradually decreases from dentation tip (red) to the base in the bony shaft (yellow), as shown in Figure 6-11 (c) and (d). Second, the mineral content is also associated with the pointing direction of the dentations, as Figure 6-11 (e) shows. Three neighboring dentations near the bifurcation are presented in the inset of Figure 6-11 (e). Their cross-section, shown in Figure 6-11 (e), demonstrates that, for each dentation, the region close to the outer surface (red)

has always higher mineralization than the inner side (green). The longitudinal cross-section of the dentations closes to the proximal end, which is provided in Figure 6-11 (f), confirms the mineralization trend described above. The element mapping from energy-dispersive X-ray spectroscopy of one dentation is provided in Figure 6-11 (g), showing its composition with high calcium and phosphorus contents but carbon deficient.

The scanning electron microscopy (SEM) images of an isolated dentation with the spine shaft beneath it are presented in Figure 6-11 (h – k), indicating that the minerals in the solid dentation have no noticeable alignment (Figure 6-11i). The spine shaft is mainly comprised of porous bone, with evidence of well-defined collagen fibrils presented in Figure 6-11 (k). The mineralization of dentations is higher than the porous bony shaft and the mineral content in each dentation also gradually decreases from the outer surface to its inner side.

Figure 6-11 The structure of the pectoral spine of thorny catfish. (a) The spine shaft is dissected from the right side. Numerous dentations sit on both anterior and posterior sides asymmetrically. (b-f) Micro-CT of the spine at different regions. (b) The region close to distal end of the spine reveals that there is a bifurcation in the pointing directions of the dentations on the posterior side, as circled with dot line. Bifurcation here means starting from the bifurcated point (circled), the dentations on distal side spike out symmetrically while on proximal side they point asymmetrically. (c) The transverse cross-section of the region close to distal end shows the central cavity (circled) is enclosed in the spine. (d) The transverse cross-section of the spine shaft closer to proximal end shows there is a gradient decrease of the mineralization from the dentations (red) to the bony shell (yellow) and the diameter of the central cavity (circled) is larger than that in the distal region. (e) The cross-section of three neighboring dentations around the bifurcated one (also shown in inset) indicates the region closer to outer surface (red) is always higher mineralized than the inner region (green). (f) The longitudinal cross-section of (d) confirms the trend of mineralization: dentation is higher mineralized than shaft and for each dentation the outer surface is higher than the inner one. (g) The SEM of the cross-section of an isolated denticle and the element mapping of carbon, calcium and phosphorus on it. (h-k) The SEM images of a denticle with the bony base after fractured in liquid nitrogen. (h) An isolated denticle sitting on the bony shaft and the surface is covered by the debris of dermis. (i) The close-up view of the surface of the denticle shows it is very solid and no distinct fibrous structure found. (j) The close-up view of the bony base (the shaft of the spine) reveals its porous structure. (l) Collagen fibrils with characteristic banded pattern confirms the shaft is a porous bone.

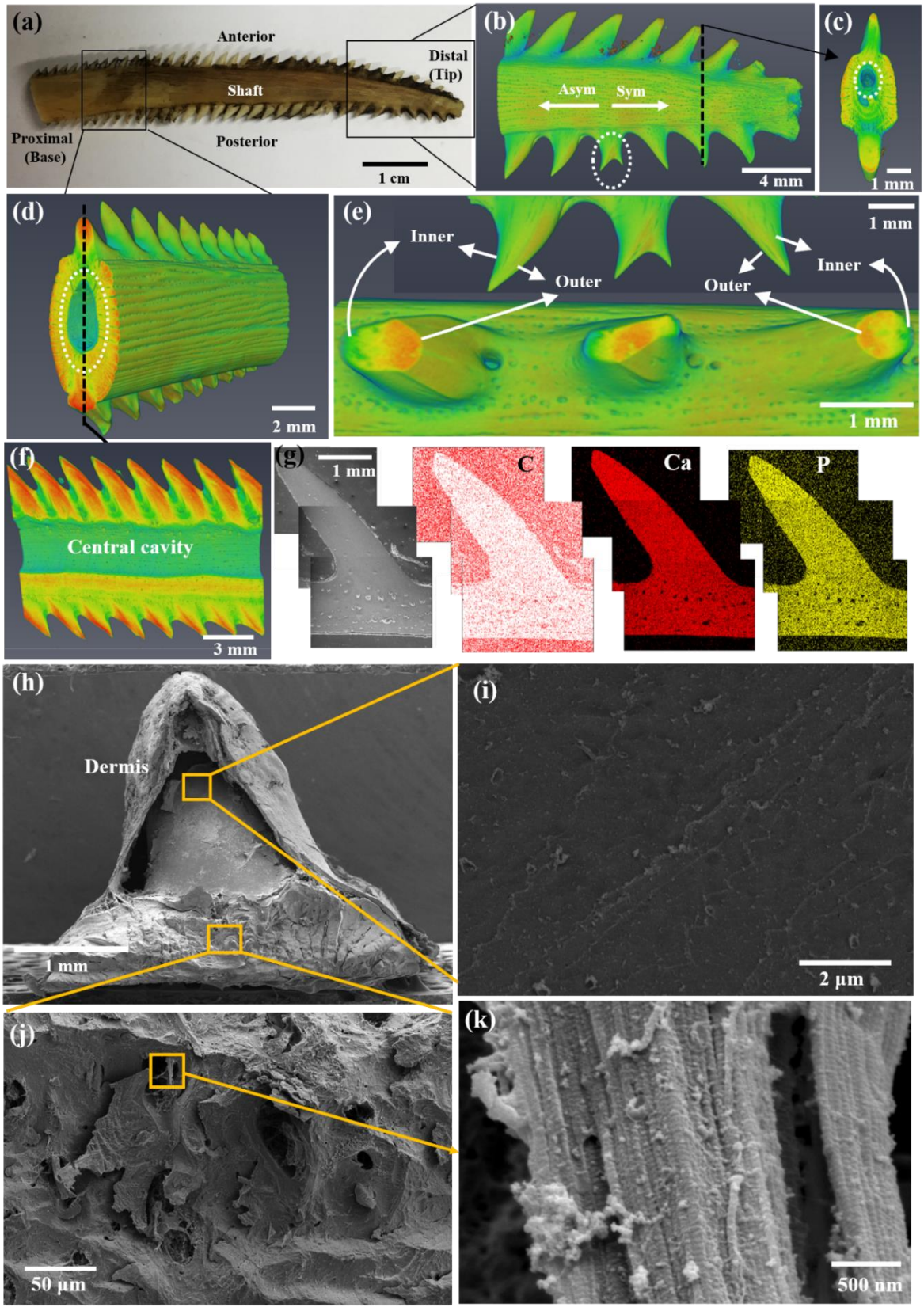
(a)
Anterior
Distal (Tip)
Shaft
Proximal (Base)
Posterior
1 cm
(b)
Asym
Sym
4 mm
(c)
1 mm
(d)
2 mm
(e)
Inner
Outer
Outer
Inner
1 mm
1 mm
(f)
Central cavity
3 mm
(g)
1 mm
C
Ca
P
(h)
Dermis
1 mm
(i)
2 µm
(j)
50 µm
(k)
500 nm

The mechanical properties are very important for the pectoral spines to be effective threatening weapon for the thorny catfish. The spines are not only sufficiently strong for damaging the predators but also quite tough through their great deformability. Figure 6-12 (a) presents the Vickers microhardness map on the longitudinal cross-section of the dentations with bony base. The micro-hardness of the dentations gradually decreases from the tip of the porous bony base in a clear gradient fashion. The hard dentation tip provides strength and stiffness for penetrating the tissue of predator and the soft porous bony base confers deformability for toughness while maintaining a low weight. Same as the strategy adapted in many other biological materials, the gradient hardness transition between different layers reduces the interfacial stress and enhances the stress redistribution, resulting to the increased the interfacial toughness[69,174].

The highly mineralized dentations are hard but still manifest some ductility, especially in the hydrated state. The SEM images of an indent on the dentation, circled in Figure 6-12 (a), are provided in Figure 6-12 (b) and (c), suggesting a great deformability of the highly mineralized dentation due to the absence of any crack formed at the corner of the well-defined indent with a clear diamond shape. The spine shaft has a hollow structure inside and the shell is composed of porous bone. The compressive stress-strain curves of 4 samples cutting from the bony shell of the hollow shaft are presented in Figure 6-13 (a) with the compression along the longitudinal direction in the fully hydrated state, as indicated in the inset. Due to the limitation of our specimens, the four samples were dissected from different regions of one spine shaft, leading to the relatively large variations in the stress-strain curves. The average strength of four tested specimens is 97.24 ± 16.03 MPa, which is much higher than the value for trabecular bone (5 ~ 10 MPa) but lower than that of compact (100 ~ 300 MPa), indicating that the porosity of the bony spine shaft is between that of cortical bone and cancellous bone[175]. The serrations and the plateau region after the yield

point in the stress-strain curves indicate that, like other bone-based tissues, the shell of the spine shaft has various crack-arresting mechanisms to prevent catastrophic failure after its initiation, making it a damage-tolerant material. The toughening mechanisms at different length scales are unfolded in Figure 6-13 (b-g). The major crack forms obliquely (Figure 6-13b), manifesting that the fatal failure is due to the shear stress generated in the uniaxial compressive load. Numerous secondary cracks are formed near the major crack, as shown in Figure 6-13 (b) and (c), which serves as an important manner for dissipating the stored elastic energy. Fibrillar bridging and pull-out behind the tip of secondary cracks reveals that the collagen fibrils are stretched during the crack advance, which reduces the stress intensity around crack tip and arrests the crack propagation extrinsically. Similar extrinsic toughening mechanisms are also found in the large fibers bridging the major crack (Figure 6-13e), mainly fibrillar delamination, bridging, and pull-out (Figure 6-13f, g) at the micrometer scales all acting in concert, conferring the spine excellent damage tolerance. In summary, the sharp dentations with gradient hardness sit on a strong and tough hollow shaft, making the pectoral fin spines a light-weight structural material with excellent mechanical performance, which serves as a powerful weapon to help the thorny catfish defend themselves actively.

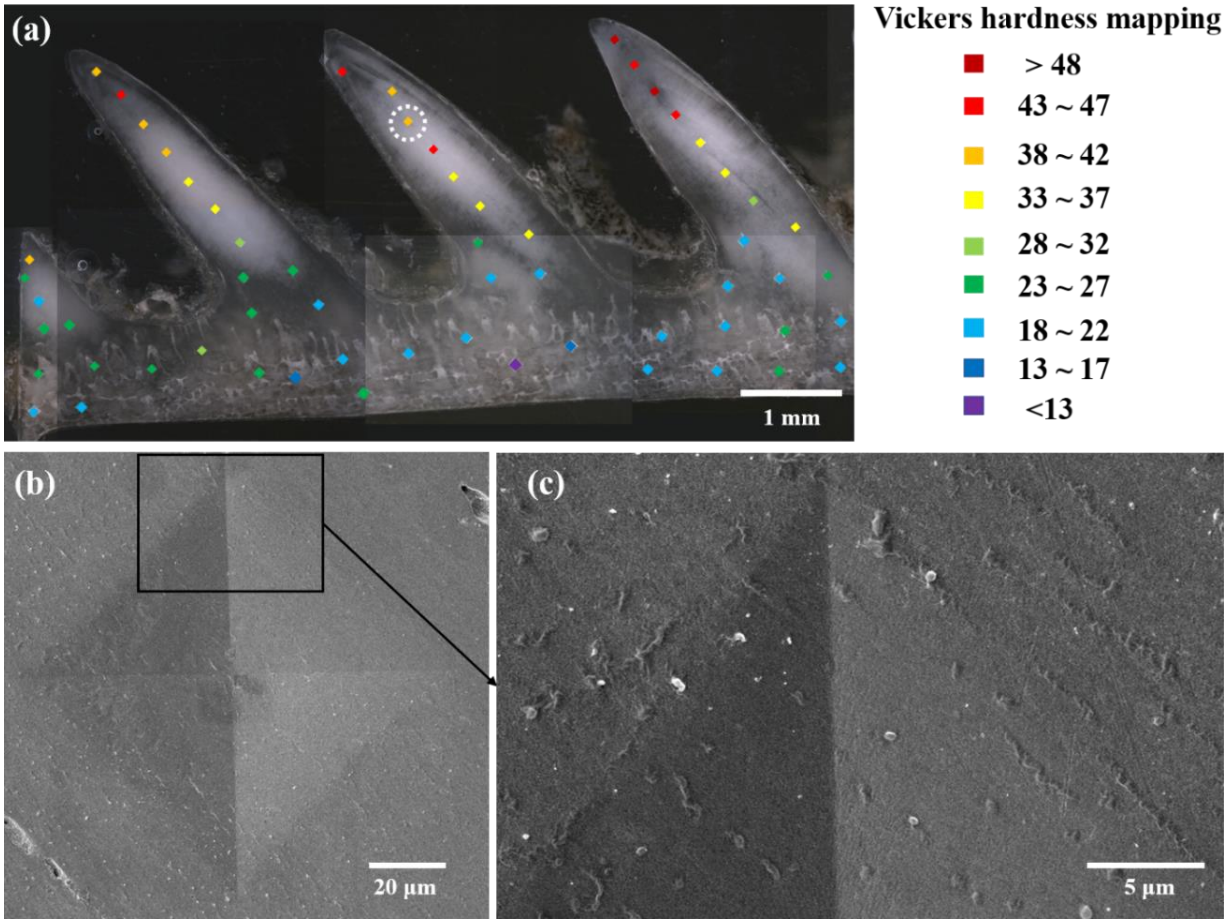

Figure 6-12 The microhardness test result on the spine. (a) The microhardness mapping on the longitudinal cross-section on the spine implies the Vicker's hardness gradually decreases from the tip of the dentations to the bony shaft. (b) The SEM of the region circled in (a) shows the clear diamond indent. (c) No crack appears on the indent corner indicating the great deformability of the denticle.

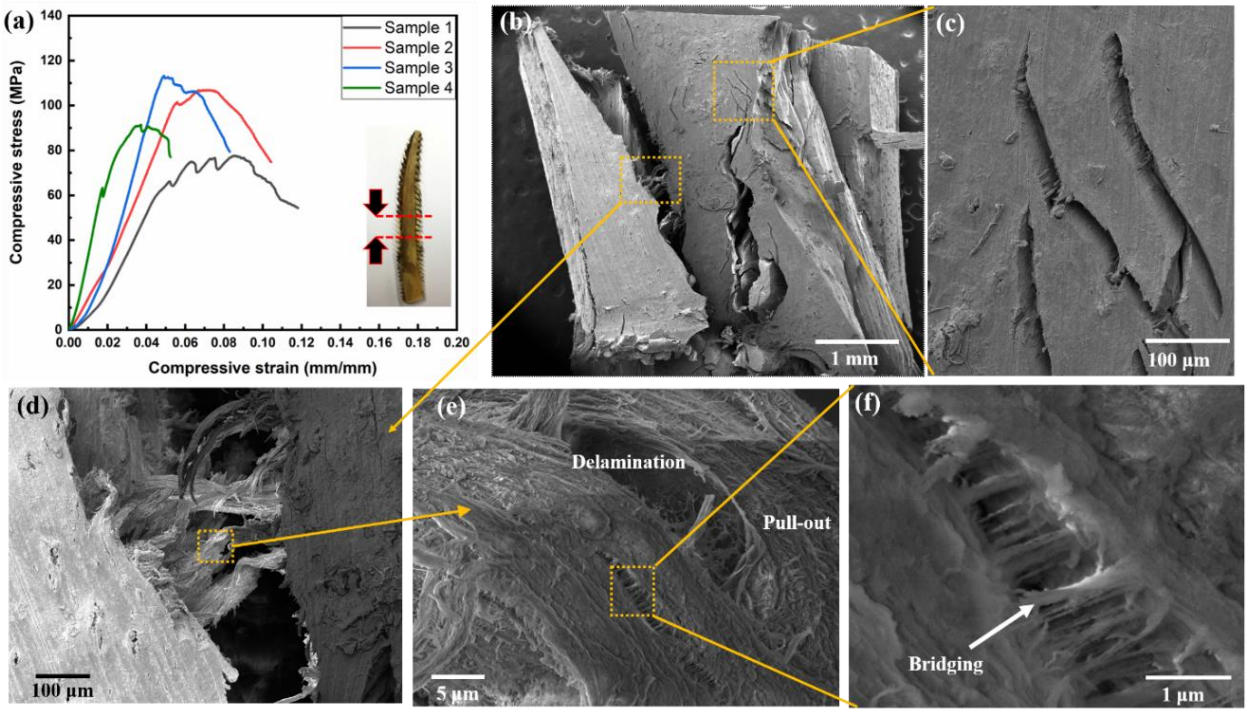

Figure 6-13 The compression test and the failure surface characterization on the spine. (a) The compressive stress-strain curves of for the spine shaft. The compression direction is shown in the inset. (b-g) SEM images of a representative after compreesive failure. (b) Oblique cracks indicate the failure is due to the shear force. (c) Numerous secondary cracks are observed around the major crack. (d) Mineralized fibers are still bridging major crack after shear fracture. (e) Delamination, pull-out and bridging of collagen fibrils on the bridging fibers. (f) Close-up view of the collagen fibril bridging.

6.3.3 Mid-lateral hooked scutes

The other unique characteristic of thorny catfish (Doradidae), which distinguishes them from other armored catfish, are the two arrays of hooked scutes embedded in the dermis along both mid-laterals. One array of the scutes was dissected as shown in Figure 6-14 (a). The micro-CT is presented in Figure 6-14 (b-d). Unlike the assembly of other fish scales or dermal plates, Figure 6-14 (b) shows that the scutes are connected without overlapping; Figure 6-14 (d) indicates that their base is curved for better anchoring on the fish body and terminates in fibers, which can significantly increase their stability. The cross-sectional views in Figures 6-14 (c) and (d) show that the scute tip is very solid with higher mineralization (yellow); the porosity gradually increases from the central region to the base, where the mineralization is lowest (blue).

There is a layered structure shape following the contour of scute outline, as highlighted by the dotted lines in Figure 6-14 (c); it is suggested that it is associated with the layer-by-layer deposition of minerals during the growth of the scutes. Figures 6-14 (e-j) present SEM images of the surface after fracturing the scutes in liquid nitrogen, revealing additional details of the inner structure. The alignment of minerals as suggested in Figure 6-14 (c) is confirmed in Figure 6-14 (e) and the base region is composed of porous bone (Figure 6-14f), with pore size varying from micrometers (Figure 6-14h) to nanometers Figure 6-14 (j). The collagen fibrils, with well-defined 67 nm d-spacing shown in Figure 6-14 (i), are wound around the pore to form a supporting wall (Figure 6-14g) but their arrangement in the solid region (area between pores) is more random, as Figure 6-14 (j) shows.

Figure 6-14 The structure of the midlateral scutes of thorny catfish. (a) There are two sets of scutes with hook shape sitting on the midlateral position of the thorny catfish on both sides. (b-d) Micro-CT of the scutes. (b) The scutes are connected with each other without overlapping. (c) The longitudinal cross-section reveals the scute tip is highly mineralized (yellow-red) and the mineralization gradually decrease to bony base (yellow-green-blue). In contrast, the porosity gradually increases from the tip to base. The contour lines of the mineral deposition are indicated with dot lines. (d) The transverse cross-section reveals the wide curved base helps the scute anchor on the fish body steadily. (e-j) SEM images of the cryo-fractured scutes. (e) The fractured surface of the tip region indicates the minerals are deposited along the direction as the dot lines indicate, consistent with the observation in (c). (f) The porous bony base is covered by debris of dermis. (g) Collagen fibrils wind around the pores forming the wall. (h) The pore size varies from nanometers to hundreds of microns. (i) The characteristic 67 nm d-spacing of the mineralized collagen fibrils. (j) The fibrils orient more randomly at the region between the pores.

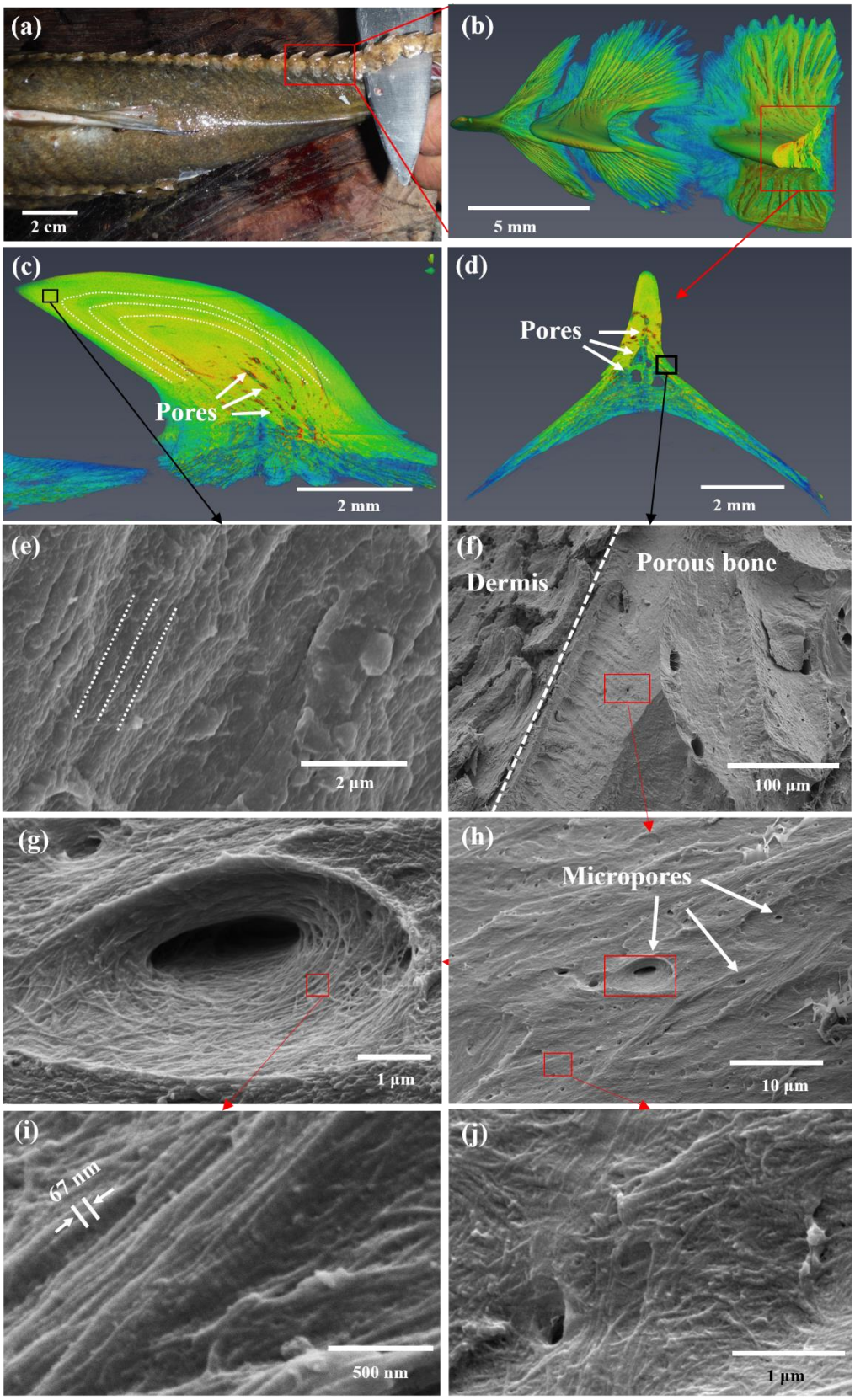
(a)
2 cm
(b)
5 mm
(c)
Pores
2 mm
(d)
Pores
2 mm
(e)
2 µm
(f)
Dermis
Porous bone
100 µm
(g)
1 µm
(h)
Micropores
10 µm
(i)
67 nm
500 nm
(j)
1 µm

The gradient structure generates varying mechanical properties of the scute, as presented in Figure 6-15 (a). Hardness mapping indicates that the scute tip and central region have higher values (red ~ yellow) which gradually decrease toward the porous base (blue ~ purple). The contour lines of the mineral alignment are also visible in Figure 6-15 (a), consistent with the observation in Figure 6-15 (c). No recognizable cracks are formed at the corners of the well-defined diamond micro-indents, as presented in Figure 6-15 (b) and (c), revealing the great deformability of the scute and making it a very tough material. Through these ingenious structural design and gradient properties, the hooked scutes can cut into soft tissue with their sharp hard tip and can accommodate the deformation and delocalize the stress by the soft porous bony base. Thus, the mid-lateral scutes serve as a supplementary weapon in addition to the pectoral spines and enhance the active defense mechanism capability.

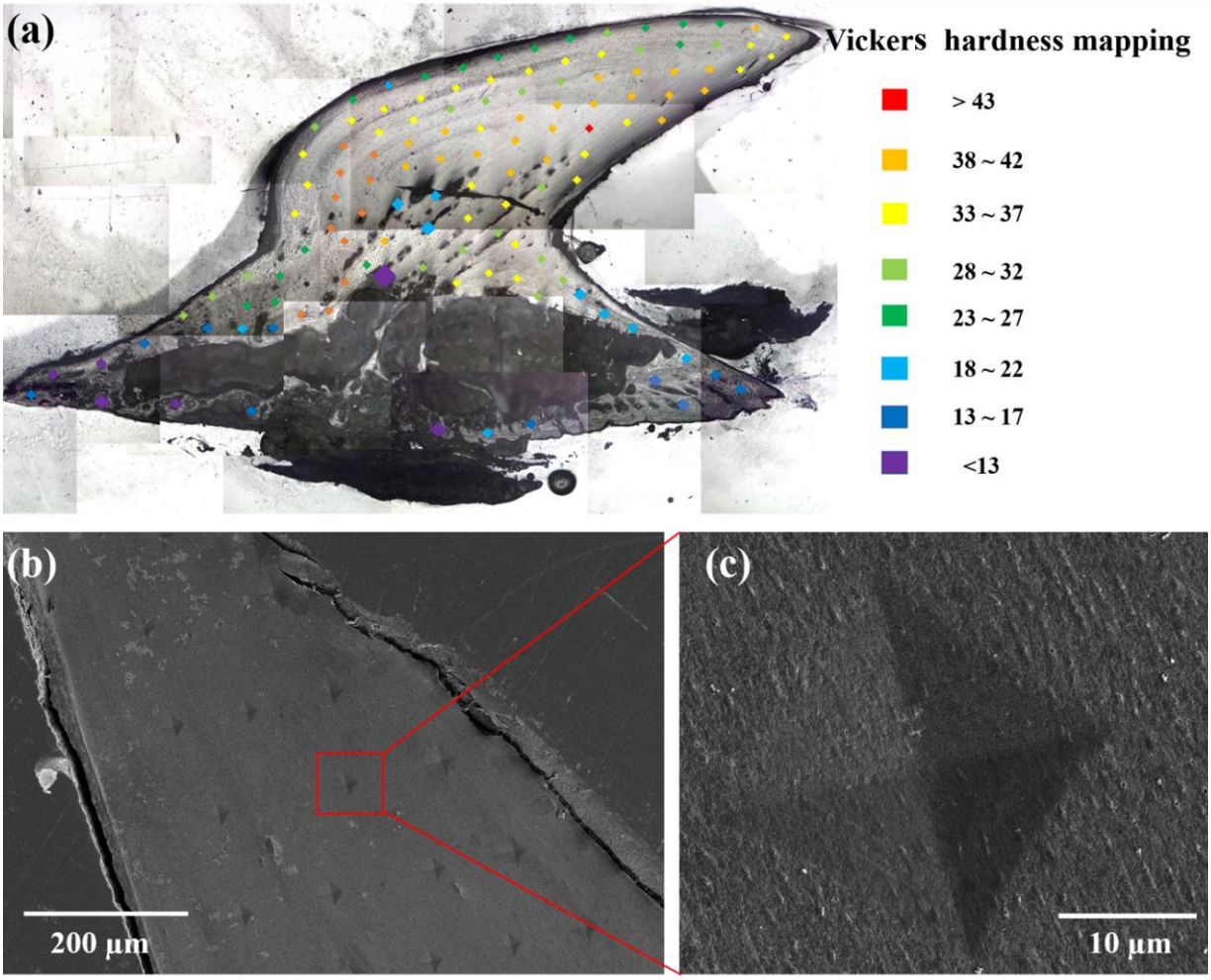

Figure 6-15 The microhardness test on the midlateral scute. (a) The micro-indentation hardness mapping on the longitudinal cross-section of the shows the there is a gradient decrease of Vicker's hardness from the hook scute to the porous bony base, consistent with the mineralization. (b) The SEM of the indents at the highly mineralized hook region show the clear diamond indents. (c) No crack appears on the indent corner indicating the great deformability of the mineralized hook on the scute.

6.3.4 Stridulation

Thorny catfish (Doradidae) are also called “talking catfish” because of their ability to produce a stridulatory sound by moving their pectoral spines. This noise generation mechanism is due to the same structure causing the locking phenomenon[176]. During each sweep of pectoral spine, at a smaller muscular force applied on the spine, the ridges on the dorsal component are rubbed against the rough surface of spinal channel and generate a series of pulses which produce the characteristic sound. Previous research quantitively identified that the channel catfish, can also produce stridulatory sound by moving the spines; the sweep duration is defined by how far the spine moves through the spinal fossa and each pulse duration is determined by the thickness of each ridge on the base of spine and how long each ridge is in contact with the spinal fossa’s surface. These measurements confirm that the stridulatory sound is based on the rubbing between the rough surfaces[177]. Many creatures can produce under water sounds via extrinsic sonic muscles such as swimbladder sounds, but the stridulatory sound is unique to catfish. Different from the drumming sounds generated by the swimbladder which serve as intraspecific communication, the stridulatory sounds are produced by the thorny catfish target predators in interspecific communication and act as a warning[168,170,178].

6.4 Summary

Based on the structural characterization and mechanical testing, we unraveled the active defense mechanism of the armored (thorny) catfish, which rely on two potent tactical weapons as summarized as follows:

a. *The sharp pectoral spines.* The unique pectoral spines of thorny catfish can be partially or fully locked under threat and provide defensive protection through their structure. The locking mechanisms are generated by two frictions: the friction generated by the dorsal component and spinal channel, combined with the friction generated by anterior component and the locking chamber. Many catfish (Siluriformes) species have a similar mechanism as a mechanical active defense which expands their circumferential size thereby increases the handling time for predators and makes them an unfavorable prey choice. Such locking ability is also associated with the stridulatory sounds produced by catfish, which serves as a warning signal to contribute to the active defense.

b. *The mid-lateral scutes.* In addition to the lockable spines, thorny catfish also possess two arrays of mid-lateral dermal scutes with sharp hooks, which also have potential cutting ability and provide supplementary active defense capability.

In addition to the ingenious structural design of the articulation of the spine and the unique assembly pattern of the dermal scutes, their materials design at the meso or micro levels, is as well impressive, conferring the pectoral spines and mid-lateral scutes excellent strength, and toughness at a small weight penalty. The first element to this success is the hollow structure of the spine shaft, the central cavity of which is elongated along the axial direction, forming a tubular-like structure and enclosed in the bony shell. By moving the mass farther from the neutral plane, the flexure/buckling resistance of the spine shaft is significantly raised with no additional weight

added, similar with the design strategies adapted in the feather rachis. Moreover, the porous structure is another important design in both shell of spine shaft and the base of the scutes for reducing weight. Taking the bony base of the mid-lateral scutes as an example, with pore size varying from nanometers to several-hundred micrometers, such porous bone not only makes considerable contribution to keep light weight, but also provides great deformability and serves as damping region that connects to the soft tissues. Last but not least, the widely used gradient structure that has been identified in the dentations on spines and solid tip of hook-shape scutes, both serving as the cutting tool for the damage the soft tissues of predators. By such functional requirement, the outer surface of the dentations and the tip region of the scutes are very hard with high mineralization. These two properties gradually decrease towards the soft bases, forming a gradient transition structurally and mechanically, which can accommodate better deformation between different components, mitigate interfacial failure, as well as reduce required mass.

All in all, by combining all these mechanical active defense mechanisms, thorny catfish successfully avoid becoming an easy prey to predators and flourishingly survive in the various ecological environments in south America. Such intricate structural and material design promises to be an inspiration for novel light-weight structural materials or innovative robotics with gradient structures. These are of great importance in biological organisms, as shown by Liu et al.[174].

Chapter 6, in part, is in preparation for publication with coauthors Z. Tang, W. Yang, R. O. Ritchie and M. A. Meyers. The dissertation author is the first author of this work.

CHAPTER 7: HYDRO-ACTUATED REVERSIBLE DEFORMATION OF PINE CONE

7.1 Introduction

Multi-functionality is a distinct characteristic of biological materials[179]. Among structural materials which are responsible for carrying load, many tissues in plants and animals can perform additional functions, such as responding to external stimuli in prescribed fashion[39,41,88]. The stimuli can be heat, light, electricity, hydration or external stress; in response to them, the tissues can change their intrinsic properties such as morphology, color, transparency or mechanical properties[39,40,43,83,180]. In this chapter we briefly introduce some biological materials that can passively change their shape depending on the moisture change and then focus on the pine cone, a classic example of reversible hydro-actuated deformation.

Plants are well-known for their lack of mobility. To disperse their seeds to a broader range and increase their germination and survivability, they have developed various ingenious strategies[84,88,181-183]. Moisture is critical for the seed to survive and the relative humidity changes with day and night and season generates a simple and controllable driving force. Many plants disperse their seeds or enable them to bury themselves into the soil through the tissue deformation that purely depends on the change of moisture[48,86].

Plants take different strategies to improve the survivability of their seeds. Ice plants open and close their seed capsules in an opposite way[46]. Since their habitats are in arid or semi-arid area, their seed capsules only open to release seeds when the relative humidity in the environment is sufficient for germination, which increases the possibility that seeds will be dispersed under favorable conditions. The bauhinia variegate[47] also opens and closes its seed pod under the favorable moisture conditions but the difference is that it opens its seed pod by the twisting when dehydrated.

Instead of designing smart ways for seed dispersal, some plants focus on the improvement of germination. The wild wheat awns can open and close their dispersal units through bending them according to the change of relative humidity between day and night, which propels the seed penetrate into the soil[48]. The Musky Heron's bill has a long tail on its seed, which can coil and uncoil very fast in response to the moisture change[49,86]. Such highly reversible coiling and uncoiling movement can effectively drill the seed into the soil. These self-burial strateties are very efficient to improve the germination and increase the survivability of the seeds.

In this chapter we cast our interest on the best known example: the pine cone. In the dry season, dehydration drives the pine cone to open and the seeds are released and carried by wind to travel for long distances. In rainy days, the weather is not favorable for the seed dispersal and so the cones are closed to protect seeds. This releasing and protection strategy is achieved through the highly reversible bending deformation of the cone scales. Previous research indicates that each scale is made up of two layers on the upper and lower sides with different structure regarding the cellulose microfibril angle. Our results bring to life new aspects of this complex mechanism.

7.2 Methods

7.2.1 Materials

7.2.1.1 Pine cone

The cones were collected from Torrey pines (*Pinus torreyana*) on Torrey Pine Road (La Jolla, CA, 92037). The scales were cut from the cones by diamond saw; all the video and images were recorded using Webcam. The sclerenchyma fibers and sclereids tissue in each cone scale were separated by a Dremel rotation tool.

7.2.1.2 Preparation of hydrogels

Alginate was kindly provided by FMC BioPolymer, LF10/60, USA. Acrylamide (AAm) (99+%) was purchased from Acros, USA. N,N0-Methylene bis(acrylamide) (MBAA), ammonium persulfate (APS) (498%), N,N,N0,N0-tetramethyl-ethylenediamine (TEMED) (499%), and calcium sulfate dihydrate (98%) were purchased from Sigma Aldrich. All materials were used as received without further treatment.

The hydrogel was synthesized based on the method proposed by Sun et al.[180] with minor modifications[181].1 g of alginate and 8 g of acrylamide were dissolved in 51 g of deionized water, and then mixed with 0.0048 g of MBAA and 0.02 g of APS, which were the crosslinker and thermal initiator for acrylamide, respectively. The mixture was stirred at room temperature for at least 2 hours until homogeneous. After that, the solution was degassed in a vacuum chamber and used as Solution 1; while 0.02 g of TEMED, the initiator accelerator, and 0.1328 g of calcium sulfate dehydrate, the ionic crosslinker for alginate, were dissolved in 5 g of deionized water, sonicated for 2 min, and used as Solution 2. Solution 1 and Solution 2 were mixed fast and homogeneously, and then rapidly poured into a customized mould with dimensions of 50 mm × 20 mm × 20 mm or 50 mm × 20 mm × 40 mm. Finally, the specimen was transferred into an oven at 53 °C for 120 minutes, after which the polymerization of AAm was complete, and a double network hydrogel was formed.

The double network gel was removed from the mould after fabrication, and then frozen at -20 °C for 24 hours, or frozen under liquid nitrogen (-196 °C) for 10 minutes; after that, the frozen samples were transferred into a freeze-dryer (Labconco freeze-dry system) for complete lyophilization, and dry microporous and microporous polymer matrices were generated. The

double network tough gel was removed from the mould after fabrication, and then dried at room temperature for two days for complete dryness.

7.2.2 Structural characterization

The micro-CT of the cone scales were conducted on air-dried samples in a Zeiss Versa 510 X-ray microscope (Zeiss, German) in National Center for Microscopy and Imaging Research (NCMIR).

The SEM (scanning electron microscopy) characterization on pine cones and hydrogels were conducted with FEI Quanta 250 (FEI, Hillsboro, OR). The pine cone samples for SEM characterization are first immersed in the 2.5% glutaraldehyde for 1 h to fix the structure and then dehydrated with an ascending series of ethanol (30, 50, 70, 90, 95 and 100 vol.% twice). To obtain the oblique fracture surface, the scale was immersed in liquid nitrogen for 30 s and fractured using forceps immediately. All pine cone and hydrogel samples were dried with Tousimis Autosamdri 815B ((Tousimis, Rockville, MD) and then sputter coated with iridium using an Emitech K575X sputter coater (Quorum Technoloties Ltd.) before observation.

7.2.3 Mechanical test

Microhardness tests were performed on the polished cross-section of pine cone scales, using a LECO M-400-H1 hardness testing machine equipped with a Vickers hardness indenter and the applied load is 200 grams. The morphology of the indents was characterized by optical microscope.

The experimental setup for actuation force testing was shown in Figure 7-9. The root of isolated cone scale was fixed by clamps and the tip part directly contacted the load cell. Based on our setup, the upward bending was generated by immersing the cone scale in a tank of hot water

(~ 80 ˚C). The generated bending force was recorded by an Instron 3367 testing machine (Instron Corp., Norwich, MA) for 2 hours.

7.2.4 Moisture sorption isotherm

The moisture sorption isotherm was conducted in an environment chamber (Model: LRHS-101-LH, Shanghai Linpin Instrument Stock Co. LTD, China). The temperature was precisely controlled at 25 ˚C. 10 isolated cone scales are tested in the environmental chamber. The relative humidity was increased from 30% to 100% with increments of 10%, and then reduced in the same way. In each step, the weight of each scale was measured until the it did not change. The absorption (moisture content) was calculated from the weight at two relative humidities (RH%) from:

$$Absorption = \frac{Weight\ of\ sample\ at\ each\ RH\%}{Weight\ of\ sample\ at\ RH\ 30\%}$$

7.3 Results

Figure 7-1 (a) and (b) present the opening and closure of a Torrey Pine cone in the dry and wet state, respectively. The polished cross-section shown in Figure 7-1 (c) indicates that the cone is comprised of two components: the bright part are the sclerenchyma fibers and the dark region is the sclereid. Previous research[45] indicates that the mechanism of bending therefore is determined by variation in the orientation of cellulose microfibrils, which control the hygroscopic expansion of the cells in the two layers. The sclerenchyma fibers have the microfibrils oriented along the cells (low microfibril angle), thus resisting elongation (Figure 7-1d), while in the sclerids, the microfibrils are wound around the cell (high microfibril angle) allowing it to elongate when moist (Figure 7-1e). The mismatch of the swelling strain between these two components of the bi-layer structure enables such highly reversible hygroscopic movements that significantly improve the dispersal and germination of the seeds.

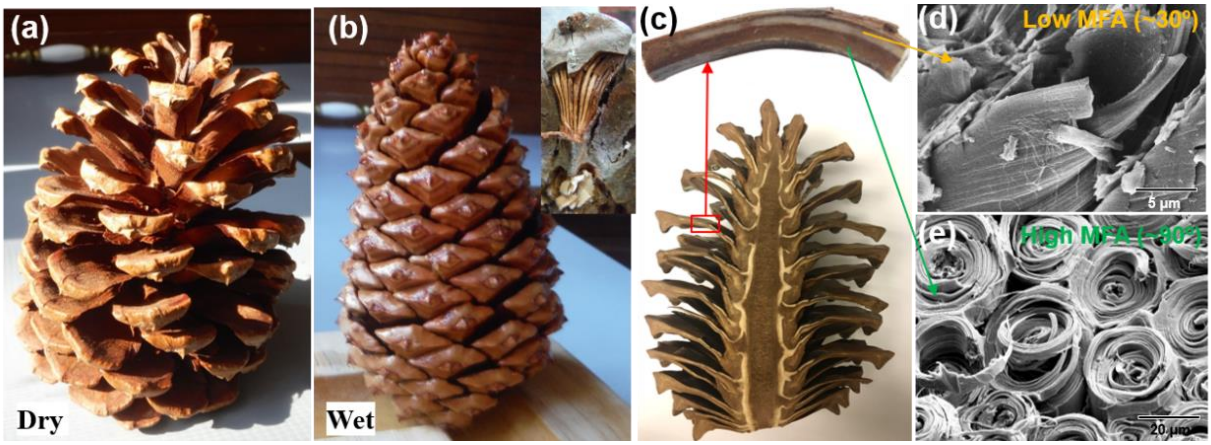

Figure 7-1 Hydro-actuated reversible deformation of pine cone. (a) The pine cone in dry season opened for releasing seeds. (b) The closed cone in wet state, protecting seeds. Inset is a broken scale revealing sclerenchyma fibers that are covered, in the intact scale, by a sclereid layer. (c) Polished cross-section of an entire cone and a portion of isolated scale, showing double-layered inner structure. The bright upper layer is composed of sclerenchyma fibers and the dark lower region primally consists of sclereids. (d, e) SEM images of cell walls in sclerenchyma fibers and sclereids, respectively.

Figure 7-2 (a-c) shows the pine cone scale bends upward which enable the closure of the entire cone when the scale is immersed in water. The total angle change for this isolated scale is almost 80°. Since the hygroscopic movement in pine cone is a diffusion-based process, the rate of the bending movement gradually decreases as the immersion time increases (Figure 7-2d).

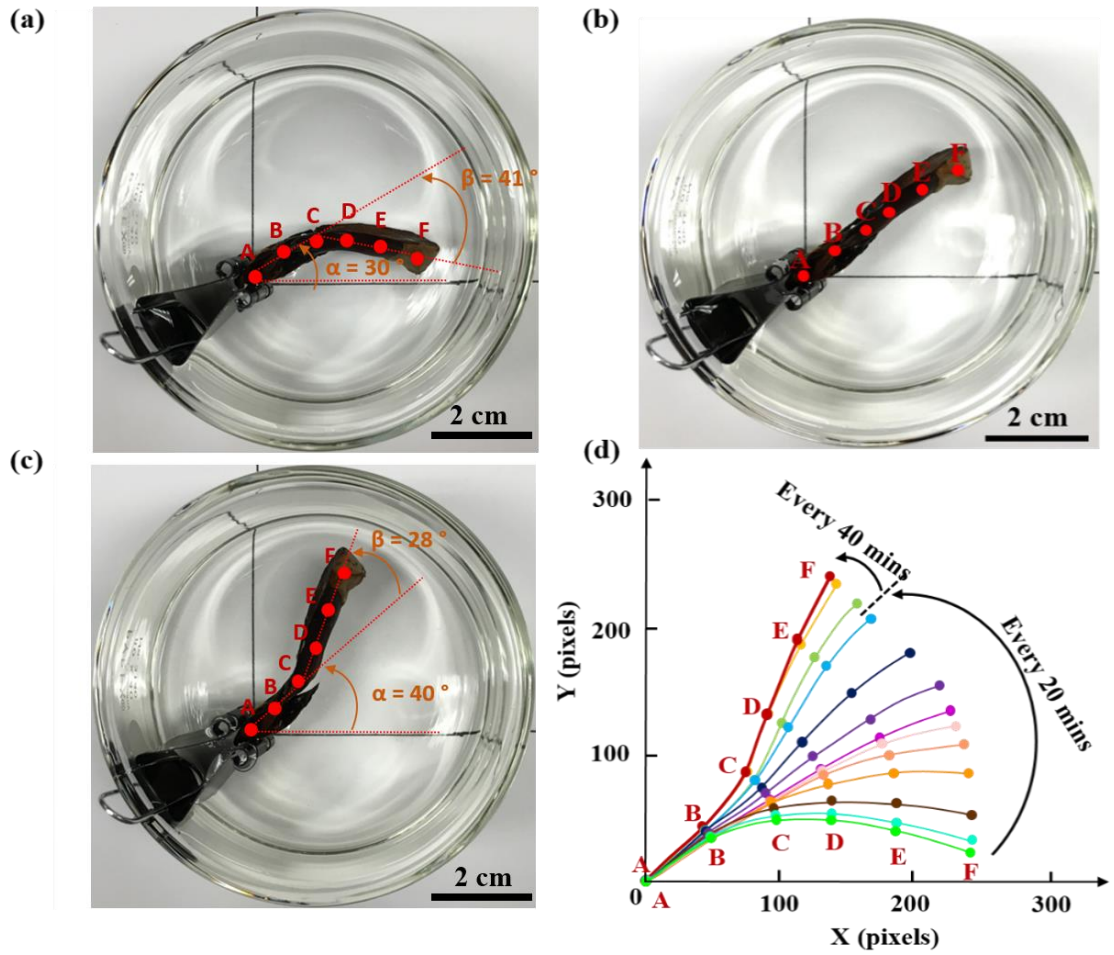

Figure 7-2 The bending movement of a single pine cone scale with hydration. (a-c) Bending process of an isolated scale with immersion in water: angle α increases from 30 to 40° whereas β decreases from 41 to 28° (d) The plot of relative movements of points A–F during wetting.

As introduced previously, the pine cone scale is basically composed of sclerenchyma fibers and sclereids and the hydroscopic movement is achieved by the this bi-layered structure presented previously[45,93]. However, during the process to confirm this mechanism, we found that the reversible hygroscopic movement of pine cone is probably not purely caused by this bi-layer structure.

The sclerenchyma fibers, an isolated fiber and the sclereid matrix were mechanically separated as shown in Figure 7-3 (a), (c) and (e), respectively. These three parts were immersed

into water independently and it is surprising to observe that, contrary to the previous hypothesis[93], the sclerenchyma fibers, an isolated fiber and the sclereid matrix all can deform with the uptake of water in the tissue, as shown in Figure 7-3 (b), (d) and (f), which suggests that the bi-layer structure proposed in previous research[93,182] is not complete. In order to unfold the mechanism of the hygroscopic movements of the pine cone, the structure of pine cone scale was characterized in detail.

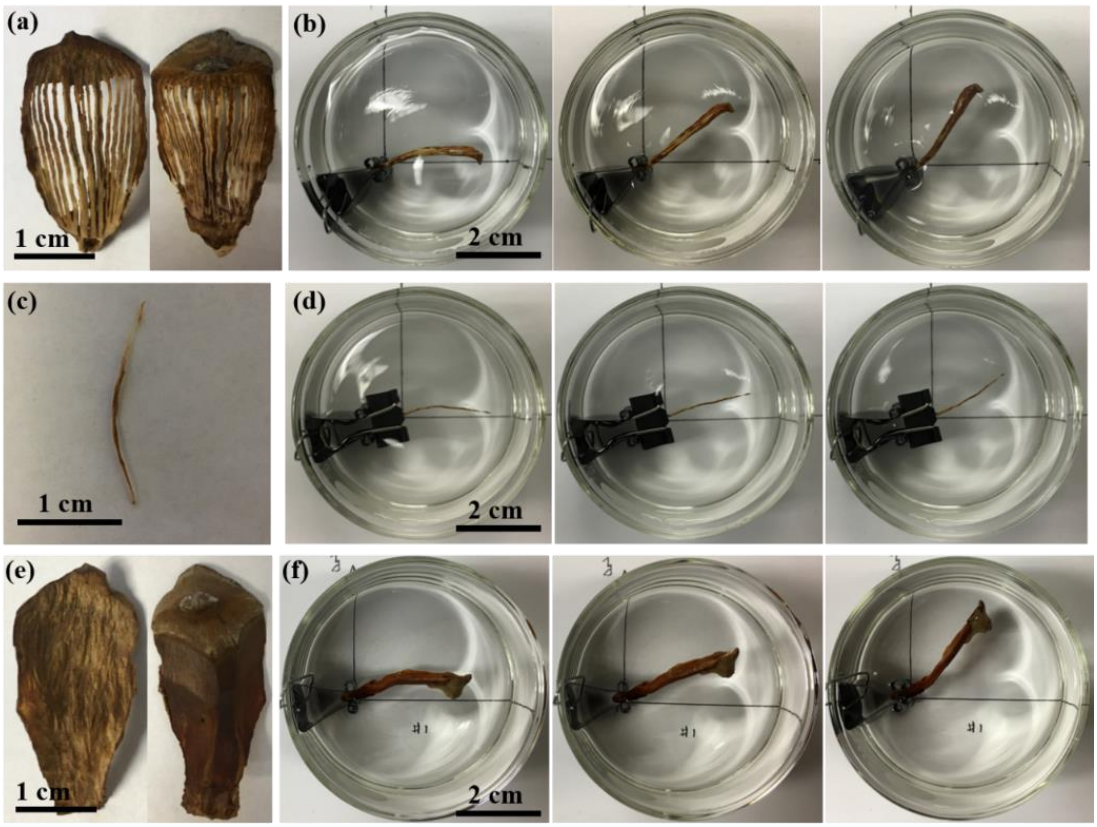

Figure 7-3 The bending movement of the two components of pine cone with hydration (a), (c) and (e) are the images of mechanically separated sclerenchyma fibers, an isolated fiber and the sclereids, respectively; their independent hygroscopic movements are shown in (b), (d) and (f), respectively.

To further investigate the other mechanisms in addition to the mismatch of MFA in each layer, the micro-CT scan of an isolated cone scale was performed, as shown in Figure 7-4. The normal view of the micro-CT scan of a cone scale is shown in Figure 7-4 (a). Figure 7-4 (b) shows the longitudinal cross-section of this scale, indicating that sclerenchyma fibers branch and become thinner from root to the head region and that the density of sclereid tissue decreases with same trend. Such gradient structural change in different regions is confirmed by Figure 7-4 (c) and (d). The close-up views of the transverse cross-section in different region presented in Figure 7-4 (e) and (f) clearly show that the porosity of sclereid tissue has a gradient structure in pine cone scale: first, the porosity gradually decreases from the region close to the fiber tissue to the surface; second, the porosity gradually increases from the root of the scale to its head. The sclerenchyma fiber is composed of numerous dead plant cells, as shown in Figure 7-4 (g) and (h), and the thickness of cell wall is not uniform among cells, varying with position. The cell wall is thinner, and the hollow tube is larger for the cells closer to the region connecting with sclereid tissue. The gradient of the porosity in sclereid tissue is confirmed with the SEM images shown in Figure 7-5 (b), (e) and (f). For the sclerenchyma fibers (Figure 7-5c), there are holes observed on the cell walls, which facilitate the water diffusion (Figure 7-5g); the microfibril angle does not seem to be constant in different cell walls and varies even in one fiber tissue (Figure 7-5h). In some regions, the microfibrils are more aligned with the axial direction of the cell (Figure 7-5d) but in others certain part of the microfibrils are almost perpendicular to the axial direction.

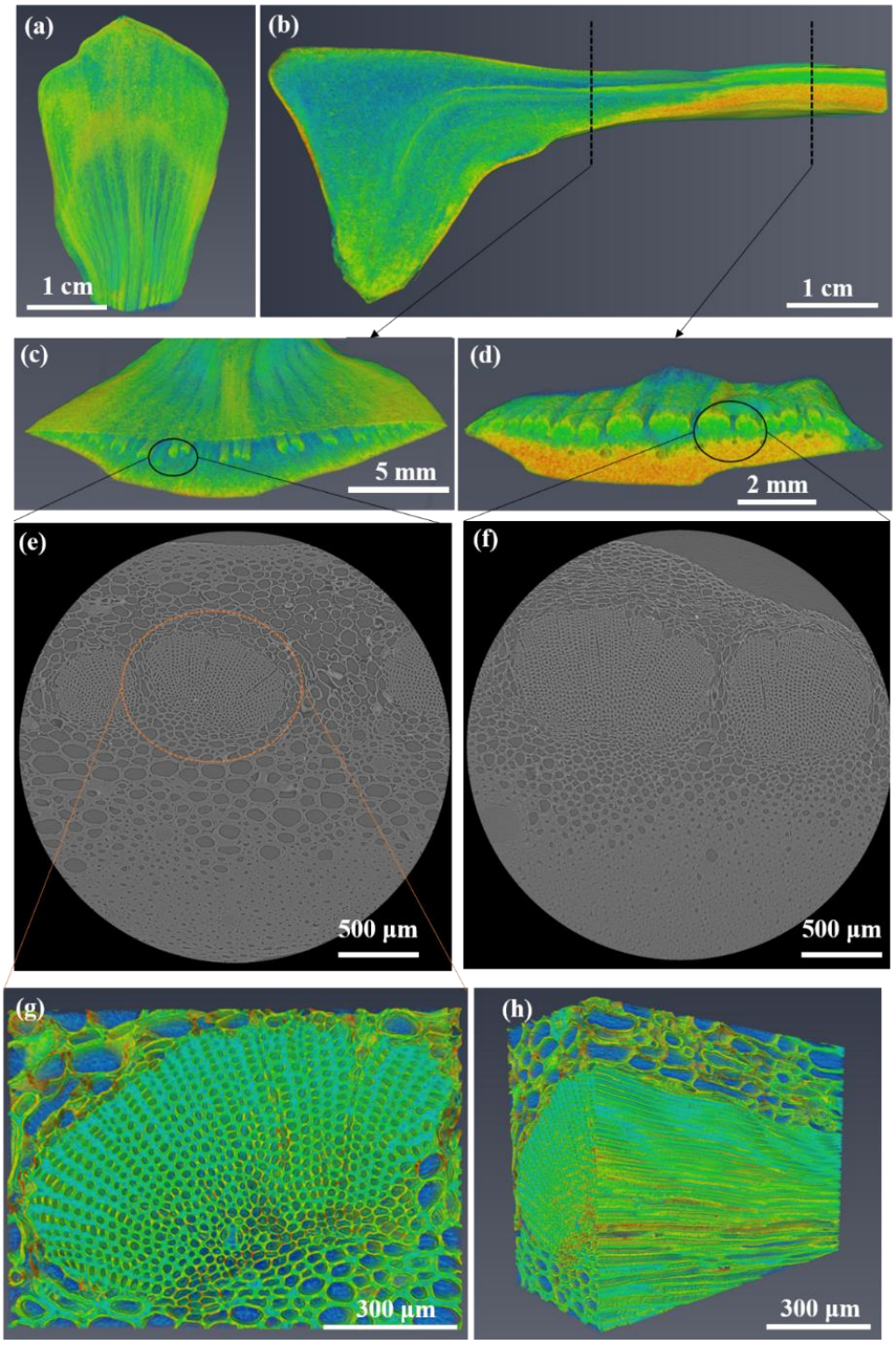

Figure 7-4 The micro computational tomography (µ-CT) of the pine cone scale. (a) Micro-CT of an isolated pine cone scale. (b) The longitudinal cross-section of the CT scan. (c,d) The transverse cross-sections of region far from the scale root and close to the scale root, respectively. (e,f) The close-up view of (c) and (d), respectively. (g,h) The close-up view of an isolated sclerenchyma fiber and its longitudinal cross-section.

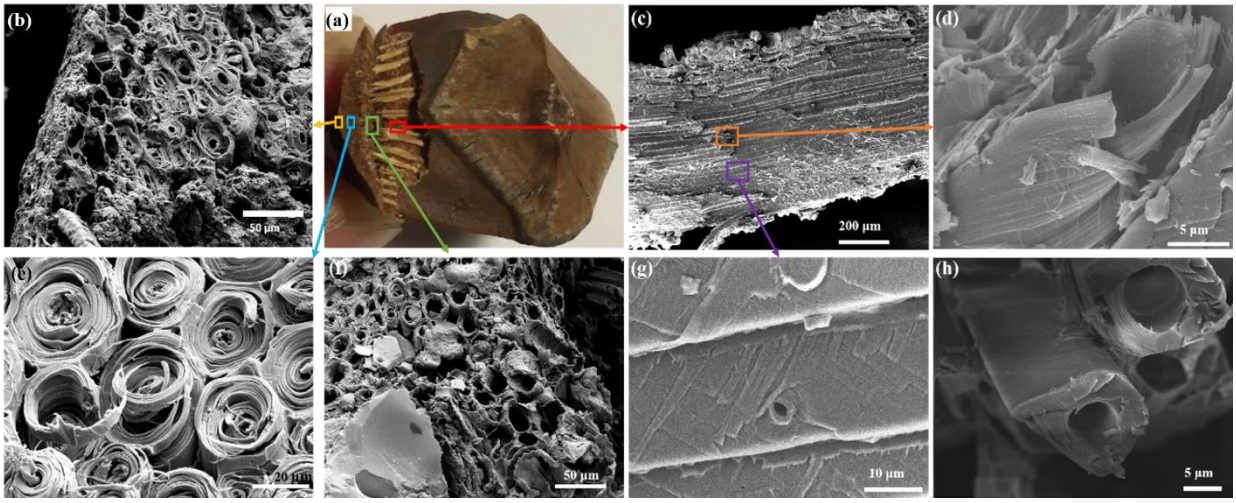

Figure 7-5 The SEM images of a pine cone scale. (a) Optical image showing the two components of pine cone scales: sclereids and sclerenchyma fibers. SEM images of pine cone scale. (b), (e) and (f) are the cross-sections of the sclereids varying in size and porosity from the surface (a) to the region close to the sclerenchyma fiber (e). (c) An isolated sclerenchyma fiber is composed of a bundle of numerous cells. (d) The fractured cross-sections of some cell walls show that the microfibrils are closely aligned with the cell axis. (g) Pore on the cell walls (marked by arrow). (h) Some cells show the microfibrils aligned more perpendicular to the axial direction.

The gradient structure generates a changing in the mechanical properties in the pine cone. Importantly, it decreases the stress concentrations at the interface between the two components. The micro-indentation mapping (Figure 7-5a) of the transverse cross-section of the cone scale shows that, at the same applied load, the indent size on the fiber tissue (Figure 7-5b) and the indent size on the dense part of the sclereid tissue (Figure 7-5c) is almost same and they have similar hardness (~ 17 HV), while the indent size on the porous region of the sclereid tissue is larger, indicating the decrease of hardness (~10 HV) in this region.

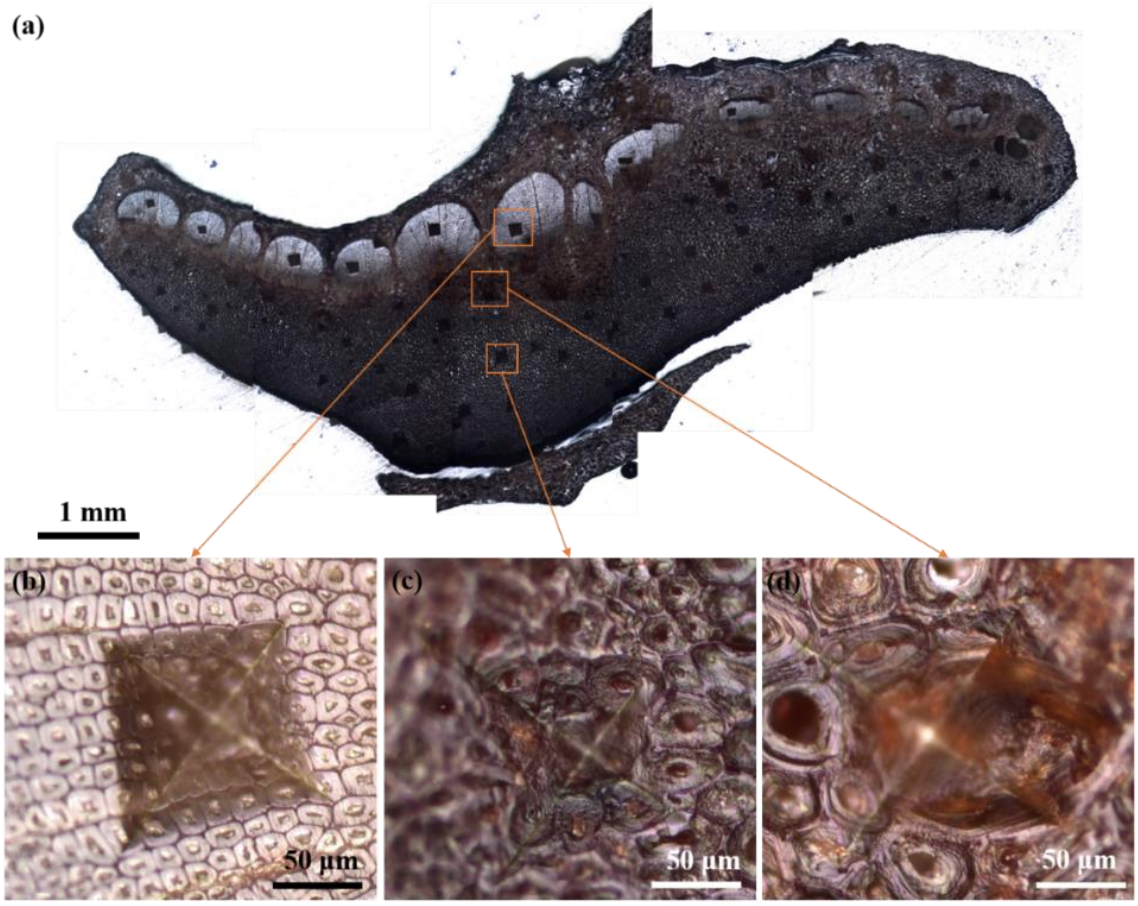

Figure 7-6 Micro-indentation on the cross-section of pine cone. (a) The overall view of the transverse cross-section of the indented pine cone scale sample. (b-d) The representatives of the indentations by a load of 200g on the transverse cross-sections of sclerenchyma fibers, the sclereids far from the fiber region and the sclereids close to fiber region, respectively.

To establish the contribution of the gradient porosity to the swelling strain mismatch in each layer of pine cone scale, we fabricated double network gels with different porosity following the methodology developed by Cai et al.[183] and and then attached them together with Ethyl cyanoacrylate, forming a bi-layered porous hydrogel with different pore sizes. The initial hydrogels were prepared with same methods and the different porosity was created by freeze-drying under different conditions. The macroporous (pore size: 50 ~ 100 μm) double network polymer was fabricated by freezing the gel at −20 °C for 24 hours prior to lyophilization, while the microporous (pore size: ~ 10 μm) double network polymer was fabricated by freezing the gel

at −196 °C for 10 minutes prior to lyophilization. Porous structures with different pore size were successfully generated in the double network polymers through the freeze-drying process. The bi-layered hydrogel was immersed in water overnight and from the selected time-lapse photo presented in Figure 7-6, a bending deformation similar to the pine cone is observed. During a given period, the hydrogel with larger pore size ha a greater ability to absorb water and the swelling strain is larger, compared to the hydrogel with smaller pore size. Based on the mismatch of swelling strains, the hydro-actuated bending deformation is achieved.

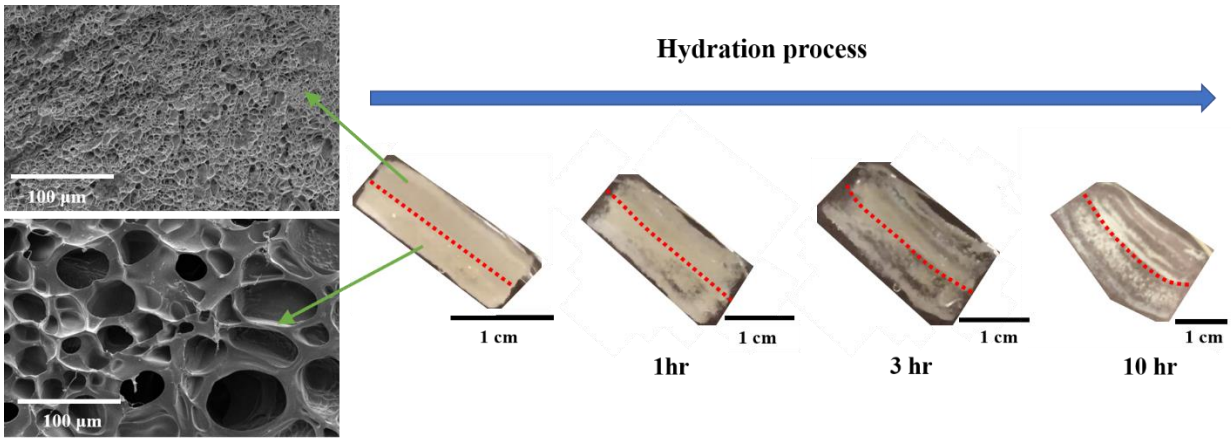

Figure 7-7 Synthesized bi-layered hydrogels with different porosity to demonstrate the contribution of gradient porosity to the hydro-actuated bending.

As far as we can see, the pine cone scale is not a simple bi-layer structure and the mechanism for the hydroscopic movement of pine cone is not purely based on the different MFA in each tissue. Based on our characterization and validation, the contribution of the gradient porosity in the structure of pine cone scale also aid the overall bending deformation of pine cone. However, more quantitative analysis and the systematic investigation of the reversibility of each component is need for discovering the more accurate self-shaping mechanism for pine cone.

Adsorption of water results in the swelling of the cell wall matrix and the amorphous cellulose with the consequent effect on the pine cone tissue. To investigate the interaction of water with cell walls, the equilibrium moisture content of the tissue is usually monitored upon increasing/decreasing relative humidity at a given temperature. The result is a sorption isotherm that provides an entire picture of the different stages of interaction with water (Figure 7-8).

Various models have been developed to understand the different adsorption stages in cell wall-water interaction with each stage corresponding to a different state of water in the cell wall. Due to various interpretations of the results, the true nature of each state is still under debate. However, studies suggest that water can exist in two different states in freshly cut samples; as free water in the porous systems such as the lumen of the cells and as bound water inside the cell walls. From the chemical point of view the hydroxyl groups of the wood constituents are the main target for attracting water molecules. Hence, starting from low relative humidity, the initial adsorption of water into the cell wall is a hydration process where the first layer of water is adsorbed and fixed on the sorption sites mainly consisting of free hydroxyl groups of hemicelluloses and the amorphous regions of cellulose[184]. The reaction is exothermic and the enthalpic gain of the system is the main driving force for adsorption of the first few layers.

The sorption hysteresis is related to the difference between the adsorption and desorption process; In adsorption the water molecules have to be adsorbed into a relatively dense structure, thus requiring a greater external pressure to re-open the structure which was collapsed during the prior drying and desorption process. While in desorption stage, water molecules have to escape from an already opened porous structure, thus requiring a relatively lower vapor pressure to maintain a specific moisture content[185].

Upon drying of the fresh samples, the water inside the cell lumen is the first to leave, till the point where the main water in the tissue is the water saturated inside the cell wall. The amount of water contained within the saturated cell wall is known as fiber saturation point (FSP)[184,185]. Water uptake/loss above this point has barely any influence on the dimension of secondary cell walls. However, adsorption/ desorption of water into the cell wall below this point results in anisotropic swelling/ shrinkage of the bulk tissue, and if restricted can exert large stresses[185]. This is exemplified by the use of wood to fracture rock. Dry wood is inserted into the hole and then wetted, generating stresses that can fracture the rock.

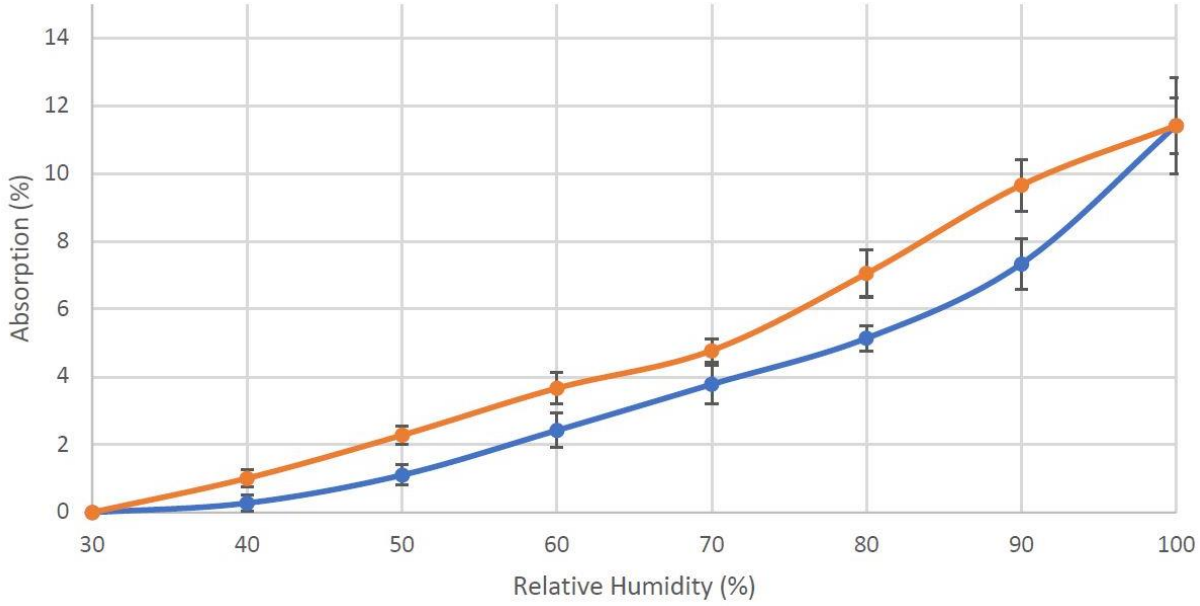

Figure 7-8 A sorption isotherm for pine cone. The equilibrium moisture content (the weight of the adsorbed water) is plotted as a function of the relative humidity (RH %). The blue line is the adsorption process and the orange line is the desorption process.

In order to unravel the actuation efficiency of the pine cone (the actuation force normalized by the tissue weight), the actuation force was tested by the experimental setup presented in Figure 7-9 (a). The cone scale with base part was fixed on the clamp tightly and the tip part was contacted

with load cell to record the generated bending force, which is actuated by immersing the cone scale in the hot water (~ 80 °C). The actuation force was recorded for 2 hours, until it is stabilized. After each test, the tested specimen was dehydrated for 24 hours in the desiccator, until the scale was retracted to the original position, and then another cycle of force test was conducted. The actuation force for four cycles tested from a representative specimen was shown in Figure 7-9 (b). Three major findings can be extracted:

First, since the hygroscopic actuation is based on the diffusion of water in pine cone tissue, the actuation force as the tissue is immersed in water also grows in an approximate linear manner, reaching a plateau when the tissue is fully hydrated.

Second, the actuation force generated by hydroscopic bending of pine cone scale is very impressive, which is around 8 to 13 N (measured at 25 °C and 50% humidity). Given the average weight of an isolated scale is ~ 1g, the hygroscopic bending of a cone scale can generate an actuation force up to 800 ~ 1300 times of its own weight, indicating that the actuation mechanism of pine cone is very efficient.

Third, as the cycles of the hydration-dehydration process continues, the maximum actuation force decreases. This c be attributed to the damage of tissue at each bending cycle. Since the swelling of the cone scale can generate large bending forces, the restriction of this bending movement causes the irreversible damage in the pine cone tissue, resulting the deterioration of the actuation performance.

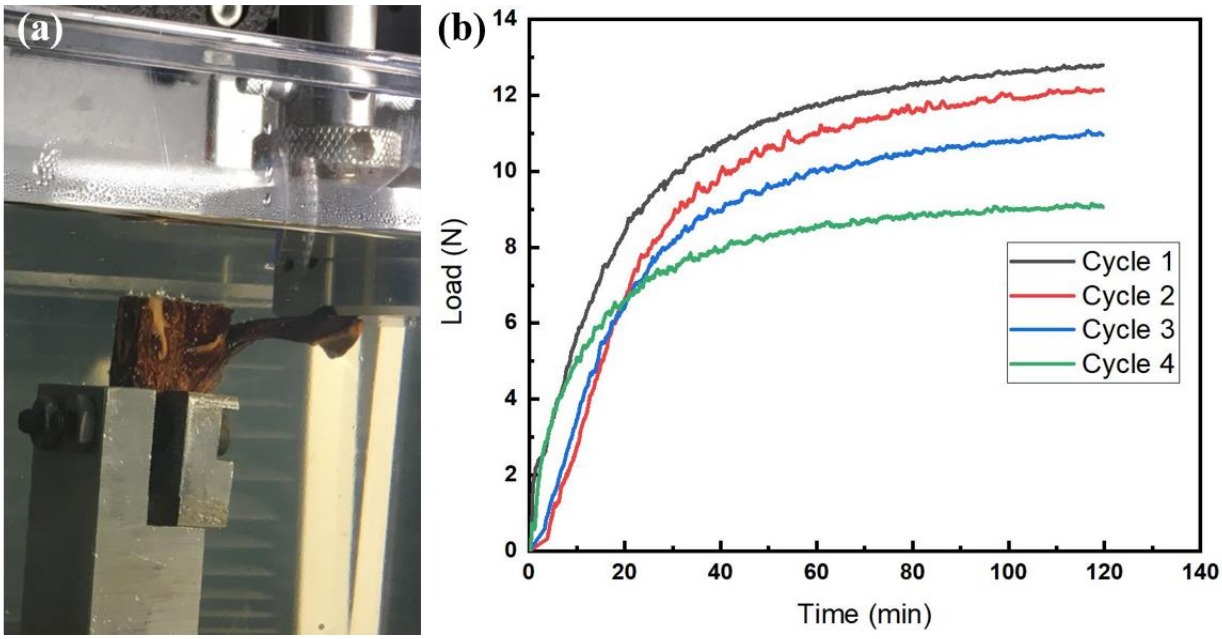

Figure 7-9 Actuation force test. (a) Experimental setup for the actuation force test. (b) The actuation force generated by the hygroscopic movement of one pine cone scale in successive cycles.

7.4 Summary

Many plants rely on the passive hygroscopic movements to disperse the seeds or improve their germination and the hydro-actuated bending of pine cone is one of the most well-known examples. Previous investigation attributes this humidity driven highly reversible deformation to the distinction of the cellulose microfibril angle in the bi-layered structure, causing differences in the directional swellability in the two layers; the mismatch of the swelling strain generates the bending movement. However, we found that in addition this, the porosity gradients in the tissue of the pine cone scale also contribute significantly to the bending deformation. This mechanism is validated by synthesized bi-layered hydrogels that we produced with distinct porosity in different layers. The combination of different microfibril angles for the two tissues comprising the pine cone (sclereid and sclerenchyma) and the gradient porosity confers the pine cone a highly efficient actuation mechanism to generate the intelligent reversible deformation stimulated by the environmental variation, which effectively improves the germination and survivability of pine cone. Our study may inspire people to develop more novel smart responsive materials with simpler simulative strategy and better biocompatibility.

Chapter 7, in part, is in preparation for publication with coauthors A. Pirosa, W. Yang, R. O. Ritchie and M. A. Meyers. The dissertation author is the first author of this work.

CHAPTER 8: CONCLUSIONS

In this dissertation, we presented our research on two topics about biological materials in detail. The first topic is the materials design for piscine defense. Driven by long history of evolution, mainly by the competition between predators and preys, fish develops numerous defense mechanisms and we grouped them into two types: the passive defense mechanism and the active one.

The passive defense mechanism developed by fish is their dermal armor: fish scales. The prevailing type of fish scale exists currently is the elasmoid scales, which protects most of living teleosts. They are overlapped with each other covering the entire fish body to provide effective shielding while retaining the overall flexibility and maneuverability. We fully investigated the structure and mechanical properties of elasmoid scales from three fish and unraveled their protection mechanisms. The major concluding remarks we found are listed as the following:

- Coelacanth fish scale. Coelacanth (*Latimeria chalumnae*) is a legendary lobe-finned fish with their morphology barely evolved in last several hundreds of million years. They have a primitive (less evolved) elasmoid scale with a unique interior structure: the loosely packed interbundle fibrils generate a matrix that acts as a binding material to confine the collagen fiber bundles in the lamellae into a double-twisted Bouligand arrangement with the external surface covered by a ridged thin mineral layer. Mechanical tensile testing coupled with SEM and in situ synchrotron SAXS revealed its unique deformation mechanisms. Such a hierarchical fibrous structure can effectively arrest crack propagation, constrain the delamination of the collagen fibrils, and enhance the stretching and sliding along the tension direction with large strain, which renders the coelacanth scale a tough material to resist predatory attacks.

- Carp fish scale: the carp (*Cyprinus carpio*) has typical modern elasmoid scales which are commonly found on teleosts. Compared with coelacanth scale, the ancient one, this more evolved scale exhibits structural simplification and mineral reduction. Although the carp scale also has a similar layered structure, a mineralized outer layer and a collagenous laminated inner core, the arrangement of collagen fibrils is different from that of coelacanth scale. The lamellae orientations in the carp scale successively rotates by 36°, forming a typical single-twisted *Bouligand* structure. Each lamella is made of thick tightly packed collagen fibrils with no evidence of the fiber bundles that are so prevalent in the primitive elasmoid scales of the coelacanth fish. The secondary 'threading' fibrils along the thickness direction, perpendicular to the lamellae, are less pronounced than that in coelacanth scales and are assumed to ensure the integrity of the scales by impeding the lamellae from separating when the scale is subjected to bending. We identified the deformation and failure mechanisms of the carp scale in Chapter 4, noting that the tensile properties are slightly anisotropic, while due to the double twisted Bouligand structure, the tensile behavior of coelacanth scale is more in-plane isotropic.
- Comparison between the carp and coelacanth scales. Using *in situ* small-angle x-ray scattering during tensile testing, the toughening mechanisms including the adaptive structural reorientation of lamellae, as well as fibrillar sliding and elastic deformation in the coelacanth and carp scale are quantified. Due to the lack of profuse interbundle fibrils, the lamellar fibrils in carp scale reach two local maxima strains at azimuthal angles of $\Psi = -20°$ and $\Psi = 10°$ to the tensile axis, instead of reaching a clear maximum fibrillar tensile strain in the tensile direction, as is the case for the coelacanth. With respect to adaptive structural reorientation within the carp scales under load, *in situ* SAXS measurements during mechanical straining of the scales demonstrate that the lamellae oriented closer to the tensile direction rotate towards it and the ones oriented far from

the loading direction rotate away from it. This behavior has been previously observed for arapaima and coelacanth fish scales. Along with lamellar rotation, fibrils closer to the loading direction are stretched whereas those closer to perpendicular to the loading direction are deformed in compression. These deformation mechanisms operate together to render the carp scale an excellent dermal armor. They may well provide further inspiration for the design advanced synthetic structural materials with unprecedented toughness and penetration resistance.

- Arapaima fish scale. The scales of arapaima provide effective protection to help them survive in the Amazon basin with piranha. Due to the larger size and higher mineralization, the arapaima scale can be prepared into fracture test specimens which is close to the requirement of a valid testing. We developed a new fixture for testing the fracture toughness of this excellent natural armor material. Our results indicate that arapaima scales exhibit an outstanding crack-growth toughness, which is high as 200 kJ.m-2 (equivalent to a stress intensity of approximatly 6.4 MPa.m½), indicating that they are the toughest biological materials based on our knowledge. This distinguished damage tolerance is conferred by various intrinsic and extrinsic toughening mechanisms to dissipate energy within the sub-layers through collagen fibrillar lamellar separation, collagen fibrillar bridging, sliding, and delamination.

- Active defense mechanisms of thorny catfish. The active defense mechanisms of thorny catfish (one of the armor catfish) is investigated by structural characterization and mechanical testing. They have two potent tactical weapons, the sharp pectoral spines and the midlateral scutes, to defend them actively when they are in danger. The pectoral spine can be locked by frictional force and the mechanisms are provided in detail in Chapter 6. Many catfish (Siluriformes) species have a similar mechanism as a mechanical active defense which expands their circumferential size thereby increases the handling time for predators and makes them an unfavorable prey choice.

Such locking ability is also associated with the stridulatory sounds produced by catfish, which serves as a warning signal to contribute to the active defense. In addition to the lockable spines, thorny catfish also possess two arrays of mid-lateral dermal scutes with sharp hooks, which also have potential cutting ability and provide supplementary active defense capability. Their materials design for these two weapons at the meso or micro levels, is as well impressive, conferring the pectoral spines and mid-lateral scutes excellent strength, and toughness at a small weight penalty. By combining all these mechanical active defense mechanisms, thorny catfish successfully avoid becoming an easy prey to predators and flourishingly survive in the various ecological environments in south America.

In the second topic, we firstly summarized some well-known hydro-actuated reversible deformation in biological systems. Many plants rely on the passive hygroscopic movements to disperse the seeds or improve their germination. These movements are accomplished by several mechanisms, including the anisotropic swelling of plant organs directed by cellulose microfibril angle in the cell wall, generated by gradient lignification, and hydro-actuated swelling enabled by the hierarchical foam-like structure. Some keratinous materials in animals such as bird feather, sheep horn and animal hair, and other biopolymers like spider silk, also manifest a highly reversible shape recovery effect stimulated by humidity change, Their shape memory capability is conferred by the dual-phase structure: the crystalline phase determines the permanent geometry and the abundant hydrogen bonds in the amorphous phase act as the ‘switch’ to tune the temporary shapes and recover them to original ones. Then we focused on the plant organs and investigated the one of the most famous examples, pine cone.

- The hydro-actuated reversible deformation of pine cone. Previous investigation attributes this humidity driven highly reversible deformation to the distinction of the cellulose microfibril angle in the bi-layered structure, which causes the different swellability in different layers and the mismatch of the swelling strain generates the bending movement. However, we found that in addition this, the porosity gradience in tissue of the pine cone scale also made significant contribution to the bending deformation. This mechanism is validated by the synthesized bi-layered hydrogels with distinct porosity in different layers. The combination of the distinction of microfibril angle and the gradient porosity confers the pine cone a highly efficient actuation mechanism to generate the intelligent reversible deformation stimulated by the environmental variation.

Through the investigation of the materials design for the passive and active piscine defense, we discovered several dermal armors and natural weapons which have outstanding mechanical properties superior to our synthetic structural materials. Our findings about the connection between the intricated hierarchical structures and the exceptional mechanical performance may well inspire innovative designs for new high-performance armor materials innovative robotics with gradient structures. Our investigation of the natural and bioinspired hydro-actuated self-shaping materials may inspire people to develop more novel smart responsive materials with simpler simulative strategy and better biocompatibility, which can fulfil different requirements in the rapid development of modern manufacturing industries based on the emerging artificial intelligence.

REFERENCES

1 Nalla, R. K., Kinney, J. H. & Ritchie, R. O. Mechanistic fracture criteria for the failure of human cortical bone. *Nat. Mater.* **2**, 164-168 (2003).

2 Suresh, S., Spatz, J., Mills, J.P., Micoulet, A., Dao, M., Lim, C.T., Beil, M. & Seufferlein, T. Connections between single-cell biomechanics and human disease states: gastrointestinal cancer and malaria. *Acta Biomaterialia* **1**, 15-30 (2005).

3 Lim, C. T., Zhou, E. H. & Quek, S. T. Mechanical models for living cells - A review. *Journal of Biomechanics* **39**, 195-216 (2006).

4 Yang, W., Sherman, V.R., Gludovatz, B., Schaible, E., Stewart, P., Ritchie, R.O. & Meyers, M.A. On the tear resistance of skin. *Nat. Commun.* **6**, 10 (2015).

5 Meyers, M. A., McKittrick, J. & Chen, P. Y. Structural Biological Materials: Critical Mechanics-Materials Connections. *Science* **339**, 773-779 (2013).

6 Simmons, A. H., Michal, C. A. & Jelinski, L. W. Molecular Orientation and Two-Component Nature of the Crystalline Fraction of Spider Dragline Silk. *Science* **271**, 84-87 (1996).

7 Keten, S., Xu, Z., Ihle, B. & Buehler, M. J. Nanoconfinement controls stiffness, strength and mechanical toughness of β-sheet crystals in silk. *Nat. Mater.* **9**, 359 (2010).

8 Launey, M. E., Buehler, M. J. & Ritchie, R. O. On the Mechanistic Origins of Toughness in Bone. *Annual Review of Materials Research* **40**, 25-53

9 Gao, H., Ji, B., Jäger, I. L., Arzt, E. & Fratzl, P. Materials become insensitive to flaws at nanoscale: Lessons from nature. *Proceedings of the National Academy of Sciences* **100** (2003).

10 Lin, A. Y.-M. & Meyers, M. A. Interfacial shear strength in abalone nacre. *Journal of Mechanical Behavior of Biomedical Materials* **2**, 607-612 (2009).

11 Yang, W., Chen I.H., Gludovatz, B., Zimmermann, E.A., Ritchie, R.O. & Meyers, M.A. Natural Flexible Dermal Armor. *Adv. Mater.* **25**, 31-48 (2013).

12 Wagner, D. O. & Aspenberg, P. Where did bone come from? An overview of its evolution. *Acta Ortho.* **82**, 393-398 (2011).

13 Ritchie, R. O. The conflicts between strength and toughness. *Nat. Mater.* **10**, 817-822 (2011).

14 Weiner, S. & Wagner, H. D. The material bone: Structure mechanical function relations. *Annual Review of Materials Science* **28**, 271-298 (1998).

15 Yang, C. Q., Wu, Z. S. & Ye, L. P. Self-diagnosis of hybrid CFRP rods and as-strengthened concrete structures. *J. Intell. Mater. Syst. Struct.* **17**, 609-618 (2006).

16 Inada, H., Okuhara, Y. & Kumagai, H. *Health monitoring of concrete structures using self-diagnosis materials*. (Springer, 2005).

17 Fukui, Y., Fukuda, M. & Fujimoto, K. Generation of mucin gel particles with self-degradable and -releasable properties. *J. Mat. Chem. B* **6**, 781-788 (2018).

18 Nakajima, N., Sugai, H., Tsutsumi, S. & Hyon, S. H. in *Asbm7: Advanced Biomaterials Vii* Vol. 342-343 *Key Engineering Materials* (eds Y. H. Kim *et al.*) 713 (Trans Tech Publications Ltd, 2007).

19 Hager, M. D., Greil, P., Leyens, C., van der Zwaag, S. & Schubert, U. S. Self-Healing Materials. *Advanced Materials* **22**, 5424-5430 (2010).

20 Wu, D. Y., Meure, S. & Solomon, D. Self-healing polymeric materials: A review of recent developments. *Progress in Polymer Science* **33**, 479-522 (2008).

21 Speck, O. & Speck, T. An Overview of Bioinspired and Biomimetic Self-Repairing Materials. *Biomimetics* **4**, 26 (2019).

22 Asquith, R. S., Blair, H. S., Crangle, A. A. & Riordan, E. Self-colored polymers based on anthraquinone residues. *J. Soc. Dye. Colour* **93**, 114-125 (1977).

23 Wang, Z., Ma, Z., Wang, Y., Xu, Z., Luo, Y., Wei, Y. & Jia, X. A Novel Mechanochromic and Photochromic Polymer Film: When Rhodamine Joins Polyurethane. *Advanced Materials* **27**, 6469-6474 (2015).

24 Oliver, K., Seddon, A. & Trask, R. S. Morphing in nature and beyond: a review of natural and synthetic shape-changing materials and mechanisms. *J. Mater. Sci.* **51**, 10663-10689 (2016).

25 Erb, R. M., Sander, J. S., Grisch, R. & Studart, A. R. Self-shaping composites with programmable bioinspired microstructures. *Nat. Commun.* **4**, 1712 (2013).

26 Gibson, J. S., Liu, X., Georgakopoulos, S. V., Wie, J. J., Ware, T. H., & White, T. J. Reconfigurable Antennas Based on Self-Morphing Liquid Crystalline Elastomers. *IEEE Access* **4**, 2340-2348 (2016).

27 Otsuka, K. & Ren, X. Physical metallurgy of Ti-Ni-based shape memory alloys. *Progress in Materials Science* **50**, 511-678 (2005).

28 Hager, M. D., Bode, S., Weber, C. & Schubert, U. S. Shape memory polymers: Past, present and future developments. *Progress in Polymer Science* **49-50**, 3-33 (2015).

29 Lai, A., Du, Z. H., Gan, C. L. & Schuh, C. A. Shape Memory and Superelastic Ceramics at Small Scales. *Science* **341**, 1505-1508 (2013).

30 Leng, J. S., Lan, X., Liu, Y. J. & Du, S. Y. Shape-memory polymers and their composites: Stimulus methods and applications. *Progress in Materials Science* **56**, 1077-1135 (2011).

31 Wang, Z., Li, K., He, Q. & Cai, S. A Light-Powered Ultralight Tensegrity Robot with High Deformability and Load Capacity. *Advanced Materials* **31**, 1806849 (2019).

32 He, Q., Wang, Z., Song, Z. & Cai, S. Bioinspired Design of Vascular Artificial Muscle. *Advanced Materials Technologies* **4**, 1800244 (2019).

33 Pikul, J. H., Li, S., Bai., H., Hanlon., R.T., Cohen, I. & Shepherd R. F. Stretchable surfaces with programmable 3D texture morphing for synthetic camouflaging skins. *Science* **358**, 210-214 (2017).

34 Geetha, M., Singh, A. K., Asokamani, R. & Gogia, A. K. Ti based biomaterials, the ultimate choice for orthopaedic implants - A review. *Progress in Materials Science* **54**, 397-425 (2009).

35 Lendlein, A. & Langer, R. Biodegradable, Elastic Shape-Memory Polymers for Potential Biomedical Applications. *Science* **296**, 1673-1676 (2002).

36 Stuart, M. A. C., Huck, W. T., Genzer, J., Müller, M., Ober, C., Stamm, M., Sukhorukov, G. B., Szleifer, I., Tsukruk, V. V., Urban, M., Winnik, F., Zauscher, S., Luzinov, I. & Minko, S. Emerging applications of stimuli-responsive polymer materials. *Nat. Mater.* **9**, 101 (2010).

37 Langer, R. & Tirrell, D. A. Designing materials for biology and medicine. *Nature* **428**, 487-492 (2004).

38 Fratzl, P. & Weinkamer, R. Nature's hierarchical materials. *Progress in Materials Science* **52**, 1263-1334 (2007).

39 Teyssier, J., Saenko, S. V., van der Marel, D. & Milinkovitch, M. C. Photonic crystals cause active colour change in chameleons. *Nat. Commun.* **6**, 7 (2015).

40 DeMartini, D. G., Krogstad, D. V. & Morse, D. E. Membrane invaginations facilitate reversible water flux driving tunable iridescence in a dynamic biophotonic system. *Proceedings of the National Academy of Sciences* **110**, 2552-2556 (2013).

41 Szulgit, G. K. & Shadwick, R. E. Dynamic mechanical characterization of a mutable collagenous tissue: response of sea cucumber dermis to cell lysis and dermal extracts. *J. Exp. Biol.* **203**, 1539-1550 (2000).

42 Thurmond, F. & Trotter, J. Morphology and biomechanics of the microfibrillar network of sea cucumber dermis. **199**, 1817-1828 (1996).

43 Allen, R. D. Mechanism of the Seismonastic Reaction in Mimosa pudica. *Plant Physiol* **44**, 1101-1107 (1969).

44 Stuhlman, O. & Darden, E. B. The Action Potentials Obtained from Venus's-Flytrap. *Science* **111**, 491-492 (1950).

45 Dawson, C., Vincent, J. F. V. & Rocca, A. M. How pine cones open. *Nature* **390**, 668-668 (1997).

46 Harrington, M. J., Razghandi, K., Ditsch, F., Guiducci, L., Rueggeberg, M., Dunlop, J. .W, Fratzl, P., Neinhuis, C., & Burgert, I. Origami-like unfolding of hydro-actuated ice plant seed capsules. *Nat. Commun.* 2, 337 (2011).

47 Armon, S., Efrati, E., Kupferman, R. & Sharon, E. Geometry and Mechanics in the Opening of Chiral Seed Pods. *Science* **333**, 1726-1730 (2011).

48 Elbaum, R., Zaltzman, L., Burgert, I. & Fratzl, P. The Role of Wheat Awns in the Seed Dispersal Unit. *Science* **316**, 884-886 (2007).

49 Abraham, Y., Tamburu, C., Klein, E., Dunlop, J. W., Fratzl, P., Raviv, U. & Elbaum, R. Tilted cellulose arrangement as a novel mechanism for hygroscopic coiling in the stork's bill awn. *J. Royal Soc. Interface 9*, 640-647 (2012).

50 Liu, Z. Q., Jiao, D. & Zhang, Z. F. Remarkable shape memory effect of a natural biopolymer in aqueous environment. *Biomaterials* **65**, 13-21 (2015).

51 Sullivan, T. N., Zhang, Y. L., Zavattieri, P. D. & Meyers, M. A. Hydration-Induced Shape and Strength Recovery of the Feather. *Advanced Functional Materials* **28**, 9 (2018).

52 Huang, W., Zaheri, A., Yang, W., Kisailus, D., Ritchie, R. O., Espinosa, H. & Mckittrick, J. How Water Can Affect Keratin: Hydration-Driven Recovery of Bighorn Sheep (Ovis Canadensis) Horns. *Advanced Functional Materials* **29**, 1901077 (2019).

53 Xiao, X. L. & Hu, J. L. Animal Hairs as Water-stimulated Shape Memory Materials: Mechanism and Structural Networks in Molecular Assemblies. *Scientific Reports* **6**, 12 (2016).

54 Agnarsson, I., Dhinojwala, A., Sahni, V. & Blackledge, T. A. Spider silk as a novel high performance biomimetic muscle driven by humidity. *J. Exp. Biol.* **212**, 1989-1993 (2009).

55 Liu, D., Tarakanova, A., Hsu, C. C., Yu, M., Zheng, S., Yu, L., Liu, J., He, Y., Dunstan, D. J. & Buehler, M. J. Spider dragline silk as torsional actuator driven by humidity. *Sci.Adv.* 5, eaau9183 (2019).

56 Yang, W., Sherman, V. R., Gludovatz, B., Mackey, M., Zimmermann, E. A., Chang, E. H., Schaible, E., Qin, Z., Buehler, M. J., Ritchie, R. O. & Meyers M. A. Protective role of Arapaima gigas fish scales: Structure and mechanical behavior. *Acta Biomaterialia* **10**, 3599-3614 (2014).

57 Yang, W., Gludovatz, B., Zimmermann, E. A., Bale, H. A., Ritchie, R. O. & Meyers, M. A. Structure and fracture resistance of alligator gar (Atractosteus spatula) armored fish scales. *Acta Biomaterialia* **9**, 5876-5889 (2013).

58 Chen, I. H., Kiang, J. H., Correa, V., Lopez, M. I., Chen, P. Y., McKittrick, J. & Meyers M. A. Armadillo armor: Mechanical testing and micro-structural evaluation. *Journal of the Mechanical Behavior of Biomedical Materials* **4**, 713-722 (2011).

59 Chen, I. H., Yang, W. & Meyers, M. A. Leatherback sea turtle shell: A tough and flexible biological design. *Acta Biomaterialia* **28**, 2-12 (2015).

60 Sire, J. Y., Donoghue, P. C. J. & Vickaryous, M. K. Origin and evolution of the integumentary skeleton in non-tetrapod vertebrates. *J. Anat.* **214**, 409-440 (2009).

61 Wang, B., Yang, W., Sherman, V. R. & Meyers, M. A. Pangolin armor: Overlapping, structure, and mechanical properties of the keratinous scales. *Acta Biomater.* **41**, 60-74 (2016).

62 Donoghue, P. C. J. & Sansom, I. J. Origin and early evolution of vertebrate skeletonization. *Microsc. Res. Tech.* **59**, 352-372 (2002).

63 Whitear, M. in *Biology of the Integument: 2 Vertebrates* (eds Jürgen Bereiter-Hahn, A. Gedeon Matoltsy, & K. Sylvia Richards) 8-38 (Springer Berlin Heidelberg, 1986).

64 Maderson, P. F. A. The Integument. A Textbook of Skin Biology. Volume 3 of Biological Structure and Function. R. I. C. Spearman. *The Quarterly Review of Biology* **49**, 269-270 (1974).

65 Sire, J. Y. & Huysseune, A. Formation of dermal skeletal and dental tissues in fish: a comparative and evolutionary approach. *Biological Reviews* **78**, 219-249 (2003).

66 Sire, J. Y. & Akimenko, M. A. Scale development in fish: a review, with description of sonic hedgehog (shh) expression in the zebrafish (Danio rerio). *Int. J. Dev. Biol.* **48**, 233-247 (2004).

67 Smith, M. M. & Hall, B. K. A developmental model for evolutoin of the vertebrate exoskeleton and teeth - the role of cranial and trunk neural crest. *Evol. Biol.* **27**, 387-448 (1993).

68 Smith, M. M. & Hall, B. K. Development and evolutionary origins of vertebrate skeletogenic and odontogenic tissues. *Biological Reviews* **65**, 277-373 (1990).

69 Bruet, B. J. F., Song, J., Boyce, M. C. & Ortiz, C. Materials design principles of ancient fish armour. *Nat. Mater.* **7**, 748 (2008).

70 Meinke, D. K. A review of cosmine: its structure, development, and relationship to other forms of the dermal skeleton in osteichthyans. *Journal of Vertebrate Paleontology* **4**, 457-470 (1984).

71 Janvier, P. *Early Vertebrates*. (Clarendon Press, 1996).

72 Sherman, V. R., Quan, H. C., Yang, W., Ritchie, R. O. & Meyers, M. A. A comparative study of piscine defense: The scales of Arapaima gigas, Latimeria chalumnae and Atractosteus spatula. *Journal of the Mechanical Behavior of Biomedical Materials* **73**, 1-16 (2017).

73 Murcia, S., Li, G., Yahyazadehfar, M., Sasser, M., Ossa, A. & Arola, D. Effects of polar solvents on the mechanical behavior of fish scales. *Mater. Sci. Eng. C-Mater. Biol. Appl.* **61**, 23-31 (2016).

74 Sherman, V. R., Yaraghi, N. A., Kisailus, D. & Meyers, M. A. Microstructural and geometric influences in the protective scales of Atractosteus spatula. *Journal of The Royal Society Interface* **13** (2016).

75 Zhu, D., Ortega, C. F., Motamedi, R., Szewciw, L., Vernerey, F. & Barthelat, F. Structure and Mechanical Performance of a "Modern" Fish Scale. *Advanced Engineering Materials* **14**, B185-B194 (2012).

76 Dastjerdi, A. K. & Barthelat, F. Teleost fish scales amongst the toughest collagenous materials. *Journal of the Mechanical Behavior of Biomedical Materials* **52**, 95-107 (2015).

77 Zimmermann, E. A., Gludovatz, B., Schaible, E., Dave, N. K., Yang, W., Meyers, M.A. & Ritchie, R. O. Mechanical adaptability of the Bouligand-type structure in natural dermal armour. *Nat. Commun.* **4**, 7 (2013).

78 Meyers, M. A., Lin, Y. S., Olevsky, E. A. & Chen, P. Y. Battle in the Amazon: Arapaima versus Piranha. *Advanced Engineering Materials* **14**, B279-B288 (2012).

79 Roberto, M. & Francois, B. Stretch-and-release fabrication, testing and optimization of a flexible ceramic armor inspired from fish scales. *Bioinspiration & Biomimetics* **11**, 066001 (2016).

80 Rudykh, S., Ortiz, C. & Boyce, M. C. Flexibility and protection by design: imbricated hybrid microstructures of bio-inspired armor. *Soft Matter* **11**, 2547-2554 (2015).

81 Funk, N., Vera, M., Szewciw, L. J., Barthelat, F., Stoykovich, M. P. & Vernerey, F. J. Bioinspired Fabrication and Characterization of a Synthetic Fish Skin for the Protection of Soft Materials. *ACS Applied Materials & Interfaces* **7**, 5972-5983 (2015).

82 Skotheim, J. M. & Mahadevan, L. Physical Limits and Design Principles for Plant and Fungal Movements. *Science* **308**, 1308-1310 (2005).

83 Forterre, Y., Skotheim, J. M., Dumais, J. & Mahadevan, L. How the Venus flytrap snaps. *Nature* **433**, 421-425 (2005).

84 Hofhuis, H. & Hay, A. Explosive seed dispersal. *New Phytologist* **216**, 339-342 (2017).

85 Llorens, C., Argentina, M., Rojas, N., Westbrook, J., Dumais, J. & Noblin X. The fern cavitation catapult: mechanism and design principles. *Journal of The Royal Society Interface* **13**, 20150930 (2016).

86 Evangelista, D., Hotton, S. & Dumais, J. The mechanics of explosive dispersal and self-burial in the seeds of the filaree, Erodium cicutarium (Geraniaceae). *The Journal of Experimental Biology* **214**, 521-529 (2011).

87 Rafsanjani, A., Brulé, V., Western, T. L. & Pasini, D. Hydro-Responsive Curling of the Resurrection Plant Selaginella lepidophylla. *Scientific Reports* **5**, 8064 (2015).

88 Elbaum, R. & Abraham, Y. Insights into the microstructures of hygroscopic movement in plant seed dispersal. *Plant Science* **223**, 124-133 (2014).

89 Fratzl, P., Elbaum, R. & Burgert, I. Cellulose fibrils direct plant organ movements. *Faraday Discuss.* **139**, 275-282 (2008).

90 Chaffey, N. Raven biology of plants, 8th edn. *Ann Bot* **113**, vii-vii (2014).

91 Wei, L. & McDonald, A. G. A Review on Grafting of Biofibers for Biocomposites. *Materials* **9**, 303 (2016).

92 Timoshenko, S. Analysis of Bi-Metal Thermostats. *J. Opt. Soc. Am.* **11**, 233-255 (1925).

93 Reyssat, E. & Mahadevan, L. Hygromorphs: from pine cones to biomimetic bilayers. *Journal of The Royal Society Interface* **6**, 951-957 (2009).

94 Rascio, N. & Rocca, N. L. Resurrection Plants: The Puzzle of Surviving Extreme Vegetative Desiccation. *Critical Reviews in Plant Sciences* **24**, 209-225 (2005).

95 Shen, J. H., Xie, Y. M., Zhou, S. W., Huang, X. D. & Ruan, D. Water-responsive rapid recovery of natural cellular material. *Journal of the Mechanical Behavior of Biomedical Materials* **34**, 283-293 (2014).

96 Wang, B., Yang, W., McKittrick, J. & Meyers, M. A. Keratin: Structure, mechanical properties, occurrence in biological organisms, and efforts at bioinspiration. *Progress in Materials Science* **76**, 229-318 (2016).

97 Wang, B. & Meyers, M. A. Light Like a Feather: A Fibrous Natural Composite with a Shape Changing from Round to Square. *Advanced Science* **4**, 1600360 (2017).

98 Huang, W., Zaheri, A., Jung, J. Y., Espinosa, H. D. & McKittrick, J. Hierarchical structure and compressive deformation mechanisms of bighorn sheep (Ovis canadensis) horn. *Acta Biomaterialia* **64**, 1-14 (2017).

99 Yu, Y., Yang, W. & André Meyers, M. Viscoelastic properties of α-keratin fibers in hair. *Acta Biomaterialia* **64**, 15-28 (2017).

100 Yu, Y., Yang, W., Wang, B. & Meyers, M. A. Structure and mechanical behavior of human hair. *Materials Science and Engineering: C* **73**, 152-163 (2017).

101 Ene, R., Papadopoulos, P. & Kremer, F. Combined structural model of spider dragline silk. *Soft Matter* **5**, 4568-4574 (2009).

102 Ene, R., Papadopoulos, P. & Kremer, F. Supercontraction in Nephila spider dragline silk – Relaxation into equilibrium state. *Polymer* **52**, 6056-6060 (2011).

103 Papadopoulos, P., Sölter, J. & Kremer, F. Hierarchies in the structural organization of spider silk—a quantitative model. *Colloid and Polymer Science* **287**, 231-236 (2009).

104 Sydney Gladman, A., Matsumoto, E. A., Nuzzo, R. G., Mahadevan, L. & Lewis, J. A. Biomimetic 4D printing. *Nat. Mater.* **15**, 413 (2016).

105 Huang, C., Wang, Z., Quinn, D., Suresh, S. & Hsia, K. J. Differential growth and shape formation in plant organs. *Proceedings of the National Academy of Sciences* **115**, 12359-12364 (2018).

106 Huang, C., Quinn, D., Suresh, S. & Hsia, K. J. Controlled molecular self-assembly of complex three-dimensional structures in soft materials. *Proceedings of the National Academy of Sciences* **115**, 70-74 (2018).

107 Reichert, S., Menges, A. & Correa, D. Meteorosensitive architecture: Biomimetic building skins based on materially embedded and hygroscopically enabled responsiveness. *Computer-Aided Design* **60**, 50-69 (2015).

108 Han, Y., Hu, J. & Chen, X. A skin inspired bio-smart composite with water responsive shape memory ability. *Materials Chemistry Frontiers* (2019).

109 Wu, Y., Shah, D. U., Wang, B., Liu, J., Ren, X., Ramage, M. H. & Scherman, O. A., Biomimetic Supramolecular Fibers Exhibit Water-Induced Supercontraction. Adv. Mater. 30, 5 (2018).

110 Denison, R. H. The early history of the vertebrate calcified skeleton. *Clin Orthop Relat Res* **31**, 141-152 (1963).

111 Schonborner, A. A., Boivin, G. & Baud, C. A. The mineralization processes in teleost fish scales. *Cell Tissue Res* **202**, 203-212 (1979).

112 Brown, G. A. & Wellings, S. R. Electron microscopy of the skin of the teleost, Hippoglossoides elassodon. *Z Zellforsch Mikrosk Anat* **103**, 149-169 (1970).

113 Zhu, D. J., Szewciw, L., Vernerey, F. & Barthelat, F. Puncture resistance of the scaled skin from striped bass: Collective mechanisms and inspiration for new flexible armor designs. *Journal of the Mechanical Behavior of Biomedical Materials* **24**, 30-401 (2013).

114 Torres, F. G., Malásquez, M. & Troncoso, O. P. Impact and fracture analysis of fish scales from Arapaima gigas. *Materials Science and Engineering: C* **51**, 153-157, (2015).

115 Murcia, S., Lavoie, E., Linley, T., Devaraj, A., Ossa, E. A. & Arola, D. The natural armors of fish: A comparison of the lamination pattern and structure of scales. *Journal of the Mechanical Behavior of Biomedical Materials* **73**, 17-27 (2017).

116 Smith, J. L. B. A living fish of Mesozoic type. *Nature* **143**, 455-456 (1939).

117 Forey, P. L. Golden jubilee for the coelacanth Latimeria-chalumnae. *Nature* **336**, 727-732 (1988).

118 Amemiya, C. T. *et al.* The African coelacanth genome provides insights into tetrapod evolution. *Nature* **496**, 311-316 (2013).

119 Hedges, S. B., Hass, C. A. & Maxson, L. R. Relations of fish and tetrapods. *Nature* **363**, 501-502 (1993).

120 Smith, J. L. The second Coelacanth. *Nature* **171**, 99-101 (1953).

121 Smith, J. L. B. LIVE COELACANTHS. *Nature* **176**, 473-473 (1955).

122 Fricke, H. & Hissmann, K. Natural habitat of coelacanths. *Nature* **346**, 323-324 (1990).

123 Millot, J. New facts about coelacanths. *Nature* **174**, 426-427 (1954).

124 Musick, J. A., Bruton, M. N. & Balon, E. K. *The biology of Latimeria chalumnae and evolution of coelacanths*. (Kluwer Academic Publishers, 1991).

125 Millot, J. 1st Observations on a living coelacanth. *Nature* **175**, 362-363 (1955).

126 Meunier, F. J. & Zylberberg, L. *The structure of the outer components of the scales of Latimeria chalumnae (Sarcopterygii : Actinistia : Coelacanthidae) revisited using scanning and transmission electron microscopy*. (Societe Francaise Ichtyologie, 1999).

127 Smith, M. The structure of the scales of Latimeria chalumnae. *Journal of zoology* **167**, 501-509 (1972).

128 Bigi, A., Burghammer, M., Falconi, R., Koch, M. H., Panzavolta, S. & Riekel, C. Twisted plywood pattern of collagen fibrils in teleost scales: An X-ray diffraction investigation. *Journal of Structural Biology* **136**, 137-143 (2001).

129 Sasaki, N. & Odajima, S. Stress-strain curve and Young's modulus of a collagen molecule as determined by the X-ray diffraction technique. *Journal of Biomechanics* **29**, 655-658 (1996).

130 Zimmermann, E. A., Schaible, E., Bale, H., Barth, H. D., Tang, S. Y., Reichert, P., Busse, B., Alliston, T., Ager, J. W. 3rd & Ritchie, R. O. Age-related changes in the plasticity and toughness of human cortical bone at multiple length scales. *Proceedings of the National Academy of Sciences* **109**, 11890-11890 (2012).

131 Lin, Y. S., Wei, C. T., Olevsky, E. A. & Meyers, M. A. Mechanical properties and the laminate structure of Arapaima gigas scales. *Journal of the Mechanical Behavior of Biomedical Materials* **4**, 1145-1156 (2011).

132 Liu, Z., Zhang, Z. & Ritchie, R. O. On the Materials Science of Nature's Arms Race. *Advanced Materials* **30**, 1705220 (2018).

133 Abrams, P. A. The evolution of predator-prey interactions: Theory and evidence. *Annual Review of Ecology and Systematics* **31**, 79-105 (2000).

134 François, J. M. Spatial Organization and Mineralization of the Basal Plate of Elasmoid Scales in Osteichthyans. *American Zoologist* **24**, 953-964 (1984).

135 Onozato, H. & Watabe, N. Studies on fish scale formation and resorption. *Cell and Tissue Research* **201**, 409-422 (1979).

136 Torres, F. G., Troncoso, O. P., Nakamatsu, J., Grande, C. J. & Gómez, C. M. Characterization of the nanocomposite laminate structure occurring in fish scales from Arapaima Gigas. *Materials Science and Engineering: C* **28**, 1276-1283 (2008).

137 Chen, P. Y., Schirer, J., Simpson, A., Nay, R., Lin, Y. S., Yang, W., Lopez, M. I., Li, J., Olevsky, E. A. & Meyers, M. A. Predation versus protection: Fish teeth and scales evaluated by nanoindentation. *J. Mater. Res.* **27**, 100-112 (2012).

138 Torres, F. G., Le Bourhis, E., Troncoso, O. P. & Llamoza, J. Structure-Property Relationships in Arapaima Gigas Scales Revealed by Nanoindentation Tests. *Polymers and Polymer Composites* **22**, 369-374 (2014).

139 Ikoma, T., Kobayashi, H., Tanaka, J., Walsh, D. & Mann, S. Microstructure, mechanical, and biomimetic properties of fish scales from Pagrus major. *Journal of Structural Biology* **142**, 327-333 (2003).

140 Gil-Duran, S., Arola, D. & Ossa, E. A. Effect of chemical composition and microstructure on the mechanical behavior of fish scales from Megalops Atlanticus. *Journal of the Mechanical Behavior of Biomedical Materials* **56**, 134-145 (2016).

141 Wakeling, J. M., Kemp, K. M. & Johnston, I. A. The biomechanics of fast-starts during ontogeny in the common carp cyprinus carpio. **202**, 3057-3067 (1999).

142 Arola, D., Murcia, S., Stossel, M., Pahuja, R., Linley, T., Devaraj, A., Ramulu, M., Ossa, E. A. & Wang J. The limiting layer of fish scales: Structure and properties. *Acta Biomaterialia* **67**, 319-330 (2018).

143 Marino Cugno Garrano, A., La Rosa, G., Zhang, D., Niu, L. N., Tay, F. R., Majd, H. & Arola, D. On the mechanical behavior of scales from Cyprinus carpio. *Journal of the Mechanical Behavior of Biomedical Materials* **7**, 17-29 (2012).

144 Bonwick, G. A., Witcomb, D. M., Davies, D. H. & Winstanley, S. Scale surface micro-structures of British freshwater cyprinidae. *Micron and Microscopica Acta* **20**, 247-253 (1989).

145 Esmaeili, H. R. & Gholami, Z. Scanning Electron Microscopy of the scale morphology in Cyprinid fish, Rutilus frisii kutum Kamenskii, 1901 (Actinopterygii: Cyprinidae). *IFRO* **10**, 155-166 (2011).

146 Liu, P., Zhu, D., Wang, J. & Bui, T. Q. Structure, Mechanical Behavior and Puncture Resistance of Grass Carp Scales. *Journal of Bionic Engineering* **14**, 356-368 (2017).

147 Murcia, S., McConville, M., Li, G., Ossa, A. & Arola, D. Temperature effects on the fracture resistance of scales from Cyprinus carpio. *Acta Biomaterialia* **14**, 154-163 (2015).

148 Browning, A., Ortiz, C. & Boyce, M. C. Mechanics of composite elasmoid fish scale assemblies and their bioinspired analogues. *Journal of the Mechanical Behavior of Biomedical Materials* **19**, 75-86 (2013).

149 Quan, H., Yang, W., Schaible, E., Ritchie, R. O. & Meyers, M. A. Novel Defense Mechanisms in the Armor of the Scales of the "Living Fossil" Coelacanth Fish. **28**, 1804237 (2018).

150 Launey, M. E. & Ritchie, R. O. On the Fracture Toughness of Advanced Materials. *Advanced Materials* **21**, 2103-2110 (2009).

151 Dirks, J. H. & Taylor, D. Fracture toughness of locust cuticle. *The Journal of Experimental Biology* **215**, 1502-1508 (2012).

152 Wu, J., Qin, Z., Qu, L., Zhang, H., Deng, F. & Guo, M. Natural hydrogel in American lobster: A soft armor with high toughness and strength. *Acta Biomaterialia* **88**, 102-110 (2019).

153 Wang, B., Sullivan, T. N., Pissarenko, A., Zaheri, A., Espinosa, H. D. & Meyers, M. A. Lessons from the Ocean: Whale Baleen Fracture Resistance. *Advanced Materials* **31**, 1804574 (2019).

154 Porter, D., Guan, J. & Vollrath, F. Spider Silk: Super Material or Thin Fibre? *Advanced Materials* **25**, 1275-1279 (2013).

155 Pereira, B. P., Lucas, P. W. & Swee-Hin, T. Ranking the fracture toughness of thin mammalian soft tissues using the scissors cutting test. *Journal of Biomechanics* **30**, 91-94 (1997).

156 Dirks, J. H. & Taylor, D. Veins Improve Fracture Toughness of Insect Wings. *PLOS ONE* **7**, e43411 (2012).

157 Song, J. H., Ortiz, C. & Boyce, M. C. Threat-protection mechanics of an armored fish. *Journal of the Mechanical Behavior of Biomedical Materials* **4**, 699-712 (2011).

158 ASTM E1820-17a, Standard Test Method for Measurement of Fracture Toughness, ASTM International, West Conshohocken, PA, 2017, www.astm.org.

159 Wegst, U. G. K., Bai, H., Saiz, E., Tomsia, A. P. & Ritchie, R. O. Bioinspired structural materials. *Nat. Mater.* **14**, 23 (2014).

160 Wegst, U. G. K. & Ashby, M. F. The mechanical efficiency of natural materials. *Philosophical Magazine* **84**, 2167-2186 (2004).

161 Derby, C. D., Kicklighter, C. E., Johnson, P. M. & Zhang, X. Chemical composition of inks of diverse marine molluscs suggests convergent chemical defenses. *J. Chem. Ecol.* **33**, 1105-1113 (2007).

162 van Gelder, R. G. The Biology of the Striped Skunk. *Journal of Mammalogy* **49**, 576-576 (1968).

163 Vandenspiegel, D., Jangoux, M. & Flammang, P. Maintaining the line of defense: Regeneration of cuvierian tubules in the sea cucumber Holothuria forskali (Echinodermata, Holothuroidea). *Biol. Bull.* **198**, 34-49 (2000).

164 Fudge, D. S. & Schorno, S. The Hagfish Gland Thread Cell: A Fiber-Producing Cell Involved in Predator Defense. *Cells* **5**, 25 (2016).

165 Blackburn, D. C., Hanken, J. & Jenkins, F. A. Concealed weapons: erectile claws in African frogs. *Biology Letters* **4**, 355-357 (2008).

166 Heiss, E., Natchev, N., Salaberger, D., Gumpenberger, M., Rabanser, A. & Weisgram, J. Hurt yourself to hurt your enemy: new insights on the function of the bizarre antipredator mechanism in the salamandrid Pleurodeles waltl. *Journal of Zoology* **280**, 156-162 (2010).

167 Vincent, J. F. V. & Owers, P. Mechanical design of hedgehog spines and porcupine quills. *Journal of Zoology* **210**, 55-75 (1986).

168 Knight, L. & Ladich, F. Distress sounds of thorny catfishes emitted underwater and in air: characteristics and potential significance. *J. Exp. Biol.* **217**, 4068-4078 (2014).

169 Bosher, B. T., Newton, S. H. & Fine, M. L. The spines of the channel catfish, Ictalurus punctatus, as an anti-predator adaptation: An experimental study. *Ethology* **112**, 188-195 (2006).

170 Forbes, L. S. Prey defense and predator handling behavior - the dangerous prey hypothesis. *Oikos* **55**, 155-158 (1989).

171 Wright, J. J. Adaptive significance of venom glands in the tadpole madtom Noturus gyrinus (Siluriformes: Ictaluridae). *J. Exp. Biol.* **215**, 1816-1823 (2012).

172 Birindelli, J. L. O., Fayal, D. F. & Wosiacki, W. B. Taxonomic revision of thorny catfish genus Hassar (Siluriformes: Doradidae). *Neotrop. Ichthyol.* **9**, 515-542 (2011).

173 Fine, M. L., Friel, J. P., McElroy, D., King, C. B., Loesser, K. E. & Newton, S. Pectoral spine locking and sound production in the channel catfish Ictalurus punctatus. *Copeia*, 777-790 (1997).

174 Liu, Z., Meyers, M. A., Zhang, Z. & Ritchie, R. O. Functional gradients and heterogeneities in biological materials: Design principles, functions, and bioinspired applications. *Progress in Materials Science* **88**, 467-498, (2017).

175 Carter, D. R. & Hayes, W. C. Bone Compressive Strength: The Influence of Density and Strain Rate. *Science* **194**, 1174-1176 (1976).

176 Nelson, J. S. *Fishes of the World*. (Wiley, 2007).

177 Vance, T. L. Variability in Stridulatory Sound Production in the Channel Catfish, Ictalurus punctatus. *Bios* **71**, 79-84 (2000).

178 Ladich, F. Comparative analysis of swimbladder (drumming) sounds in three families of catfishes. *Bioacoustics* **8**, 185-208 (1997).

179 Meyers, M. A. & Chen, P. Y. *Biological Materials Science: Biological Materials, Bioinspired Materials, and Biomaterials*. (Cambridge University Press, 2014).

180 Sun, J. Y., Zhao X., Illeperuma, W. R. K., Chaudhuri, O., Oh, K. H., Mooney, D. J., Vlassak, J. J. & Suo, Z. Highly stretchable and tough hydrogels. *Nature* **489**, 133-136 (2012).

181 He, Q. G., Wang, Z. J., Yan, Y. M., Zheng, J. L. & Cai, S. Q. Polymer nanofiber reinforced double network gel composite: Strong, tough and transparent. *Extreme Mech. Lett.* **9**, 165-170 (2016).

182 Dawson, J., Vincent, J. F. V. & Rocca, A. M. How pine cones open. *Nature* **390**, 668-668 (1997).

183 Sun, B., Wang, Z., He, Q., Fan, W. & Cai, S. Porous double network gels with high toughness, high stretchability and fast solvent-absorption. *Soft Matter* **13**, 6852-6857 (2017).

184 Engelund, E. T., Thygesen, L. G., Svensson, S. & Hill, C. A. S. A critical discussion of the physics of wood-water interactions. *Wood Sci. Technol.* **47**, 141-161 (2013).

185 Skaar, C. in *The Chemistry of Solid Wood* Vol. 207 *Advances in Chemistry* Ch. 3, 127-172 (American Chemical Society, 1984).